Studying of Some Mechanical Properties of Reactive Powder Concrete Using Local Materials

Mohammed Mansour Kadhum
Assistant Professor, PhD
Department of Civil Engineering
College of Engineering
University of Babylon
Email:drmohalkafaji@gmail.com

ABSTRACT

This research aims to investigate and evaluate a reactive powder concrete (RPC) cast using economical materials. Its mechanical properties were investigated and evaluated by studying the effects of using different cement and silica fume contents and locally steel fibers aspect ratios as reinforcement for this concrete. A compressive strength of about 155.2MPa, indirect tensile strength of 16.0MPa, modulus of elasticity of 48.7GPa, flexural strength of 43.5MPa, impact energy of 3294.4kN.m and abrasion loss 0.59% have been achieved for reinforced RPC contains 910 kg/m^3 cement content, silica fume content 185 kg/m^3 of cement weight and fiber volume fraction 2%. The water absorption values were 1.5 times higher for the normal strength concrete in comparison with the reactive powder concrete.

Keywords: reactive powder concrete, mechanical properties, abrasion, impact strength, steel fibers

دراسة بعض الخواص الميكانيكية لخرسانة المساحيق الفعالة باستخدم مواد محلية

أ.م.د. محمد منصور كاظم
قسم الهندسة المدنية
كلية الهندسة / جامعة بابل

الخلاصة

يهدف هذا البحث لتحري وتقييم خرسانة المساحيق الفعالة المصنوعة من استخدام مواد اقتصادية. تم دراسة وتقييم خواصها الميكانيكية باستخدام انواع مختلفة من السمنت وغبار السيلكا والياف الحديد المحلية الصنع. من النتائج العملية المستحصلة لوحظ بان مقاومة الانضغط للخرسانة كانت 155,2 ميكاباسكال، 16,0 ميكاباسكال مقاومة الشد الغير مباشرة، 48,7 ميكاباسكال معامل المرونة الاستاتيكي، 43,5 ميكاباسكال لمقاومة الانثناء، 3294,4 كن.م و 0.59% فقدان الاحتكاك وهذه القيم تحققت لخرسانة المساحيق الفعالة المسلحة بالالياف بنسة حجمية 2% والحاوية على سمنت 910 كغم/م^3 ومحتوى السيلكا 185 كغم/م^3 من وزن السمنت. اما مقدار الامتصاص فقد سجل من الشغل العملي 1.5 مرة اكثر للخرسانة الاعتيادية مقارنة بخرسانة المساحيق الفعالة.

الكلمات الرئيسية: خرسانة المساحيق الفعالة, الخواص الميكانيكية, الاحتكاك,مقاومة الصدم, الالياف الحديدية

1. INTRODUCTION

1.1 Background

The development of concrete material may be divided into several stages. The first is the traditional normal strength concrete (NSC). The second is the high strength concrete (HSC) that is considered to be the strongest and stiffest cement based material. HSC has a compressive strength of approximately 70 MPa, a flexural strength of about 10 MPa and a Young's modulus of 14 to 42 GPa. Now, given the improvements on a microscopic scale, the technology of the Reactive Powder Concrete (RPC) is covered by one of many patents in a range known as Ultra High Performance Concretes **,Xiaoa, et al., 2004.**

Reactive powder concrete (RPC) is a new generation concrete with ultra-high performance and it was developed through microstructure enhancement techniques for cementitious materials **,Richard and Cheyrezy, 1995.** As eliminated the coarse aggregates, reduced the water-cementitious material ratio, lowered the CaO to SiO_2 ratio by introducing the silica components, and incorporated steel micro-fibres **,Chan and Chu, 2004.** RPC has a remarkable strength and very high ductility. Its ductility is about 250 times higher than that of conventional concrete **,Shaheen, and Shrive, 2006.** Nowadays, RPC seems to be a promising material for special pre-stressed and precast concrete members. Due to ultra-high mechanical performance of RPC, the thickness of concrete elements can be reduced **, Aïtcin, 2003.**

RPC represents one of the most recent technological leaps witnessed by the construction industry. It lies at the forefront in terms of innovation, aesthetics and structural efficiency, **Prabha, et al., 2010.** This new family of materials has compressive strengths of 170 to 230 MPa and flexural strength of 30 to 50 MPa, depending on the type of fibers used **,Moallem 2010 and AL-Hassani, 2014.** Additionally, it has a tensile strength of between 6 and 13 MPa that is maintained after first cracking. The traditional concrete has tensile strengths on the order of 2 to 4 MPa that is lost when cracking occurs **,Washer, et al., 2003.** It has also an increased resistance to abrasion, erosion, corrosion and greatly reduced permeability to moisture, chlorides and chemical attack **,Moallem 2010 and Abdelrazig, 2008.** In order to achieve ultra-high strength and ductility, RPC should contain some steel micro-fibres and has a very low water-cementitious material ratio **,Talebinejad, et al., 2004.** When cracking appears on a very small scale, the fibres intervene to prevent the microscopic crack from being propagated and causing the ruin of the structure. During multi-cracking of material, action known as of "bridging" of cracks by fibres involves many micro-mechanisms.

One of the most significant assets of RPC is the improvement in compressive strength; RPC has been demonstrated to achieve compressive strengths ranging from 23-33 ksi (158-228MPa) **,Perry and Zakariasen, 2003.** This improvement in compressive strength has far exceeded the results achieved with conventional concretes and may allow for the possibility of RPC to be more competitive in markets that have been typically dominated by steel construction **,Harris, 2004.** The significant improvements in compressive strength are complimented by the fact that RPC also exhibits tensile strength that has not been demonstrated in conventional concretes. This tensile strength allows the material to support both pre-cracking and post-cracking loads without experiencing the brittle failure that would be common in a conventional concrete. RPC has demonstrated tensile strengths ranging from 0.9-1.7ksi (6-12) MPa with various curing regimes and standard ASTM testing methods **,Kjellsen** and **Atlassi, 1999.** These tensile strengths were achieved as a result of the interaction of the steel fibers on the microscopic level and their ability to sustain load after the onset of cracking **,Harris, 2004.**

In addition to the improvements in tensile strength, UHPC can also achieve flexural strengths ranging from 5,000–7,200 psi (35-50 MPa) **,Perry** and **Zakariasen, 2003.** This combination of

the tensile and flexural strength makes UHPC an extremely ductile material, capable of supporting significant loads beyond cracking **,Harris, 2004.**

Experimental study carried out on the tensile behaviour of different Ultra High Performance Fiber Reinforced Concrete (UHPFRC) mixes using four types of high strength steel fibers; straight with aspect ratio 65, hooked with aspect ratio 79, high twisted with aspect ratio 100, and low twisted with aspect ratio 100 with different volume fractions (1%, 1.5%, 2% and 2.5%). The results showed that both the tensile strength and the maximum post-cracking strain are significantly improved by using deformed steel fibers instead of smooth fibers. Moreover the path of the stress strain curves of UHPFRC reinforced with hooked steel fibers and UHPFRC reinforced with twisted steel fibers are similar up to the peak load of UHPFRC reinforced with hooked steel fibers. While UHPFRC reinforced with hooked steel fibers begins softening at post cracking strain $\varepsilon tp = 0.46\%$, UHPFRC reinforced with twisted steel fibers keeps increasing the tensile stress up to post cracking strain $\varepsilon tp \approx 0.6\%$ **,Wille, et al., 2011.**

The mechanical properties and impact resistance of RPC containing silica fume and ground granulated blast furnace slag (GGBFS) and fly ash as a replacement by weight of cement were studied. To improve ductility, steel fibers with polypropylene fibers in hybrid were used. All specimens were cured in 20°C and 90°C for 7, 14 and 28 days. The test results showed that the modulus of elasticity is 50 to 60GPa. Initial results from simple impact load test on 1000 mm square, and 100mm thick unreinforced slab supported on all sides, were very encouraging. The concrete on the top was powdered under repeated impacts but there was no indication of tensile cracking. After 70 impacts, a cone of concrete sheared off from the underside of the slab when the thickness of the slab had been reduced by the powdering on the top surface **,Marios, et al., 2003.** The mechanical properties and impact resistance of RPC were investigated. Tests on the mechanical properties indicated that RPC has enhanced tensile strength and ductility; i.e. Flexural strength values are likely to be between (30-60) MPa and fracture energies above 10000 J/m^2.It has been shown that concrete with compressive strength as high as 200 MPa and flexural strength as high as 40 MPa can be produced in the laboratory and the addition of steel fibers to the RPC mixes increase not only the flexural strength and ductility but also increase the compressive strength **,Soutsos, et al., 2001.**

1.2 Research Objectives

In this context, the present study is devoted to investigate the feasibility of manufacturing reactive powder concrete RPC mixtures with its ultra mechanical properties using locally available materials in Iraq. The main variables are; cement content, silica fume content and steel fibers. In this research, the available sand with its suitable size for this type of concrete and two types of cement ordinary Portland and sulphate resisting Portland cement are used instead of using expensive materials such as quartz powder and steel aggregates to produce comparable mixtures as most researchers do. The experimental test program is performed to study the behaviour of the RPC under the previous variables in compressive strength, modulus of elasticity, indirect tensile strength, flexural strength, water absorption and impact strength. In this research, the effect of compressive strength and number of blows on abrasion loss of normal and reactive powder concrete was taken into consideration. This research provides data for the researchers concerning main properties of RPC manufacturing using economical (local) available materials.

2. EXPERIMENTAL SET-UP

All tests in this research were carried out in the Construction Materials Laboratory in Civil Engineering Department, College Engineering, Babylon University. The materials used, preparing, casting, curing of test specimens and testing procedures were discussed in this section.

2.1 Materials

2.1.1 Cement

Two types of Portland cement, conforming to the IQS 5/1984 are used. The first type is ordinary Portland cement (OPC) and the other sulphate resistant Portland cement (SRPC) (ASTMC150- type I and type V) manufactured by united cement company commercially known (TASLUJA-BAZIAN). The chemical and physical properties of these types of cement are presented in **Table 1**. Test results indicate that the adopted cement conforms to Iraqi specifications **(IQS No.5/ 1984)**.

2.1.2 Silica fume

Silica fume has been used as a mineral admixture added to the RPC mixes of this study. It is a waste by-product of silicon and silicon alloys industry consisting mainly of non-combustible amorphous silica (SiO_2) particles. It was produced by Iraq Ferro Alloys Corporation. Silica fume is used with (20%) as replacement of cement. The chemical composition and physical requirements show that the silica fume conforms to the chemical and physical requirements of **ASTM C1240-05** specifications see **Table 2**.

2.1.3 Fine aggregate

Al-Ekhaider natural sand of 4.75mm was used as fine aggregate. The grading of original fine aggregate is shown in **Table 3**. The sand was washed and cleaned by water several times, later it was speared out and left in air to dry before use. Results indicate that fine aggregate grading is within the requirements of the Iraqi Specification No.45/1984. For RPC, very fine sand with maximum size 600µm was used. This sand was separated by sieving, its grading satisfied the fine grading in accordance with the Iraqi Specification No.45/1984. **Table 4** illustrates the sieve analysis of the separated fine sand. **Table 5** shows the specific gravity, sulfate, and absorption content of fine aggregate, the latter being within the requirements of the Iraqi specification No.45/1984.

2.1.4 Water

Clean, drinkable, fresh and free from impurities tap water used for both making and curing the tested specimens.

2.1.5 Admixtures superplasticizer: high range water reducing admixture

The high range water reducing admixture used in this study is a third generation super plasticizer for concrete and mortar, it is Aqueous solution of modified Polycarboxylates, which is known commercially as SikaViscocrete-5930.Itis High Performance Super plasticizer Concrete Admixture, It is imported from Sika company in Egypt. SikaViscocrete-5930 has been primarily developed for applications where the highest durability and performance are required.SikaViscocrete-5930 is free from chlorides and complies with **ASTM C494-99** type G and F. The technical description is shown in **Table 6**.

2.1.6 Steel fibers

Short discrete iron wire used as alternative of standard fiber which used at different volume fraction with aspect ratio (l/d = 37.5). The fibers are used to increase tensile capacity and improve ductility. The steel fibers used in this investigation are clean of rust or oil of straight steel wire fibers. The used steel fibers are chopped or cut from steel wires that locally used to link the reinforcement bar to the stirrups. The steel wires are cut into the desired length which was 30 mm omit. The fibers used are of diameter 0.8 ±0.02 mm where as the diameter that usually used in nearly all the research in producing RPC which was 0.2 mm. This type of fiber is very cheap in comparison with the other types of steel fibers and is available in all markets in Iraq. The fiber use confidence with **ASTM E 882** and the tensile test were done in laboratory of materials at the University of Babylon. The properties of the steel fibers used are shown in **Table 7**.

2.2 Determination of the Workability of Concrete Mixtures

The flowability was tested by the flow table test in accordance with ASTM C-1437. **Fig. 1** shows flow table device and workability test. The flow is the resulting increase in average base diameter of the mortar mass, expressed as a percentage of the original base diameter of flow table cone (100 mm), i.e.:

$$Flow, D_{flow} = \frac{D - 100}{100} \times 100$$

Where:

D: Average diameter of the spread mix measured in four directions, (mm).

2.3 Strength Activity Index for Mineral Admixture

Reference and high performance mortars were prepared for pozzolanic activity. All mortars consist of 1 part of cement or cementitious materials and 2.75 parts of graded standard sand by weight in accordance with ASTMC311-05. **Table 8** shows w/c or w/cm ratio and pozzolanic activity index. The pozzolanic activity index (P.A.I.) with Portland cement was determined as follows, according to **ASTM C311-05**.

P.A.I. = (A/B) ×100

Where:

A: average compressive strength of test mix cube.

B: average compressive strength of reference mix cube.

2.4 Mixing Procedure

All trial mixes were performed in a small rotary mixer of 0.01m^{3}capacity, while the mixes of RPC specimens were performed in a rotary mixer of 0.09 m^3 for RPC concrete. Before using the mixer, any remaining concrete from previous batch was cleaned off. A damp cloth was used to wipe the pan and the blades of the mixer. The silica fume powder was mixed in dry state with the required quantity of cement for 5 minutes to ensure uniform dispersion of the reactive powder particles throughout the cement particles. Then, fine sand was loaded into the mixer and mixed for 5 minutes. The required amount of tap water was added to the rotary mixer within 1 minute. Then all the super plasticizers were added and mixed for an additional 5 minutes. When steel fibers were used, they were introduced, and dispersed uniformly. These were added slowly to the rotary mixer after the rest of the materials had been properly mixed and the concrete had a wet appearance and mixed for an additional 2 minutes. The same mixing procedure, schematized in

Fig. 2, was rigorously applied for each batch. The mixing of one batch requires approximately 20 minutes from adding water to the mix.

2.5 Mixtures Proportions

The mixture ratios were based on guidelines and specifications given in several different approaches presented in literature. The composition of normal weight concrete (NC) with water-to-cement ratio (W/C) of 0.35 is given in Table 8. Cement dosage of RPC is generally higher than 1000 kg/m^3 to achieve ultra-high strength under very low water/cement ratios. A high amount of cement not only affects the production costs, but also has negative effects on the heat of hydration and may cause shrinkage problems. Mineral admixtures can be a feasible solution to overcome these problems in RPC. **Table 9** summarizes the mixture designs of RPC produced in this study; the water-cementitious material ratio of 0.175 used in this study is also included in this table.

2.6 Concrete Samples

Samples were divided into four groups. (i) standard cubes of dimensions 50×50×50 mm for measuring the compressive strength and water absorption, (ii) cylinders of 100 mm diameter and 200 mm height for measuring the indirect tensile strength and the modulus of elasticity and (iii) prisms of 50×50×300 mm to measure the flexural strength and (iv) cylinders of 150 mm diameter × 65 mm height for measuring the impact strength. All tests in this research were carried out to investigate the main properties of RPC samples as reported in this section.

2.7 Compressive Strength and Water Absorption Test

The compressive strength test was carried out according to **B.S: 1881: part 116** using a digital testing machine with a capacity of 2000 kN. Three cubs were cast for each mix at each age, for determination of compressive strength. Cubes were removed from curing solution at age of 3, 28 and 56 days.

In general, either the **ASTM C642 or BS1881:122** standards can be used for the water absorption test of RPC specimens. In this study, the latter was referred to. The cylindrical specimens were dried in oven for 24 hours first and then its oven-dried weight was measured denote by WD. Then the dried specimens were saturated completely in water for one hour, one day, three days and seven days, respectively. Then the specimens were taken out of water, wiped out the excessive water on the surface of specimen with cloth and measured its saturated weight denoted as WW. The water absorption ratio Ra is simply defined as

$$R_a = \frac{W_W - W_D}{W_D} \times 100\% \tag{1}$$

1) Prism Flexural Test: The concrete modulus of rupture was determined by testing prism specimens in conformity with **ASTM C 78-02**. Each prism was simply supported and subjected to a two point loading using an electrical testing machine with a capacity of 2000 kN.

2) Tension Test: Indirect tension test (splitting method) has been determined by testing standard cylinders for every mix depending on **ASTM C496-05** specification. A 2000 KN capacity compression testing machine was used.

3) Modulus of Elasticity Test: This test was carried out on cylindrical specimens. The 40% of ultimate compressive strength of concrete specimen was applied on the concrete cylinders to perform the elastic modulus test as specified by **ASTM C-469**. The specimens were tested at age

28 days and the average of three specimens was adopted. A 2000 kN capacity compression testing machine was used to apply a compressive axial load and compress meter (dial gauge with accuracy 0.01 mm and a maximum capacity of 10 mm) was used.

4) Impact Strength Test: The impact resistance (dynamic energy absorption as well as strength) is one of the important attributes of RPC and there are several methods to find impact resistance, the test done according **ACI 544.2R**, using drop-weight test which is modified according CBR hummer test using three cylinders at 28 days age. **Fig. 3** states the device and specimen tested. The test measure the impact resistance depending on number of blows necessary to cause prescribed levels of distress in the test specimen. The hammer is dropped repeatedly, and the numbers of blow cause first visible crack on the top and cause ultimate failure are both records.

The test specimen is supported by a rigid base. In practice both supports and boundary conditions of a fiber concrete element may be quite different from those adopted in the test. The manual application of the impact load tends to be tedious and inconvenient particularly if several hundreds of blows are required to produce final failure. Nevertheless the falling weight test method appears to take into account the properties of the matrix, the nature of the fiber, the nature of interfacial zone between particles of the matrix as well as between fiber surface and matrix. Impact toughness of RPC was measured by number of blows for first crack and failure, using the equation blow:-

$$W=n\times m\times g\times h \quad (2)$$

Where,

W: impact energy (Joule (J) or kN.m);

n: impact number;

h: the height hammer drops (457mm);

g: accelerating velocity (9.81m/s^2);

m: weight of hammer (4.536kg).

5) Abrasion Test: The abrasion resistance of NSC and RPC was measured through testing according to **ASTM C944**, in which a rotating abrading wheel bears on and wears away the concrete surface for a period of two minutes. One modification to the standard test method was made in this program. The reported test results are the product of 10 total minutes of abrasion representing five two-minute cycles completed on each specimen. The abrasion testing was performed on three specimens from each of the NSC and RPC. However, as abrasion resistance is highly dependent on the surface condition of the concrete, each specimen was tested on three different surfaces. First, all specimens were tested on the surface formed by casting NSC and RPC against the steel mould in which they were produced. Following these tests, the cast (and now abraded) surface was sandblasted until it displayed a uniform texture. The testing was then repeated for this sandblasted surface. Finally, the testing was again repeated for all the specimens subsequent to having the test surface ground plane using a cylinder end grinder. The weight loss due to abrasion was measured.

3. TEST RESULTS AND DISCUSSION

3.1 Mechanical Properties

The test results for mechanical properties in this study are summarized in **Table 10**. The compressive strength is one of the important properties of hardened RPC, and in general, is the characteristic material value for the classification of concrete in national and international codes. To study the effect of different types of cement and fiber contents on compressive strength of RPC and NC, several mixes were tested at ages of (3, 28 and 56) days to determine strength

development as a function of age, three cubes are used within this test. The highest measured 28-day compressive strength values for the mixes of the NC and RPC specimens are shown in **Fig. 4.**

It is obvious from the results slight increment compressive strength of concrete by (7.4, 11.1, 17.0 and 23.6) % from mixes contain steel fibers (0.5, 1, 1.5, 2) % volume fraction respectively relative to the control (RPC without steel fiber) for both types of cement approximately at the age of test 28 days. The development of compressive strength for RPC may be come from the effect of high performance superplasticizer (visco crete 5930) as a water reduction on compressive strength, and because the low water cementitious ratio used in RPC mixes. Over and above the chemical reaction of (pozzolanic materials) micro silica fume with calcium hydroxide released from cement hydration leading to improve compressive strength, reduce the micro cracking, reduce voids and strengthen the microstructure. The chemical reaction starts at early ages 3days, and increases till the age of 28 days. It is noted that, unlike the normal weight concrete specimens with the failure modes of either in crushed state or two separated pieces, these failed RPC specimens are still kept together by the steel fibers

The flexural strength, expressed as the modulus of rupture. The values of flexural strength of the specimens considered in the present investigation are summarized in **Table 10** and plotted in **Fig. 5**. It is worthwhile to note that the fibrous concrete mixes really standout higher in the flexural strength when compared to the non-fibrous concrete mixes for both concrete NC and RPC. Results presented in Table above indicated that for mixes which contain steel fiber of volumetric ratio (0.5, 1, 1.5, and 2) % respectively, the modulus of rupture after 28 days of curing increased by (38.3, 58.7, 100.4 and 109.6) % and (38, 57.6, 96.2 and 107.1) % for ordinary Portland cement and sulfate resisting cement respectively relative to the reference concrete mix that is without fibers. RPC also shows significant increase in flexural tensile strength in comparison with normal concrete, where this increment is about five times that for the normal concrete. It is obvious from the results that the addition of steel fibers to normal concrete increased flexural strength, where this increment is about 1.5 times that for the normal concrete.

The tensile strength of NC and RPC is much lower than the compressive strength, because of the ease with cracks which propagate under tensile loads, and is usually not considered in design. However, it is an important property, since cracking in concrete is most generally due to the tensile stresses that occur under load, or due to environmental changes. The tensile strength increases with age for all mixes as shown in **Fig. 6**. All fibrous mixes demonstrated higher splitting tensile strength relative to plain mix at all curing ages. Splitting tensile strength indicated significant increase in strength due to the inclusion of steel fibers. The split-cylinder loading configuration causes vertical compressive stress and lateral tensile stress in the cylinder. This biaxial stress state has a definite effect on the post cracking behavior while the cylinders with fibers are cracked at failure without separation. The mode of failure in RPC cylinders without micro steel fiber is done by splitting the specimen into two symmetrical parts whereas the mode of failure in specimen with steel fiber was done by splitting the specimen but still as one mass with crack along the specimen. The mode of failure in normal concrete NC without steel fiber was done by splitting the specimen to two parts with crashing some parts of the specimen but the specimen with steel fiber was splitting and stills the parts together and there were lateral side cracks.

The modulus of elasticity is strongly influenced by the concrete materials and their proportions, **MAHDI, 2009**. The static modulus of elasticity results for all mixes is presented in **Table 10** and **Fig. 7**. It can be noticed that the increase in steel fibers ratio show only slight increases in the static modulus of elasticity. This may be because the modulus of elasticity was calculated to the

stress corresponding to 40% of the ultimate load, so it is determined prior to concrete cracking; therefore, the fibers were not activated. The highest value of 51.3GPa was measured in the mix (NRPC2). The lowest value of the modulus of elasticity which equalled slightly over 26.2GPa was measured in the case of the mix (SNC0). The types of cement did not have significant effect on the measured values. In general, the modulus of elasticity increased due to the presence of steel fiber and silica fume.

Brittleness factor is the ratios between splitting tensile strength to compressive strength which represent the degree of hardness of fiber reinforce concrete which increased with the increase of volume fraction friction of fiber. The values of the Brittleness factor for all main types of mixes are shown in **Fig. 8**. In this figure, the graph of coefficient of brittleness is increasing by increasing the volume fraction friction of fiber. This result indicates that splitting tensile strength of RPC shows ability well because of tensile performance of fibers. Depending on this experimental result, increase of volume fraction friction of fiber helped rise of ductile behavior of RPC. The ratios of decrease for water absorption are in range of 49.0 to 66.7% imply this test method although is rather simple but seem to properly reflect the function of pozzolanic reaction and type of cement and shown in **Fig. 9**.

In the **Figs. 10 and 11,** the graph of brittleness factor is reducing by increasing the volume fraction of fibers. This result indicates that splitting tensile strength of concrete fibered shows ability well because of tensile performance of steel fibers. Depending on this experimental result, increase of volume fraction of fibers helped rise of ductile behavior of NC and RPC.

3.2 Impact Strength and Abrasion Test

Improved impact resistance is one of the important attributes of RPC. The number of blows required causing first crack and ultimate failure for reference and RPC reinforced with different percent of volume fraction of steel fiber are summarized in **Table 11** and plotted in **Fig.12. Fig. 13** reveals the fracture toughness increased with increased fiber volume. This behaviour related to the bond strength between the steel fiber and cement paste. The test results illustrate that the number of blows or the energy required causing initial crack and ultimate failure for RPC specimens reinforced with different volume fraction of steel fibers is higher than that of reference concrete. It is clear that the impact strength or the number of blows causing first crack and ultimate failures significantly increase as the fiber content increases and for different types of cement. Generally using ordinary Portland cement show higher impact strength (No. of blows) at both first crack and ultimate load than sulphate resisting cement for both types of concrete NC and RPC. It can be recognized that the failure surfaces of the fiber reinforced concrete specimens differ clearly from those of the plain concrete through the specimen of non-fiber reinforced dispread to several pieces in less number of blow after the first crack appears while fiber reinforced specimens still almost together after ultimate failure and displayed different modes of failure. Although the falling weight test is a simple, practical test carried out under rather arbitrary conditions and can give an indirect assessment of the

- The test specimen is supported by a rigid base. In practice both supports and boundary conditions of a fiber concrete element may be quite different from those adopted in the test.
- The manual application of the impact load tends to be tedious and inconvenient particularly if several hundreds of blows are required to produce final failure.

Nevertheless the falling weight test method appears to take into account the properties of the matrix, the nature of the fiber, the nature of interfacial zone between particles of the matrix as well as between fiber surface and matrix.

Abrasion resistance can be an important parameter for any concrete that is exposed to contact with other materials. The average weight loss per 2 minute abrading results is shown in **Fig. 14**. The highest value of 3.82% was measured in the SNC0 mix. The lowest value of the abrasion loss which equaled slightly over 0.59% was measured in the case of the NRPC2 mix. The type of cement did not have significant effect on the measured values. In general, the abrasion loss decreased due to the presence of steel fibers and depended on the type of concrete. The addition of steel fiber in the composite produces a denser and stronger surface, which results in a higher resistance to abrasion. It is obvious that particle loss under mechanical abrasion effect is much more difficult in the vicinity of steel fibers. Results indicated that addition of steel fibers (2%) decreased weight loss due to abrasion by 45% and 44% for RPC and NC respectively. RPC demonstrated very low abrasion compared to NC. This result was more pronounced in the case of plain matrices.

Fig. 15 shows the relationship between compressive strengths and mass losses for NC and RPC. Mechanical properties were compared with abrasion loss values and a good correlation was obtained. The relations follow exponential functions. It is well known that compressive strength is the most important factor governing the abrasion resistance of concrete **(Laplante, et al., 1991)**. Steel fiber reinforcement improves not only flexural performance but also compressive strength in the case of ultra-high performance concrete. Furthermore, relationship between the compressive strength of fiber reinforced RPC and the mass loss is meaningful.

3.3 Statistical Evaluation of Test Results

The compressive strength, number of blows and abrasion loss are given in Table 12. A multiple regression analysis was applied to obtain the following relationship among compressive strength, number of blows and loss on abrasion.

The comparison of experimental and estimated loss on abrasion (obtained from Eq. 3) as well as 95 % confidence intervals is shown in **Fig. 16**. The estimated values are in excellent agreement with the experimental values obtained in this study. The coefficient of correlation between estimated and experimental values is 95%. In the other words, with a few exceptions, the differences between calculated and experimentally obtained values are within a range of ±2.45.

$$LOA=4.67-0.0037\times NB-0.022\times fc \quad (3)$$

Where,

LOA : 28-day abrasion loss of normal and reactive powder concrete,

fc : 28-day compressive strength of concrete, (MPa),

NB : number of blows.

4. CONCLUSION

The presented results showed that it is feasible to produce reactive powder concretes from locally materials applying reactive powder concretes principles and packing density theories. The 28-day compressive strength and the rheology of the normal and of the reactive powder concretes appeared to be comparable. A compressive strength of 172.4MPa, indirect tensile strength of 17.1MPa, modulus of elasticity of 51.3GPa and flexural strength of 48.2MPa were approached for steel fibers reactive concrete samples of 910 kg/m^3 cement content and 230 kg/m^3 silica fume (NRPC2). The use of fine sand whose grain size is (<600μm) improves the compressive strength due to the more dense microstructure of the cement matrix. RPC without fibers is a brittle material and fails suddenly and violently.

The addition of steel fiber to concrete increases the impact resistance of the composite significantly. The increase in the steel fibers volume fraction and using ordinary Portland cement

led to a good increase in the impact resistance of the normal concrete and RPC specimens. Also addition of steel fibers in discrete forms to RPC changes its brittle mode of failure into a more ductile. It is recommended to use of steel fibers as an enhancing material to RPC. It seems that RPC is a good alternative material under mechanical abrasion exposure due to heavy traffic loads. The abrasion loss of NC and RPC can be estimated from compressive strength and number of blows results. The proposed equation has a sufficient reliability.

Finally, it can produce an economic RPC using locally available materials in Iraq, in order to manufacturing a pre-cast ultra high strength concrete with ultra mechanical properties (RPC). Further improvement of the mechanical properties of normal and reactive powder concretes could be achieved by, for instance, incorporation of locally fibers or non-fibers either in both concretes or only in the transition zone. In this case a more detailed study is needed.

5. ACKNOWLEDGMENTS

We wish to thanks the Department of Civil Engineering, College of Engineering, Babylon University for providing an opportunity to do project work in the laboratory. National Center for Construction Laboratories and Researches (NCCLR) in Baghdad Governorate.

References

Xiaoa, J., Schneiderb, H., Donneckeb, C., and Konigb, G., 2004, *Wedge Splitting Test on Fracture Behaviour of Ultra High Strength Concrete*, Construction and Building Materials, 18:359-365.

Richard, P., and Cheyrezy, M., 1995, *Composition of Reactive Powder Concretes*, Cement and Concrete Research, 25(7), 1501-1511.

Shaheen, E., and Shrive, N., 2006, *Optimization of Mechanical Properties and Durability of Reactive Powder Concrete*, ACI Materials Journal, 103(3), 444-451,.

Aïtcin, PC., 2003, *The Durability Characteristics of High Performance Concrete*, A review Journal Cement Concrete Composite, 25(3), 409-420.

Prabha., S.L, Dattatreya, J.K., Neelamegam, M., and Seshagirirao, M.V., 2010, *Study on Stress-Strain Properties of Reactive Powder Concrete under Uniaxial Compression*, International Journal of Engineering Science and Technology 2(11):6408-6416.

Washer, G., Fuchs, P., and Graybeal, B., 2003, *Elastic Properties of Reactive Powder Concrete*, International Symposium on Nondestructive Testing in Civil Engineering (NDT-CE 2003), Germany.

Moallem, M.R., 2010, *Flexural Redistribution in Ultra-High Performance Concrete Lab Specimens*, M.Sc. Thesis, *Russ College of Engineering and Technology*, Ohio University, USA.

Al-Hassani, H.M., kalil, W.I., and Danha, L.S., 2014, *Mechanical Properties of Reactive Powder Concrete with Various Steel Fiber and Silica Fume Contents*, Acta Tehinca Corviniensis, Bulletin of Engineering Tom.

Abdelrazig, B., 2008, *Properties and Applications of CeraCem Ultra High Performance Self Compacting Concrete*, Proceeding of the International Conference on Construction and Building Technology 20:217-226.

Talebinejad, I., Bassam, SA., Iranmanesh, A., and Shekarchizadeh, M., 2004, *Optimizing Mix Proportions of Normal Weight Reactive Powder Concrete with Strengths of 200-350 MPa Ultra High Performance Concrete (UHPC)*, International Symposium on Ultra High Performance Concrete, 133-141.

Perry, V.H., and Zakariasen, D., 2003, *Overview of UHPC Technology, Materials, Properties, Markets and Manufacturing*, Concrete Bridge Conference, Orlando, FL.

Harris, D. K., 2004, *Characterization of Punching Shear Capacity of Thin UHPC Plates*, Faculty of the Virginia Polytechnic Institute and State University.

Kjellsen, K. O., and Atlassi, E. H., 1999, *Pore Structure of Cement Silica Fume Systems Presence of Hollow-Shell Pores*, Cement and Concrete Research, 29(1): pp.133-142.

Wille, K., Kim, D. J., and Naaman, A. E., 2011, *Strain-Hardening UHP-FRC with Low Fiber Contents*, Materials and Structures, Vol. 44, No.3, pp. 583-598.

Marios, N.S., Stephen, G.M., and Konstantinos, K., 2003, *Mix Design, Mechanical Properties and Impact Resistance of Reactive Powder Concrete (RPC)*, Report Prepared for Department of Civil Engineering, The University of Liverpool, Liverpool, UK., pp.1-10.

Soutsos, M., Millard, S., and Karaiskos, K., 2001, *Mix Design, Mechanical Properties, and Impact Resistance of Reactive Powder Concrete (RPC)*, University of Liverpool, Liverpool, UK, pp. 1-10.

Iraqi Specification, No. 5, 1984, *Portland Cement*, Ministry of Planning, Central Organization for Standardization and Quality Control.

ASTM C 1240, 2005 *Standard Specification for the Use of Silica Fume as a Mineral Admixture in Hydraulic Cement Concrete*, Mortar and Grout", Vol. 4, pp. 1.

Iraqi Specification, No. 45, 1984, *Aggregate from Natural Sources for Concrete and Construction*, Ministry of Planning, Central Organization for Standardization and Quality Control.

ASTM C494-99, 1999, *Chemical Admixture for Concrete*, Annual Book of ASTM Standards American Society for Testing and Materials, Vol.04-02, PP. 245-252.

ASTM C311-02, 2002, *Standard Test Method for Sampling and Testing Fly Ash or Natural Pozzolans for Use in Portland Cement Concrete*, Annual Book of ASTM Standard American

Society for Testing and Materials, Vol. 04.02.

B.S. 1881, part 116, 1989, *Method of Determination of Compressive Strength of Concrete Cubes*, British Standards Institution.

ASTM C78-02, 2002, *Standard Test Method for Flexural Strength of Hydraulic-Cement Mortars*, Vol. 04.02, 6pp.

ASTM C 496/C 496M, 2005, *Standard Test Method for Splitting Tensile Strength of Cylindrical Concrete Specimens*, Vol. 04.02.

ASTM C469-02, 2002, *Standard Test Method for Static Modulus of Elasticity and Poisson's Ratio of Concrete in Compression*.

ACI Committee 544, 1989, *Measurement of Properties of Fiber Reinforced Concrete*, (ACI 544R.2-R99), American Concrete Institute, Detroit.

MAHDI, B.S., 2009, *Properties of Self Compacted Reactive Powder Concrete Exposed to Saline Solution*, Ph.D. Thesis, Building and Construction Engineering Department, University of Technology, Baghdad, p.223.

Laplante, P, Aitcin, P.C, and Vezna D., 1991, *ASCE Journal Materials Civil Engineering*, 3, 19.
DOI: 10.1061/ (ASCE) 0899-1561(1991)3:1(19)

Table 1. Chemical composition and physical properties of cement.

Materials	OPC	SRPC	Limits of Iraqi Specification No.5/1984	
			OPC	SRPC
CaO	62.41	62.33	---	---
SiO_2	19.78	21.14	---	---
Al_2O_3	4.98	3.54	---	---
Fe_2O_3	3.48	5.16	---	---
SO_3	2.47	2.24	≤ 2.8% if C_3A >5%	≤ 2.5% if C_3A <5%
MgO	2.35	2.35	≤ 5%	≤ 5%
Alkalis	1.13	1.18	---	---
L.O.I.	3.40	2.06	≤ 4%	≤ 4%
I.R.	1.28	1.45	≤ 1.5%	≤ 1.5%
L.S.F.	0.95	0.90	0.66-1.02	0.66-1.02
Main Compounds (Bogue's Equation) Percentage by Weight of Cement				
Tricalcium Silicate C_3S	58.20	55.47	---	---
Dicalcium Silicate C_2S	12.91	18.85	---	---
Tricalcium Aluminate C_3A	7.30	0.66	---	≤ 3.5%
Tetracalcium Aluminoferrite C_4AF	10.58	15.68	---	---
Physical Properties				
Fineness, Blain method cm^2/gm	3460	3150	≥ 2300	≥ 2500
Compressive strength, MPa 3 days 7 days	23 32	19 27	≥ 15 ≥ 23	
Setting time(Vicat's method) Initial, minute Final (hours:minute)	180 3:30	130 2:45	≥ 45 min ≤ 10 hours	

Table 2. Chemical composition and physical analysis of silica fume.

Oxide Composition	Oxide Content	ASTM C-1240 Limitations
CaO	1.25	---
SiO_2	89.16	≥ 85
Al_2O_3	0.36	---
Fe_2O_3	1.16	---
SO_3	0.90	---
MgO	2.45	---
Na_2O	0.05	---
K_2O	0.07	---
L.O.I	3.80	≤ 6.0
Moisture content	0.80	≤ 3.0
Physical Properties		
Percent retained on 45µm (No.325) sieve, max, %	7	≤ 10
Pozzolanic activity index % at 7 days accelerated curing	147	≥ 105
Specific surface, min, (m^2lgm)	21	≥ 15

Table 3. Grading of the fine sand.

Sieve Size [mm]	Cumulative Passing %	Limits of Iraqi Specification No.45/1984, Zone 3
10	100	100
4.75	97	90-100
2.36	92	85-100
1.18	88	75-100
0.600	71	60-79
0.300	30	12-40
0.150	10	0-10

Table 4. Grading of the separated fine sand.

Sieve Size [mm]	Cumulative Passing %	Limits of Iraqi Specification No.45/1984, Zone 4
10	100	100
4.75	100	95-100
2.36	100	95-100
1.18	100	90-100
0.600	100	80-100
0.300	45	15-50
0.150	11	0-15

Table 5. Chemical properties of the fine aggregate.

Physical Properties	Test Results	Limits of Iraqi Specification No.45/1984
Specific gravity	**2.7**	---
Sulfate content	0.09 %	≤ 0.5 %
Absorption	0.75 %	---

Table 6. Technical description of SikaViscocrete-5930.

Basis	Aqueous Solution of Modified Polycarboxylate
Boiling	100°C
Hazardous Decomposition products (hazardous reactions)	No hazardous reactions known.
Odor	None
Appearance	Turbid liquid
Colour	Turbid liquid
Specific gravity	1.08 kg/It. ± 0.005
pH	7-9
Chloride content	None
Toxicity	Non-Toxic under relevant health and safety codes.
Storage	Protected from direct sunlight and frost at temperatures between + 5°C and + 35°C.

Table 7. Properties of the used steel fibers.

Property	Specifications
Relative density	7860 Kg/m^3
Ultimate straight tensile strength	670 MPa
Form	Straight
Average length	30 mm
Diameter	0.8mm ± 0.02mm
Aspect ratio (Lf/Df)	37.5

Table 8. Pozzolanic Activity Index and w/c or w/cm Ratios for Test Mortars.

Index	SF% by wt. of Cement	W/C or WCM to Give Flow 110±15	P.A.I
M*	---	0.50	---
M - 25SF - HRWRA**	20	0.35	147

*Mortar with standard sand.
**Mortar with standard sand, 20% silica and 5% super- plasticizer (sika viscocrete 5930) by weight of cementitious.

Table 9. Composition of NC and RPC..

Ingredient	Cement kg/m^3	Water kg/m^3	SP kg/m^3	Sand kg/m^3	Gravel kg/m^3	Silica Fume kg/m^3
NC	440	154	60	635	1045	-
RPC	910	160	80	960	-	185

Table 10. Mechanical properties of NC and RPC specimens.

Type of Concrete	Mix	Compressive Strength [MPa]			Flexural. 28 Day [MPa]	Splitting. 28 Day [MPa]	Modulus of Elasticity 28 Day [MPa]	Brittleness Ffactor	Water Absorption Ratio [%]	
		3 day	28 day	56 day					3 day	28 day
Normal concrete	NNC0	31.4	45.3	50.7	7.8	5.9	28.5	0.130	1.01	1.59
	NNC0.5	38.3	61.4	68.8	8.9	7.9	34.0	0.129	1.01	1.61
	NNC1	43.7	72.6	81.3	9.6	9.1	37.9	0.125	1.02	1.62
	NNC1.5	51.5	77.8	87.1	10.2	10.7	39.6	0.138	1.03	1.65
	NNC2	55.1	82.4	92.3	10.8	11.6	41.4	0.141	1.04	1.67
	SNC0	28.3	42.1	47.6	7.3	5.5	26.2	0.131	1.07	1.71
	SNC0.5	34.4	57.0	64.4	8.4	7.3	31.3	0.128	1.08	1.73
	SNC1	39.1	67.5	76.3	9.0	8.5	34.9	0.126	1.08	1.75
	SNC1.5	45.8	72.4	81.8	9.6	10.0	36.4	0.138	1.09	1.77
	SNC2	49.9	76.6	86.6	10.2	11.0	38.1	0.144	1.10	1.78
Reactive powder concrete	NRPC0	103.4	139.5	160.4	23.0	9.7	40.0	0.070	0.63	0.96
	NRPC0.5	114.0	149.8	172.3	31.8	12.0	45.2	0.080	0.65	0.98
	NRPC1	120.2	155.0	178.3	36.5	13.2	47.8	0.085	0.65	1.00
	NRPC1.5	131.0	163.2	187.7	46.1	16.7	49.7	0.102	0.67	1.01
	NRPC2	134.8	172.4	198.3	48.2	17.1	51.3	0.099	0.69	1.02
	SRPC0	88.0	125.6	143.2	21.0	8.9	38.0	0.071	0.66	1.03
	SRPC0.5	97.3	134.8	153.7	29.0	11.0	42.9	0.082	0.68	1.05
	SRPC1	102.0	139.5	159.0	33.1	12.0	45.4	0.086	0.69	1.07
	SRPC1.5	111.2	146.9	167.5	41.2	15.0	47.2	0.102	0.71	1.08
	SRPC2	115.6	155.2	176.9	43.5	16.0	48.7	0.103	0.72	1.08

Table 11. Impact resistance of NC and RPC specimens.

Type of Concrete	Mix	AbrasioL loss (% by wt.)	No. of Blows up to		Average Impact Energy (J or kN.m) for	
			First crack	Ultimate failure	First crack	Failure crack
Normal concrete	NNC0	3.68	39	63	793.1	1281.1
	NNC0.5	3.25	54	85	1098.1	1728.5
	NNC1	2.68	68	97	1382.8	1972.6
	NNC1.5	2.33	76	106	1545.5	2155.6
	NNC2	2.06	81	116	1647.2	2358.9
	SNC0	3.82	39	61	793.1	1240.5
	SNC0.5	3.37	51	82	1037.1	1667.5
	SNC1	2.75	64	94	1301.5	1911.6
	SNC1.5	2.40	73	105	1484.5	2135.2
	SNC2	2.11	79	113	1606.5	2297.9
Reactive powder concrete	NRPC0	1.07	64	89	1301.5	1809.9
	NRPC0.5	0.94	79	113	1606.5	2297.9
	NRPC1	0.77	88	142	1789.5	2887.7
	NRPC1.5	0.67	96	151	1952.2	3070.7
	NRPC2	0.59	99	165	2013.2	3355.4
	SRPC0	1.13	61	87	1240.5	1769.2
	SRPC0.5	1.00	74	110	1504.8	2236.9
	SRPC1	0.83	84	139	1708.2	2826.7
	SRPC1.5	0.72	92	147	1870.9	2989.3
	SRPC2	0.60	90	162	1830.2	3294.4

Table 12. Measured and estimated abrasion loss values.

Type of Concrete	Mix	Abrasion Loss (% by wt.)		No. of Blows up to Ultimate Failure	Compressive Strength [MPa]
		Measured	Estimated		
Normal concrete	NNC0	3.68	3.41	63	45.3
	NNC0.5	3.25	2.97	85	61.4
	NNC1	2.68	2.67	97	72.6
	NNC1.5	2.33	2.52	106	77.8
	NNC2	2.06	2.37	116	82.4
	SNC0	3.82	3.49	61	42.1
	SNC0.5	3.37	3.08	82	57.0
	SNC1	2.75	2.79	94	67.5
	SNC1.5	2.40	2.64	105	72.4
	SNC2	2.11	2.52	113	76.6
Reactive powder concrete	NRPC0	1.07	1.18	89	139.5
	NRPC0.5	0.94	0.86	113	149.8
	NRPC1	0.77	0.63	142	155.0
	NRPC1.5	0.67	0.41	151	163.2
	NRPC2	0.59	0.15	165	172.4
	SRPC0	1.13	1.50	87	125.6
	SRPC0.5	1.00	1.21	110	134.8
	SRPC1	0.83	1.00	139	139.5
	SRPC1.5	0.72	0.80	147	146.9
	SRPC2	0.60	0.55	162	155.2

Figure 1. Flow table device used.

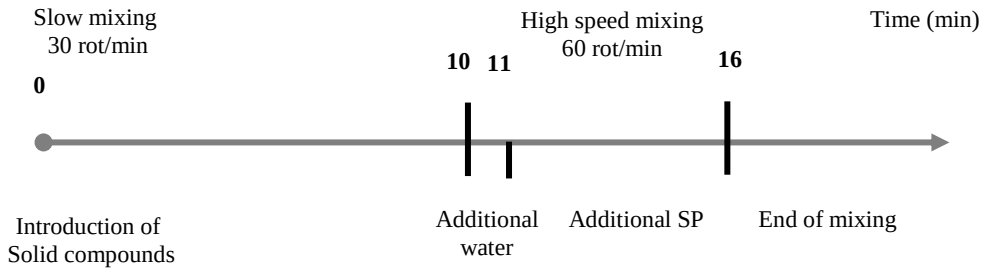

Figure 2. Mixing procedure of RPC.

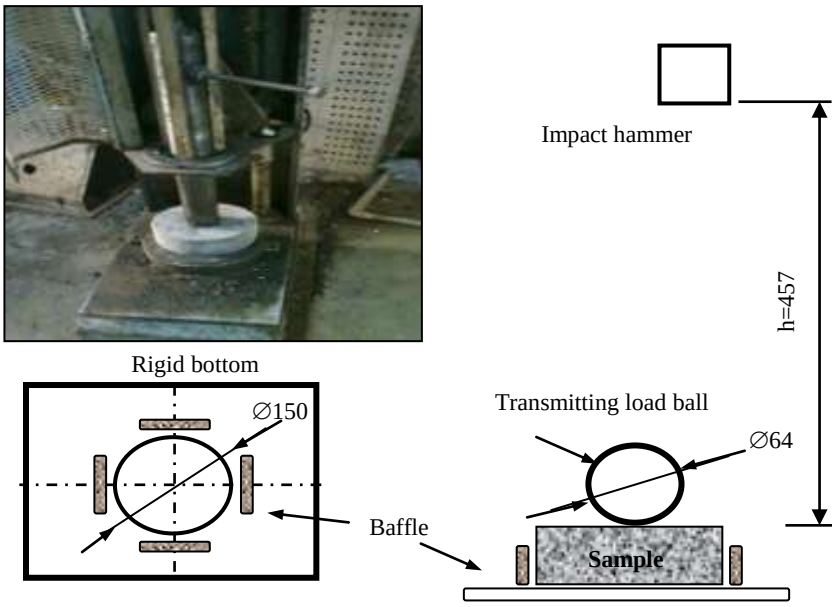

Figure 3. Impact test.

This test was conducted in the laboratory of College Engineering-Civil Department- Babylon University.

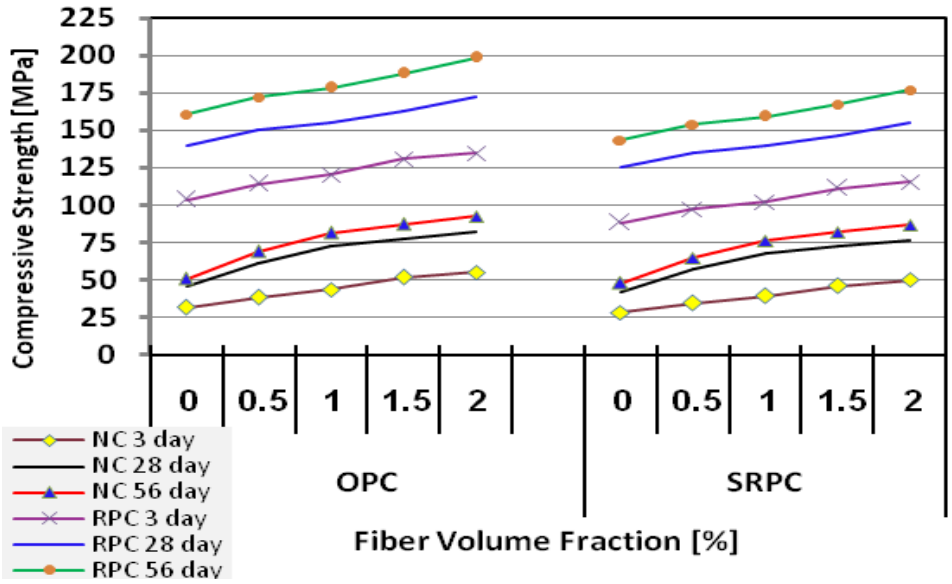

Figure 4. Effect of volume fraction and type of cement on the compressive strength.

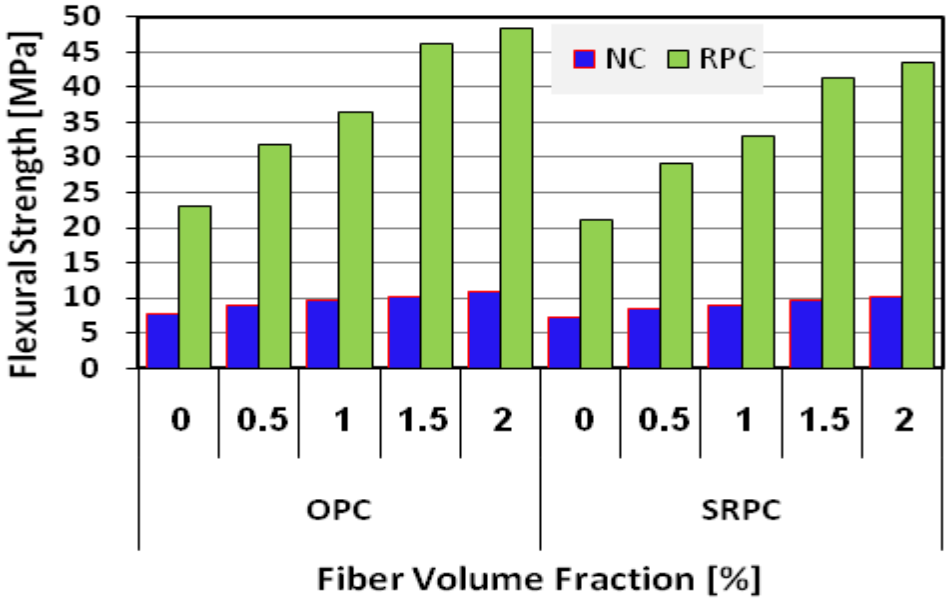

Figure 5. Effect of volume fraction and type of cement on the flexural strength.

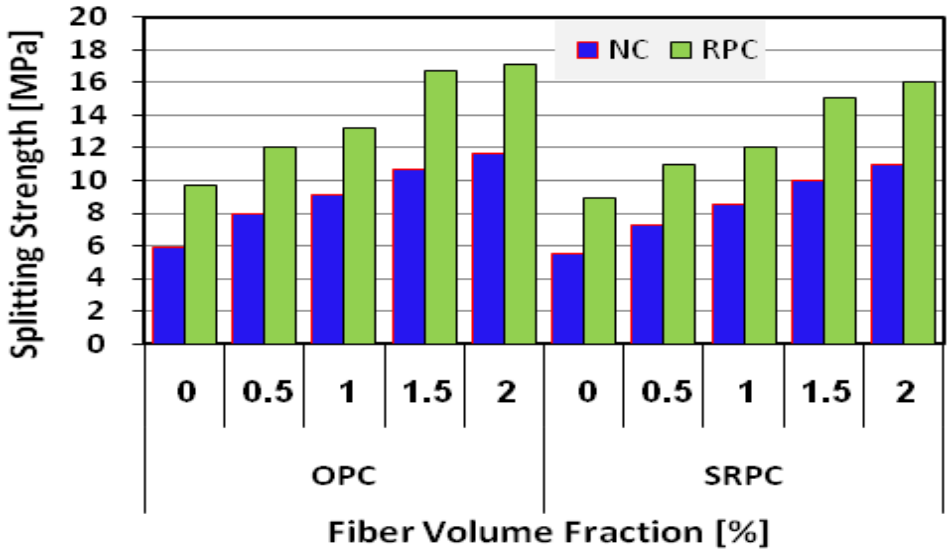

Figure 6. Effect of volume fraction and type of cement on the splitting strength.

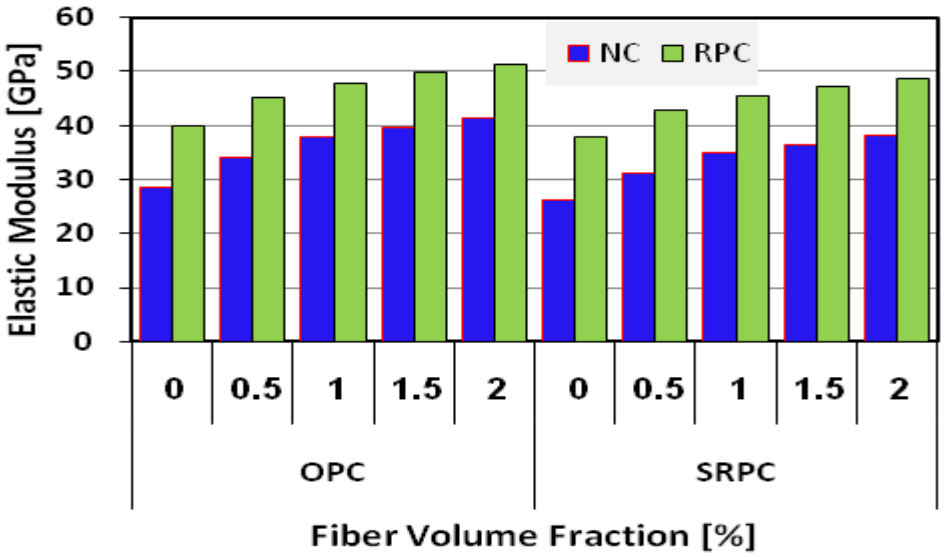

Figure 7. Effect of volume fraction and type of cement on the elastic strain.

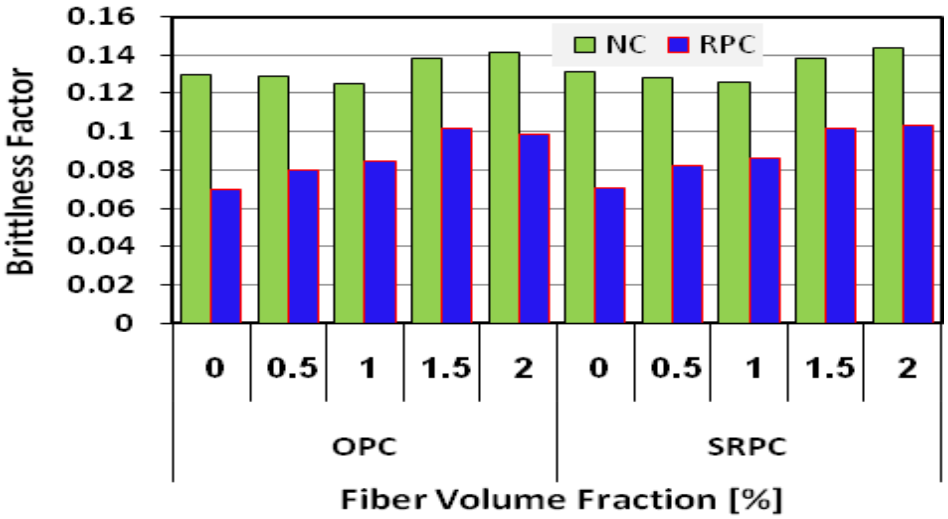

Figure 8. Effect of volume fraction and type of cement on the brittleness factor.

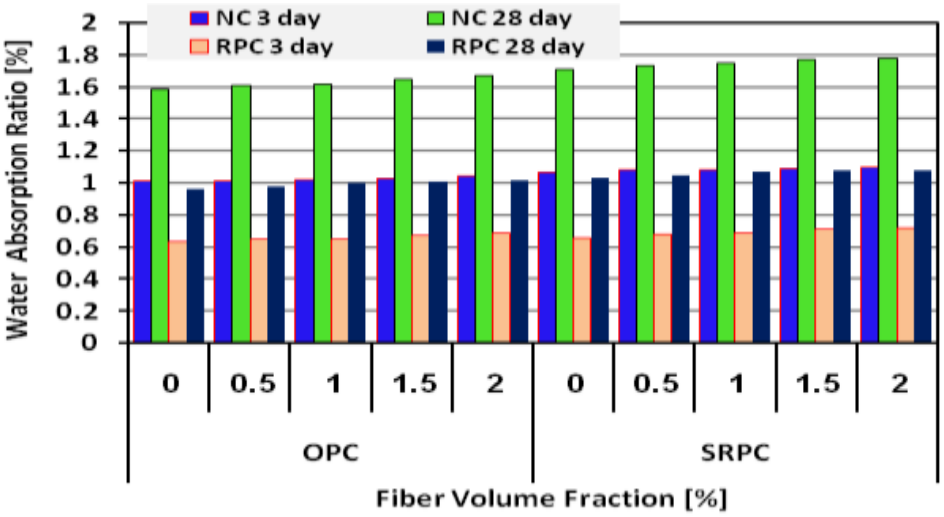

Figure 9. Effect of volume fraction and type of cement on the water absorption.

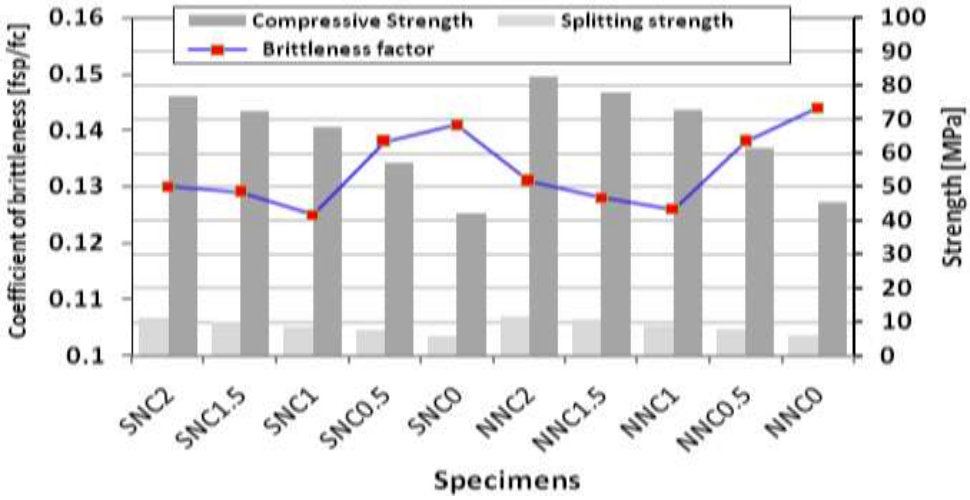

Figure 10. Compressive strength, splitting tensile strength and brittleness factor of NC.

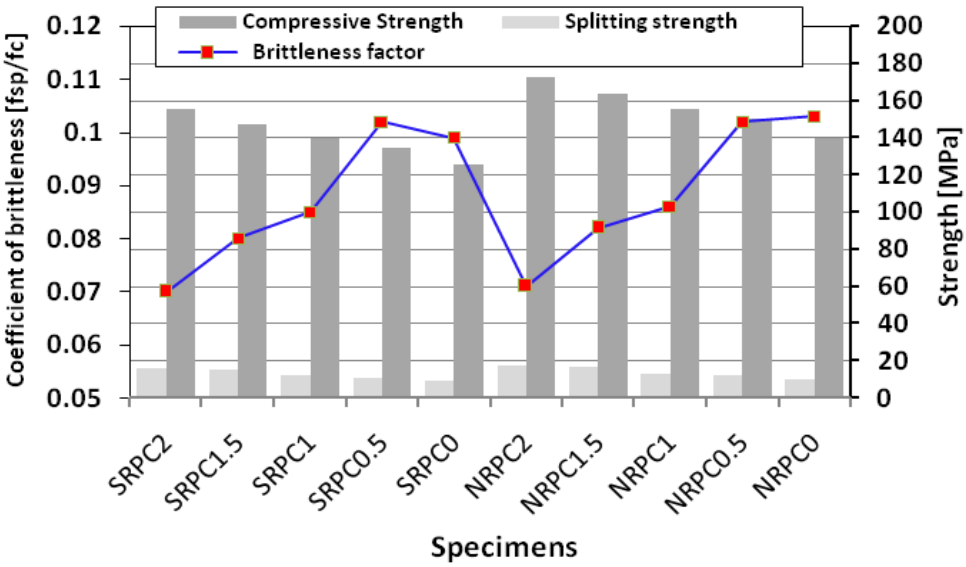

Figure 11. Compressive strength, splitting tensile strength and brittleness factor of RPC.

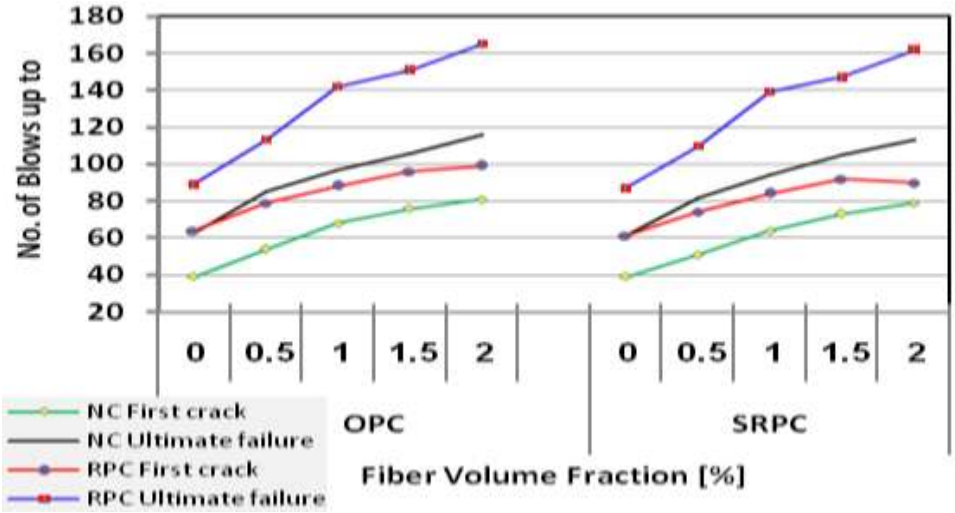

Figure 12. Effect of volume fraction and type of cement on the impact strength.

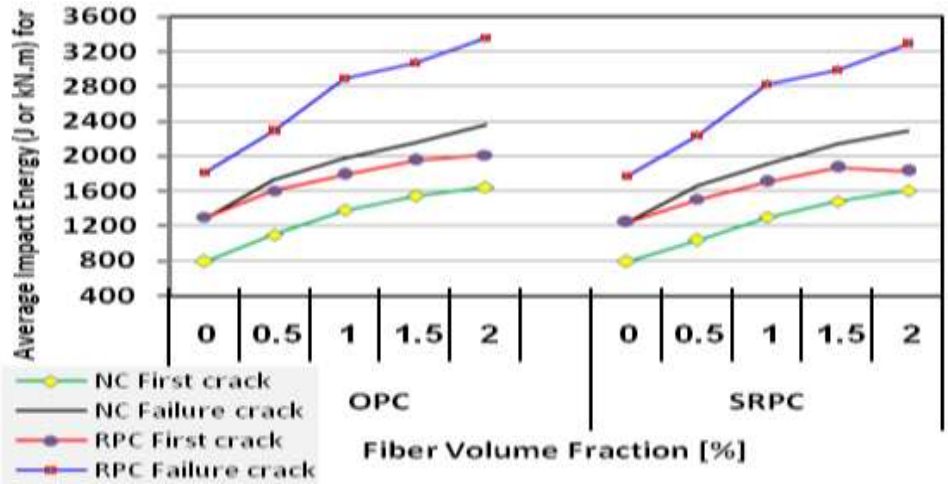

Figure 13. Effect of volume fraction and type of cement on the first and failure crack.

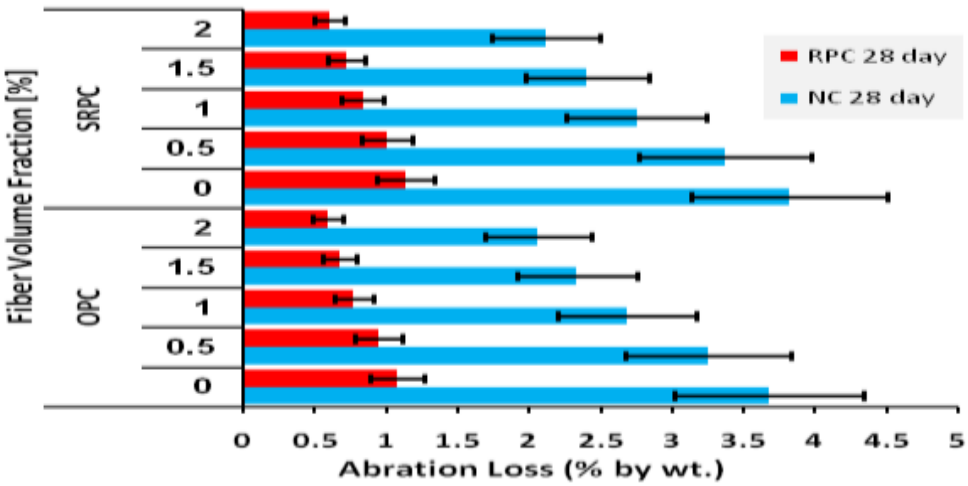

Figure 14. Effect of volume fraction and type of cement on the abrasion loss.

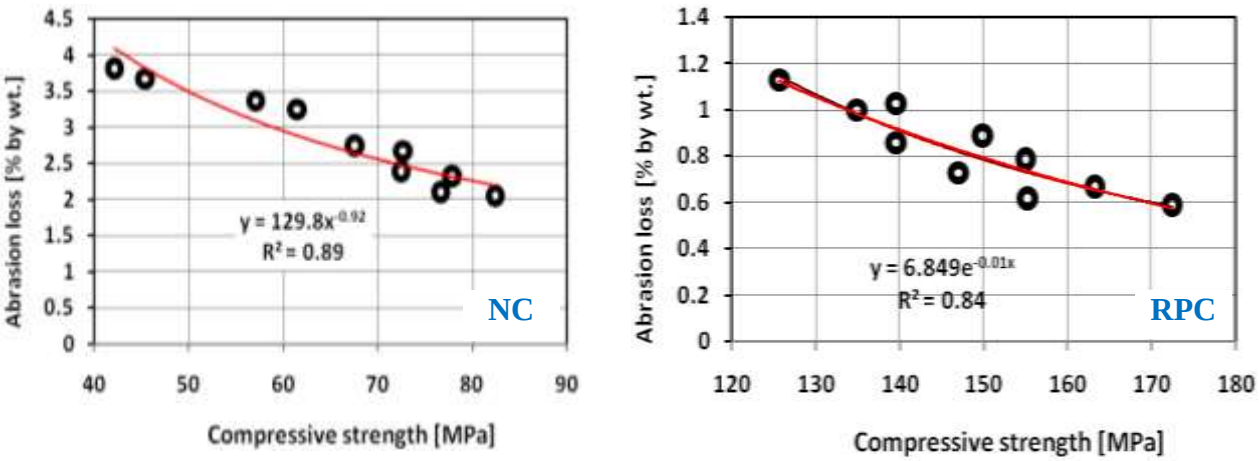

Figure 15. Compressive strength vs abrasion loss for NC and RPC.

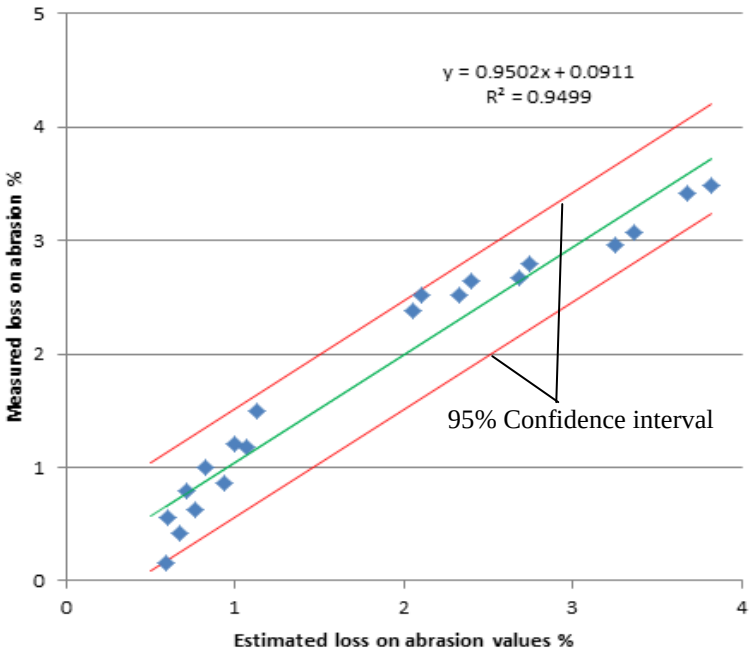

Figure 16. Comparison of experimental and theoretical abrasion loss for NC and RPC.

Evaluation of Alum/Lime Coagulant for the Removal of Turbidity from Al-Ahdab Iraqi Oilfields Produced Water

Basma Abbas Abdul-Majeed
Assistance Professor
College of Engineering
University of Baghdad
E-mail:basma1957@yahoo.com

Hussein Basim Oleiwi
Ph.D. Chemical Engineer
College of Engineering
University of Baghdad
E-mail:husseinbasim537@yahoo.com

ABSTRACT

The removal of turbidity from produced water by chemical coagulation/flocculation method using locally available coagulants was investigated. Aluminum sulfate (alum) is selected as a primary coagulant, while calcium hydroxide (lime) is used as a coagulant aid. The performance of these coagulants was studied through jar test by comparing turbidity removal at different coagulant/ coagulants aid ratio, coagulant dose, water pH, and sedimentation time. In addition, an attempt has been made to examine the relationship between turbidity (NTU) and total suspended solids (mg/L) on the same samples of produced water. The best conditions for turbidity removal can be obtained at 75% alum+25% lime coagulant at coagulant dose of 80 mg/l at pH 6 and 120 min for sedimentation time. At these conditions, the turbidity reading was reduced from 92 to 2.1 NTU.

Key words: coagulation, turbidity, alum, produced water.

تقييم مخثر الشب ـ النورة في ازالة العكورة من المياه المصاحبة لأنتاج النفط من حقول الأحدب العراقية

أ.م.د. بسمة عباس عبدالمجيد
كلية الهندسة- جامعة بغداد

حسين باسم عليوي
دكتوراه هندسة كيمياوية

الخلاصة

في هذا البحث تمت دراسة ازالة العكورة من الماء المنتج بطريقة التخثر/ التلبد وباستخدام مخثرات متوفرة محلياً. تم استخدام كبريتات الالمنيوم (الشب) كمخثر رئيسي بينما استخدم هيدروكسيد الكالسيوم (النورة) كمخثر مساعد. تم دراسة اداء هذه المخثرات بطريقة الدفعة وباستخدام فحص الجرة وذلك بمقارنة ازالة العكورة من الماء تحت ظروف مختلفة مثل نسبة المخثر / المخثر المساعد و كمية المخثر و الدالة الحامضية للماء وزمن التركيد. بالاضافة الى ذلك, تم عمل دراسة مختبرية لمعرفة العلاقة بين درجة العكورة (وحدة كدرة) ومجموع المواد الصلبة المعلقة (مليغرام لكل لتر) لنماذج مختلفة من الماء المنتج. بينت النتائج بأن المخثرات المستخدمة اظهرت افضل اداء في ازالة العكورة وان الجرعة الامثل للمخثر هي ٨٠ مليغرام لكل لتر والرقم الهيدروجيني الامثل هو ٦ وافضل زمن التركيد كان١٢٠ دقيقة وان افضل نسبة مخثر/ مخثر مساعد كانت ٧٥% شب مع ٢٥% نورة. تناقصت قراءة العكورة من ٩٢ الى ٢,١ وحدة كدرة عند هذه القيم المثلى.

الكلمات الرئيسية: التخثر, العكورة, الشب, المياه المنتجة.

1. INTRODUCTION

Treating oilfield water can help facilitate additional water management options for operators such as beneficial uses that in the short and long term can potentially provide certain community and economic advantages. Treated produced water has the potential to be a valuable product rather than a waste. A large number of methods were used as treatment technologies such as heat treating, gas flotation, chemical separation, membranes, filtration, and biological degradation. Several methods are available to remove the suspended solids or turbidity (like cuttings, sand, clay particles, and microorganisms) and their methods are filtration, coagulation, gravity separation, and biological treatment, **Arthur, 2005.**

All waters, especially produced water, contain both dissolved and suspended particles. Coagulation and flocculation processes are used to separate the suspended solids portion from the water. The suspended particles vary considerably in source, composition charge, particle size, shape, and density. Correct application of coagulation and flocculation processes and selection of the coagulants depend upon understanding of the interaction between these factors, **,Smita, et al., 2012.**

Turbidity is cloudiness or haziness of water (or other fluid) caused by individual particles that are generally invisible to the naked eye. It is a characteristic related to the concentration of suspended solid particles in water and has been adopted as an easy and reasonably accurate measure of overall water quality, **Tseng, 2000.** World Health Organization (WHO) has set the guideline value for the residual turbidity in drinking water at 5 Nephelometric Turbidity units (NTU), **Connachie, et al., 1999.** Although turbidity purports to measure approximately the same water quality property as total suspended solids, but the later is more useful because it provides an actual weight of the particulate material present in the sample. While a relationship can be established between turbidity and suspended solids, this relationship can and will change spatially and temporally due to variations in solid composition and stream energy, **Rasmussen, 1995.**

For all water types, there are many parameters that affect coagulation performance for turbidity removal including the character and concentration of the particular material, chemical and physical properties of the water, mixing time, mixing speed, and temperature. The common parameters are coagulant type, dose, pH, and settling time, **,Uyak** and **Toroz, 2007.** The coagulation process utilizes what is known as a chemical coagulant to promote particle agglomeration. **Eilbeck** and **Mattock, 1987** presented a list of common coagulants in treating wastewater. They mentioned that the most frequently used coagulants are iron and aluminum salts and especially, for economic reasons, aluminum sulfate and ferric chloride. Coagulants are sometimes assisted with further chemicals, known as coagulant aids. They essentially are polyelectrolytes and lime alkalinity addition, **Kiely, 1997.**

The aim of this work was to study the feasibility of turbidity removal from real produced water from Al-Ahdab Oilfields by alum and lime coagulants. The process was examined for the first time in Iraq under different values of coagulant/ coagulants aid ratio, coagulant dose, water pH, and sedimentation time.

2. MATERIALS

2.1 Produced Water

A volume of produced water obtained for sampling from Al-Ahdab Oilfields, 180 km south-east of Baghdad, was stored in a plastic container for the duration of the study. Samples of this water were analyzed chemically in the Al-Ahdab Oilfields and results are listed in **Table 1.**

2.2 Coagulants

The chemical coagulants used in the present study were aluminum sulfate and calcium hydroxide. Aluminum sulfate (Alum) is selected as a primary coagulant, while calcium hydroxide (lime) is used as a coagulant aid. Alum is a white crystalline solid with the formula $Al_2(SO_4)_3.18H_2O$ with purity of 97.3%wt. Lime is a very fine white powder. It has the chemical formula of $Ca(OH)_2$, purity of 95%wt. The selected coagulants have been chosen in this work due to their physical and chemical properties which give their ability to remove turbidity on their molecular species from the bulk liquid. Also, they are of low cost and are locally available.

3. EXPERIMENTAL PROCEDURE

All coagulation experiments were conducted in six-place conventional jar-test apparatus. Six beakers with 1 liter volume of produced water are used at time of experiment. The study includes the effect of coagulant/ coagulant aid ratio, coagulant dose, pH, and sedimentation time on turbidity removal. Different combinations of coagulant dose (20, 40, 60, 80, 100, and 120 mg/l), pH (3, 4, 5, 6, 7, and 8), and sedimentation time (30, 60, 90, 120, 150, and 180 min) were tested. The pH was adjusted by adding drops of HCl (0.1M) or NaOH (0.1M) prior to the addition of coagulant. To simulate coagulation, flocculation, and sedimentation conditions, rapid mixing at 200 rpm was performed for 3 min, followed by slow mixing for 30 min at 30 rpm and final step (0 rpm) for 60 min settling time, **Degremont, 1979.** After completing the settling time, supernatant was withdrawn with a plastic syringe from near 3 cm below the liquid-air interface for analysis of turbidity and total suspended solids. All the experiments were carried out at ambient temperature of 20-25 C^o.

Total suspended solids (TSS) are that portion of the total solids that are retained on a filter paper (Cellulose nitrate membrane, approximately 0.45 mm pore size). Before sampling, filter papers were prepared by first soaking them in distilled water, drying them at 100 C^o, weighing and recording their weights. Now, a measured volume (100 ml) of produced water is passed through the filter. The filter containing the residue is then dried in an oven for one hour at 100 C^o. The sample is then cooled and weighed. The increase in weight represents TSS. Finally, TSS was calculated by using the equation below, **APHA, 1998.**

$$TSS\left(\frac{mg}{l}\right) = \frac{(A-B)}{C} \times 1000 \qquad (1)$$

where A = final weight of the filter (mg), B = initial weight of the filter (mg), and C = volume of water filtered (l). This inexpensive TSS tells much about the produced water character and can be run in less than two hours with fairly inexpensive equipment.

4. RESULTS AND DISCUSSION

4.1 Evaluation of the Percentage Ratio of Coagulant/Coagulant Aid

Different doses of aluminum sulfate (alum) as a primary coagulant with the coagulant aid (lime) were added to the produced water with initial turbidity as 92 NTU, uncontrolled pH as 5.8, coagulant dose as 60 mg/l, and 60 min as sedimentation time. The results are shown in table 2. Examining this table, it is clear that there was an improvement in the turbidity removal when

25% lime were used as a coagulant aid in conjunction with 75% alum compared to alum alone and this can be regarded as the best coagulant. **Lin, et al., 1971** showed that the addition of alum to water releases hydrogen ions and consequently lowers the pH. Unless the hydrogen ions can be removed, the formation of an effective floc, $Al(OH)_3$, is impossible. The hydrogen ions can be removed by the alkalinity in natural water or by the addition of lime. This finding is in agreement with **,Degremont, 1979** and **Kiely, 1997.** They mentioned that if there is insufficient alkalinity in the water with high turbidity, alkalinity is added by means of lime addition, even with small amount, to improve the alkalinity and optimize coagulation.

4.2 Effect of Coagulant Dosage

Coagulant dosage was one of the most important parameters that have been considered to determine the best condition for the performance of coagulant used (75%alum+25%lime) in coagulation/ flocculation process. The effect of coagulant dosage on the removal of turbidity is shown in **Fig. 1**. Coagulant dosage was varied from 0 to 120 mg/l while other parameters were kept constant at pH 5.8 and 60 min for sedimentation time. From **Fig. 1**, it can be seen that the best dose of coagulant was 80 mg/l and the removal efficiency of turbidity was 91.41%. It is noticed that turbidity values are decreasing for coagulant dosage level of 0 to 80 mg/l and gradually increasing for dosage level of 100 to 120 mg/l. This may be explained by: high dose of the coagulant in the suspension caused charge stabilization of colloid particles, due to the adsorption of counter ions (in this case was Al^{+3}). Increasing the dose of coagulant more than 80 mg/l raised the turbidity because the excess adsorption of the counter ions caused the charge of colloidal particles to become positive (i.e. re-stabilization of the colloidal particles). The results obtained in this study are similar to those reported by **Ghaly et al., 2007** who reported that colloidal particles are negatively charged and upon addition of aluminum sulfate to wastewater, the Al^{+3} ions are attracted to these particles. At the point of complete charges neutralization, the colloids begin to agglomerate due to collisions between particles. If excess coagulant is added to the wastewater, the results are a reverse of the net charge on the colloidal particles (from negative to positive). Particle re-stabilization by charge reversal allowed greater amounts of smaller particles to remain in solution, thus increasing the total solids as well as the color intensity of the treated water.

4.3 Effect of pH

In the coagulation/ flocculation process, pH is very important as the coagulation occurs within a specific pH range. An optimum pH range, in which metal hydroxide precipitates occur, should be determined to establish best conditions for coagulation. In this study, a range of pH between 3 to 8 was selected. The results of the study showing the effect of pH on the removal of turbidity are presented in **Fig. 2**. To determine the best pH value, coagulant dosage was maintained at 80 mg/l and 60 min for sedimentation time. The best pH was determined at a value of 6 followed by 5 and 7 and the turbidity removal was 91.09% as shown in **Fig. 2**. It was found that the percentage of turbidity removal was increased at pH from 3 to 6 and then it declined for pH 7 to 8. The obtained results are in accordance with those obtained by **Degremont, 1979** and **Sadeddin et al., 2011,** which indicated that aluminum salts work best in a pH range of 5.5-7.4. Outside this range, a higher concentration of dissolved aluminum is liable to be found.

4.4 Effect of Sedimentation Time

In this experiment, the sedimentation times were varied from 30 to 180 minutes. Other parameters were kept constant at pH 6 and 80 mg/l for coagulant dosage. The effect of sedimentation time on coagulation process is given in **Fig. 3**. From this figure, it can be seen

that the turbidity decreased with increasing settling time and it reached equilibrium at 120 min. At this point, removal efficiency of turbidity was 97.72 %. Further increase in time had no effect on turbidity removal. This result explained that almost all flocs produced after the coagulation and mixing process have settled to the bottom of the sludge layer after 120 min. The settling process is mainly affected by the gravity where heavier flocs will settle faster than dispersed particle.

4.5 Turbidity versus Total Suspended Solids

Both turbidity and total suspended solids (TSS) are defined by the method used to measure them. Turbidity is an optical measurement; it depends on the number of particles in the sample and their shape and size. While TSS is a gravimetric measurement, it depends on the total mass of filterable material in the sample, **Rasmussen, 1995, Fig. 4**. The final relationship between turbidity and TSS at Al-Ahdab oilfields produced water was shown in **Fig. 5**. This figure confirms the existence of a strong linear relationship between turbidity readings and TSS concentrations. High coefficient of determination (R^2=0.972) value was obtained for this relationship. From the published NTU-TSS relationship, **Irvine, et al., 2002** and **Hannouche, 2011.** It is seen that it can vary considerably between different aquatic systems and even at different times for the same stream, so there is no universal correlation of turbidity and TSS.

5. CONCLUSIONS

The aluminum sulfate (alum) combination with coagulant aid (lime) provided higher removal efficiencies of turbidity compared to coagulation with alum alone. The added alum to water causes the release of hydrogen ions which lowers the pH.

The best conditions for turbidity removal using a jar test process can be obtained at 75% alum+25% lime coagulant ratio at coagulant dosage of 80 mg/l at pH 6 and 120 min for sedimentation time. This dose caused colloid particles to be charge stabilized, while increasing the dose increase the turbidity where re-stabilization occurs.

At these conditions, the NTU reading was reduced from 92 to 2.1. The TSS-turbidity relationship may be both site and time specific, so the relationship is normally unique for a particular catchment and within a particular period of time.

6. REFERENCES

- American Public Health Association, APHA, 1998, *Standard Methods for the Examination of Water and Wastewater*. 20th edition.

- Arthur D., Langhus G., and Patel C., 2005, *Technical Summary of Oil and Gas Produced Water Treatment Technologies*. Commissioner's environment produced water treatment Tech.

- Connachie, G. L., Folkard, G.K., Matawali, M. A. and Surtherland, J.P., 1999, *Field Trials of Appropriate Hydraulic Flocculation Process*. J. Water Research, 33 (6), 1425-1434.

- Degremont, 1979, *Water Treatment Handbook*. 5th Ed; Distributed by Halsted Press N.Y.

- Eilbeck W. J. and G. Mattock, 1987, *Chemical Processes in Waste Water Treatment*. England: Ellis Horwood Limited. Chapter 11.

- Ghaly A.E., A. Snow and B.E. Faber, 2007, *Effective Coagulation Technology for Treatment of Grease Filter Wash Water*. American Journal of Environmental Sciences 3 (1), p: 19-29.

- Hannouche, G. Chebbo, G. Ruban, B. Tassin, B. J. Lemaire, and C. Joannis, 2011, *Relationship Between Turbidity and Total Suspended Solids Concentration Within a Combined Sewer System*. Water Science and Technology (64), 12.

- Irvine K.N., E.L. Somogye, and G.W. Pettibone, 2002, *Turbidity, Suspended Solids, and Bacteria Relationships in the Buffalo River Watershed*. Middle States Geographer (35), p: 42-51.

- Kiely Gerard, 1997, *Environmental Engineering*. Copyright, McGraw-Hill International Limited (UK).

- Lin S. D., R. L. Evans, and D. B. Beuscher, 1971, *Algal Removal by Alum Coagulation*, Illinois State Water Survey, Urbana, Report of Investigation 68.

- Rasmussen, T.C., 1995, *Erosion and Sedimentation: Scientific and Regulatory Issues*, Report developed by Georgia Board of Regents scientific panel on evaluating the erosion measurement standard defined by the Georgia Erosion Sedimentation Act.

- Sadeddin K., Naser A., and Firas, A., 2011, *Removal of Turbidity and Suspended Solids by Electro-Coagulation to Improve Feed Water Quality of Reverse Osmosis Plant*, Desalination Journal (268), p: 204-207.

- Smita S. Borchate, G. S. Kulkarni, S. V. Kore, and V. S. Kore, 2012, *Application of Coagulation-Flocculation for Vegetable Tannery Wastewater*, International Journal of Engineering Science and Technology (4), p: 1944-1948.

- Tseng T., Segal B.D., and Edwards M., 2000, *Increasing Alkalinity to Reduce Turbidity*, Journal of the American Water Works Association (92), p: 44-52.

- Uyak, V. and Toroz, I., 2007, *Disinfection by-Product Precursors Reduction by Various Coagulation Techniques in Istanbul Water Supplies*. Journal of Hazardous Materials (141) p: 320-328

Table 1. Analysis of produced water from Al-Ahdab oilfields, date: 2-3-2013.

Parameter	Value	Permissible Limit
pH	5.5-5.9	6.5-8.5
Turbidity (NTU)	92	5
TSS (mg/l)	2520	30
Density (kg/m^3)	1095	_

Table 2. The percentages of the coagulant doses**.**

Sample No.	Coagulants	Final Turbidity (NTU)	Removal Efficiency (%)
1	100 % alum + 0 % lime	54.4	40.87
2	75 % alum + 25 % lime	12.8	86.09
3	50 % alum + 50 % lime	37.2	59.57
4	25 % alum + 75 % lime	61.4	33.26
5	0 % alum + 100 % lime	73	20.65

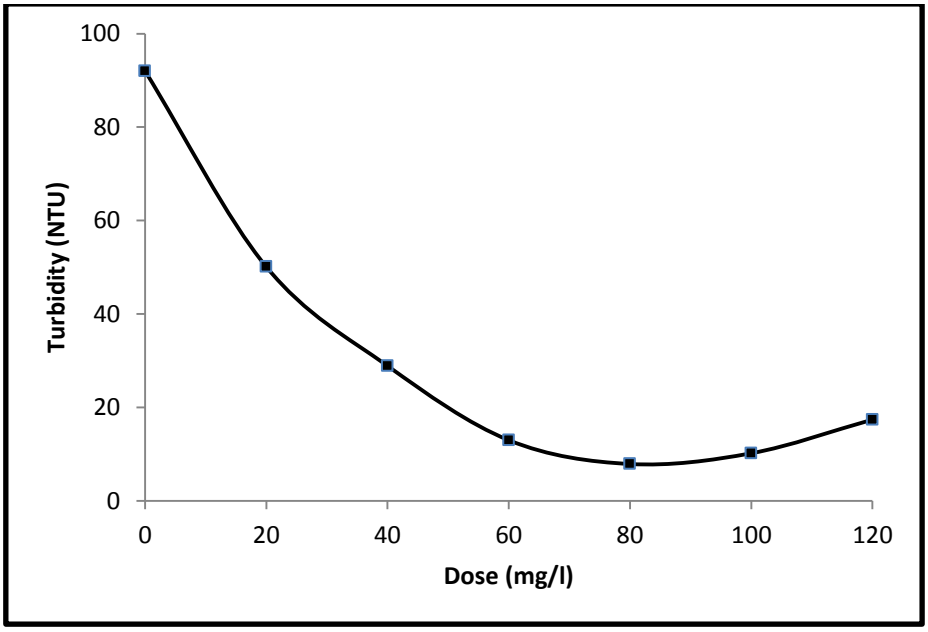

Figure 1 The effect of coagulant dosage on turbidity removal from produced water.

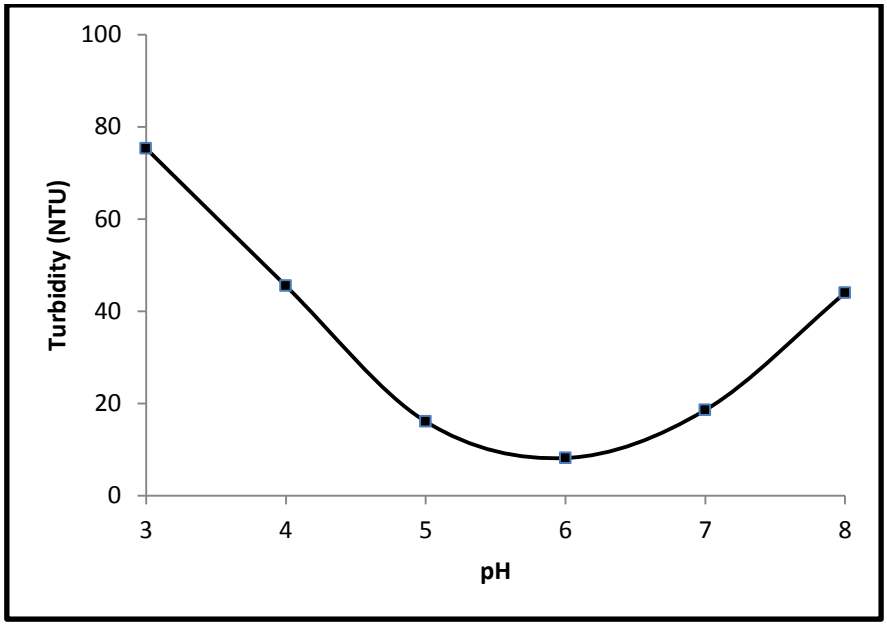

Figure 2. The effect of pH on turbidity removal from produced water**.**

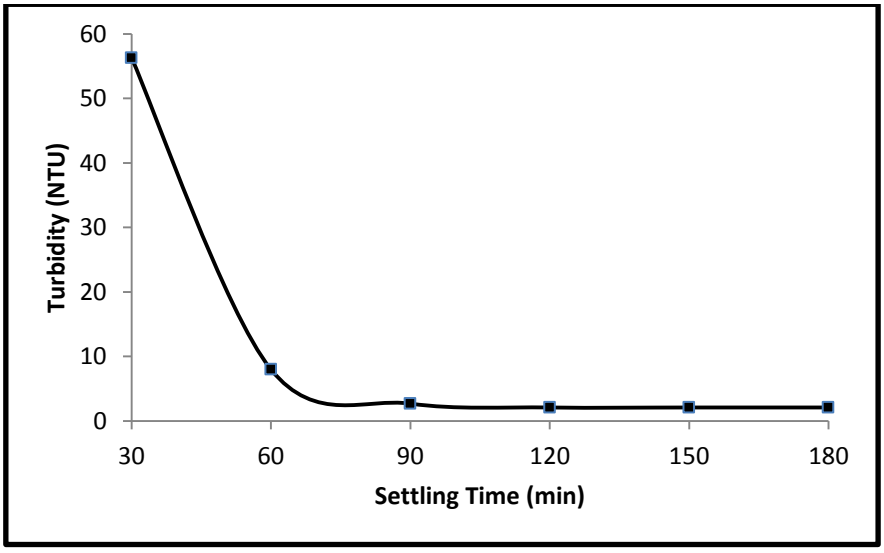

Figure 3. The effect of sedimentation time on turbidity removal from produced water.

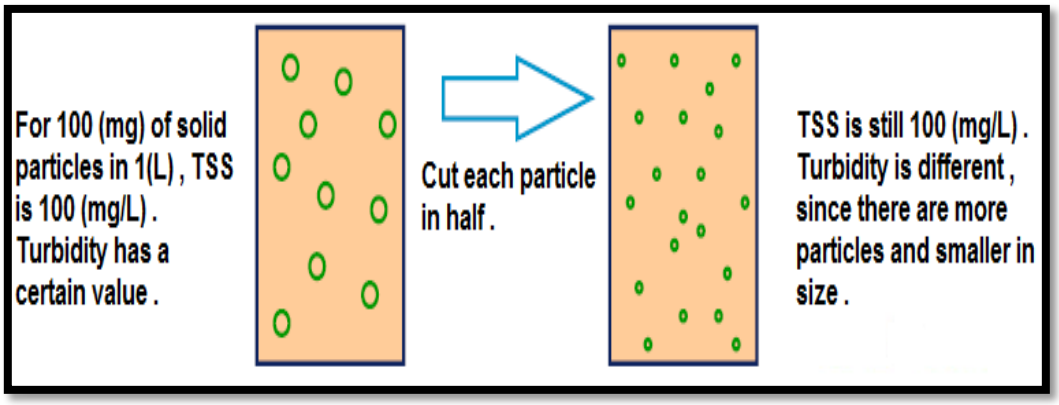

Figure 4. Turbidity compared to TSS**.**

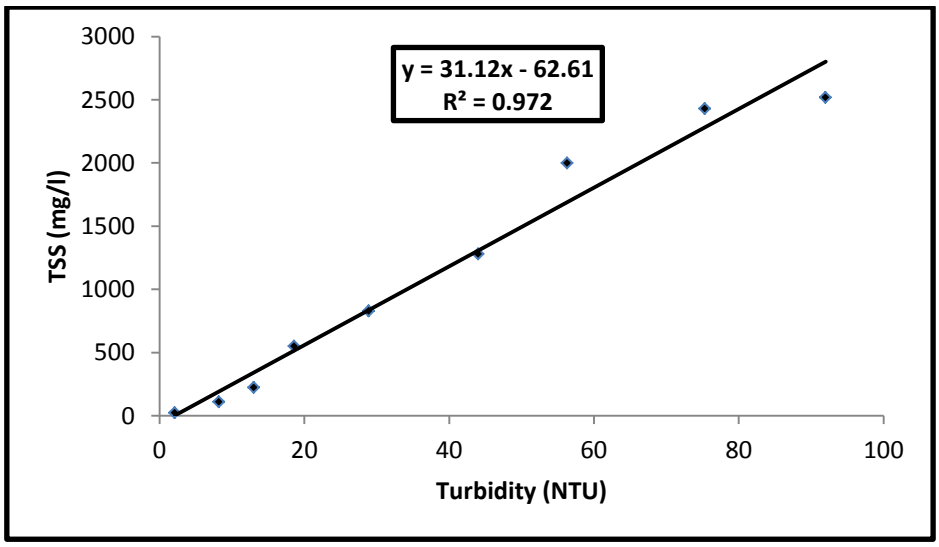

Figure 5. Turbidity-TSS relationship at Al-Ahdab oilfields produced water.

Desulfurization of AL-Ahdab Crude Oil using Oxidative Processes

Neran Khalel Ibrahim
Professor
Department of Chemical Engineering
University of Technology
E-mail: neran_ibrahim@yahoo.com

Saja Mohsen Jabbar
Assistant Lecturer
Department of Chemical Engineering
University of Technology
E-mail:smuhcin@yahoo.com

ABSTRACT

Two different oxidative desulfurization strategies based on oxidation/adsorption or oxidation/extraction were evaluated for the desulfurization of AL-Ahdab (AHD) sour crude oil (3.9wt% sulfur content). In the oxidation process, a homogenous oxidizing agent comprising of hydrogen peroxide and formic acid was used. Activated carbons were used as sorbent/catalyst in the oxidation/adsorption process while acetonitrile was used as an extraction solvent in the oxidation/extraction process. For the oxidation/adsorption scheme, the experimental results indicated that the oxidation desulfurization efficiency was enhanced on using activated carbon as catalyst/sorbent. The effects of the operating conditions (contact time, temperature, mixing speed and sorbent dose) on the desulfurization efficiency were examined. The desulfurization efficiency measured at the best operating conditions(optimum conditions): 60℃, 500rpm, 60min contact time and sorbent dose of 0.7g AC/100 ml AHD crude, was 32.8% corresponding to a sulfur content of 2.6 wt%. Applying the same optimum operating conditions and at 3:1 solvent/oil ratio, the oxidation/extraction method gave comparable desulfurization efficiency of 31.5%.

Key words: desulfurization technologies, oxidative desulfurization, adsorption, extraction, activated carbon.

ازالة الكبريت من نفط خام الاحدب بأستخدام عملية الاكسدة

نيران خالد ابراهيم
قسم الهندسة الكيمياوية
الجامعة التكنولوجية

سجا محسن جبار
قسم الهندسة الكيمياوية
الجامعة التكنولوجية

الخلاصة

في هذا البحث تم تقييم نوعين من عمليات الأكسدة لأزالة مركبات الكبريت من نفط خام الأحدب الحامضي (محتوى كبريتي = 3.9 wt%) وهي العمليات المستندة الى عمليات الأكسدة/الأمتزاز أو الأكسدة/ الأستخلاص. في عملية الأكسدة تم استخدام نظام بيروكسيد الهيدروجين /حامض الفورميك كمادة مؤكسدة. استخدم الكاربون المنشط كعامل مساعد / كمادة مازة في عملية الآكسدة/امتزاز بينما استخدم الأسيتونايترايل كمذيب في عملية الآكسدة/ أستخلاص. دلت النتائج على ان الكاربون المنشط كان له دور كبير في زيادة كفاءة عملية الآكسدة/امتزاز. تم دراسة تأثير المتغيرات العملية (زمن التلامس، درجة الحرارة، سرعة الخلط، وكمية المادة المازة) على كفاءة عملية الأكسدة/ الأمتزاز . كانت كفاءة عملية الأكسدة/ امتزاز في افضل ظروف العمل (60℃، 500rpm، 60min، 0.7g كاربون منشط لكل 100ml من النفط الخام) تقريبا 32.8% (محتوى كبريتي= 2.6wt%) وهي مقاربة لكفاءة عملية الأكسدة/الأستخلاص (31.5%) والتي اجريت تحت نفس الظروف العملية وباستخدام نسبة 3:1 مذيب/نفط خام.

الكلمات الرئيسية: تكنولوجيا عمليات ازالة الكبريت، ازالة الكبريت بطريقة الأكسدة، الأمتزاز، الأستخلاص، الكاربون المنشط.

1. INTRODECTION

A common problem facing refineries around the world is that crude oils are becoming heavier, with higher sulfur contents. This result in higher sulfur levels in both straight-run and secondarily processed fuels. Therefore, it is preferable to reduce the sulfur content of crude oil before the oil is refined.

The current HDS technology cannot be suited for the desulfurization of sour crude oil since it leads to shortened catalyst life and more hydrogen consumption, so the production cost will increase. Studying new desulfurization processes is the key to bring more profit to the oil refining companies. A lot of effective work is being done to reduce or eliminate the pollution resulted from processing of sour crude oils and many new technologies for the desulfurization of crude oil are being studied recently.

,Reda, 2006 used oxidative desulfurization assisted by 35 kHz frequency ultrasonic irradiation to reduce the sulfur content of East Baghdad crude oil. The experimental results revealed that the highest removal efficiency was about 76% at 60°C, 80W/cm^{2} sonication power intensity applied for 12 minutes.

Torkmani et al., 2008 isolated the first native fungus, identified as Stachybotrys sp. which is able to remove sulfur and nitrogen from heavy crude oil selectively at 30°C. This fungus was able to desulfurize 76% and 64.8% of the sulfur content of Iranian heavy crude oils (Soroush and Kuhemond oil fields) with initial sulfur contents of 5wt% and 7.6wt% in 72 and 144 h, respectively.

Lin et al., 2010 studied the oxidative desulfurization (ODS) of Azeri crude oil under the electric field. The desulfurization process was carried out in the electric desalting unit. The desulfurization rate of crude oil reached about 77 at 115°C, a desulfurizer dosage of 200µg/g, and a demulsifier dosage of 50µg/g. Also the test results showed that the density and viscosity of crude oil decrease with the removal of sulfur compounds while other basic properties of crude oil are little affected after desulfurization process.

Hammad et al., 2012 treated high sulfur content crude oil feed stream by combined solvent extraction and hydrotreating and provided a treated crude oil product stream of substantially reduced sulfur content and without significant volume loss.

Wang et al., 2013 investigated the simultaneous desulfurization and demetalization of crude oil by electric desalting based on the oxidation of alkyl thiophene and nickel compounds with the compound of Chitosan Schiff Base under the condition of microwave irradiation. By using the optimized conditions for microwave irradiation , up to 56% of sulfur and 82% of nickel removal rates were achieved for model compounds in crude oil samples.

Hosseini and Hamidi, 2014 examined the effect of ultrasonic irradiation on the removal of sulfur from sour crude oil (5.2wt% sulfur) using oxidative method. The results showed a desulfurization efficiency of about 93.2% when ultrasound irradiation was used.

Oxidative desulfurization (ODS), as the name implies, involves a chemical reaction between an oxidant and sulfur that facilitates desulfurization. ODS involves two conceptually different steps. The first step is the sulfur oxidation, which oxidize the organic sulfur compounds to their corresponding sulfoxides, Eq.(1) and sulfones, Eq.(2).

$$R\text{-}S\text{-}R + 1/2\ O_2 \rightarrow R\text{-}(SO)\text{-}R' \quad (1)$$

$$R\text{-}S\text{-}R' + O_2 \rightarrow R\text{-}(SO_2)\text{-}R' \quad (2)$$

The sulfoxides and sulfones have two properties that are different from the unoxidized sulfur compounds and that facilitate desulfurization. First they are more polar, which increase selectivity during solvent extraction and adsorption. Second, the C-S bond

strength is decreased when the sulfur is oxidized therefore it is easier to remove the oxidized sulfur by thermal decomposition from the unoxidized sulfur compounds. The second step is the sulfur removal, which exploits the properties of the oxidized sulfur to effect their removal by extraction, adsorption, distillation, or decomposition methods.
In the present work the capability of two oxidative desulfurization schemes to desulfurize AL-Ahdab Iraqi crude oil with initial sulfur contents of 3.9wt% was studied. The factors that affect this process such as contact time, temperature, mixing speed and sorbent dose were investigated.

2. MATERIALS AND METHODOLOGY

2.1 Materials

Acetone, acetonitrile and methanol (>99.0% purity) were obtained from Aldrich. Formic acid (>99% purity) and hydrogen peroxide (30 wt%) were obtained from Fluka. Granular activated carbon (AC) was obtained from local markets, the physical specification of the activated carbon, as measured in the laboratories of Petroleum Research and Development Center/Ministry of Oil are summarized in **Table 1.** All the chemicals were used as received without any further treatment. Al-Ahdab (AHD) crude oil (API = 25.8, SG = 0.896, Sulfur content = 3.9 wt%) obtained from Al-Daura refinery was used as a feed stock.

2.2 Method of Analysis:

The total sulfur content of the untreated and treated crude oil samples was determined by SELFA-2800 sulfur in oil analyzer (Horiba, USA). The test method is based on ASTM D-4296. All total sulfur measurements were performed by Central laboratory of AL-Daura Refinery.
The desulfurization efficiency is calculated as the ratio of sulfur removed to that initially present in crude oil, Eq.(3).

$$DE\ \% = \frac{C_o - C}{C_o} \times 100 \qquad (3)$$

2.3 Experimental Procedure

2.3.1 Oxidation/adsorption experiments

In the oxidation/adsorption experimental runs, 100ml of Al-Ahdab crude oil, 3ml hydrogen peroxide, 4ml formic acid, 5ml distilled water, and the required dose of activated carbon (0.2 to 0.7g) was heated to the required temperature (35 to 60 ^{0}C) and stirred at 500 rpm for the required period of time (15 to 60 min). The contents were allowed to cool to room temperature and the reaction mixture is transferred to a vacuum filtration system to separate the activated carbon particles from the reaction mixture for which the sulfur content is measured. A simplified process flow diagram is given in **Fig. 1**.

2.3.2 Oxidation/extraction experiments

In each oxidation experiment, 100 ml of AHD crude oil was mixed with an aqueous solution consisting of 3 ml hydrogen peroxide, 4ml formic acid and 5ml distilled water and introduced into the reactor. The reaction mixture was continuously stirred at 500 rpm and 60°C for 60 min. Afterword stirring for the required contact time, the aqueous and oil phases were decanted in a separation funnel. This oxidized feedstock was used throughout the extraction experiments.

In the extraction run, 20ml of AHD crude oil with an appropriate amount of solvent according to the preset solvent/oil ratio were charged into 500ml three-necked flat-bottomed glass reactor equipped with a condenser and a thermometer. The reactor was then placed in a constant-temperature water bath and the mixture was stirred at 300 rpm for 30 min at 30°C. The dispersion formed was then allowed to separate in a separation funnel into two distance phases. The aqueous phase was removed and the oil phase (treated crude oil) was analyzed for the total sulfur content measurements. Each experimental run was repeated 2 to 3 times and each data point was determined based on the mean value with slandered deviation of 1-3%. A simplified process flow diagram is given in **Fig. 2**.

3. RESULTS AND DISCUSSION

3.1 Oxidation / Adsorption Desulfurization

Among the several oxidants that have been used in ODS processes, hydrogen peroxide (H_2O_2) is preferentially chosen as the primary oxidant due to its environmentally benign properties as stated by **Javadli and De Klerk, 2012.** However, H_2O_2 needs to be activated in the presence of a catalyst. Among the different oxidation systems, H_2O_2/carboxylic acid especially formic acid has the advantages of reaction simplicity and commercial availability as proposed by **Mamaghani, et al., 2013.**

Activated carbon is a material with well-developed porous structure, large surface area and many surface oxygen-containing functional groups. To elucidate the effect of activated carbon as a catalyst/sorbent on sulfur removal from AHD crude oil the following operating variables were studied.

3.1.1 Effect of catalyst/sorbent dose

The sorbent dosage is an important parameter, since it determines the capacity of a sorbate at a given initial concentration. As shown in **Fig.3** the rate of sulfur removal increases gradually in direct relationship with the increase in catalyst/sorbent dose. This is an expected result because as the amount of sorbent increased, the available surface area increased, thereby exposing more active sites for the binding of sulfur species. Moreover, it was thought that activated carbon catalyzes the decomposition of hydrogen peroxide to produce hydroxyl radicals that act as strong oxidizing agents like perhydroxyl ions (OH^{-2}) that can easily oxidize the refractory sulfur compounds into sulfones as explained by **Zhou et al., 2009.**

On increasing the sorbent dose beyond 0.7g the desulfurization efficiency is almost constant and no more sulfur is further removed from the solution. This implied that there were enough active sites for sulfur compounds oxidation in the case of activated carbon dose amount of 0.7g**.**

3.1.2 Effect of reaction time

The effect of the reaction time is shown in **Figs.4** and **5** for high and low mixing speeds**.** At a contact time of 60 minutes and 500 rpm, the desulfurization efficiency obtained was 32.8%, but to obtain the same desulfurization efficiency at lower speed (200 rpm) it needs mixing time of about two hours. Increasing the mixing time increases the contact time between the unoxidized sulfur and the oxidation system on one hand and between the oxidized sulfur and the sorbent on the other hand. Besides, on increasing the mixing speed fine emulsions are formed between the two immiscible liquids, which is beneficial when working with biphasic systems. When these emulsions are formed, the surface area

available for reaction between the two phases is significantly increased, enhancing the mass transfer in the interfacial region, thus increasing the rate of reaction.
Moreover **Fig.5** indicates that no significant change in desulfurization efficiency is obtained beyond 2 hours contact time. This is due to the adsorption of alkyl-substituted sulfoxides and sulfones, produced during the oxidation process on the surface of activated carbon, thus suppressing the adsorption process in accordance of **Campos-Martin et al., 2010.** At this point of time, it is thought that a dynamic equilibrium is reached and the amount of sulfur adsorbed indicates the adsorption capacity.

3.1. 3 Effect of reaction temperature
The effect of temperature on the removal of total sulfur was studied at range of 35-60°C. The results show that temperature has large effect on removal of total sulfur. **Fig.6** indicates clearly a strong dependence of desulfurization efficiency on temperature. The desulfurization efficiency increased from 16.4% to 32.8% by increasing the temperature range from 35 to 60˚C.
The main function of oxidants is that they can donate oxygen atoms due to electrophilic addition reaction to the sulfurous compounds present in crude oil to convert them into respective sulfones or sulfoxides. The rate of decomposition of H_2O_2 during oxidative desulfurization is dependent on the temperature and concentration of the peroxide present in the compound. The increase in temperature leads to the increase in the rate of free radical formation and also indicates that there is activation energy for the adsorption process. At low temperature, the adsorption process is basically governed by weak Van der Waals forces; however at higher temperature chemisorption and probably chemical reaction dominate showing an increase in the sorption capacity.
Increasing the reaction temperature beyond 60℃ and operating at mild operating pressure causes the loss of valuable volatile hydrocarbons in crude oil. Moreover, crude oil is very complex mixture that contains alkenes and aromatics, and these compounds can also be oxidized consuming part of the oxidant and degrading the quality of the crude oil. These undesirable oxidation reactions are evident at temperatures of about 80–90°C, For this reason, the reaction has to be conducted at temperatures lower than 80°C and short reaction times as found by **Campos-Martin et al., 2010.** Moreover, **Manatt et al., 2004,** found that when the temperature exceeds 70°F, H_2O_2 rapidly decomposed and reduce the oxidation rate.

3.2 Oxidation/Extraction Desulfurization
The efficiency of extractive desulfurization is limited by the solubility of the organosulfur compounds in the solvent. So, appropriate solvent selection is very important for efficient desulfurization. In the present work, methanol, acetone and acetonitrile were chosen in a pre-screening step as potential solvents. The effect of solvent type and solvent to oil ratio (S/O) on the desulfurization efficiency of AHD crude oil have been investigated to select the most effective solvent and the best (S/O) ratio. The results, as presented in **Fig.7** show that acetonitrile performed the best as an extraction solvent in the desulfurization of AHD crude oil. **Martinie et al., 2010** showed that the sulfur removal ability of acetonitrile is mostly due to its higher polarity as compared with acetone and methanol.
Acetonitrile is used widely as an extractive agent in desulfurization of petroleum fractions due to its high polarity, volatility (having a relatively low boiling point at 355K and can be easily separated by distillation) and its low cost as clarified by **Shiraishi, 2000.**
As can be observed from **Fig.7,** acetonitrile extracting ability increases with increasing its ratio. For acetonitrile, on increasing the solvent/oil ratio from 1:1 to 3:1, the desulfurization

efficiency increased from about 10.3% to 28.5%. An increase in the level of desulfurization can be expected by increasing the solvent/oil ratio. However, on the other hand, an increase in the solvent/oil ratio leads to a decrease in the oil recovery. Similar findings were obtained by **Sobati et al., 2010.**

The main problem is related to the presence of two phases: an oil phase with the oxidized polar sulfur compound and a polar solvent which is not soluble in the oil phase. For this reason, there is some mass transfer limitation between the two phases. Accordingly, the increase in solvent/oil ratio facilitates the transfer of oxidized sulfur compounds at the polar-apolar interface, increasing notably the mass transfer across the interphase as explained by **Campos-Martin et al., 2010.**

Using single stage extraction treatment with acetonitrile, **Fig.8** indicates a decrease in the sulfur content of AHD crude from 3.9 wt% to 2.7 wt%, corresponding to a desulfurization efficiency of 31.5 %, while maintaining a high crude oil recovery yield. These findings indicate that oxidation/extraction process is an efficient desulfurization method and comparable with oxidation/adsorption, **Fig.9,** for treating sour crude oil.

4. CONCLUSIONS

1. The oxidation desulfurization efficiency can be enhanced by using activated carbon as a catalyst and sorbent since activated carbon can catalyze the decomposition of hydrogen peroxide to produce hydroxyl radicals that act as strong oxidizing agents.
2. The oxidation desulfurization efficiency increases with increasing; reaction temperature, time and mixing speed. The optimum operating conditions are 60˚C, 60 min and 500rpm.
3. The extraction of sulfur compounds from AHD crude oil with acetonitrile shows better performance as compared to acetone and methanol due to its higher polarity.
4. The oxidation desulfurization catalyzed by activated carbon is comparable to oxidation/extraction method. The desulfurization efficiencies of both methods are 32.8 and 31.5% respectively.

ABBREVIATIONS

AC	Activated carbon
AHD	Al-Ahdab Crude oil
API	American Petroleum Institute
HDS	Hydrodesulfurization
ODS	Oxidative Desulfurization
OSC	Organosulfur Compounds
SG	specific Gravity

REFERENCES

- Campos-Martin, J. M., Capel-Sanchez, M. C., Presas, P., and Fierro, J. L.G., 2010, *Oxidative Processes of Desulfurization of Liquid Fuels*, J Chem. Technol. 85, 879-890.
- Hammad, A. D., Zaki, Yusuf and Al-Rasheedi, N., 2012, *In-Situ Electrochemical Desulfurization of Crude Oil and its Fraction*, Saudi Aramco Journal of Technology.
- Hosseini. H. and Hamidi, A., 2014, *Sulfur Removal of Crude Oil by Ultrasound-Assisted Oxidative Method* International Conference on Biological, Civil and Environmental Engineering (BCEE-2014) March 17-18, Dubai (UAE)
- Javadli, R., and De Klerk, A., 2012, *Desulfurization of Heavy Oil*, Appl. Petrochem Res, March.
- Lin, L. Hong, Fanfei, M., Ning, W., and Yiyi, H., 2011, *Optimization Study on Oxidative Desulfurization of Crude Oil under Electric Field*, China Petroleum Processing and Petrochemical Technology.
- Mamaghani, A., H., Fatemi, S., and Asgari, M., 2013, *Investigation of Influential Parameters in Deep Oxidative Desulfurization of Dibenzothiophene with Hydrogen Peroxide and Formic Acid*, International Journal of Chemical Engineering, 14, pp.53-67.
- Manatt L., S., and Manatt, R., M., 2004, *The Hydrogen Peroxide/Water System and Its Excess Thermodynamic Functions*, European journal, 10(24), pp. 6540-6557.
- Reda A., N., 2006, *Desulfurization of Crude Oil Using Ultrasound Technique*, M.Sc., Thesis, University of Baghdad.
- Shiraishi, Y., Hirai, T.,and Komasawa, I., 2000, Ind. Eng. Chem. Res., PP. 2826.
- Sobati, M., A., Asghar, M., D., and Mohammad, S., 2010, *Liquid-Liquid Extraction of Oxidized Sulfur-Containing Compounds of Non-Hydrotrated Kerosene*, Fuel Processing Technology, 91(2), pp. 1386-1394.
- Torkamani, S., Shayegan, J., Yaghmaei, S., and Alemzadeh, I., 2008, *Study of the First Isolated Fungus Capable of Heavy Crude Oil Biodesulfurization*, Journal of Chemical Technology & Biotechnology, 83(12):1689 - 1693. ,
- Wang, G., Zhang, J., and Yin, L., 2013, *Catalytic Oxidative Desulfurization of Benzothiophene with Hydrogen Peroxide over Fe/AC in Biphasic Model Diesel-Acetonitrile System*, Korean J. Chem. Eng., 52, pp. 1-7.
- Zhou, X., L., Tan, Q., Yu, X., and Novaro, O., (2009), *Removal of Dibenzothiophene in Diesel by Oxidation over Promoted Activated Carbon Catalyst*, Kinetics and Catalysis, 50(4), pp. 543-549

Table 1. Physical properties of activated carbons.

Test	Results
Surface area (m^2/g)	702
Pore volume (cm^3/g)	0.59
Bulk density (g/cm^3)	0.72
Particle density (g/cm^3)	1.91
Particle Size	1mm

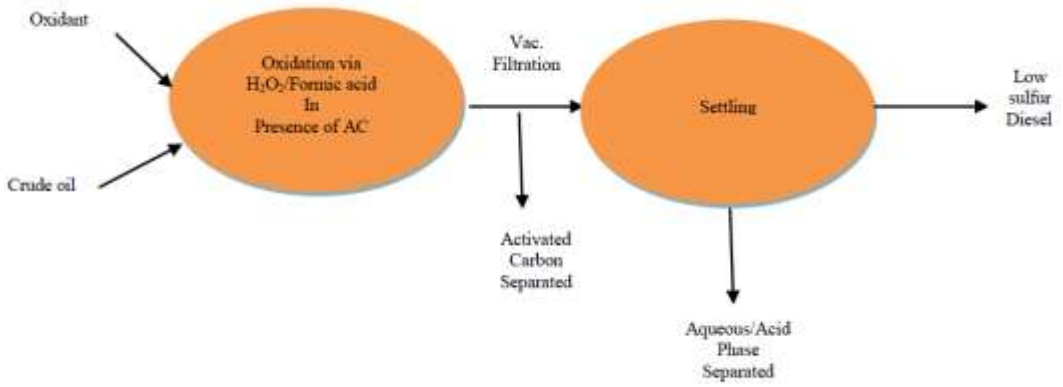

Figure 1. General process flow of diagram for adsorptive desulfurization.

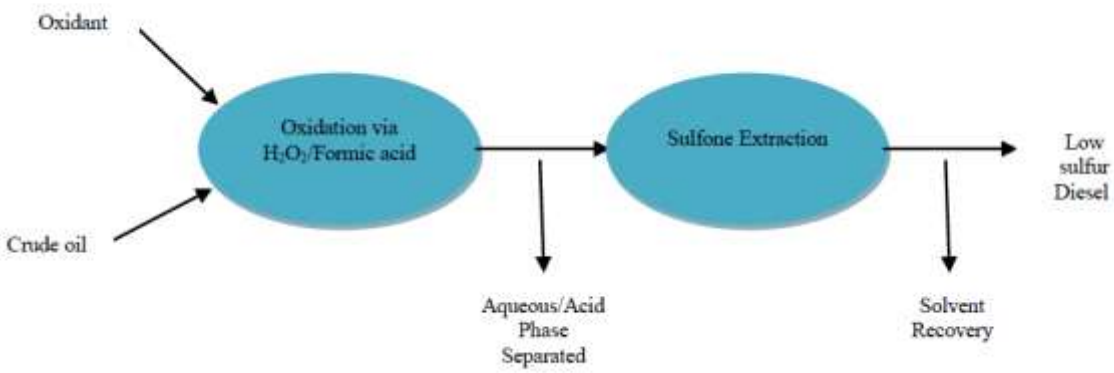

Figure 2. General process flow of diagram for extractive desulfurization.

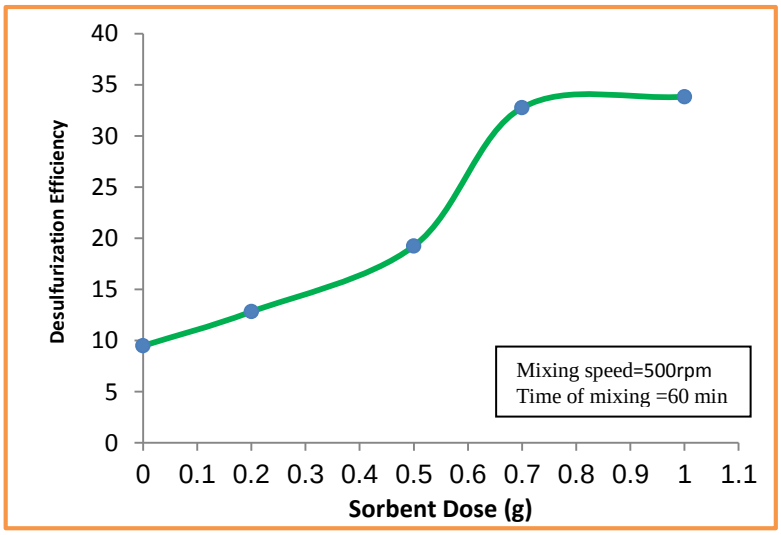

Figure 3. Effect of sorbent dose on the desulfurization efficiency.

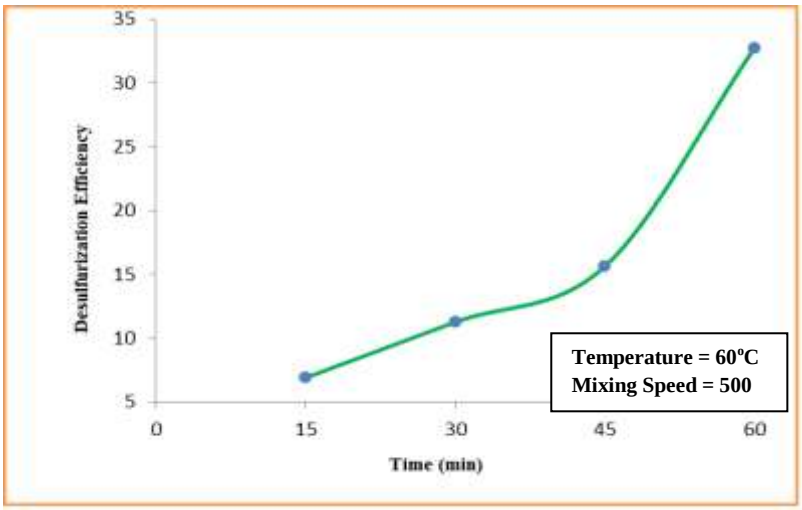

Figure 4. Effect of contact time on the desulfurization efficiency.

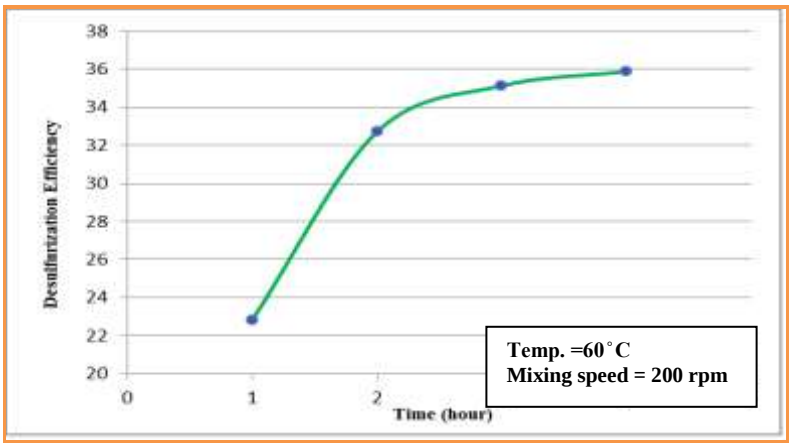

Figure 5. Effect of contact time on the desulfurization efficiency.

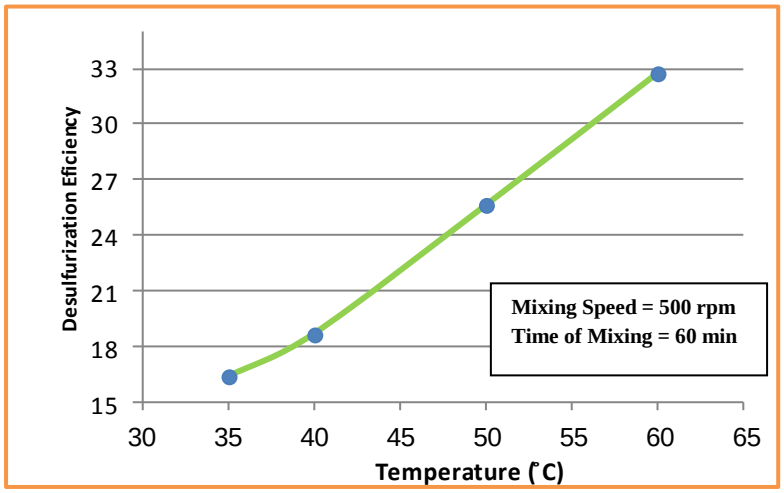

Figure 7. Effect of operating temperature on the desulfurization efficiency.

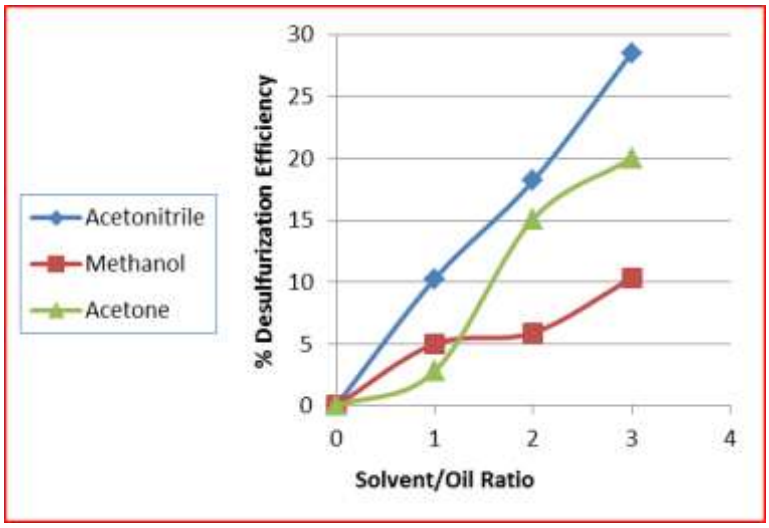

Figure 8. Effect of solvent/oil ratio on desulfurization efficiency.

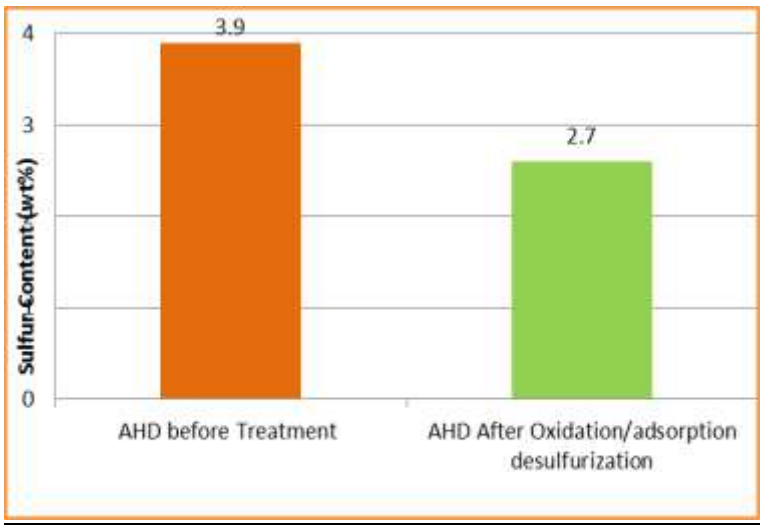

Figure 9. Effect of the oxidation/adsorption treatment on the sulfur content.

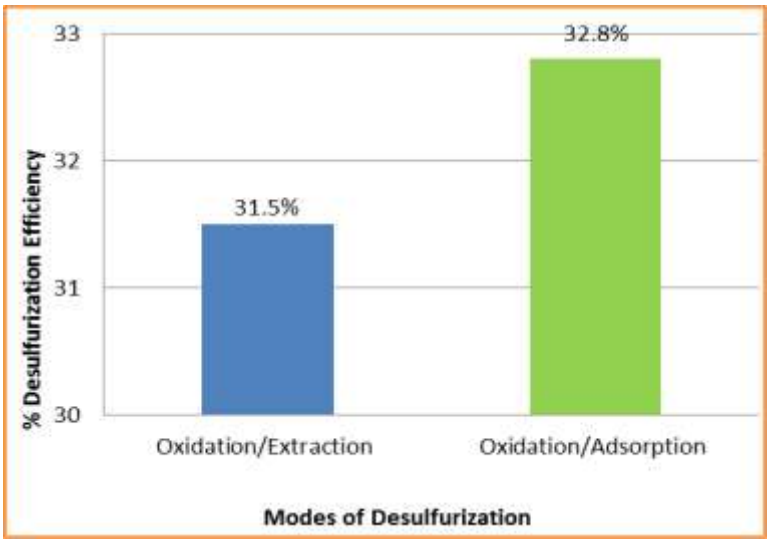

Figure 10. Effect of the oxidative mode on the desulfurization efficiency.

Cathodic Protection for Above Ground Storage Tank Bottom Using Data Acquisition

Naseer Abbood Issa Al Haboubi
Assistant Professor
Department of Chemical Engineering,
University of Al-Nahrin, Baghdad, Iraq
E-mail: ***naseer@habobi.com***

Abstract

Impressed current cathodic protection controlled by computer gives the ideal solution to the changes in environmental factors and long term coating degradation. The protection potential distribution achieved and the current demand on the anode can be regulated to protection criteria, to achieve the effective protection for the system.

In this paper, cathodic protection problem of above ground steel storage tank was investigated by an impressed current of cathodic protection with controlled potential of electrical system to manage the variation in soil resistivity. Corrosion controller has been implemented for above ground tank in LABVIEW where tank's bottom potential to soil was manipulated to the desired set point (protection criterion 850 mV). National Instruments Data Acquisition (NI-DAQ) and PC controllers for tank corrosion control system provides quick response to achieve steady state condition for any kind of disturbances.

Key words: cathodic protection; impressed current; above ground tank bottom; control; DAQ.

السيطرة على الحماية الكاثودية لقاعدة الخزان فوق الارض باستخدام بطاقة تبادل البيانات

ا. م. د. نصير عبود عيسى الحبوبي

قسم الهندسة الكيمياوية / جامعة النهرين

الخلاصة

تقدم السيطرة بواسطة الحاسوب على نظام الحماية الكاثودية ذات التيار القسري حلا مثاليا للمتغيرات المؤثرة منها العوامل البيئية مثل الرطوبة وتدهور طلاء المعدن على المدى الطويل ولتحقيق توزيع جهد الحماية الكاثودية من خلال تنظيم التيار اللازم على الأنود للوصول الى حدود الحماية الفعالة للنظام.

في هذا البحث، درست الحماية الكاثودية لقاعدة الخزان من الحديد الصلب فوق سطح الأرض من خلال تسليط تيار الحماية الكاثودية مع إمكانية التحكم في التيار الكهربائي الواصل الى قطب الانود لمعالجة الفرق الحاصل بالجهد نتيجة التغيير في قيمة مقاومة التربة الكهربائية والتي تتأثر بالرطوبة، تم التحكم على تآكل الخزانات فوق الأرض بواسطة نظام الـ LABVIEW وذلك من خلال تغيير الجهد الواصل عبر التربة الى قاعدة الخزان السفلية إلى نقطة مختارة سلفا 850 ملي فولت.

منظومة السيطرة على التآكل المتالفة من حاسوب ووحدة التحكم NI-DAQ لحماية الخزان توفر استجابة سريعة لتحقيق حالة الاستقرار بالجهد اللازم للحماية لأي نوع من الاضطرابات.

الكلمات الرئيسية: حماية كاثودية، تيار قسري، قاعدة خزان فوق سطح الارض، سيطرة، بطاقة تحصيل البيانات.

1. INTRODUCTION

Storage facilities for petroleum products usually consist of a collection of above ground storage tanks called a tank farm. The tanks are cylindrical in shape, constructed of steel, and rest on the soil. The tank bottom, then, is subject to the same corrosion issues as are buried pipelines. The provision of cathodic protection to tank bottoms is, if anything, more critical than is provision of cathodic protection to pipelines. As the tank bottom is supported by the ground and is subjected to only hydrostatic pressures, the bottom can be made of thinner metal than is used for pipelines, which operate under pressure. Because the metal is thinner, it can be more easily perforated by even low rates of corrosion. The provision of cathodic protection to the bottoms of above-ground storage tanks for petroleum products, however, presents unique design issues as compared to pipelines, **Riemer , et al., 2005.**

Corrosion occurs in aqueous (water-containing) environments and is electrochemical in nature. The aqueous environment is also referred to as the electrolyte and, in the case of underground corrosion, is moist soil. The corrosion process involves the removal of electrons (oxidation) of the metal, **Peabody, 2001.**

It is well known that all metallic structures buried or immersed, and even concreted, inevitably undergo the phenomenon of corrosion once plunged in an electrolyte. Cathodic protection (*CP*), after a good passive protection, is an efficient means of stopping the process of corrosion. It lowers the potential of the protected metallic structure to the value where the reaction of corrosion cannot take place; this potential is known as "threshold of immunity" **,Jain A. K et al., 2011** and **Javadi, et al., 2014.**

External cathodic protection systems are applicable to tanks of any size where the soil corrosivity is sufficient to reduce the tank bottom life to an unacceptably short period. One of the key indicators of corrosivity is the soil resistance. Soil resistivity is used not only to evaluate corrosivity, but also to design the anode ground bed **,Philip, 2009.**

In most cases, it requires energy from an electrical energy source to impress the current. This power to provide the needed current to prevent corrosion with appropriate potential that change due environmental conditions. For this purpose, a lot of experimental work has been done. In this case, a regulated power supply derived by electronic circuit signal from *DAQ* powered cathodic protection system has been designed. The developed circuit allows potentials to be all the time at desired (proper) limits 0.85-0.9V [If a tank has a potential of -850 mV with respect to the copper/copper-sulfate cell then it is usually considered protected. [Protection Criterion The well-known protection criterion for steel in soils of -850 mV with respect to a saturated copper/copper sulfate reference electrode *CSE* was reportedly pioneered by **,Robert**, dating back to **1933**.

When the soil resistivity changes, PC software takes care of this and changing the voltages thru manipulating *DAQ* analog output to anode keep the potential 0.85 V - 1.10V. On the other hand, to stop corrosion entirely, in recent years, there has been increasing interest in the development of efficient corrosion control to improve *CP*. Thus, several control circuits intended to regulate *ICCP* have been designed and discussed **,Kharzi, et al., 2009.**

In this work, to overcome this difficulty, an automatically regulated cathodic protection system with *DAQ* control is proposed. This system senses the variations of the surrounding medium resistivity by measuring the impressed voltage E_i of the bottom of the tank branch against a buried reference electrode $Cu/CuSO_4$ (*CSE*) and adjusts automatically the (*DC*) output voltage of the adapter circuit so that the current is kept nearly constant at the required level regardless of the soil resistivity variations. This system is developed around the *PC–NI DAQ* which controls

the output voltage of the anode, the charging voltage from Power supply **Fig. 1**. The acquisition of the different parameters, as well as the measure of the impressed voltage against the buried reference electrode *CSE*, is allowed by the *DAQ* ports. By using this suggested system, two important goals are achieved. The first one is the prevention of corrosion, because the metallic structure will always receive the exact current required for protection. The second goal is the reduction of maintenance costs and system costs by using high-efficiency power conditioners.

In this study an optimized cathodic protection system has been developed for tuning output voltage of the interface adapter to keep the current of protection (impressed current) nearly constant in order to reach the protection criterion. On the other hand, the cost powered system is improved by the efficient use of its generated electric power by way of the maximum power.

2. SYSTEM DESCRIPTION

Storage tank bottoms of steel structure subject to transitional environments due to changes in soil type (moisture content). Changes simulates the height of the water table or season rains, for example, will affect not only the availability of water but also the access of oxygen to the protected structure surface *PSS*. Transitions between different soil types will also result in different exposure conditions for different parts of the *PSS*. These variations can affect the value of potential on the tank bottoms surface and the ability of the cathodic protection *CP* system to provide adequate protection. A combination of different soil in laboratory and field measurements on operating conditions bottom vessel (1 m diameter) has been used to study the effect of varying moisture content and water level on the level of cathodic protection for tank bottoms subjected to environmental conditions. In both laboratory tests and field trials, the degree of protection was found to depend on the availability of cathodic reactants (O_2 and/or H_2O), **,Philip, 2009.**

Tank to soil potential under protection is measured using $Cu/CuSO_4$ (*CSE*). It is fed as input signal to analog input module of the Data Acquisition Card (*DAQ*) [NI 6009]. Desired set point 0.85 V (normally between -0.85 to -1.1 Volts) is entered manually. Controller module gives output based on the set point (*SP*). This controller operates in direct acting mode (increase in error increases the controller output) **Fig. 1**.

Controller module output is assigned to analog output module of *DAQ*. Output of the controller dynamically varies the triggering base of transistor. Single phase AC power supply is fed to the transistor. Step down transformer (220/30 Volts) *positive terminal* is connected as load to the transistor collector [regulated power supply] and emitter feed the anode (30 cm long, 5 cm in diameter) of high cast iron silicon which is buried 0.5 m (center) down the bottom of the tank and the *negative terminal* to tank body, **Fig. 2**.

By using computer to control corrosion thru software and modeling program built in LABVIEW Fig. 3 to maximize the effectiveness of impressed current cathodic protection *ICCP*. Computer modeling provides the tools to predict how a particular system will perform even for the most complex situations. It can provide quantitative information on the protection potentials achieved and the life of the system, thus reducing the risk of systems not meeting the design goals and enabling future management of assets to be planned effectively.
Virtual Instrumentation controller front panel is presented in **Fig. 3**. Over protection window will become red in color when tank to soil potential *(TSP)* is greater than -1.0 Volts, under protection window will become red if the *TSP* is less than -0.85 Volts. When the controller is set in *without control* mode, set point will directly go as output. In manual mode if the *set point* is 0.85 then *controller output* will also be 0.85 Volts. Under the *Auto TSP* mode, it will try to maintain the *TSP* as per the *Set Point*.
Block diagram (program written in LABVIEW), inputs (error and change in error) are used and one single output (controller output) is used. For corrosion control purpose, *TSP* is used as process value. Here formula blocks are used to convert the sign. In this design, *TSP*, controller output voltage and controller output current are measured through *DAQ* input channels controller output is sent through *DAQ* output channel.

3. RESULTS AND DISCUSSIONS

One of the main conditions to be satisfied by an *ICCP* system is that the protected structure is to be fed by a constant current determined by the structure's metal, the area, and the surrounding medium. However, due to the environmental conditions, *CP* resistance changes significantly due to the anode-to-earth resistance being affected by the variations of the surrounding medium resistivity accordingly to extreme dry-to-wet conditions, which leads to the variation of the output current (impressed current).
Sandy soils taken to study electrical soil resistivity changes with wide range of moisture content, these experiments were taken using four points method **Fig. 4**.

Soil resistivity is an electrical characteristic of the soil/groundwater which affects the ability of corrosion currents to flow through the electrolyte (soil/groundwater).

Resistivity is a function of soil moisture and the concentrations of ionic soluble salts and is considered to be most comprehensive indicator of a soil's corrosivity. Typically, the lower the resistivity, the higher will be the corrosivity of variation.
Starting the experiments with initial conditions of electrical soil resistant equal to 1400 ohm cm at 30% water content under the bottom of the tank, calculating the current and voltage required to achieve tank to soil potential -880 mV which means the structure are protected.

By changing in moisture of soil by adding water (therefore soil resistivity decreases to ≈ 1000 ohm cm) **Fig. 6** followed in disturbance with tank to soil potential **Fig. 7** potential, this drives the *DAQ* to compensate the difference in protected potential thru program built in LABVIEW Fig. 3 to reach the acceptable soil potential (the controlled variable) measured thru CSE copper/copper sulfate electrode by manipulating anode voltage fed form regulated power supply derived by *DAQ*.
Response of the controller is shown in **Fig. 7**. Initially electrolyte conductivity is varied by adding water and controller performance is observed. Controller brought the process value (*TSP*) towards the set point 850 mV. Variation in soil resistance affects corrosion process which, accelerates corrosion by access of O_2 results in a positive shift in potential as more current is

required to electrochemically reduce the oxidant and the tank bottoms is less easily polarized. Under some circumstances, the access of water has the same effect. Although more aerobic conditions lead to more positive potentials, the tank bottoms is not necessarily less well protected. In many dry and/or high resistivity soils, the tank bottoms surface may well be passive because of the high interfacial pH and/or high O_2 concentration **,Fraser , 2011.** In both cases the controller is taking corrective action and bringing process value towards set point.
Fig. 7 also shows response time takes about 2 min which is practically acceptable, many experiments taken (decreasing moisture/increasing electrical soil resistivity) the results approximately agree with the limits of period time.

4. CONCLUSIONS

In this work, a controller for the cathodic protection for above ground tank, has been developed, implemented and evaluated. The model is based on a *PC DAQ* controller were written by LABVIEW. The following conclusions may be drawn from constructing and testing this system;

1. The close control protects the bottom tank from the corrosion. The controller was flexible, and the model corresponded well with the changing of the soil resistivity (the current always try to keep the voltage on the tank base at the set point with 850 mV under protected at some points to 1000 mV under over protected at other points. This is with the acceptable range.
2. *PC* controllers for tank corrosion control system because of quick response to achieve steady state condition for any kind of disturbances, it is very flexible and easy to operate. Design and development of virtual instrumentation Corrosion controller has been implemented for above ground tank. It prevents the tank corrosion by precisely controlling the tank to soil potential at the desired level, conventional *PID* and without controller, better time domain response is obtained about 2 min.
3. In the conventional controllers, operator intervention is more and during start up to be kept in without controller with tank to soil potential reversely increases with soil resistivity for time duration of around 1.5 min occurs over/under protection before putting in the with controller mode.
4. *PC DAQ* requirements can be successfully reduced. Hence, significant cost savings are achievable.
5. New controller is designed so that, to take minimum power to *ICCP*, therefore the overall efficiency of the system is improved significantly. Moreover, a new circuit model is proposed for underground tank bottoms lines and can be used in the simulation of cathodic protection systems. In simulation, the worst conditions have been considered to increase the lifetime of the system and to cause the designed system to be useful in different climatic condition.
6. There are no restrictions to apply this control protection system for different structure geometry, and can be used for the case of structure in offshore, subsea or onshore including shallow coastal waters. Materials include steel - coated or uncoated; other metals; reinforced concrete and hybrid structures. *CP* system will perform over time so that can improve the timing and optimum of *ICCP*.

REFERENCES

- Fraser King, Russell Given, Robert G. Worthingham and Greg Van Boven, 2011, *Effect of Transitions in the Water Table and Soil Moisture Content on the Cathodic Protection of Buried Pipelines*, J. Pressure Vessel Technol. 133(1), 011703,

- Jain A K, Peratta C, Baynham J, Adey R. A., 2011, *Optimization of Retrofit Cathodic Protection (CP) Systems Using Computational Modeling by Evaluating Performance of Remnant and Retrofit CP Systems, Taking into Account Long-Term Polarization Effects*, NACE Corrosion.

- Javadi M., J.Javidan, M. Salimi,2014, *Cathodic Protection of an Underground Pipeline by Photovoltaic Power System Using Intelligent Method*, International Journal of Renewable Energy Research., Vol.4, No.2.

- Kharzi S., M. Haddadi and A. Malek, 2009, *Optimized Design of a Photovoltaic Cathodic Protection*, The Arabian Journal for Science and Engineering, Volume 34, Number 2B.

- Peabody A.W., 2001, *Control of Pipeline Corrosion* – Second Edition, NACE International, The Corrosion Society.

- Philip E. Myers, 1997, *Above Ground Storage Tanks*, McGraw-Hill.

- Riemer D.P., M.E. Orazem, 2005, *A Mathematical Model for the Cathodic Protection of Tank Bottoms*, Corrosion Science 47, 849–868.

- Robert J. Kuhn, 1933,*Cathodic Protection of Underground Pipelines from Soil Corrosion*, Proc. Am. Petroleum Inst. 14, Sec. IV, 153.

Abbreviations

AC	Alternating Current
CP	Cathodic protection
CSE	Copper/copper Sulfate reference electrode
DAQ	Data Acquisition
DC	Direct Current
ICCP	Impressed Current Cathodic Protection
NI	National Instruments
PC	Personal Computer
PID	Proportional Integral Derivative controller
PSS.	Protected Structure Surface
SP	Set Point
TSP	Tank to Soil Potential

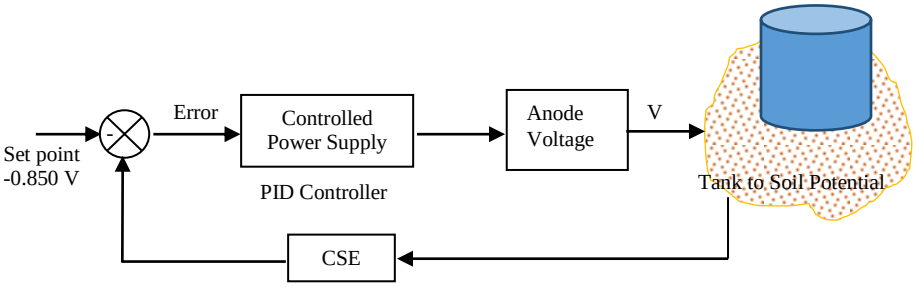

Figure 1. Close loop control for tank to soil potential.

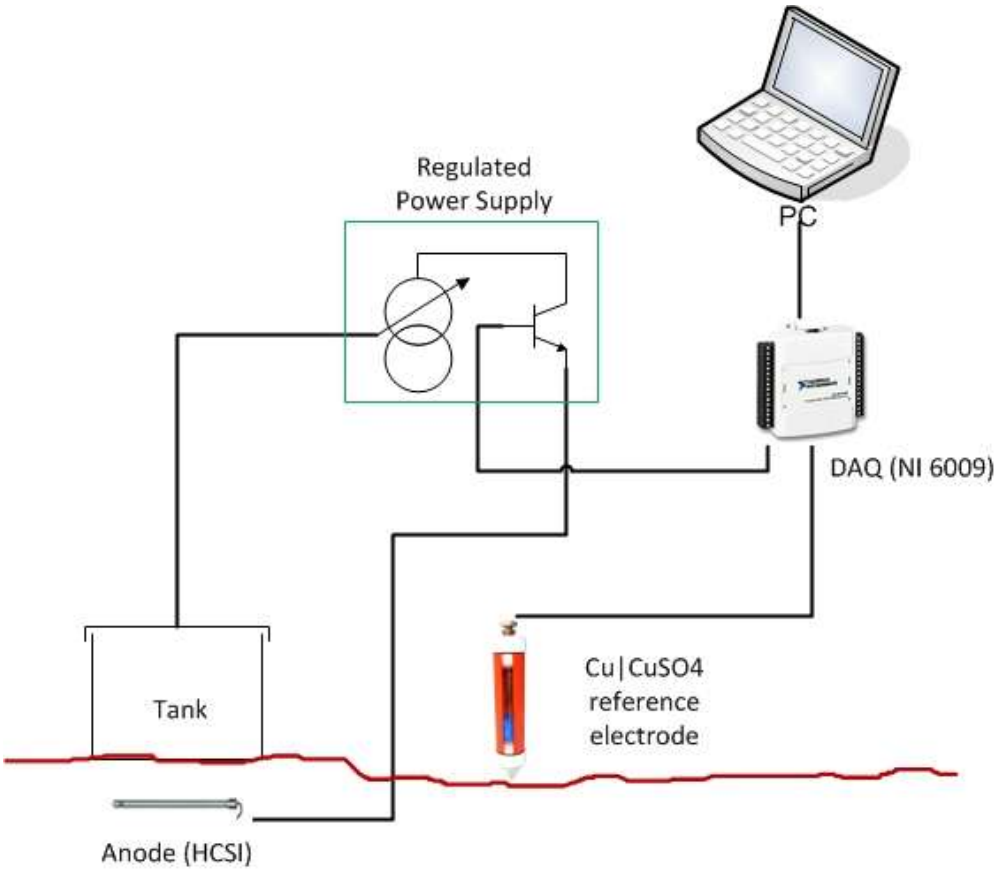

Figure 2. Schematic diagram for tank ICCP.

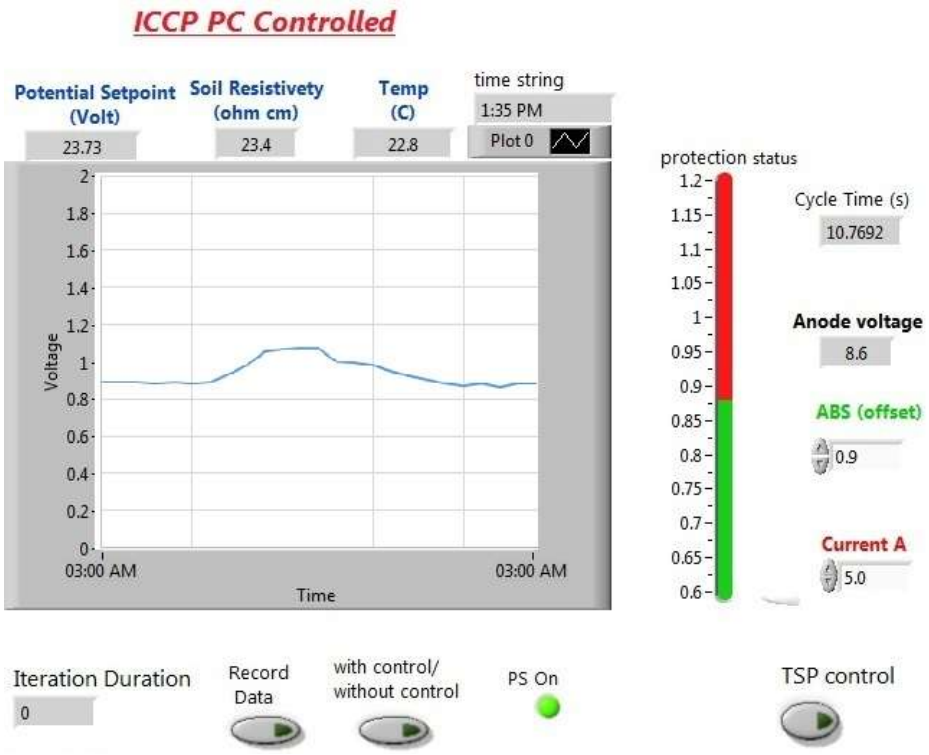

Figure 3. Front panel of impressed currents cathodic protection controller.

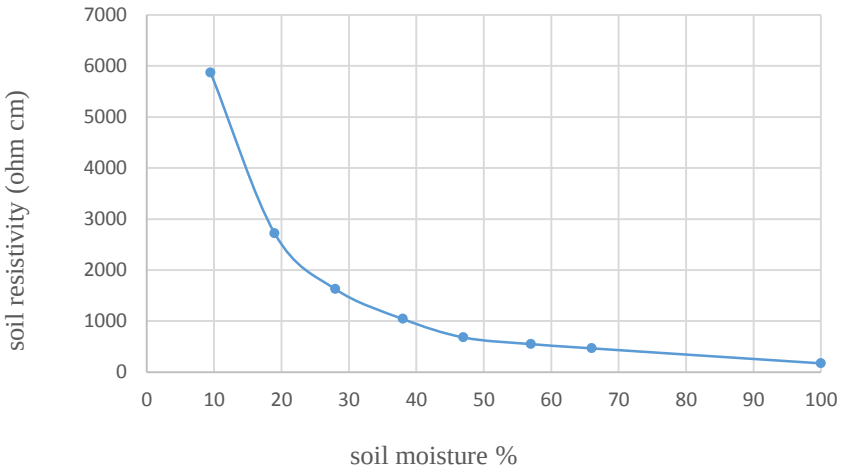

Figure 4. Soil resistivity vs. soil moisture.

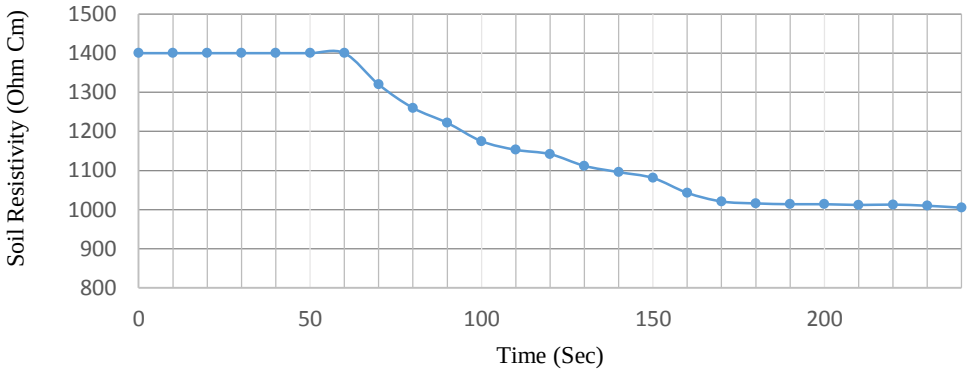

Figure 5. Soil resistivity change vs. time.

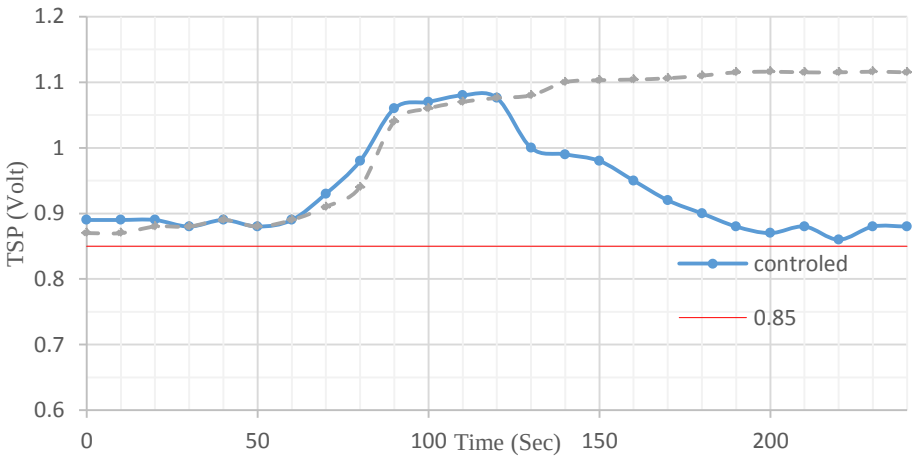

Figure 6. Tank to soil potential vs. time.

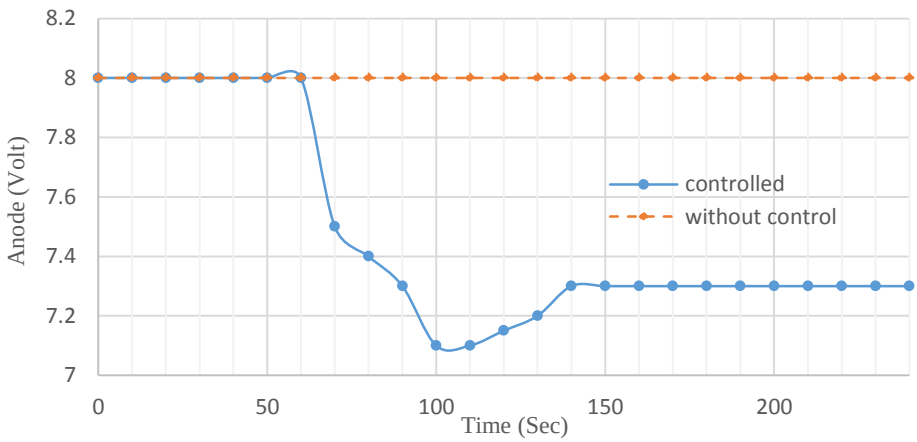

Figure 7. Supplied voltage to anode vs. time.

Optimal Location of Static Synchronous Compensator (STATCOM) for IEEE 5-Bus Standard System Using Genetic Algorithm

Asst. Prof. Dr. Firas Mohammed To'aima
Electrical Engineering Department
College of Engineering
University of Baghdad
E-mail: dr.firasmt@gmail.com

Mr. Yasser Nadhum Al-Aani
Iraqi National Control Center
Ministry of Electricity
Bghdad - Iraq
E-mail: yasernadhum@yahoo.com

Hassan Ali Abdulmajeed Salbi
Electrical Engineering Department
College of Engineering
University of Baghdad
E-mail: Hassansalbi@yahoo.com

ABSTRACT

Heuristic approaches are traditionally applied to find the optimal size and optimal location of Flexible AC Transmission Systems (FACTS) devices in power systems. Genetic Algorithm (GA) technique has been applied to solve power engineering optimization problems giving better results than classical methods. This paper shows the application of GA for optimal sizing and allocation of a Static Compensator (STATCOM) in a power system. STATCOM devices used to increase transmission systems capacity and enhance voltage stability by regulate the voltages at its terminal by controlling the amount of reactive power injected into or absorbed from the power system. IEEE 5-bus standard system is used as an example to illustrate the technique used. Results showed that the STATCOM was able to reduce the voltage deviation and the apparent power losses with minimum possible size of installation capacity for STATCOM devices. GA plays its own requirements by finding best location and best size of STATCOM devices.

Key words: facts, statcom, genetic algorithm.

الموقع الأمثل للمعوض التزامني الثابت لمنظومة IEEE ذات (5) عقدة القياسية بأستخدام الخوارزمية الجينية

أ.م.د. فراس محمد طعيمة
قسم الهندسة الكهربائية
كلية الهندسة
جامعة بغداد

ياسر ناظم العاني
مركز السيطرة الوطني العراقي
وزارة الكهرباء
بغداد – العراق

حسن علي عبد المجيد سلبي البياتي
قسم الهندسة الكهربائية
كلية الهندسة
جامعة بغداد

الخلاصة

النُهج الارشادية تطبق تقليديا لايجاد الحجم الامثل والموقع الامثل للاجهزة المرنة لنظام نقل التيار المتناوب (FACTS) في أنظمة القدرة. تقنية الخوارزمية الجينية (GA) طبقت لحل مشاكل هندسة الطاقة المثلى معطية نتائج أفضل من الطرق التقليدية. هذا البحث يوضح تطبيق (GA) لايجاد الموقع والحجم الامثل للمعوض التزامني الثابت (STATCOM) في نظام القدرة. يستعمل (STATCOM) لزيادة سعة أنظمة النقل وتحسين استقرارية الفولتية عن طريق تنظيم الفولتية عند الاطراف (الأحمال) بواسطة التحكم بمقدار القدرة غير الفعالة المحقونة أو الممتصة من منظومة القدرة. المنظومة الكهربائية ذات (5) عقدة القياسية لـ IEEE أستخدمت كمثال لتوضيح التقنية المستخدمة. أظهرت النتائج بأن الجهاز كان قادرا على تقليل أنحراف الفولتية وخسائر القدرة الظاهرية, مع أقل حجم ممكن للسعة التنصيبية لأجهزة (STATCOM). (GA) لعبت دورهم من خلال ايجاد الموقع الامثل والحجم الامثل لأجهزة (STATCOM).

الكلمات رئيسية: الاجهزة المرنة لنظام نقل التيار المتناوب, المعوض التزامني الثابت, الخوارزمية الجينية.

1. INRODUCTION

Recently network blackouts related to voltage collapse tend to occur from lack of reactive power support in heavily stressed conditions, which are usually triggered by system faults. Reactive power has received less attention recently until the Great Blackout in August 2003 in the northeastern US, which showed that the reactive power in US power systems was not very well planned and managed, **Zhang, et al., 2006.**

Reactive power including its planning process had received tremendous interest after the 2003 Blackout from utilities, independent system operators, researchers, and the government. Power electronics based equipment, or flexible AC transmission systems (FACTS), provide proven technical solutions to voltage stability problems. Especially, due to the increasing need for fast response for power quality and voltage stability, the shunt dynamic Var compensators such as Static Var Compensators (SVC) and Static Synchronous Compensators (STATCOM) have become feasible alternatives to a fixed reactive source, and therefore have received intensive interests, **Meena, et al., 2013.**

The Static Synchronous Compensator (STATCOM) is a shunt device which employs one of the latest technologies of FACTS and power electronic switching devices in electric power transmission systems to control the voltage and power flow. The STATCOM regulates the voltage at its terminal by controlling the amount of reactive power injected into or absorbed from the power system. When the system voltage is low, STATCOM generates reactive power and when the system voltage is high STATCOM absorbs reactive power. The purpose behind installing STATCOMs is crucial in deciding where to install them and the sufficient number and size of each STATCOM. The locations of STATCOMs have a significant impact on the power flow control performance.

In this paper, STATCOM was proposed to reduce the apparent power loss and solve voltage fall problem for the IEEE 5-bus standard system, this performance has been done by using minimum possible size of the reactive power injected or absorbed by the STATCOM devices, while satisfying the stability limits in order to reduce the estimated installation cost of STATCOM devices. The locations and sizes in MVAr of the STATCOM devices will be calculated by means of one of the optimization algorithm, namely, “Genetic Algorithm” (GA), **Salbi, 2014.**

GA is one of the commonly used methods to solve several optimization problems. GA can be used only for the types of problems where solutions can be represented by chromosome. GA starts by a randomly generated population of solutions, which will be improved through a repetitive application of mutation, crossover, and selection operators. Individual solutions are selected through a fitness-based process, where the more adapted solution is typically more likely to be selected.

2. STATIC SYNCHRONOUS COMPENSATOR (STATCOM)

STATCOM is a second generation FACTS device used for shunt reactive power compensation. The principle of STATCOM is the reactive power compensation where the reactive power and voltage magnitude of the system can be adjusted such as shown in **Fig. 1**. It consists of three paths: shunt (coupling) transformer, voltage source converter (VSC), and capacitor. The reactive power is distributed in the power system by the converter control **,Lin, et al., 2009.**

Where $V\,i\,\angle\theta\,i$: are the bus voltage and its phase angle of power system.

$V\,s\,\angle\theta\,s$: is the STATCOM voltage and its phase angle.

The SATCOM active P and reactive power Q are given in Eqs. (1) and (2).

$$P = \frac{V_S V_i}{X_S} \sin\delta \qquad (1)$$

$$Q = \frac{V_i^2}{X_s} - \frac{V_s V_i}{X_s}\cos\delta \quad (2)$$

Where *Xs:* is coupling transformer equivalent reactance

$$\delta = \theta s - \theta i \quad (3)$$

The STATCOM is a combination of a voltage sourced converter and an inductive reactance and shunt connected to power system. The converter supplies leading current to the AC system if the converter output voltage *Vi* is made to lead the corresponding AC system voltage *VS*. Then it supplies reactive power to the AC system by capacitive operation. Conversely, the converter absorbs lagging current from the AC system; if the converter output voltage *Vi* is made to lag the AC system voltage *VS* then it absorbs reactive power to the AC system by inductive operation. If the output voltage is equal to the AC system voltage, the reactive power exchanges.

3. GENETIC ALGORITHM

Genetic algorithm (GA) is one of the evolutionary Algorithms search technique based on mechanism of natural selection and genetics. It searches several possible solutions simultaneously and do not require prior knowledge or special properties of the objective function, **Eseosa, et al., 2012.**

GA starts with initial random generation of population of binary string, calculates fitness values from the initial population, after which the selection, cross over and mutation are done until the best population is obtained. GA encodes the variables of the optimization function and runs a searching process that explores the searching space in parallel. The searching mechanism starts with an initial set of solutions generated randomly and called "*Population*". This initial set up solutions satisfies the equality and inequality constraints of the problem. Each individual solution in the population is called "*Chromosome*". The movement of the algorithm towards the global point is directed by fitness function evaluation of the chromosomes. GA uses the criteria of natural selection to evolve the chromosomes through successive iterations called "*Generations*". New chromosomes (offspring) are formed by crossover and/or mutation operators. And by continuous evaluation of each chromosome during each generation, and by using selection techniques, a new generation is formed. Typically GA consist of three phases,

(1) Generation
(2) Evaluation
(3) Genetic operation

3.1 Generation

In this phase number of chromosomes equal to population size is generated and each is of length equals to string length. The size of population is direct indication of effective representation of whole search space in one population. The population size affects both the ultimate performance and efficiency of GA. If it is too small it leads to local optimum solution. The selection of string length depends on the accuracy and resolution requirement of the optimization problem. The higher the string length, the better the accuracy and resolution. But this may lead to slow convergence.

3.2 Evaluation

In the evaluation phase, suitability of each of the solutions from the initial set as the solution of the optimization problem is determined. For this function called *"fitness function"* is defined.

This is used as a deterministic tool to evaluate the fitness of each chromosome. The optimization problem may be minimization or maximization type. In the case of maximization type, the fitness function can be a function of variables that bear direct proportionality relationship with the objective function **,Sivanandam, et al., 2008.**
For minimization type problems, fitness function can be function of variables that bear inverse proportionality relationship with the objective function or can be reciprocal of a function of variables with direct proportionality relationship with the objective function. In either case, fitness function is so selected that the most fit solution is the nearest to the global optimum point. The programmer of GA is allowed to use any fitness function that adheres to the above requirements. This flexibility with the GA is one of its fortes.

3.3 Genetic Operation

In this phase, the objective is the generation of new population from the existing population with the examination of fitness values of chromosomes and application of genetic operators. These genetic operators are *reproduction, crossover, and mutation.* This phase is carried out if we are not satisfied with the solution obtained earlier. The GA utilizes the notion of survival of the fittest by transferring the highly fit chromosomes to the next generation of strings and combining different strings to explore new search points.

i. Reproduction

Reproduction is simply an operator where by an old chromosome is copied into a Mating pool according to its fitness value. Highly fit chromosomes receive higher number of copies in the next generation. Copying chromosomes according to their fitness means that the chromosomes with a higher fitness value have higher probability of contributing one or more offspring in the next generation.

ii. Cross over

It is recombination operation. Here the gene information (information in a bit) contained in the two selected parents is utilized in certain fashion to generate two children who bear some of the useful characteristics of parents and expected to be more fit than parents.
Crossover is carried out using any of the following three methods:
(a)Simple or Single Point Crossover
(b) Multi point crossover
(c) Uniform crossover

iii. Mutation

This operator is capable of creation new genetic material in the population to maintain the population diversity.
It is nothing but random alteration of a bit value at a particular bit position in the chromosome.
Some programmers prefer to choose random mutation ‘or’ alternate bit mutation. *“Mutation Probability (Pm)”* is a parameter used to control the mutation. For each string a random number between ‘0’ and ‘1’ is generated and compared with the Pm. if it is less than Pm mutation is performed on the string. Sometimes mutation is performed bit-by-bit also instead of strings. These results in substantial increase in process time but performance of GA will not increase to the recognizable extent **,Gen, et al. 2008.**
So this is usually not preferred. Thus obviously mutation brings in some points from the regions of search space which otherwise may not be explored. Generally mutation probability will be in the range of 0.001 to 0.01. This concludes the description of Genetic Operators.

4. OBJECTIVE FUNCTIONS

Three objective functions were considered in this paper, which are the apparent power losses (operational efficiency), voltage deviation (system security and service quality) and minimum possible value of reactive power injected/absorbed by the STATCOM (economic benefits). These objective functions can be summarized as follows:

A. Apparent Power Losses

The apparent power loss of the transmission line is one of the essential objectives for the optimization problem in the electrical power system when it gathers the active and reactive components in one formula. Then the apparent power losses of the transmission lines are given as:

$$S_{losses} = \sum_{i=1}^{Nt}\left(\left| P_{si} - \mathrm{P_{ri}} \right| + j\left[\left| Q_{si} - \mathrm{Q_{ri}} \right| - \{Q_{si}^{ch} + Q_{ri}^{ch}\} \right] \right) \quad (4)$$

In which

$$Q_i^{ch} = V_i^2 \frac{B_i}{2} \quad (5)$$

Where S_{losses} are the apparent power losses in MVA. Nt is the number of transmission lines. P_{si} and P_{ri} are the sent and received active power of the line *i*, respectively. Q_{si} and $Q_{ri}$are the sent and received reactive power of the line *i*, respectively. Q_{si}^{ch} and Q_{ri}^{ch} are the sent and received charging reactive power of the line *i*, respectively. V_i is the voltage magnitude at bus *i*. B_i represents the susceptance of the π-model transmission line *i*, **Salbi, 2014.**

B. Voltage Deviation

The bus voltage is one of the most important security and service quality indexes. Therefore, minimizing the voltage drop will increase the system security. The voltage deviation of the system is given as, **Vedam, et al., 2009.**

$$V_D = \sum_{i=1}^{Nb} \frac{(V_{ref} - V_i)^2}{V_{ref}} \quad (6)$$

The reference voltages for generator (PV) bus are fixed, thus, the equation becomes:

$$V_D = \sum_{i=1}^{Nd} (V_{ref} - V_i)^2 \quad (7)$$

Where

V_D is the voltage deviation. V_{ref} is the reference voltage for bus *i*. $\mathrm{V_i}$ is the specified voltage magnitude at bus *i*. Nb is the number of buses. Nd is the number of load buses.

C. Minimum Possible Size of STATCOM in MVar

This objective states that the injected/absorbed reactive power in Mvar should be as minimum as possible to satisfy the optimization and load flow requirements, which will lead to getting a minimum size of STATCOM Min_{MVar} and so minimizing STATCOM initial cost.

Many different sizes and Standardized configurations of STATCOM are available and the may be used in bands such as: ±25MVar, ±35MVar, ±50MVar, ±100MVar, and above. These units can be configured as a fully parallel operating system. It is well known that the FACTS devices can be used to provide reactive power compensation.
Table 1 gives an idea about the estimated cost of various reactive power sources including all FACTS devices, **Mathur, et al., 2002.**

5. OTTIMIZATION OF MULTIOBJECTIVE FUNCTION

The optimization problem may have a singleobjective function or multi objective functions. The multiobjective optimization problem can be defined as the problem of finding a vector of decision variables that satisfies the constraints and optimizes a vector function whose elements represent the objective functions. Most of the real world problems involve more than one objective, making multiple conflicting objectives interesting to solve as multi objective optimization problems. Multiobjective problem can be formulated as **,Zitzler, 1999.**

Minimize

$$Y(x,u) = [f_1(x,u), \dots\dots, f_n(x,u)] \tag{8}$$

While satisfying

$$g(x,u) = [g_1(x,u), \dots\dots, g_{m1}(x,u)] = 0 \tag{9}$$

$$h(x,u) = [h_1(x,u), \dots\dots, h_{m2}(x,u)] \leq 0 \tag{10}$$

Where:
n is the number of objectives required to minimize or maximize. m_1 and m_2 are the number of equality and inequality constraints, respectively.
Compared with the single objective problems, multiobjective problems are more difficult to solve, since there is no unique solution. There is a set of acceptable trade-off optimal solutions. This set is called Pareto front. The preferred solution, the one most desirable to the decision maker, is selected from the Pareto set **,Kong, et al., 2009.**
There are several methods that can be used to solve multiobjective problems using single objective approximations. The weighted sum method is used in this work to solve the Pareto front problem. Weighted sum method changes a weight multiplier among the objectives in the objective function to obtain the Pareto front. Then, the multiobjective optimization problem will take the following general form:

$$F(x,u) = w_1 f_1(x,u) + w_2 f_2(x,u) + \cdots + w_m f_m(x,u) \tag{11}$$

Where:

$$0 \leq w_i \leq 1 \tag{12}$$

$$\sum_{i=1}^{m} w_i = 1 \tag{13}$$

6. CASE STUDY

The Genetic algorithm technique will be implemented to find the fitness function solutions for the proposed cases as shown in **Fig. 2**. The aim is to find the best locations of the STATCOM devices as well as the value of injected or absorbed reactive power from each one to satisfy the minimum values for the three proposed objectives. Two operational case studies will be discussed and analyzed in details in this research to clarify the significance of the proposed STATCOM device including the location and the size. The algorithm will be applied on the IEEE 5-bus standard system, based on the location and the size results of STATCOM.

The proposed algorithm is restricted to the following parameters, **Salbi, 2014.**

- The number of STATCOM devices that will be installed is one for the case of IEEE 5-bus standard system.
- The maximum and minimum limits of STATCOM used is :
  $-25MVar \leq Q_{STATCOM} \leq +25MVar$
- The algorithm is appropriate that only one STATCOM device is allowed to be installed at nominated bus.
- The STATCOM devices can be installed only at load buses (PQ).The slack bus and (PV) buses are excluded.
- GA parameters for the two case studies are:
  Population size = 65
  Maximum number of generations = 80
  Cross over probability = 0.8
  Mutation probability = 0.003

7. RESULTS

Fig. 3 shows the single line diagram for the IEEE 5-bus standard system which contains (2) generators, (7) transmission lines, and (3) load buses. The real data for the IEEE 5-bus test system are given in **Table 2.** The number of STATCOM devices that can be used is $0 \leq N_{STATCOM} \leq 3$. Only one STATCOM device with maximum and minimum size limits of ±25 MVar was sufficient to satisfy the stability requirements. GA solves the multiobjective function with equal weights for all factors (S_{losses} , V_D, and Min_{MVar}). The results show that the STATCOM optimal location is at bus (4) with the size of (22.5806 MVar) as an injected reactive power to the system. Obviously, the voltage deviation and the apparent power losses are reduced when compared with the uncompensated system using the conventional Newton-Raphson power flow. **Table 3** shows the STATCOM location, the size of injected MVar, the estimated cost, and the comparison between V_D and S_{loss} for the two cases.

In the STATCOM localization problem, it was noticed that the algorithm found the solution after around 2 generations. Nevertheless, the number of generations in each case is set to be 80 to explore all search space and prevent the algorithm from falling in local minima. For this optimum case, the evolution of the best individual (minimum objective function value) for each generation of GA with the value of the fitness function is to be minimized which collect three objective functions as shown in **Fig.4**.

The bus voltage magnitudes for the two cases uncompensated (before installing STATCOM) and compensated (after installing STATCOM using GA) are illustrated in **Fig. 5.** From **Table 3** and **Fig. 5**, it can be seen that when the reactive power is injected by a STATCOM device in bus 4 (selected by GA), a better improvement in the network voltage level occurs with reducing the voltage deviation by 53.95%. Also the STATCOM effect is attained to reduce apparent power loss by 2.25%.

8. CONCLUSION

In this work, GA was proposed as an algorithm to find the best locations and sizes of STATCOM devices. The algorithm was applied to IEEE 5-bus standard system. The proposed algorithm was implemented using MatLab programming language. Three objectives were taken into account, namely, apparent power losses, voltage deviation, and minimum possible size in MVar injecting or absorbing by the proposed device of STATCOM. GA was used to solve the multiobjective optimization problem. The three objectives were combined in one objective function using weighting method. The application of the algorithm successfully found the optimum location and the size of STATCOM. STATCOM reduced the apparent power losses of the grid as well as enhanced voltage profile by reducing voltage deviation from its nominal value for all load nodes. The optimization algorithm was always restricted to the system voltage limits, STATCOM's proposed limits, generators reactive power limits, etc.

REFERENCES

- Eseosa, O., and Odiase, F. O., 2012, *Efficiency Improvement of Nigeria 330kV Network using Flexible Alternating Current Transmission System (FACTS) Devices*, International Journal of Advances in Engineering & Technology (IJAET), Vol. 4, No. 1, PP. 26-41.

- Gen, M., Cheng, R., and Lin, L., 2008, *Network Models and Optimization Multiobjective Genetic Algorithm Approach*, Springer-Verlag, London.

- Kong, J., and Jeyasurya, B., 2009, *Multiobjective Power System Optimization Including Security Constraints*, International Conference on Intelligent System Applications to Power Systems (ISAP), Curitiba, PP.1-5.

- Lin, W., Lu, K., Huang, C., Ou, T., and Li, Y., 2009, *Optimal Location and Capacity of STATCOM for Voltage stability Enhancement using ACO plus GA*, IEEE/ASME International Conference on Advanced Intelligent Mechatronics, Singapore, PP.1915-1920.

- Mathur, R. M., and Varma, R. K., 2002, *Thyristor-Based FACTS Controllers for Electrical Transmission Systems*, IEEE Press, New York.

- Meena, M. E., and Gupta, R., 2013, *Transmission Loadability Enhancement by Using FACT Devices with Fuzzy Logic Controller*, International Journal of Advanced Research in Computer Science and Electronics Engineering (IJARCSEE), Vol. 2, No. 8, PP.599-606.

- Salbi, H. A., 2014, *Optimal Location of Static Synchronous Compensator (STATCOM) for Iraqi National (400kV) Super High Voltage Grid using Genetic Algorithm*, A thesis submitted in fulfillment of requirements for award of the Master of engineering, Electrical Department, Engineering College, University of Baghdad.

- Sivanandam, S. N., and Deepa, S. N., 2008, *Introduction to Genetic Algorithms*, Springer-Verlag, Berlin.

- Vedam, R. S., and Sarma, M. S., 2009, Power *Quality VAR Compensation in Power Systems*, Taylor & Francis Group, CRC Press, Boca Raton.

- Zhang, W., Li, F., and Tolbert, L. M., 2006, *Optimal Allocation of Shunt Dynamic Var Source SVC and STATCOM: A Survey*, IET International Conference on Advances in Power System Control, Operation and Management (APSCOM), Hong Kong, PP. 1-7.

- Zitzler, E., 1999, *Evolutionary Algorithms for Multiobjective Optimization: Methods and Applications*, Computer Engineering and Networks Laboratory, Doctoral Dissertation, Swiss Federal Institute of Technology Zurich, Zurich.

NOMENCLATURE

Min_{Mvar}: minimum reactive power supplied by STATCOM
$N_{STATCOM}$: number of STATCOMs
P: active power
Q: reactive power
$Q_{STATCOM}$: reactive power of STATCOM
S_{losses}: apparent power losses
V_D: voltage deviation
V_s: ac bus voltage
V_i: STATCOM bus voltage
θs: phase angle of power system
θi: phase angle of STATCOM
Xs: coupling transformer equivalent reactance
Nt: number of transmission lines
Q_i^{ch}: charging reactive power of line *i*
B_i : susceptance of the π-model transmission line *i*
Nd: number of load buses
$F(x,u)$: multiobjective optimization function

Table1. Cost estimates for FACTS controllers.

Controller	Cost
Shunt Capacitor	8$US /Kvar
Conventional series capacitor	20$US /Kvar
SVC	40$US /Kvar – controlled part
TCSC	40$US /Kvar – controlled part
STATCOM	50$US /Kvar
UPFC series portion	50$US /Kw – series power flow
UPFC shunt portion	50$US /Kvar – controlled part

Table2. The input branch data for the IEEE 5-bus standard system.

From Bus	To Bus	R p.u.	X p.u.	B p.u.
1	2	0.02	0.06	0.06
1	3	0.08	0.24	0.05
2	3	0.06	0.18	0.04
2	4	0.06	0.18	0.04
2	5	0.04	0.12	0.03
3	4	0.01	0.03	0.02
4	5	0.08	0.24	0.05

Table3. Results of comparison between uncompensated and compensated cases.

Case	Voltage deviation V_D	Apparent power loss S_{loss}(MVA)	Bus location	Minimum injected size in MVar Min_{MVar}	Estimated cost ($\$\times 10^5$)
Uncompensated	0.0569	15.9568	__	__	__
Compensated *using one STATCOM*	0.0262	15.5975	4	22.5806	11.2903

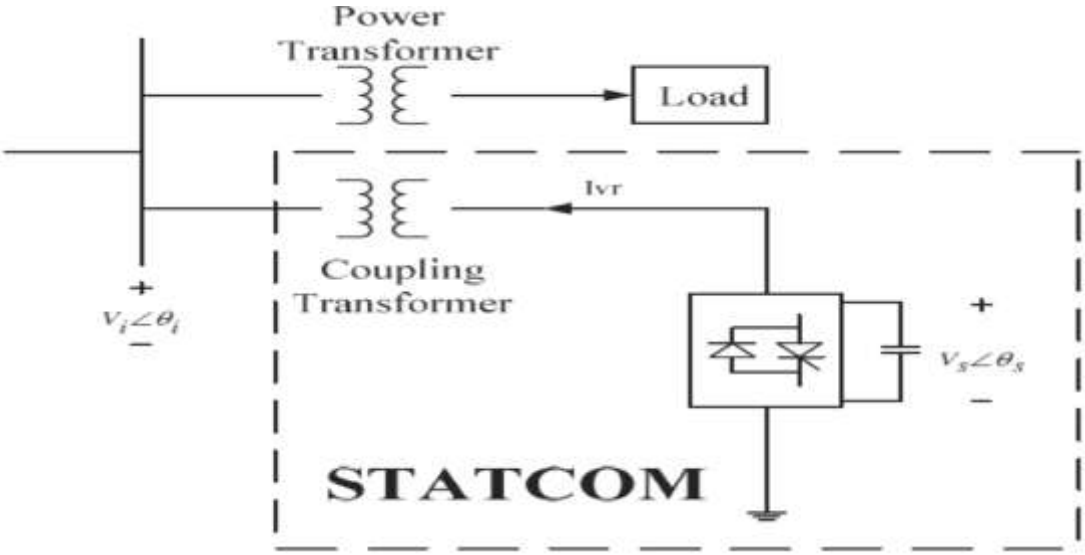

Figure 1. Block diagram of a typical STATCOM.

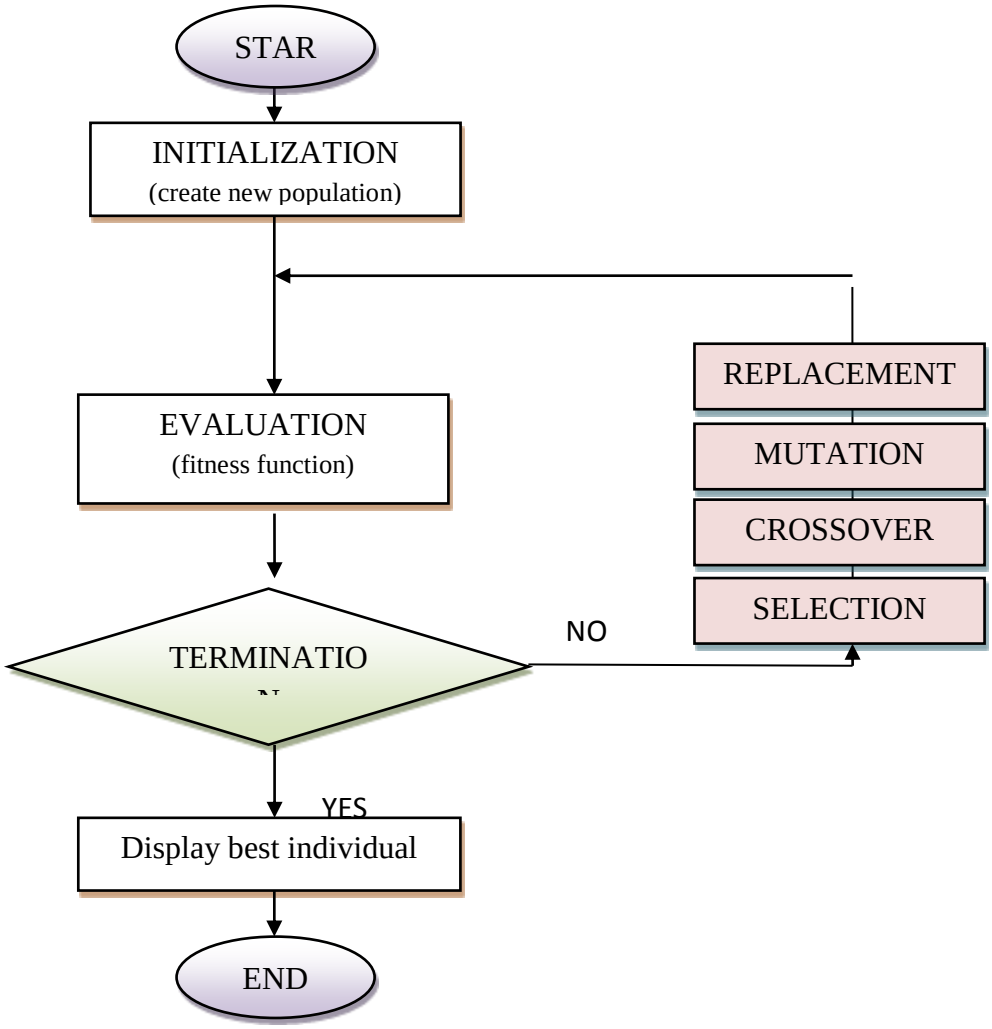

Figure 2. The proposed implemented Genetic Algorithm (GA).

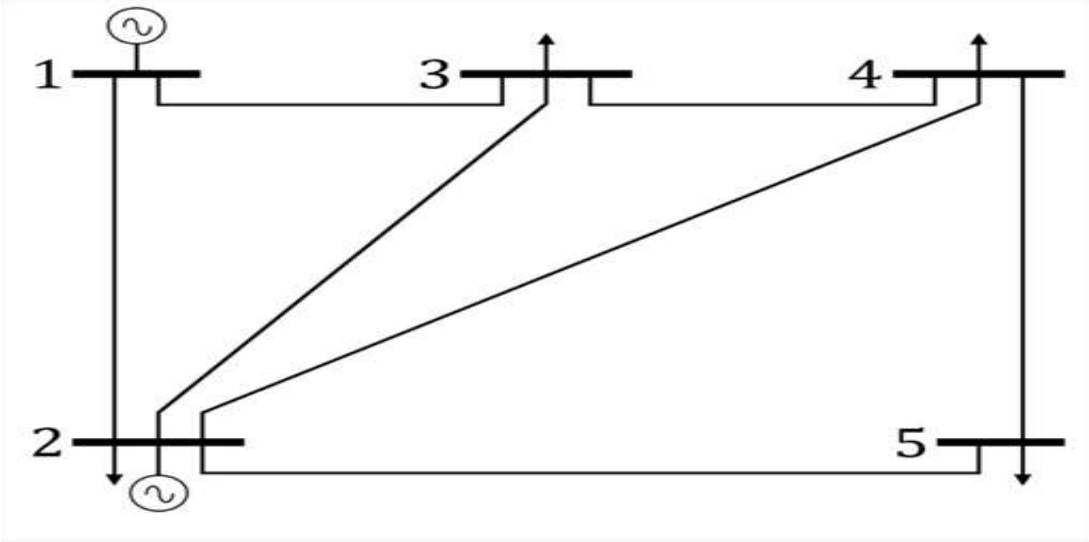

Figure 3. Single line diagram of IEEE 5-bus standard system.

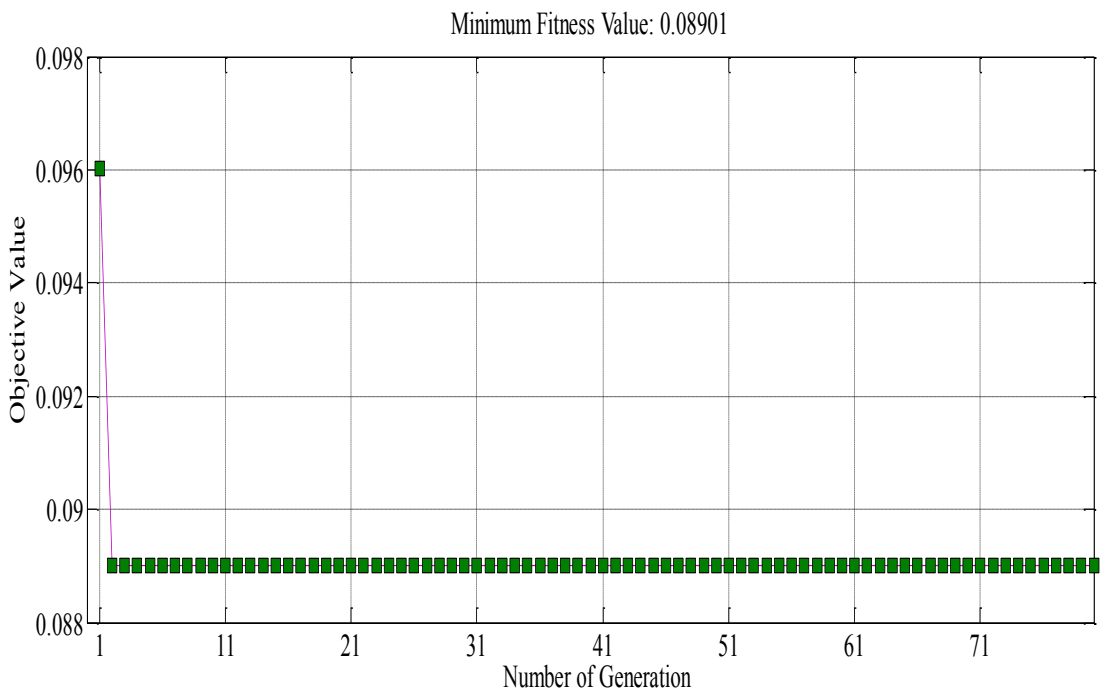

Figure 4. Best individual evolution for each generation in GA for IEEE 5-bus standard system.

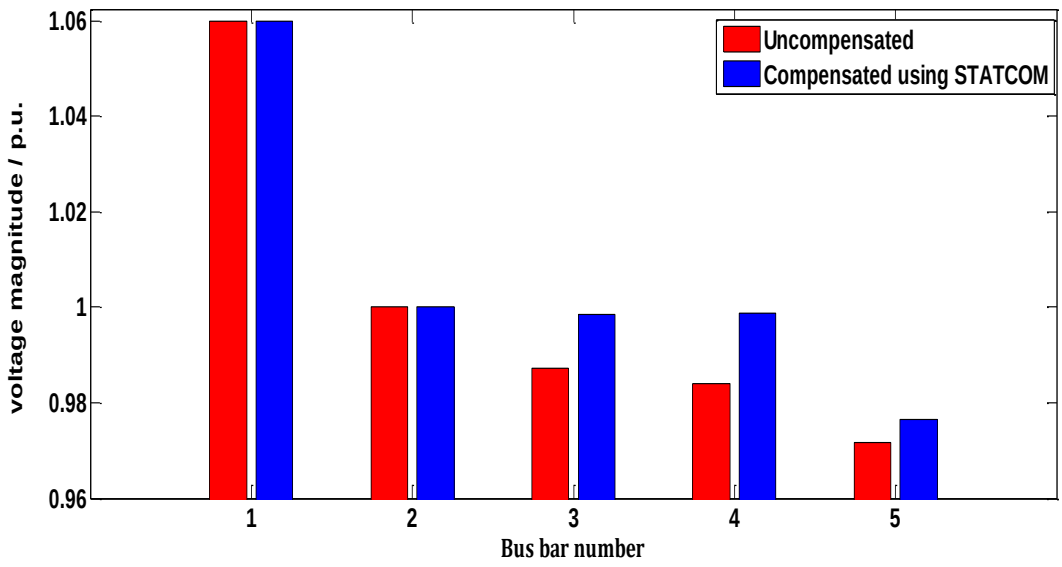

Figure 5. Bus voltage magnitudes before and after installing one STATCOM (in bus no.4) for IEEE 5-bus standard system.

Block-Iterative Frequency-Domain Equalizations for SC-IDMA Systems

Lect. Salah Awad Salman
Department of Information Systems
College of Computer, University of Anbar
Email: salah_eng1996@yahoo.com

ABSTRACT

In wireless broadband communications using single-carrier interleave division multiple access (SC-IDMA) systems, efficient multiuser detection (MUD) classes that make use of joint hybrid decision feedback equalization (HDFE)/ frequency decision-feedback equalization (FDFE) and interference cancellation (IC) techniques, are proposed in conjunction with channel coding to deal with several users accessing the multipath fading channels. In FDFE-IDMA, the feedforward (FF) and feedback (FB) filtering operations of FDFE, which use to remove intersymbol interference (ISI), are implemented by Fast Fourier Transforms (FFTs), while in HDFE-IDMA the only FF filter is implemented by FFTs. Further, the parameters involved in the FDFE/HDFE filtering are derived according to the minimum mean square error (MMSE) criteria, and the feedback symbol decisions are directly designed from soft detection of the decoded signals at the previous iteration. The simulation results including comparisons with those of frequency domain equalization (FDE), SC-FDE-IDMA and multi-carrier OFDM-IDMA schemes, with cyclic prefixing (CP) and zero padding (ZP) techniques, show that the combination of FDFE-IC/HDFE-IC provides an efficient solution with good performance for IDMA systems in ISI channels. Moreover, these iterative structures with block equalization yield a much lower complexity than equivalent existing structures, making them attractive for a wealth of applications.

Key words: frequency-domain equalization, interference cancellation.

التعادلات الكتلية- المتكررة وبمجال ترددي لأنظمة (SC-IDMA)

م. صلاح عواد سلمان
قسم نظم المعلومات
كلية الحاسوب/ جامعة الأنبار

الخلاصة

في الأتصالات المذاعة اللاسلكية بأستخدام حاملة منفردة لأنظمة (IDMA) , أصناف اكتشاف المستخدم الكفوء التي تستخدم تقنيات ازالة التشويش مع (HDFE) او (FDFE) اقترحت بالترابط مع تشفير القناة للتعامل مع عدة مستخدمين عبر قنوات المسارات المتعددة. في (FDFE-IDMA) ,عمليات الفلترة الأمامية والخلفية في (FDFE) والتي تستخدم لأزالة التشويش البيني (ISI) قد تم انجازها بأستخدام (FFTs), بينما في (HDFE-IDMA) فقط الفلتر الأمامي تم أنجازه باستخدام (FFTs) . وكذلك المتغيرات الموجودة في فلترة (FDFE/HDFE) قد تم اشتقاقها نسبة الى قاعدة (MMSE), وقرارت القيم المعادة قد تم تصميمها من الأكتشاف المرن للأشارات المشفرة بالتكرار السابق. نتائج المحاكاة المتضمنة مقارنات مع تلك التي تتضمن المعادلة بمجال التردد (FDFE), أنظمة (FDE-IDMA) و (OFDM-IDMA) مع تقنيات (CP) و(ZP), أظهرت بأن تركيبات (FDFE-IC/HDFE-IC) توفر حل كفوء مع أداء جيد لأنظمة (IDMA) في قنوات (ISI) . وكذلك فان هذه التراكيب المتكررة مع التعادل الكتلي تنتج تخفيض كبير للتعقيدات الرياضية من تلك التراكيب الموجودة وبذلك تجعلها جذابه للعديد من التطبيقات.

الكلمات الرئيسية: تعادل المجال الترددي، الغاء التشويش.

1. INTRODUCTION

In recent years, wireless communication systems have been widely used to offer a broadband access on a common channel and deliver high-data-rate in numerous applications, which range from wireless LANs, to digital audio and video broadcasting. Further, the latest wireless systems require low power consumption and low complexity to support various applications on multiple access channels. Therefore, multiple access schemes are needed to share and allocate the channel resources to multiple users, causing multiple access interference (MAI) and significant multipath channel distortion. To compensate for such distortion, various architectures based on IDMA systems, **,Weitkemper, et al., 2008 ,Ping, et al., Oct. 2007 ,Guo, et al., 2006** and **Guo, et al., 2008** had been proposed in literature.

For moderately dispersive channels, the Rake based IDMA receiver **,Weitkemper, et al., 2008 ,Ping, et al., 2007 ,Guo, et al., 2006** and **Guo, et al., 2008** is the most common solution that provides a good balance between performance and complexity. The multi-user detection (MUD) in Rake-IDMA receiver has a linear complexity and the related detection costs at the chip rate for such receivers become a serious issue in ISI channels. As the channel dispersion increases, the equalization process become increasingly challenging due to the increase in the number of resolvable paths and the performance of Rake receivers degrades significantly. Moreover, the performance of such schemes with traditional IC schemes is also limited by the MAI from other active users. By combining IDMA and orthogonal frequency division multiplexing (OFDM), an efficient multiuser system, OFDM-IDMA **,Ping, et al., 2007** and **Zhang, et al., 2008**, is formed which efficiently combats ISI by the cyclic prefixing (CP) technique in OFDM, and MAI by iterative detection with IDMA **,Weitkemper, et al., 2008.** With regard to non-linear structures, a time domain (TD) DFE comprises a FF filter, operating at the chip rate, and a feedback (FB) filter has been proposed for IDMA systems on dispersive channels **,Aliesawi, et al., 2011.** While it is attractive for its performance, its complexity comparable to linear equalization (LE) and may be significant, especially for very dispersive channels, due to both the signal processing and the design of the FF and FB filters.

For channels with long-delay spread, SC-IDMA approaches with frequency domain equalization (FDE) in **,Lim, et al., 2007** was computationally simpler than corresponding time domain equalization (TDE), and can reduce some of the RF implementation problems **,Lakshmanan, et al., 2009 ,Falconer** and **Ariyavisitakul, 2002** and **Falconer, et al., 2002.** However, SC-FDE systems have similar performance, efficiency and low signal processing complexity advantages as OFDM, and in addition are less sensitive to RF impairments than OFDM that requires predistortion techniques. More recently, an iterative block IBDFE and hybrid time-frequency domain HDFE structures with a considerable reduction of complexity had been proposed **,Benvenuto and Tomasin, 2002 ,Benvenuto and Tomasin, 2005 ,** and **Benvenuto and Tomasin Jun., 2002.** The HDFE structure does not yield a simple solution for the design of the feedforward filter (FF).

Since filtering operations are implemented in FD by FFT, IBDFE yields a significant lower complexity in the filter design and it does not require any matrix inversion as the case in TDDFE. However, such schemes can be used efficiently with IC techniques to remove both multiple access interference (MAI) and ISI using iterative detection techniques. IBDFE approach was also used for CP assisted SC-CDMA systems in **,Benvenuto** and **Tomasin, Sep. 2005.** By performing various FD operations, the performance of such block-based DFEs, can be improved due to the possibility of selecting longer filters. Further, the classical non-iterative TD-DFE and HDFE based multiuser systems suffer from error-propagation phenomena and are not able to cancel the precursors of the ISI.

In this paper, the application of the HDFE and IBDFE/FDFE structures are extended to SC-IDMA systems. The resulting structures are denoted as HDFE-IDMA and FDFE-IDMA, respectively. The proposed structures have the benefits of a TD-DFE in terms of performance with much lower computational complexity, especially when severely time-dispersive channels are considered due to the FFT based frequency-domain implementation. The paper is organized as follow. In Section 2, the system model and the data transmission format that will be used in the SC-IDMA implementation are described. The iterative structures of the HDFE-IDMA and FDFE-IDMA detectors as well as the description of the HDFE-IC, FDFE-IC and the design of filter coefficients are considered in Section 3. The complexity of the proposed schemes is given in Section 4 and is compared with that of the other structures **,Ping, et al., 2007.** The performance is shown in Section 4 with simulations on downlink broadband communication. In Section 5, the conclusions of the proposed schemes are drawn.

2. DATA TRANSMISSION MODEL

For a wideband IDMA transmission in **Fig.1**, the information bits, $d^k(n)$ of user k are first encoded using error correction code and repetition code, $c^k(m), m = 0,1,\dots,N_s - 1$ with spreading factor N_s. The chips are then interleaved by a user-specific interleaver Π_k. FEC and MUX denote forward error correction and multiplexer device, respectively. The MUX allows one or more input signals to be selected or combine into one transmitted signal. The user-specific interleavers are generated randomly and independently. The obtained data sequence with rate, $1/(TN_s)$, can be written after mapping as **,Dinis, et al., 2007.**

$$s^k(m + nN_S) = \Pi^k[c^k(m)d^k(n)], \;\; k = 0,1,\dots,K-1 \qquad (1)$$

where K is the number of active users transmitting simultaneously. The transmitted signal $s^k(n)$ is multiplexed with a training sequence $t^k(n)$ with length that is not lower than the channel length, and then modulated with a pulse-shaping filter that exhibits a raised cosine frequency response.

At the base station, the received signal $r(n)$ is filtered by a matched filter and then sampled at the rate $1/(TN_s)$. By denoting, $h_p^k(n)$, with $p = 0,1,\dots,N_p - 1$, the channel fading coefficients for the user k, the baseband received signal $r(n)$ includes the sum of the signals of all users, can be expressed as

$$r(n) = \sum_{k=0}^{K-1}\sum_{P=0}^{N_{p-1}} h_p^k(n)s^k(n-p) + w(n), \qquad (2)$$

where $w(n)$, represents the additive noise process with variance, $\sigma^2 = \frac{N_0}{2}$, and zero mean. In uplink transmission, the channel $h_p^k(n)$ for each user k can be modelled as the sum of delayed paths with different phases and attenuations. Analogously, the received signal in the FD, R, can be written as

$$R = [R_1, R_2, \dots, R_N]^T = \sum_{k=1}^{K} H^k S^K + W, \qquad (3)$$

where $[.]^T$denotes the transpose, S^k, W and H^k are the FFTs of s^k, w, and h^k, respectively **,Lakshmanan, et al., 2009** and **Dinis, et al., 2007.**

3. FDE-DFE BASED SC-IDMA RECEIVERS

The proposed structure in **Fig. 2** processes the received data $r(n)$ in an iterative fashion. For better detection, the hybrid time-frequency domain HDFE or frequency domain FDFE is integrated with IC scheme to combat the effects of both intersymbol interference (ISI) and MAI. In fact, the frequency-domain filtering of HDFE must be performed on a per-block basis, while the feedback section must be fed with the previous detected symbols whose decisions are performed in the TD **,Falconer, et al., 2002** and **Benvenuto and Tomasin, 2002.** The HDFE in **Fig. 3** operates on blocks of the $r(n)$, and after a transient due to the first received samples, FFT is applied to successive blocks of received samples. To avoid the delay inherent in the block FFT signal processing, the FF filter part operates in the FD, while the transversal filtering for the FB part operates in the TD.

The FDFE in **Fig. 4** includes the FF filter coefficients in the FD, W_{FF} with $n = 1, \dots N$, which partially mitigates part of the interference; and the FB filter coefficients W_{FB} with length $n = 1, \dots N$, which removes the residual interference generated by both the pre-cursors and post-cursors of the channel impulse response. The detector takes soft information $r(n)$ and delivers after some processing refined log-likelihood ratios (LLRs) $L_m\,[s^k(n)]$, which are based on *a priori* known information $L_d\,[s^k(n)]$ and the information gained by the equalization.

The effectiveness of HDFE/FDFE with IC filter is limited by the reliability of the detected data at the previous iteration. During each iteration, the filter is applied to a received data, and tentative feedback decisions, $\hat{s}^k(n)$, made in the previous iteration are then used to construct and subtract out an estimate of the ISI and MAI. With each iteration, increasingly refined soft decisions, $\tanh(L_d[s^k(n)/2\,)$, are generated using this strategy. However, the cancellation and detection procedures may be iterated a few times in order to increase the reliability of the detected data.

3.1 HDFE Filter Design

In **Fig. 3**, the FFT output coefficients of the HDFE, $(r(n))$, are multiplied by the complex valued FF coefficients, $\boldsymbol{G}_{FF}(n)$. An IFFT is applied to the equalized complex valued samples, $IFFT(FFT(r(n))\boldsymbol{G}_{FF}(n))$. The estimated ISI due to $\hat{s}^k(n)$ is computed using FB feedback taps and subtracted symbol by symbol from the resulting TD sequence of FF filter.

The soft feedback detected data $\hat{z}\ \ (n)$ at the previous iteration is used as input to the FB filter to generate the FB vector. The FF and FB coefficients are designed in order to minimize the sum of the power of the filtered noise and the power of the residual interference as **,Falconer** and **Ariyavisitakul, 2002. ,Falconer, et al., 2002. ,Benvenuto** and **Tomasin, 2005** and **Benvenuto** and **Tomasin, Jun. 2002.**

$$J_{MMSE} = E\{\,|\tilde{z}(n) - \hat{z}(n)\,|^2\,\}$$

$$= \frac{1}{N}\sum_{n=0}^{N-1} \sigma_w^2\,|\,\boldsymbol{G}_{FF}(n)|^2 + \sigma_z^2|1 - (\,\boldsymbol{G}_{FF}(n)H(n) + \,\boldsymbol{G}_{FB}(n)|^2], \qquad (4)$$

by assuming the past decisions are correct and in order to compute filters coefficients, the cost function is written as a function of $\boldsymbol{G}_{FB}(n)$

$$\boldsymbol{G}_{FF}(n) = \frac{H^*(n)(1-\boldsymbol{G}_{FB}(n))}{|H(n)|^2 + \frac{\sigma_w^2}{\sigma_z^2}}, \tag{5}$$

inserting Eq. (5) in Eq. (4) we obtain

$$J_{MMSE} = \frac{\sigma_w^2}{N}\sum_{n=0}^{N-1}\frac{|1-\boldsymbol{G}_{FB}(n)|^2}{|H(n)|^2 + \frac{\sigma_w^2}{\sigma_z^2}} \tag{6}$$

by applying the gradient method to minimize the cost function J_{MMSE}, we obtain the linear system of L equations with L unknowns $A_{MMSE}\boldsymbol{w}_{FB} = b_{MMSE}$, where $\boldsymbol{w}_{FB} = [w_{FB,1} \dots w_{FB,L}]^T$.

$$[A_{MMSE}]_{n,l,m} = \sum_{n=0}^{N-1}\frac{e^{-j2\pi(n(l-m))/N)}}{|H(n)|^2 + \frac{\sigma_w^2}{\sigma_z^2}}, 1 \le m, l \le L_s \tag{7}$$

$$[b_{MMSE}]_m = \sum_{n=0}^{N-1}\frac{e^{-j2\pi(nm/N)}}{|H(n)|^2 + \frac{\sigma_w^2}{\sigma_z^2}}, 1 \le m \le L \tag{8}$$

when $\sigma_w^2 \to 0$, the minimum mean square error (MMSE) solution will reduce to the zero forcing (ZF) solution. Hence, the HDFE output can be described as **,Aliesawi, et al., 2011.**

$$\hat{y}(n) = IFFT(FFT\big(r(n)\big)\boldsymbol{G}_{FF} - \sum_{l=1}^{L} w_{FB}(n)\hat{z}(n). \tag{9}$$

Since the feedback part of the HDFE performs only multiplications and symbol by symbol subtraction of feedback symbols, the FB is also simple and it could be made with L taps as required for adequate performance.

3.2 FDFE Filter Design

In **Fig.** 4, the vector, W_{FF}^{it}, at iteration it, is element-wise multiplied with R_n to produce the output vector Y_{FF}^{it} as

$$Y_{FF}^{it} = W_{FF}^{it} R_n , \tag{10}$$

the feedback detected data $\hat{z}^{it}$, is transformed by a FFT to result $\hat{Z}^{it}$, and then multiplied with W_{FB}^{it}, to yield the FB output vector Y_{FB}^{it} as

$$Y_{FB}^{it} = W_{FB}^{it}\,\hat{Z}^{it}, \tag{11}$$

Since Y_{FB}^{it} depends on the feedback detected data $\hat{z}^{it}$, at the previous iteration, when no detected data is available at, $it = 1$, the $\hat{Z}^{it}$ is set as

$$\hat{Z}^{it} = 0, n = 1, \dots, N \tag{12}$$

At the combining point, the vector signal Y^{it} is obtained as

$$Y^{it} = Y_{FF}^{it} + Y_{FB}^{it}, \tag{13}$$

The Y^{it} is transformed by an inverse discrete Fourier transform (IFFT) to result the TD vector signal as an input to the IC scheme

$$z = \frac{1}{N} W^H Y^{it}, \tag{14}$$

where W^H is the N by N FFT matrix. The outputs of IC scheme after deinterleaving Π_k^{-1} and despreading are sent to the kth user decoder. The output of the decoders after spreading and interleaving Π_k is subtracted from $L_m[s^k(n)]$ to form the extrinsic information of the user k. The effectiveness of the FDFE-IC to cancel the channel effects is limited by the reliability of the detected data at the previous iteration. Indeed, the iterative process gradually increases the reliability of the detected data. However, by performing FDFE filtering operations in the FD through the FFT, the complexity of processing can be reduced.

The FF and FB filters are designed to minimize the resulting mean square error (MSE), where the expectations are taken with respect to the transmitted data, the detected data and the noise. By assuming a *priori* statistic of the involved signals, the correlation among the errors on the data is ignored and the correlation coefficients at iteration (it) can be defined as **,Lakshmanan, et al., 2009 ,Benvenuto and Tomasin, 2005** and **Dinis, et al., 2007.**

$$corr_{z,\hat{z}^{(it-1)}} = E[\, z(n)\hat{z}^{(it-1)}(n)\,], \tag{15}$$

The cost function J^{it}, is written as **,Zhang, et al., 2008** and **Falconer** and **Ariyavisitakul, 2002.**

$$J^{it} = \{ \quad |\hat{z}^{it}(n) - z(n)|^2 \}. \tag{16}$$

By applying Parseval's theorem and using Eq. (10), the J^{it} can be written as

$$J^{it} = \frac{1}{N^2} \sum_{n=0}^{N-1} E\{ \quad |G_{FF}^{it} R_n + W_{FB}^{it}\, \hat{z}^{(it-1)}\ (n) - z(n)|^2 \}. \tag{17}$$

From substituting Eq. (3), and by taking the expectations in Eq. (17) with respect to the data and the noise, the J^{it} is written as

$$J^{it} = \frac{1}{N^2} \sum_{n=1}^{N} |G_{FF}^{it}|^2 M_w + |G_{FF}^{it}\ H - 1|^2 M_{z(n)} + |W_{FB}^{it}|^2 M_{\hat{Z}^{(it-1)}(n)} + 2Real\left\{ W_{FB}^{(it)^*} \left(G_{FF}^{it}\ (n) H - 1 \right) corr_{z,\hat{z}^{(it-1)}} \right\}, \tag{18}$$

where $M_{z(n)} = E[\quad |S|^2]$, and M_w is the average power of the MAI and noise signals in the FD, respectively. To derive the filters that minimize the above equation, the FB filter imposes the constraint that the filter removes both pre-cursors and post-cursors, but doesn't remove the desired components, i.e, it must be

$$\sum_{n=0}^{N-1} W_{FB}^{it} = 0 \tag{19}$$

By taking the gradient method with respect to the FB filter coefficients, under the above constraint, yields the solution

$$W_{FB}^{it} = \frac{corr_{z,\hat{z}^{(it-1)}} |HG_{FF}^{it} - Gamma^{it}|}{M_{\hat{Z}^{(it-1)}}}, \tag{20}$$

$$Gamma_n^{it} = \sum_{n=1}^{N} H\, G_{FF}^{it}, \tag{21}$$

by inserting W_{FB}^{it} in cost function and setting to zero the gradient with respect to the FF coefficients, we obtain

$$G_{FF}^{it} = \frac{H^*}{M_w + M_{z(n)}(1 - \frac{|corr_{z,\hat{z}^{(it-1)}}|^2}{M_{z(n)} M_{\hat{z}^{(it-1)}(n)}})H^2} \tag{22}$$

On the other hand, when perfect knowledge of the transmitted data is available, the correlation coefficients becomes

$$corr_{z,\hat{z}^{(it-1)}} = M_{z(n)} \quad , \tag{23}$$

and $M_{\hat{z}(n)} = M_{z(n)}$. From Eq. (22) and Eq. (20), the FF filter is matched to the channel, i.e,

$$G_{FF}^{it} = \frac{H^*}{M_{z(n)}}, \tag{24}$$

while the FB filter removes all the ISI. A first estimate of the disturbance power is obtained as in **Benvenuto and Tomasin, 2005**

$$\hat{\sigma}_e^{it} = \sqrt{\frac{1}{N}} \sum_{n=1}^{N} |\hat{z}(n)^{it} - z(n)|^2 \,, \tag{25}$$

3.3 Interference Generation and PIC Scheme

The impact of MAI can be removed by applying a parallel (IC) scheme. In PIC, the MAI produced by the other users accessing the same channel, is removed in parallel for all users. As compared with the successive IC scheme, PIC requires a short processing delay to complete the

cancellation operation **,Peijun and Rappaport, 1998.** The soft symbols $z(n)$ after equalization are given to the IC and the LLRs for each user are obtained using **,Aliesawi, et al., 2011.**

$$L_m[s^k(n)] = \frac{2\{z(n) - E[z(n)] + \sum_{k=1}^{K} E[s^k(n)]\}}{\sum_{k=1}^{K} var[s^k(n)] + \sigma_w^2 - var[s^k(n)]}, \forall\, k, n \tag{26}$$

The extrinsic information $L_m[s^k(n)]$, is processed by the deinterleavers and the despreaders. The decoders generate the bit-level extrinsic LLRs, which are also processed by the interleavers and the spreaders.

While the IC scheme is used to reduce MAI, the purpose of interference generation block is to regenerate the interference due to user k by reconstructing the original transmitted signals of one or more users. The new extrinsic information, $L_d[s^k(n)]$, based on the *a priori* means, $E[s^k(n)] = \tanh\{L_d[s^k(n)]/2\}$, and variances, $var[s^k(n)] = 1 - (E[s^k(n)])^2$, is calculated and mapped to suitable constellation points, to form new decision symbols $\hat{s}^k(n)$. The $\hat{s}^k(n)$ symbols are summed to form the MAI signal as

$$\hat{z}(n) = \sum_{k=1}^{K} \hat{s}^k(n), \tag{27}$$

and fed to the FB filter. As the IC operation progresses, the estimates of the MAI improves and, in later stages of the iterative scheme, the data estimates of all the users have been obtained.

4. SIMULATION RESULTS

4.1 Simulation Conditions

In this section, simulations results of HDFE-IDMA and FDFE-IDMA schemes are presented and compared with those of FDE-IDMA and multi-carrier OFDM-IDMA schemes, with CP and ZP techniques **,Guo, et al., 2008.** All of the schemes use the same encoding scheme, a rate 1/2 convolutional code with generator polynomial $(23, 35)_8$, followed by repetition code with length $N_s = 6$. The length of the transmitted block for each user is 256 with four active users. The number of iterations is 3 for all the schemes. The interleaved chips after QPSK modulation are linearly superimposed and transmitted over a bandwidth of 4 MHz with equal power allocation and uniform phase distribution. In the considered scenario, the transmitted signals undergo independent dispersive Rayleigh fading channels with an exponential power delay profile and normalized root-mean square delay spread. The channel is assumed to be known and time-invariant. The cyclic extension, ZP and CP, have been set to $CP, ZP \geq Np$.

4.2 BER Performance Comparison

In **Fig.** 5, the BER as a function of the E_b/N_o is presented for the proposed schemes. For comparison, the performance of FDE-IDMA and OFDM-IDMA with CP is also shown. The cyclic extension has been set to 25 and the feedback filter of HDFE has been set to $L + 1$ taps. The performance of HDFE-IDMA clearly outperforms other IDMA structures, including OFDM-IDMA and FDE-IDMA, and approaches the 10^{-4} BER level at high E_b/N_o. The proposed HDFE-IDMA scheme results a gain of about 2 dB at BER=10^{-3}. When compared with the other schemes, the proposed FDFE-IDMA structure yields a gain of about 1.5 dB at BER 10^{-3}. The OFDM-IDMA has similar performance to FDE-IDMA for moderate E_b/N_o.

Figs. 6 and 7 show the performance comparison for different IDMA schemes with different number of active users K. For large active users, the performance decreases since the residual interference levels and the error propagation can be high. However, the FDFE/HDFE is effective in reducing the ISI generated by the dispersive channels. It is also noticed in **Fig. 8** that the first two iterations result a significant improvement, while the improvement of further iterations is reduced and the performance gains associated to the iterative procedure are higher for small K. However, the large K requires the independent processing of ISI and MAI that is carried out in such proposed schemes. This makes the proposed schemes an attractive choice when coding schemes are involved and the structures allow equalization and coding to be done separable.
The performance of OFDM-IDMA and FDE-IDMA with ZP is also drawn in **Fig. 9** and compared with that of HDFE-IDMA and FDFE-IDMA. The proposed structures are clearly outperforms other schemes and results an improvement of about 1 dB at BER 10^{-3}, due to the equalizer's ability. Further, the FDE-IDMA has similar performance to OFDM-IDMA for high E_b/N_o. The improvement in FDFE-IDMA performance can be explained as a result of the iteration process and the improved FB part that is able to remove both precursors and postcursors of ISI. Moreover, the iterative process gradually increases the reliability of the detected symbols and reduces the effects of the error propagation that limits the performance of non-iterative DFE based schemes.

4.3 Complexity Comparison

In this section, the computational complexity, per chip (a QPSK symbol), per user, of the various IDMA schemes is evaluated in **Table 1** in terms of the number of complex multiplications (nCMuls). The nCMul is taken as parameter because it consumes more hardware than addition and other operations. The comparison does not take into account the decoders, despreaders, spreaders and interleavers operations since these operations are identical in both receivers. An example with $K = 4, L = 24,\ it = 3$ and $N = 256$ is also given.
In the OFDM-IDMA scheme, the independent treatment of ISI and MAI reduces the processing cost of MUD. There is approximately a factor of L between the detection cost for TD schemes and that for multicarrier scheme. The IC block has linear complexity in frame length and is independent of L. The FFT costs for one chip $(N \times \log_2 N)/2$ complex multiplications and $(N \times \log_2 N)$ additions/subtractions for N chips. For the OFDM-IDMA scheme, according to the algorithm given in **,Yueqian, 2007** , there are approximately 1120 CMuls, per chip, per user involved in detection process. Since OFDM demodulation is carried out for all users before the iterative detection process, the FFT cost is independent of the user number K, the path number L, and the iteration number. In contrast, there are approximately 67680, 41640 CMuls for the FDE-IDMA and TD-DFE-IDMA, respectively. When compared to OFDM-IDMA, DFE-IDMA has an increased complexity due to the TD filtering operations. Moreover, the FDE-IDMA has a significantly higher complexity than both OFDM-IDMA and DFE-IDMA. Indeed, the filter design for OFDM-IDMA is much less complex than that for other systems.
In the FDFE-IDMA, after an initial FFT to obtain the vector R, at each it, the filters' coefficients require one CMul and two IFFT per block, except for the last iteration that requires only an IFFT. In each block, we have N_d data symbols only, the remaining $(N - N_d)$ are training symbols sent for channel estimation. The overall complexity for FDFE is, $[((N/2\ \log_2 N - N) + N)/N_d - N/N_d]$ and for IC is, $2 \times K$. While the inversion of a correlation matrix of size Q in the design of the TD-DFE and HDFE has a complexity of $O(Q^3)$ and $O(Q^2)$, respectively. The HDFE-IDMA results a computation reduction of about one-third when compared with TD-DFE-IDMA. In turn, FDE-IDMA reduces complexity, with respect to HDFE-IDMA, of another 55%-65%. The channel estimation was not considered because these schemes except the TD-

DFE-IDMA need the same estimate of the channel frequency domain response, which can be obtained by known techniques in **Edfors, et al., 1998** and references therein.

However, in the design of the FF and FB filters of FDFE-IDMA, H^2 has to be calculated by channel estimation, while one division and two multiplications are needed for each iteration. The complexity of these turbo structures may vary significantly according to the dispersion of the channel. However, FF and FB filters in FDFE-IDMA have a very simple implementation because no matrix operations are involved and the provided complexity may be negligible for low or moderate dispersion channels.

5. CONCLUSIONS

In this paper, an equalization and IC scheme, HDFE-IC and FDFE-IC, in conjunction with coding have been considered for wideband IDMA systems. In the proposed HDFE-IDMA structure, the signal processing and the FF filter design of the HDFE that operates on blocks of the data are performed entirely in the FD. While in the proposed FDFE-IDMA structure, both the FF and FB filtering operations are performed in the FD, which yields a reduced complexity with respect to existing IDMA receivers. The performance gain of HDFE-IDMA is significant when it is compared with the performance of OFDM-IDMA and SC-FDE-IDMA. Moreover, the integration of FDFE and IC outperforms significantly HDFE-IDMA, OFDM-IDMA and FDE-IDMA. However, the application of FD techniques makes SC-IDMA with DFE a potentially valuable alternative to multicarrier systems and a variety of issues remain to be explored in future research.

6. References

Aliesawi, S., Tsimenidis, C., Sharif, B., and Johnston, M., Oct 2011, *Iterative Multiuser Detection for Underwater Acoustic Channels*, IEEE J. Ocean Eng., vol. 36, pp.728–744.

Benvenuto, N., and Tomasin, S., 2002, *Block Iterative DFE for Single Carrier Modulation*, IEE Electronic Letters, vol. 39.

Benvenuto, N., and Tomasin, S., Nov. 2005, *Iterative Design And Detection of A DFE in the Frequency Domain*, IEEE Trans. on Comm., vol. 53, no. 11.

Benvenuto, N., and Tomasin, S., Jun. 2002, *On the Comparison Between OFDM and Single Carrier Modulation with A DFE Using A Frequency-Domain Feedforward Filter*, IEEE Transactions on Comm., vol.50, no.6, pp.947-955.

Dinis, R., Silva, P. and Gusmao A., 2007, *IB-DFE Receivers with Space Diversity for CP-Assisted DS-CDMA and MC-CDMA Systems*, Euro. Trans. Telecomms., vol.0, pp.1-12.

Edfors, O., Sandell, M., Beek, J., Wilson, S. K., and Börjesson, P. O., 1998, *OFDM Channel Estimation By Singular Value Decomposition*, IEEE Trans. Comm., vol.46, pp. 931–939.

Falconer, D., and Ariyavisitakul, S. L., Oct. 2002, *Broadband Wireless Using Single Carrier and Frequency Domain Equalization*, 5th Intern. Symp. on Wireless Personal Multimedia Comm., vol.1, pp.27-36.

Falconer, D., Ariyavisitakul, S.L., Benyamin-Seeyar, A., and Eidson, B., Apr 2002, *Frequency Domain Equalization for Single-Carrier Broadband Wireless Systems*, IEEE Comm. Magazine, vol.40, no.4, pp.58-66.

Guo, Q., Yuan, X., and Ping, L., Apr. 2006, *Interleave Division Multiple-Access*, IEEE Trans. on Wireless Comm., vol.5, no.4, pp.938-47.

Guo, Q., Yuan, X., and Ping, L., 2008, *Single- and Multi- Carrier IDMA Schemes with Cyclic Prefixing and Zero Padding Techniques*, European Trans. on Telecomm.

Lim, J., Choi, C., Yune, T. and Im, G., Jun 2007, *Iterative Multiuser Detection for Single-Carrier Modulation with Frequency-Domain Equalization*, IEEE Comm. Letters, vol. 11.

Lakshmanan, M., Noormohammed, V., and Nandakumar, S., Jun 2009, *Frequency Domain Equalization for Single Carrier Wireless Systems*, International Conf. on Control, Automation, Comm. and Energy Conservation.

Ping, L., Wang, P., and Wang, X., Oct. 2007, *Recent Progress in Interleave-Division Multiple-Access (IDMA)*, IEEE Military Communications Conference (MILCOM 2007), pp.1-7.

Ping, L., Guo, Q., and Tong, J., 2007, *The OFDM-IDMA Approach to Wireless Communication Systems*, IEEE Wireless Communications Magazine, vol.14, no.3, pp.18-24.

Peijun, S., and Rappaport, T.S., 1998, *Parallel Interference Cancellation (PIC) Improvements for CDMA Multiuser Receivers Using Partial Cancellation Of MAI Estimates*, IEEE Global Telecommunications Conf., GLOBECOM 1998, vol.6, pp.3282-3287.

Tomasin, S., and Benvenuto, N., Sep. 2005, *Frequency Domain Intereference Cancellation and Nonlinear Equalization for CDMA Systems*, IEEE Trans. Wireless comm., vol.4, pp.2329-2339.

Weitkemper, P., Wubben, D., and Kammeyer, K. D., Oct. 2008, *Delay-Diversity in Multi-User Relay Systems with Interleave Division Multiple Access*, IEEE International Symposium on Wireless Communication Systems (ISWCS'08).

Yueqian, L., 2007, OFDM-*IDMA Wireless Communication Systems*, M.Sc. thesis, City University of Hong Kong.

Zhang, R., and Hanzo, L., 2008, *Three Design Aspects of Multicarrier Interleave Division Multiple Access*, IEEE Transactions on Vehicular Technology, vol.57, no.6, pp.3607-3617.

List of Abbreviations

BER: bit error rate
CP: cyclic prefixing
FF: feedforward
FB: feedback
FDFE: frequency decision-feedback equalization
FFTs: Fast Fourier Transforms

FDE: frequency domain equalization
HDFE: hybrid decision feedback equalization
IC: interference cancellation
ISI: intersymbol interference
IBDFE: iterative block decision feedback equalization
IFFT: inverse Fast Fourier Transform
LE: linear equalization
LLRs: log-likelihood ratios
MUD: multiuser detection
MMSE: minimum mean square error
MAI: multiple access interference
nCMuls: number of complex multiplications
OFDM: orthogonal frequency division multiplexing
PIC: parallel interference cancellation
QPSK: quadrature phase shift key
SC-IDMA: single-carrier interleave division multiple access
TD: time domain
TDE: time domain equalization
ZP: zero padding
ZF: zero forcing

List of Symbols

$c^k(m)$: repetition code
$d^k(n)$: information bits of user k
$\boldsymbol{G}_{FF}(n)$: complex valued FF coefficients in HDFE
$h_p^k(n)$: the channel fading coefficients for the user k
H^k: the FFT of h^k
it: iteration number
J_{MMSE}: the cost function
K: number of active users
L: number of FB filter taps
$L_d\ [s^k(n)]$: *a priori* known information
$L_m[s^k(n)]$: the LLRs for user k
M_w: the average power of the MAI and noise signals
m: time index after coding
n: time index of transmitted bits
N: number of transmitted bits
N_s: spreading factor
N_d: number of data symbols
N_p: number of paths
N_0: noise power
p: path index
$r(n)$: the received signal
R: the received signal in FD
$\hat{s}^k(n)$: tentative feedback decisions
$s^k(n)$: the transmitted signal
S^k: the transmitted signal in FD

$t^k(n)$: the training sequence
$\hat{y}(n)$: the output of HDFE
T: time period
$w(n)$: the additive noise process
W_{FF} : FF filter coefficients in the FD
W_{FB}: FB filter coefficients in the FD
W^H: the N by N FFT matrix
z: the input to the IC block
$\hat{z}\ \ (n)$: the soft feedback detected data
σ^2: variance
$\hat{\sigma}_e^{it}$: disturbance power
Π_k: user-specific interleaver
Π_k^{-1}: dinterleaver for the user k

Table 1. Complexity comparison of the various IDMA schemes.

Structure	nCMuls	nCMuls for considered simulation scenario
OFDM-IDMA	$(N \times \log_2 N)\frac{1}{2} + 8 \times K \times it$	1120
FDE-IDMA	$N \times \log_2 N + N^2 + 8 \times K \times it$	67680
DFE-IDMA	$[(M_{FF} + M_{FB} + M_{FF}^3) + 2 \times K] \times it$	41640
HDFE-IDMA	$[\left(\frac{N}{N_d} \times \log_2 N + M_{FB}\right) + ((2N_p)^2 + 2N + N\log_2 N) + 2 \times K] \times it$	15578
FDFE-IDMA	$[((N/2\ \log_2 N - N) + N)/N_d - N/N_d] \times it + [(3 \times it + 1) \times N] + 2 \times K \times it$	2844

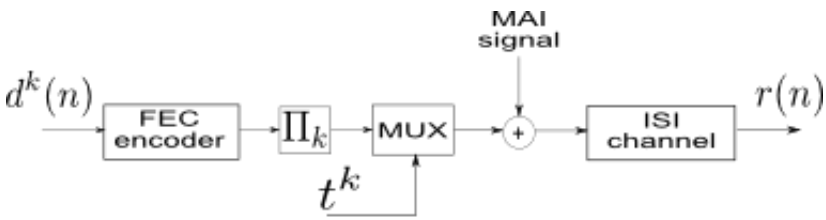

Figure 1. The discrete time block diagram of an IDMA transmitter for user-k.

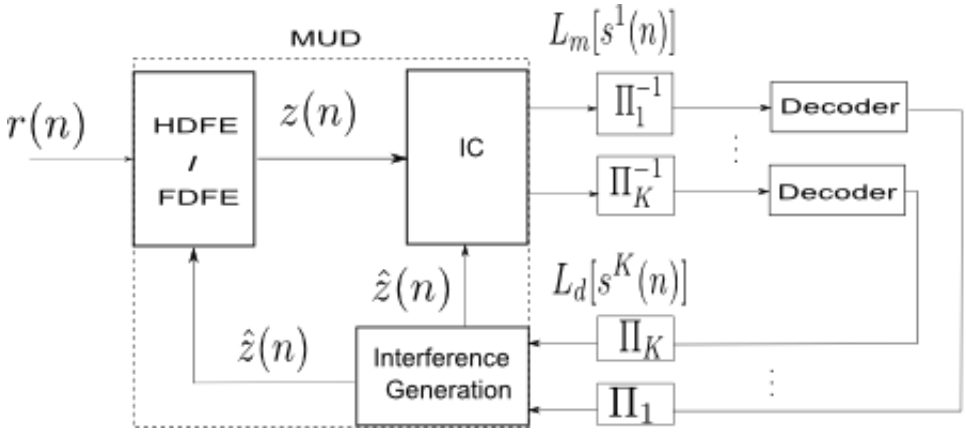

Figure 2. Iterative multiuser detector with FDE for SC-IDMA receiver.

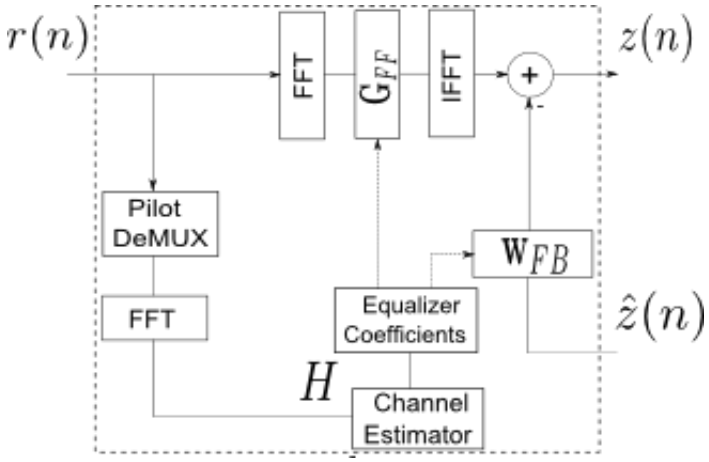

Figure 3. HDFE with FF filter in FD and FB filter in TD.

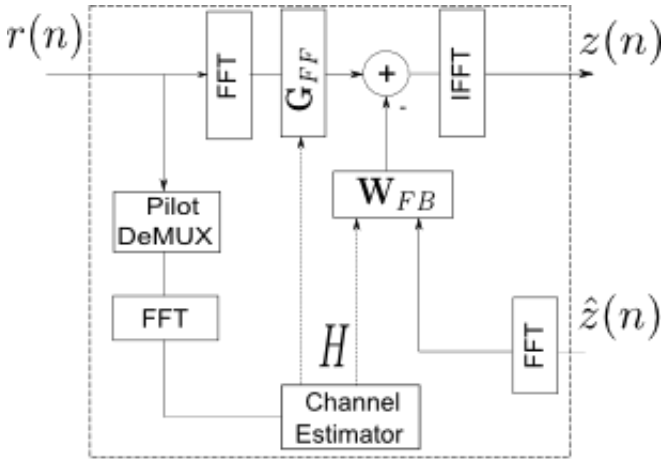

Figure 4. FDFE with FF and FB filters in FD.

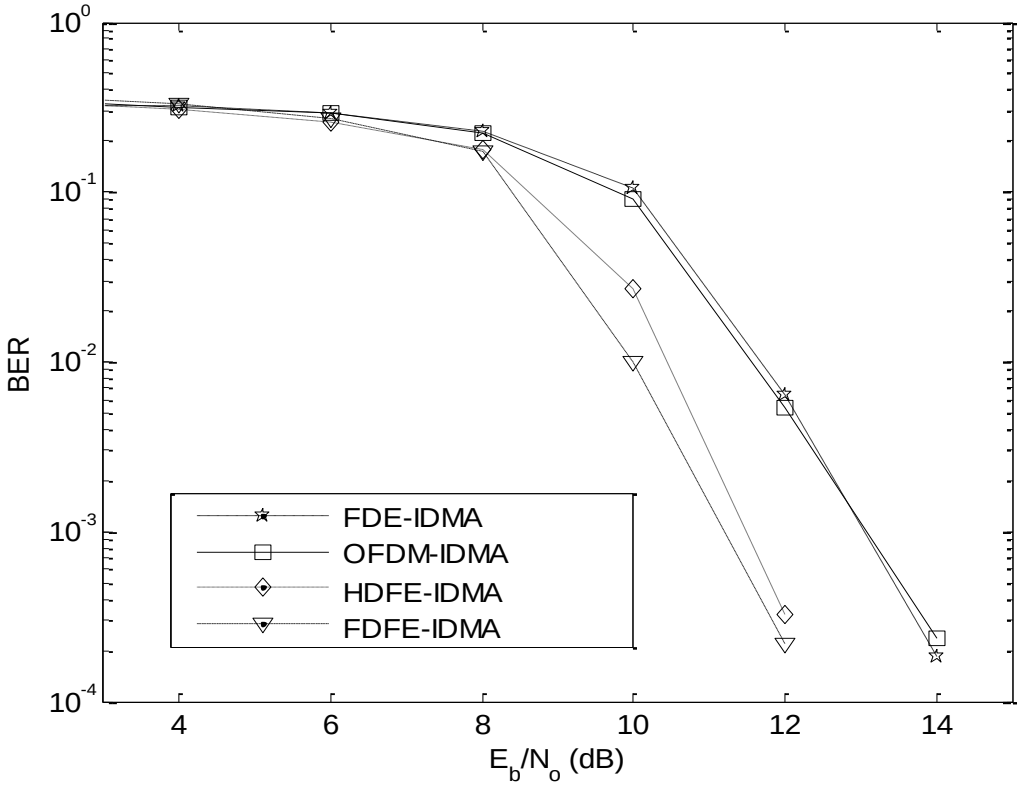

Figure 5. Performance comparison between HDFE-IDMA, FDFE-IDMA and FDE-IDMA, OFDM-IDMA with CP.

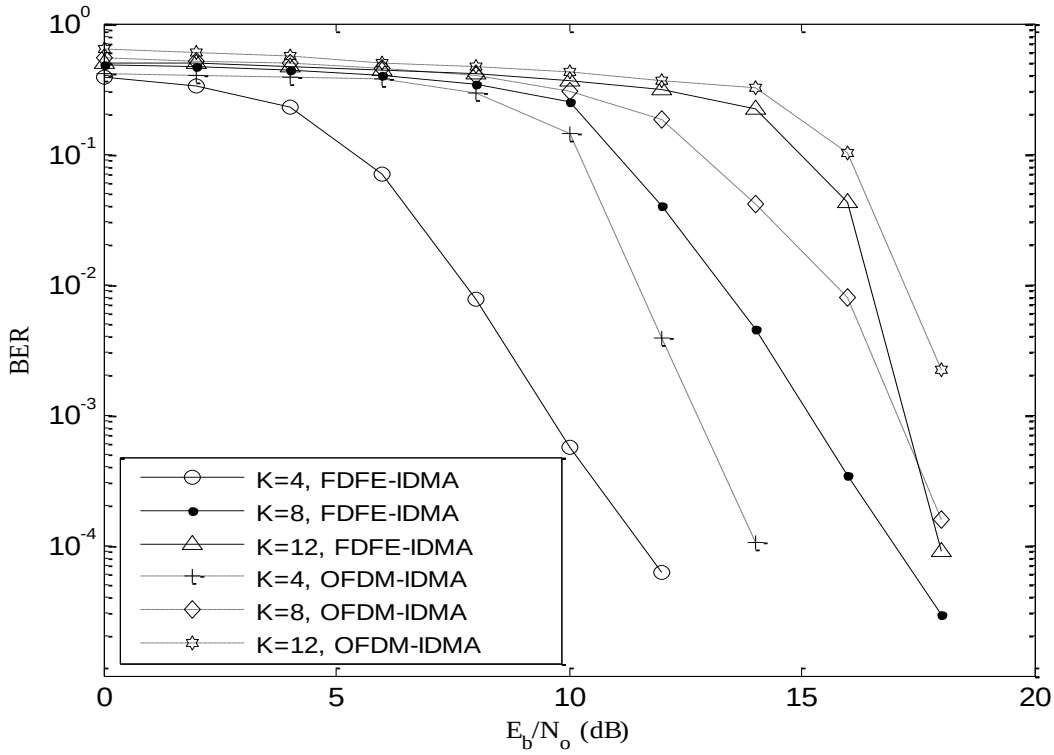

Figure 6. Performance of FDFE-IDMA (solid lines) and OFDM-IDMA (dashed lines) with different number of active users K.

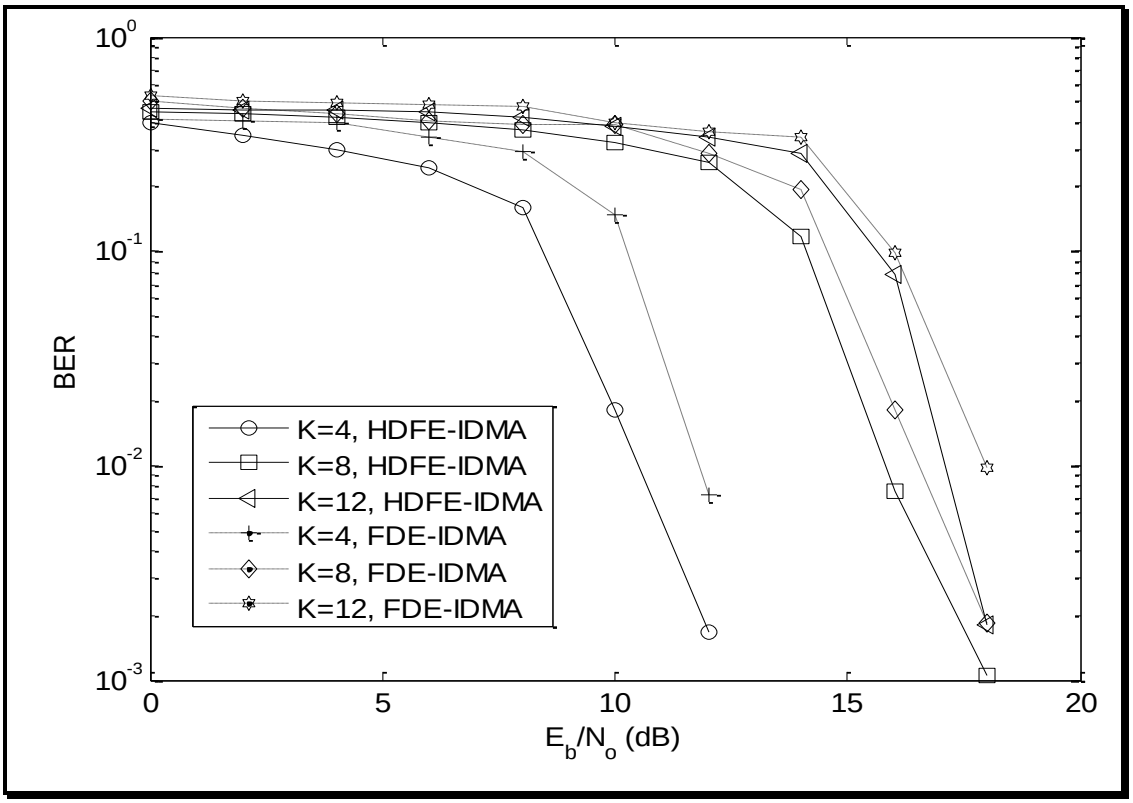

Figure 7. Performance of HDFE-IDMA (solid lines) and FDE-IDMA (dashed lines) with different number of active users K.

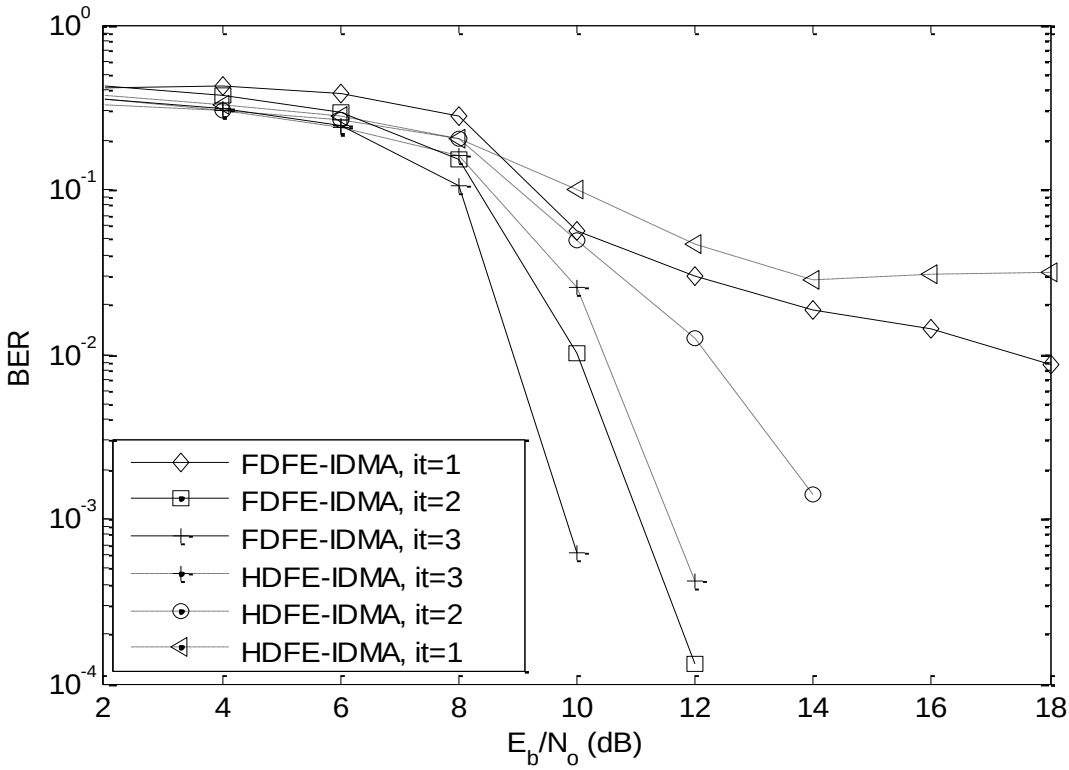

Figure 8. Performance comparison between FDFE-IDMA (solid lines) and HDFE-IDMA (dashed line) with different it number.

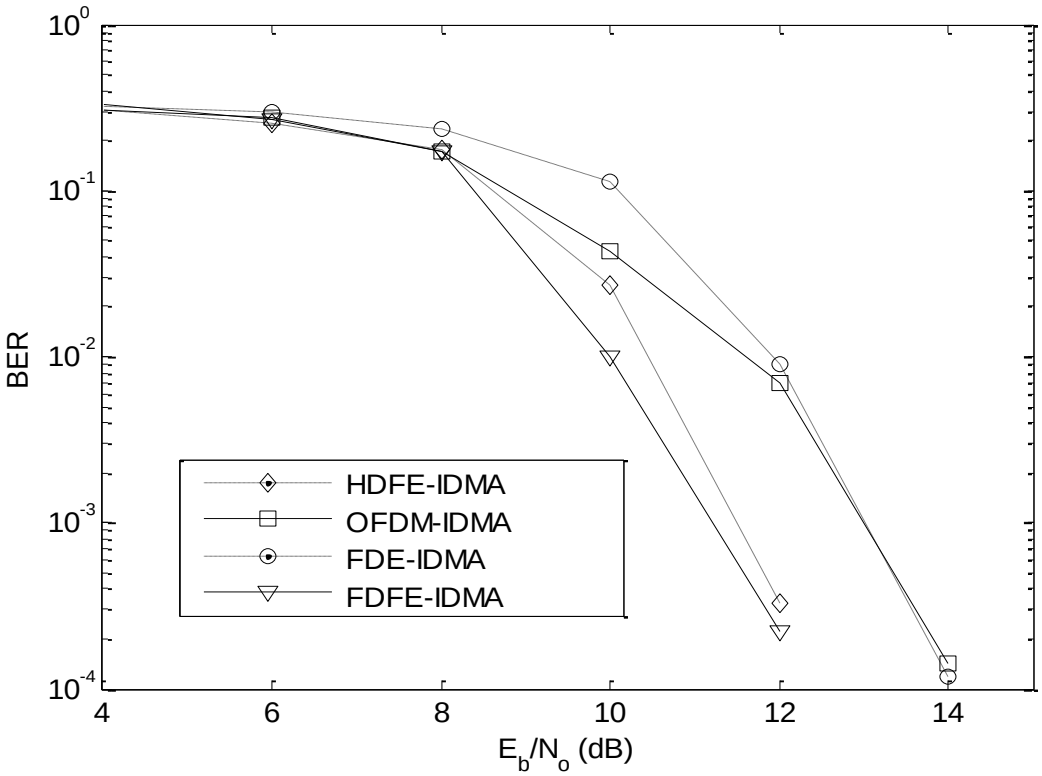

Figure 9. Performance comparison between HDFE-IDMA, FDFE-IDMA and FDE-IDMA, OFDM-IDMA with *ZP*.

Spiking Neural Network in Precision Agriculture

Nadia Adnan Shiltagh
Assistant professor Dr.
Computer Engineering/ Baghdad University
E-mail:dr-nadiaat@hotmail.com

Hasnaa Ahmed Abas
Computer Engineering/Baghdad University
E-mail:en_hasnaa@yahoo.co.uk

ABSTRACT

In this paper, precision agriculture system is introduced based on Wireless Sensor Network (WSN). Soil moisture considered one of environment factors that effect on crop. The period of irrigation must be monitored. Neural network capable of learning the behavior of the agricultural soil in absence of mathematical model. This paper introduced modified type of neural network that is known as Spiking Neural Network (SNN). In this work, the precision agriculture system is modeled, contains two SNNs which have been identified off-line based on logged data, one of these SNNs represents the monitor that located at sink where the period of irrigation is calculated and the other represents the soil. In addition, to reduce power consumption of sensor nodes Modified Chain-Cluster based Mixed (MCCM) routing algorithm is used. According to MCCM, the sensors will send their packets that are less than threshold moisture level to the sink. The SNN with Modified Spike-Prop (MSP) training algorithm is capable of identifying soil, irrigation periods and monitoring the soil moisture level, this means that SNN has the ability to be an identifier and monitor. By applying this system the particular agriculture area reaches to the desired moisture level.

Key words: precision agriculture, wireless sensor network, spiking neural network, modified chain-cluster based mixed.

الشبكة العصبية المتصاعدة في الزراعة الدقيقة

أ.م.د. نادية عدنان شلتاغ
هندسة الحاسبات/جامعة بغداد

حسناء احمد عباس
هندسة الحاسبات/جامعة بغداد

الخلاصة

في هذا البحث, تم عرض نظام الزراعة الدقيقة بالاعتماد على شبكة الاستشعار اللاسلكية. تعتبر رطوبة التربة واحدة من العوامل البيئية المؤثرة على المحصول. فترة السقي يجب ان تراقب. الشبكات العصبية لها القدرة على تعلم سلوك التربة الزراعية بغياب التمثيل الرياضي. هذا البحث يقدم نوع معدل من الشبكة العصبية التي تسمى بالشبكة العصبية المتصاعدة. في هذا العمل, النظام الزراعي الدقيق, الذي تم تمثيله, يحوي اثنين من الشبكات العصبية المتصاعدة SNN التي تم تعريفها بدون اتصال (off-line) بالاعتماد على بيانات مسجلة, واحدة من هاتين SNN تمثل المُراقب الذي يقع في الوحدة المركزية حيث يحسب فترة السقي و الاخر يمثل التربة, بالاضافة الى ذلك , لتقليل الطاقة المستهلكة لعقد الاستشعار, تم استخدام خوارزمية توجيه معدلة (MCCM). وفقا لهذه

الخوارزمية (MCCM) فأن عقد الاستشعار سترسل بياناتها الاقل من عتبة مستوى الرطوبة الى الوحدة المركزية . الشبكة العصبية المتصاعدة مع خوارزمية التدريب المعدلة MSP قادرة على : تعريف التربة, تعريف فترة السقي و مراقبة مستوى رطوبة التربة, وهذا يعني ان SNN يمكنها ان تكون مُعرف و مُراقب. بتطبيق هذا النظام فأن المنطقة الزراعية ستصل الى مستوى الرطوبة المطلوبة.

1. INTRODUCTION

In Precision Agriculture (PA), various parameters including soil type and temperature vary dramatically from one region to the other and therefore any irrigation system must be flexible enough to adapt to the constraints**, Kumar**, **et al., 2013.** Wireless Sensor Networks (WSNs) can play an important role because of their ability of providing real-time data collected by spatially distributed sensors. More specifically, a WSN is a wireless network composed by a set of autonomous, low-power, and low-cost devices (called *nodes*) using sensors to cooperatively monitor physical quantities. WSNs have been already used for PA purposes especially for monitoring environmental parameters**, Martinelli, et al., 2009.** PA is a new development in traditional agriculture. In PA, production environment is monitored, and the monitored data is used to derive the most suitable environment management decision which employs control and adjustment solutions to obtain better product yield. Greenhouse shed is one of the typical means in PA. In order to achieve precision control to the production environment, it is necessary to perform three tasks: Firstly, monitoring parameters such as temperature, Secondly, control and management decision is determined based on the analysis of the collected data. Finally, based on the control decision, automatic or manual control mechanism is implemented, Xia**, et al., 2011.** PA ensures quicker response time to adverse climatic conditions, better quality control of the produce and yet a lower labor cost **,Anurag et al., 2008.** WSN is a major technology that drives the development of PA. An important issue that arises in PA is the type of parameters to be sensed, which apart from the regular environmental parameters like temperature, humidity**, Valada, et al., 2012.**

2. PRECISION AGRICULTURAL SYSTEM AND SPIKING NEURAL NETWORK

General block diagram of agricultural soil for precision agricultural system is shown in **Fig. 1.** To construct a precision agricultural system, this requires two SNN. These two SNNs must be identified and trained through Modified Spike-Prop training algorithm (MSP).

2.1 Spiking Neural Network Structure

The structure of SNN is shown in **Fig. 2**. The feedforward SNN is constructed in three layers: two units in input layer H, seven units in hidden layer I and one unit in output layer J. Each connection between input and hidden layer, hidden and output layer consists of six delayed sub-connection or synapses k as shown in **Fig. 3**. Number of hidden units and number of synapses in each sub-connection are chosen through trial and error.

2.2 The Modified Spiking Neural Network Training Algorithm

In MSP the starting of processing information is begun after encoding process. In encoding process, the real information RI is encoded with respect to time interval T such that the

smallest value in the pattern R_{min} takes the largest value of time interval t_{max} and the largest value in the pattern R_{max} takes the smallest value of time interval t_{min}, the actual coded information $t_h^{(act)}$ will be calculated by Eq. (1) **,Oniz, et al, 2008.**

$$t_h^{(act)} = t_{max} - round(\, t_{min} + \frac{(RI - R_{min})(t_{max} - t_{min})}{(R_{max} - R_{min})}\,) \tag{1}$$

Where $round$ is a function that approximates the float element to the nearest integer.

The decoding equation can be derived from Eq. (1) by solving for RI.

$$RI(t_j) = \frac{\left(t_{max} - t_j - t_{min}\right) \times (R_{max} - R_{min})}{(t_{max} - t_{min})} + R_{min} \tag{2}$$

MSP algorithm passes into two phases. In the first phase, feedforward phase, each neuron can spike at most once only during the time interval T, when its membrane potential m exceeds threshold value ϑ. The feedforward phase usually begins from hidden layer I and check every neuron i consequently if it is spiked or not. If the neuron i is spiked the algorithm goes to the next neuron $i + 1$ in the same layer, else MSP algorithm calculates the membrane potential $m_i(t)$ according to Eq. (3) based on input spikes $t_h^{(act)}$of neuron h at input layer H.

$$m_i(t) = \sum_{h=1}^{NH} \sum_{k=1}^{D} w_{hi}^k(R)\, \varepsilon(t - t_h^{(act)} - d^k) \tag{3}$$

Where w_{hi}^k : connection weight between neuron h and neuron i for the synapse k.
d^k : delay value of the synapse k.

$$\varepsilon(t) = \frac{t}{\tau}\, e^{1 - \frac{t}{\tau}} \tag{4}$$

Where τ is the time-constant and $\varepsilon(t) = 0$ for $t \leq 0$ to insure causality **,Thiruvarudchelvan,et al, 2013.**

If $m_i(t)$ exceeds threshold at particular instant t , then the neuron i will be forbidden from spiking more during the remaining time interval T, else it will be reset in next instant $t + 1$. After second layer's neurons has finished, the algorithm goes to the output layer J and repeat the same procedure, but in this case the spikes of hidden layer will be inputs to the output neurons. When T interval has been finished, then the backpropagation phase begins. After feedforward phase has been finished the second phase begins where the synapses' weights of connection will be updated. Opposed to feedforward the backpropagation begins from output layer and return back to the hidden layer.

The two phases will be repeated, if the Root Mean Square Error (RMSE) is less than desired value of error. The learning rate η will be updated after end of each epoch according to the Eq. (5) **,Huijuan, et al. 2012.**

$$\eta(epoch+1)=\begin{cases} a\,.\eta(epoch) & \text{if } error(epoch+1)<error(epoch) \\ b.\eta(epoch) & \text{if } error(epoch+1)>c.error(epoch) \\ \eta(epoch) & \text{if } error(epoch+1)=error(epoch) \end{cases} \quad (5)$$

Where a, b and c are constants and their values are chosen by trial and error.

3. SYSTEM IDENTIFICATION

The input to the soil, which represents agricultural soil, is the Irrigation Period (IP) and the output is Moisture Level (ML).The mathematical model of the soil that will be identified depending on logged data. Soil can be considered as input/output system with unknown structure and unknown parameters, in the training process mapping between input-output data will be done by SNN through MSP training algorithm. The Non-Parametric identification is done.

Fig. 4 shows the identification of soil using SNN. The present state of IP and Actual Moisture Level (AML) are fed as the inputs to spiking neural network. Moisture Level Spiking Neural Network (MLSNN) is trained off-line to adapt MLSNN's weights to optimize soil response. Weights are updated according to the error between the output of soil (ML) and the output of MLSNN ($\widehat{ML}$), as described in Eq. (6).

$$error = ML - \widehat{ML} \quad (6)$$

The input signal of soil, which is IP, must be calculated and processed. Another plant, which is called irrigation plant, is used to calculate IP. Irrigation plant is identified based on logged data. Logged data is forwarded to Irrigation Period Spiking Neural Network (IPSNN) which is trained off-line by MSP training algorithm. The inputs to IPSNN are AML and Desired Moisture Level (DML) and the output is estimated Irrigation Period ($\widehat{IP}$). **Fig. 5** Shows block diagram of the irrigation plant identification.

4. SPIKING NEURAL NETWORK WITH MODIFIED SPIKE-PROP ALGORITHM AGRICULTURAL SYSTEM

The objective is to construct an agricultural model to keep the moisture level around the desired set-point after applying particular irrigation period to avoid dry or too much wetted soil. **Fig. 6** shows the block diagram of the agricultural system. The monitor at first, encode the real values of moisture level with respect to time. Then the following procedure will be repeated for all encoded data:

1. Monitoring plant or IPSNN produces IP according to the inputs: AML and DML.
2. IP will be set to MLSNN. MLSNN will produce $\widehat{ML}$ according to IP and AML. The current $\widehat{ML}$ must be around DML value.

When all packets have been completed, the sink will return the IPs values to the sensors. As a result all the coverage areas have their moisture level monitored by sink thereby saving the moisture level around desired moisture level.

5. SIMULATION RESULTS

The simulation of precision agriculture system model is explained by using Spiking Neural Network (SNN) with Modified Spike-Prop training algorithm (MSP). The agricultural system is simulated using MATLAB R2012a simulator. The simulation of wireless sensor network for precision agriculture system is shown in **Fig. 7**. The network consist of one hundred stationary sensor nodes placed in a $(25 \times 100)\ meter$ with one sink node. Network specification mentioned in **Table 1**.

The compression between Modified Chain-Cluster based Mixed (MCCM) and Chain-Cluster based Mixed (CCM) routing algorithm with respect to energy consumption of cluster head nodes is shown in the **Fig. 8**. Minimum and maximum values of energy consumption for both CCM and MCCM are: (0.0037, 0.0568) and (0.0030, 0.0511) respectively, so the enhancement percentage of energy consumption is from 10% to 18.9%.

5.1 Identification Results

The general specification of SNN with MSP training algorithm is presented in the **Table 2**. The spike-response functions ε with $\tau = 3$ for one connection of six synapses are shown in **Fig. 9**. Notice that first curve starts from 1 because ε function has one delay, also the final curve starts with 6 because ε function has six delays. Summation of spike-response functions of **Fig. 9** along T is shown in **Fig. 10**. The identification process is done for moisture level and irrigation plant using SNNs:

5.1.1 Irrigation period spiking neural network identification

Irrigation Period Spiking Neural Network (IPSNN) specification is mentioned in Table (2). IPSNN of **Fig. 5** is identified through MSP training algorithm by using logged training samples. The training samples are: Actual Moisture Level (AML), Desired Moisture Level (DML) and Irrigation Period (IP) values as shown in Table (3). The training samples of Table (3) are converted to spikes, then they enter to the training stage. After the IPSNN is trained for 100 epochs, output of IPSNN ($\widehat{IP}$) will converge to the desired IP and the final values of the weights are saved. Result of IPSNN identification is shown in **Fig. 11**. To check validation of identified IPSNN, the saved weights of identification stage are used with another set of data; the result of validation is shown in **Fig 12**.

5.1.2 Moisture level spiking neural network identification

Moisture Level Spiking Neural Network (MLSNN) specification mentioned in **Table 2**. MLSNN of **Fig. 4** is identified based on logged data. **Fig. 13** shows MLSNN identification. As it is clear from **Fig. 13**, the output of MLSNN ($\widehat{ML}$) is converged to the Desired Moisture Level (DML) this means that MLSNN provide acceptable moisture level for corresponding part of agricultural area. MLSNN is trained for 100 epochs and the final weights will be saved. After training has finished, the RMSE

reaches 0.500. To check validation of identified MLSNN, the saved weights of identification stage are used as initial weights with another set of data; the result of validation is shown in **Fig. 14**.

5.2 Simulation Results of Agricultural System

Sensor nodes packets are random values between 3% and 13% of moisture level; they will be transmitted to the sink node using MCCM. The moisture level of the first strip reaches to the DML as shown in **Fig. 15**. **Table 4** presents the AML, DML, and IP for the first strip after decoding. As it is clear from Table (4), IP values are proportional to the difference between AML and DML. For example at the first sensor node the difference between AML and DML is 26.86 so the IP is 11.98, but at second sensor node the difference between AML and DML is 10.07 so the IP is 5.90 and it is less than first IP and not vice versa. When the AML is greater than DML this means that the corresponding agricultural area does not need irrigation; therefore; the IP will be zero like node 26 its moisture is 10.89 and the DML is 10 so IP is zero. IP values for all nodes are shown in **Fig. 16.**

Moisture level of all sensor nodes in the network is shown in **Fig. 17**, these values are coded values and the real values are obtained after decode them. **Fig. 18** shows the real values of **Fig. 17**. As it is clear the output of MLSNN, converges to the DML, then all agricultural area is at desired moisture level.

6. CONCLUSIONS

From the simulation results, the following points can be noted:

- MCCM is better than CCM, because in MCCM the sensor node transmit its packet if the moisture level is less than the threshold value; this means that the energy consumption is less. The energy consumption is diminished in proportional with number of transmitted packets. From other side of view, MCCM reduce the congestion and overhead on the network.
- SNN with modified Spike-Prop training algorithm learned quickly, it has good results in identification of the moisture level and the irrigation.
- SNN has capability of monitoring IP of **Fig. 6**, and this is proved in the results as shown in **Figs. 16** and **17**.

REFRENCES

- Anurag, D., Roy, S., and Bandyopadhyay, S., May 2008, *Agro-Sense: Precision Agriculture Using Sensor-Based Wireless Mesh Networks*, First ITU-T kaleidoscope academic conference – innovation in NGN: future Network and service, IEEE.

- Capraro, F., Patifio, D., Tosetti, S., and Schugurensky, C., April 2008, *Neural Network-Based Irrigation Control for Precision Agriculture*, International Conference on Networking, Sensing and Control, IEEE.

- Huijuan, F., Jiliang, L., and Fei, W., July 2012, *Fast Learning in Spiking Neural Networks by Learning Rate Adaptation*, Chinese Journal of Chemical Engineering.

- Kumar, N., D., Pramod, S., and Sravani, C., August 2013, *Intelligent Irrigation System*, International Journal of Agricultural Science and Research, ISSN 2250-0057, Vol. 3, Issue: 3.

- Martinelli, M.,Ioriatti, L.,Viani, F., Benedetti, M. and Massa, A., July 2009, *A WSN-Based Solution for Precision Farm Purposes*, IEEE.

- Oniz, Y., Kaynak, O., and Abiyev, R., March 2013, *Spiking Neural Networks for the Control of a Servo System*, IEEE.

- Thiruvarudchelvan, V., Crane, J., W., and Bossomaier, T., April 2013, *Analysis of SpikeProp Convergence with Alternative Spike Response Functions*, IEEE.

- Valada, A., Kohanbash, D., and Kantor, G., 2012, *Design and Development of a Wireless Sensor Network System for Precision Agriculture*, citeseer.

- Xia, J., Tang, Z., Shi, X., Fan, L., and Li, H., December 2011, *An environment monitoring system for precision agriculture based on wireless sensor networks*, Seventh International Conference on Mobile Ad-hoc and Sensor Networks.

Symbols

Symbol	Description	Unit
d^k	Delay of specific synapse	msec
$m_i(t)$	Membrane potential of hidden layer neurons	Unit less
$t_h^{(act)}$	Actual spiking time of neurons at input layer	msec
w_{hi}^k	Weight between input and hidden layer	Unit less
NH	Number of neuron in input layer	Unit less
RI	Real input pattern	Unit less
T	Time interval	msec
h	Neuron sequence in input layer	Unit less
i	Neuron sequence in hidden layer	Unit less
t	Current time	msec
ε	Spike response function	msec
η	Learning rate	Unit less
ϑ	Threshold value for spiking	Unit less

Table 1. Wireless sensor network specification.

Parameter	Value
Number of nodes	$100\ node$
Number of strips	$5\ strip$
Number of nodes in one strip	$20\ node$
Sink node position	(120,13)
Coverage area	$100 \times 25\ meter$
Distance between two nodes vertically	$5\ meter$
Distance between two nodes horizontally	$5\ meter$
Packet size	$2\ k\ bit$
routing	MCCM algorithm
Energy of running transmitter	$50\ nJ/bit$
Energy of running amplifier	$100\ pJ/bit * meter^2$

Table 2. SNN specification.

Parameter	Value	Unit	Description
network topology	2,7,1	Unit less	Number of units in Input/Hidden/output
$\boldsymbol{\eta}$	0.00l	Unit less	Learning rate value initially
$\boldsymbol{a, b, c}$	1.38 , 1.14 , 0.8	Unit less	Constants of adaptive learning rate
$\boldsymbol{\tau}$	3	msec	Time constant
$\boldsymbol{\vartheta}$	1.5	Unit less	Threshold value for spiking
$\boldsymbol{T}$	1-80	msec	Time interval
$\boldsymbol{D}$	6	msec	Number of delay synapses per connection
$\Delta\boldsymbol{t}$	0.1	msec	Step size
$\boldsymbol{w}$	[0-1]	Unit less	Initial weights of hidden and output layer

Table 3. Training samples values of identification, **Capraro, et al., 2008.**

No.	AML(%)	IP(hr.)	DML(%)
1	5	9.5	32
2	17	7.3	27
3	7	15	45
4	20	10.3	35
5	8	3.8	15
6	7	1.1	8
7	3	9.3	32
8	11	8.6	29
9	10	13	42
10	20	9.7	32
11	11	8	28
12	10	14	45
13	23	9.4	32
14	12	9.8	34
15	13	14	45
16	12	5.7	20
17	8	8.3	28
18	10	3.5	15
19	4	8.5	29
20	18	8	28

Table 4. AML, DML and IP for the first strip.

NO.	AML (%)	IP(hr.)	DML (%)
1	11.14	11.98	38
2	8.93	5.90	19
3	4.39	12.55	40
4	3.84	5.90	19
5	3.49	3.24	10
6	9.01	3.26	10
7	9.53	10.27	33
8	5.98	6.84	22
9	3.98	10.08	32
10	8.24	4.38	14
11	3.34	2.86	9
12	6.43	14.06	45
13	8.82	11.03	35
14	5.78	8.75	28
15	9.97	12.55	40
16	4.75	6.85	22
17	12.44	4.76	15
18	9.07	4.38	14
19	10.72	3.83	12
20	5.13	11.98	38

Figure1. General system block diagram.

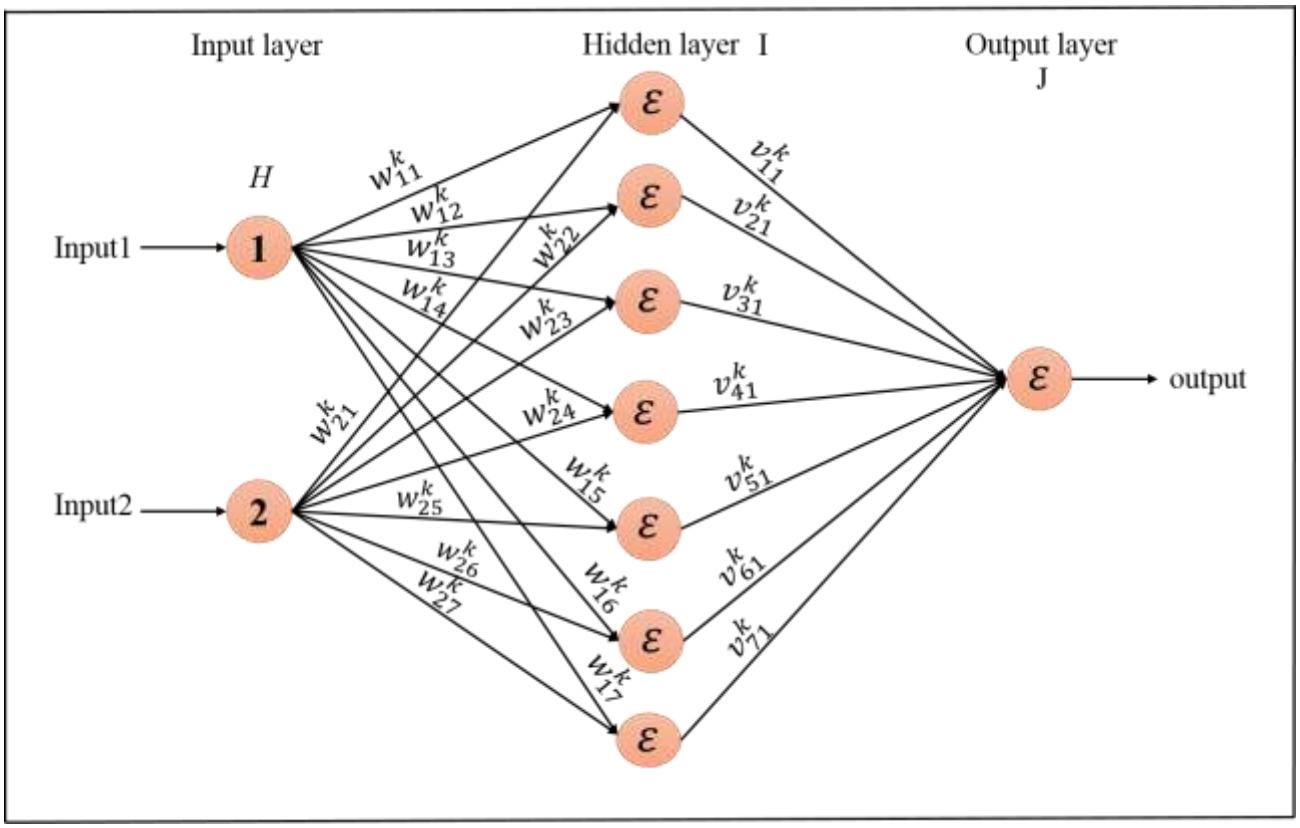

Figure 2. Structure of SNN.

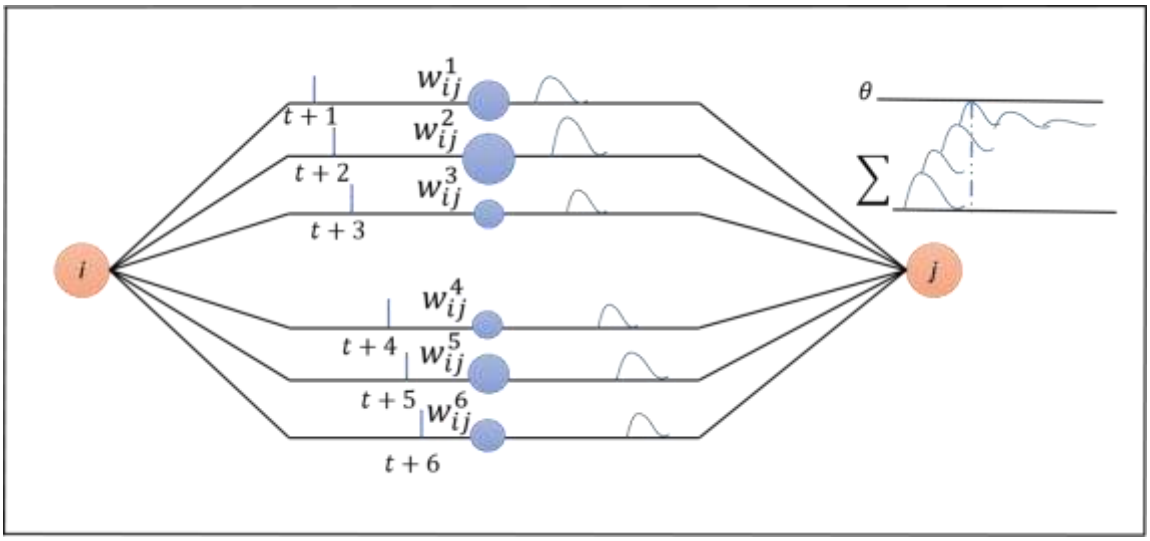

Figure 3. Sub-connection consist of six synapses.

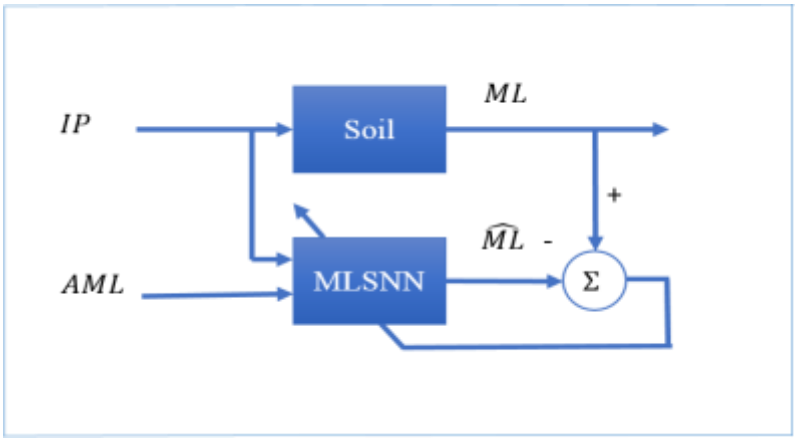

Figure 4. Soil plant identification.

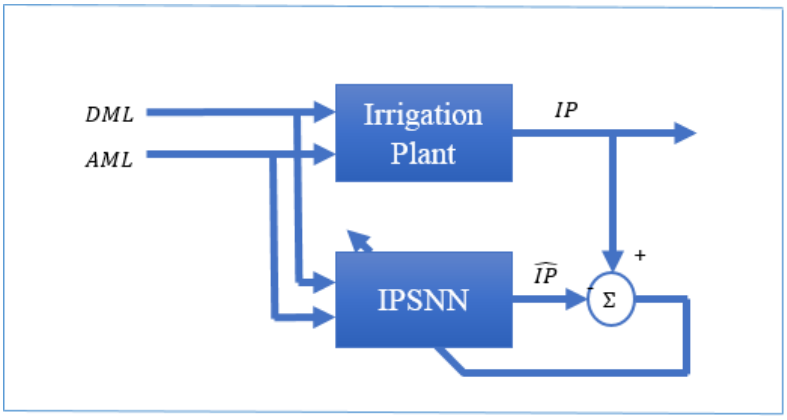

Figure 5. Identification of Irrigation Length Interval.

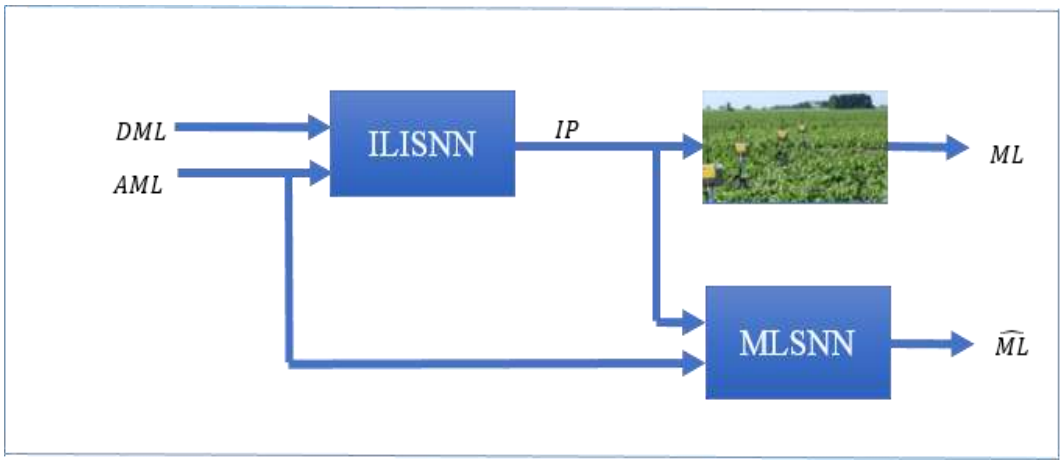

Figure 6. Block diagram of agricultural system.

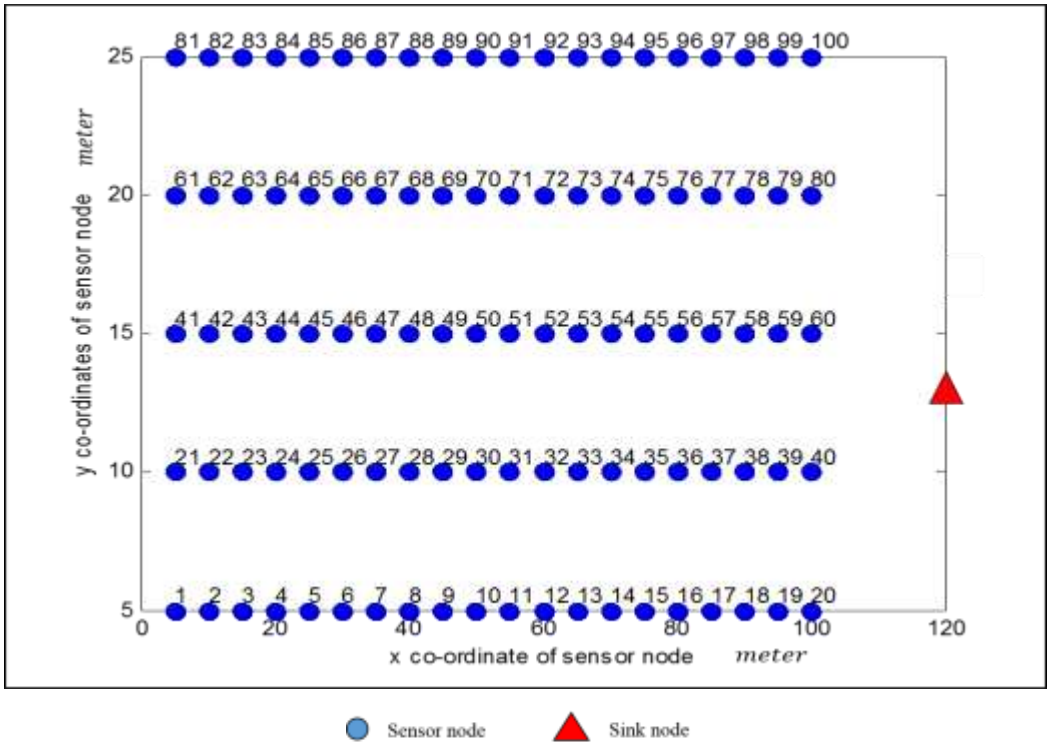

Figure 7. Sensor nodes distribution in particular area.

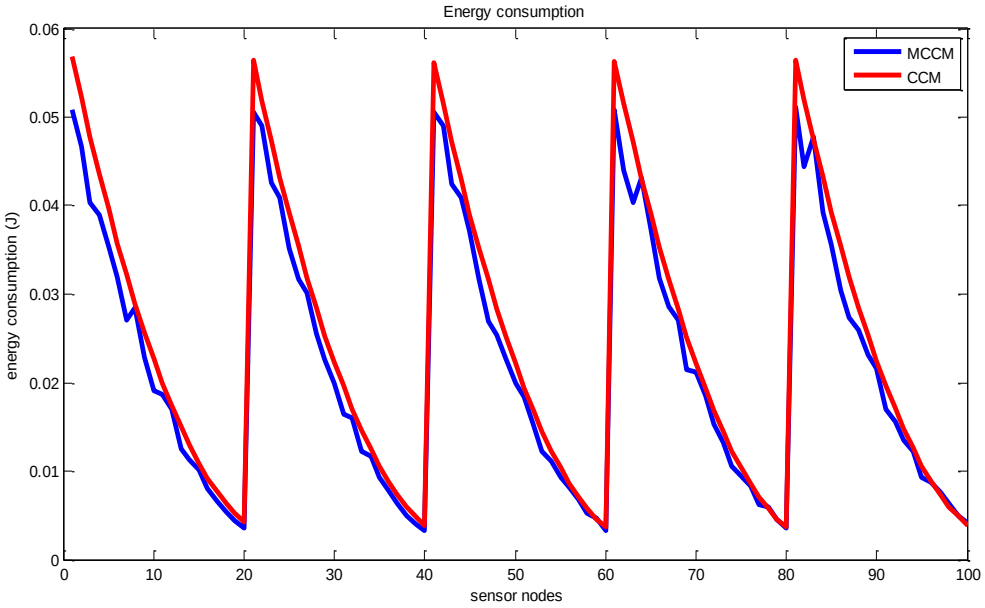

Figure 8. The compression of energy consumption.

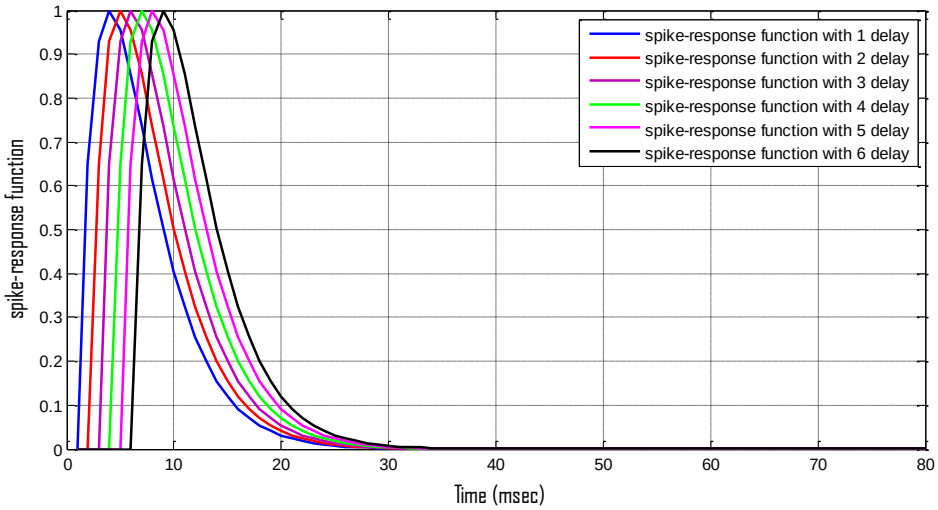

Figure 9. Spike-response functions for one connection.

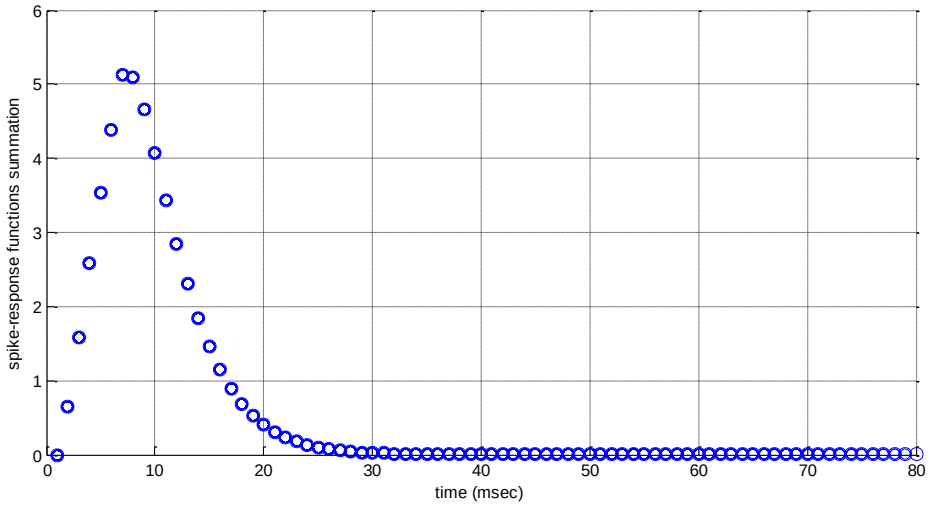

Figure10. Summation of spike-response function.

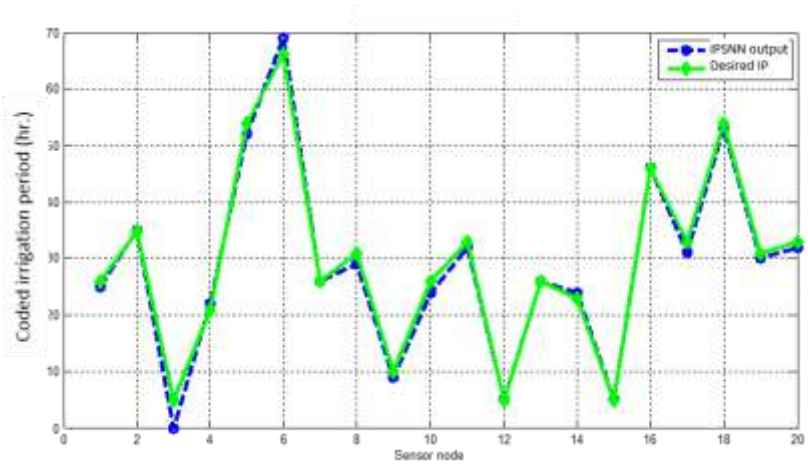

Figure 11. IPSNN identification.

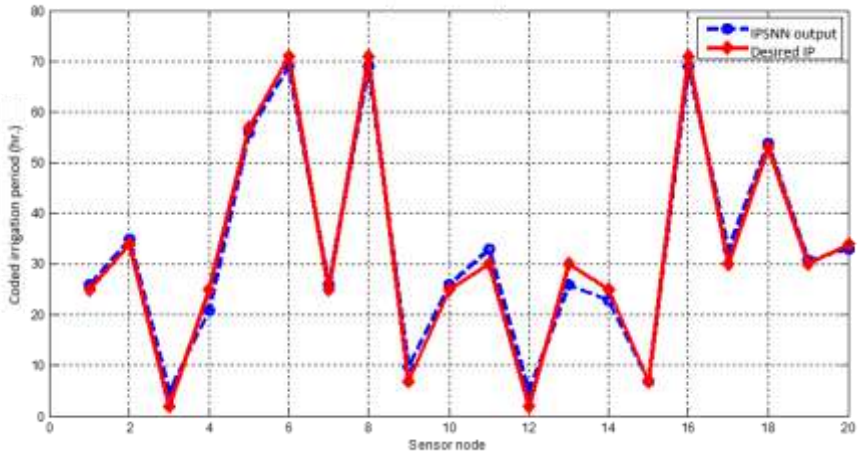

Figure 12. IPSNN validation.

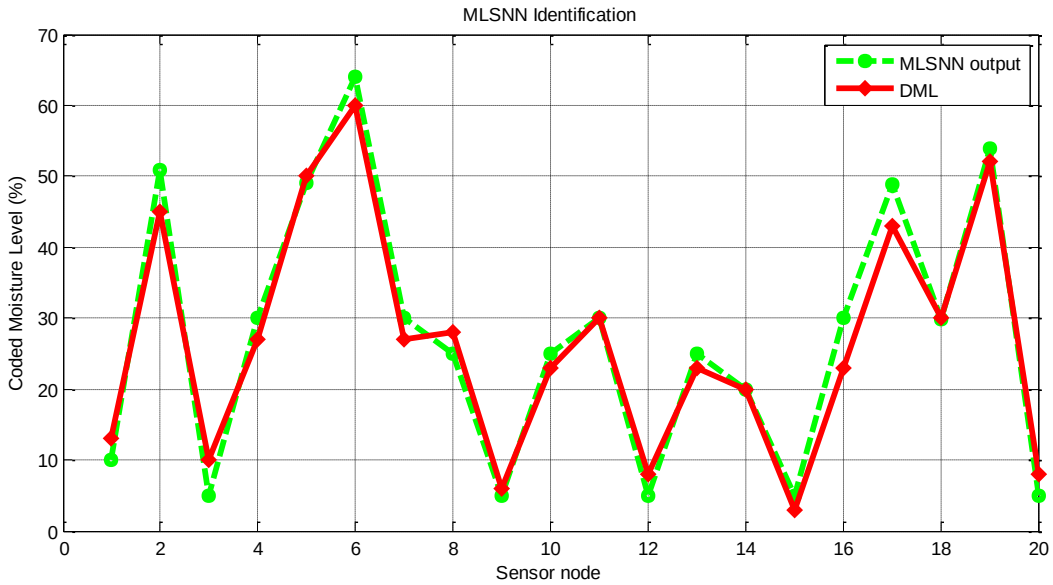

Figure 13. MLSNN identification.

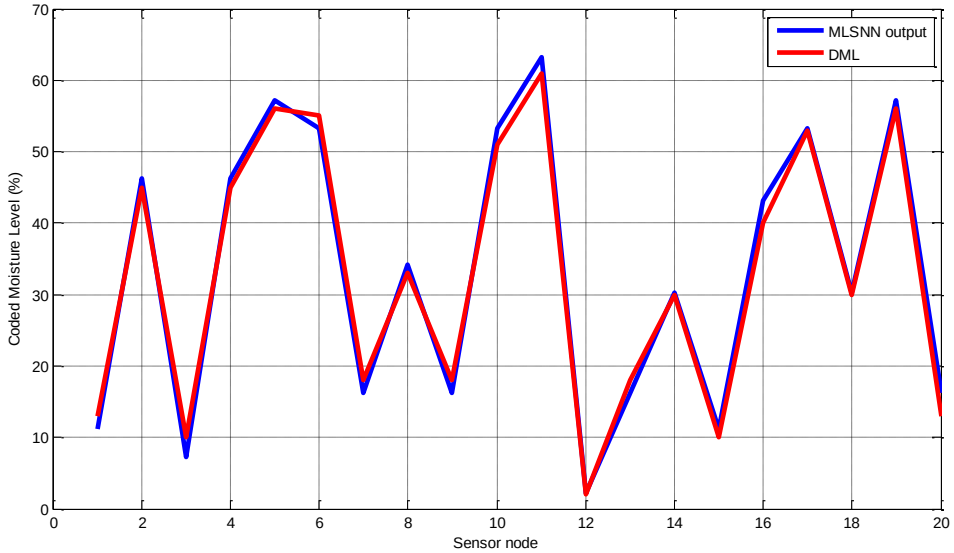

Figure 14. MLSNN validation.

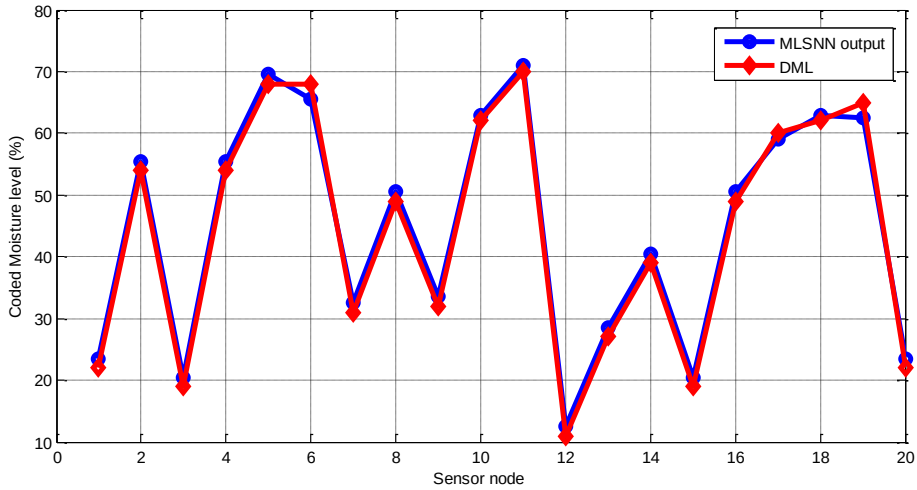

Figure 15. Moisture level of the first strip.

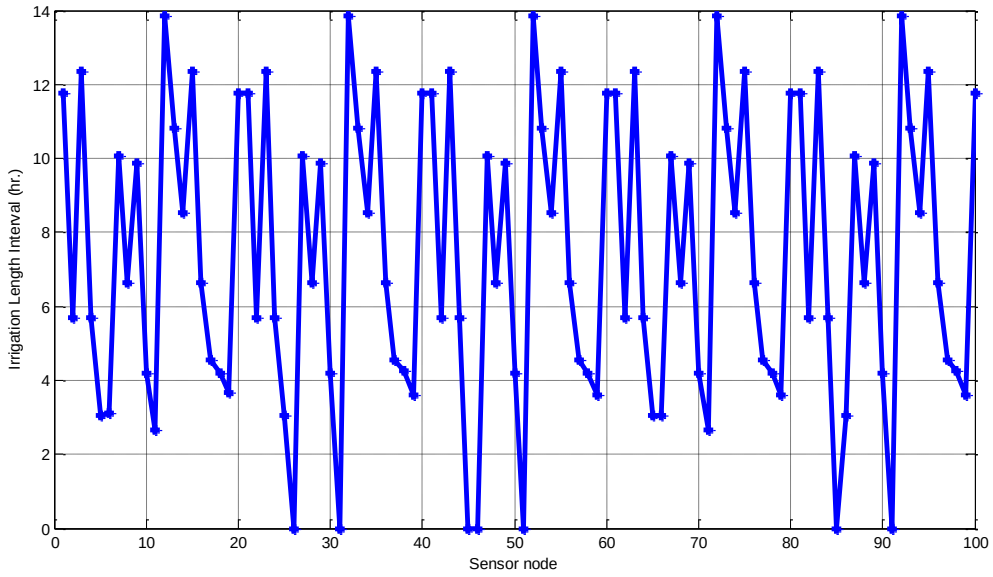

Figure 16. Irrigation length interval required for all nodes.

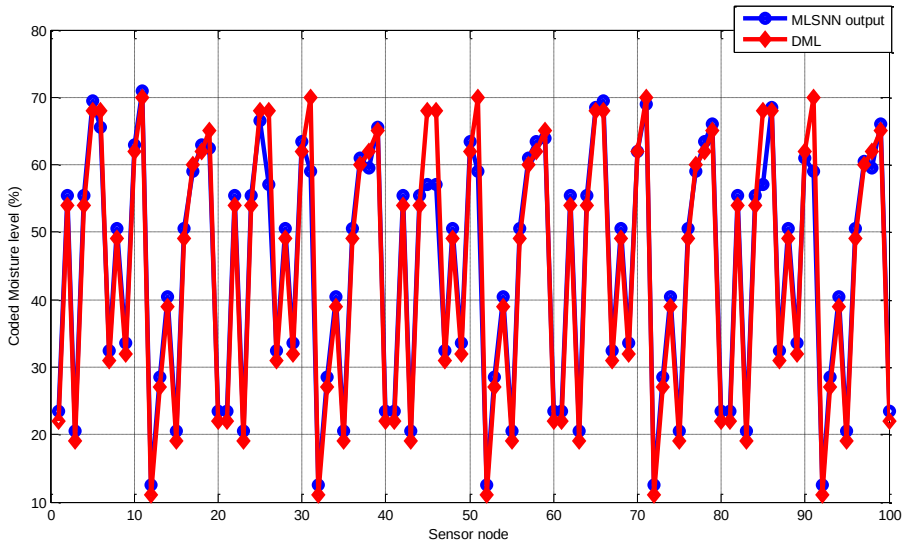

Figure 17. The moisture level for all nodes.

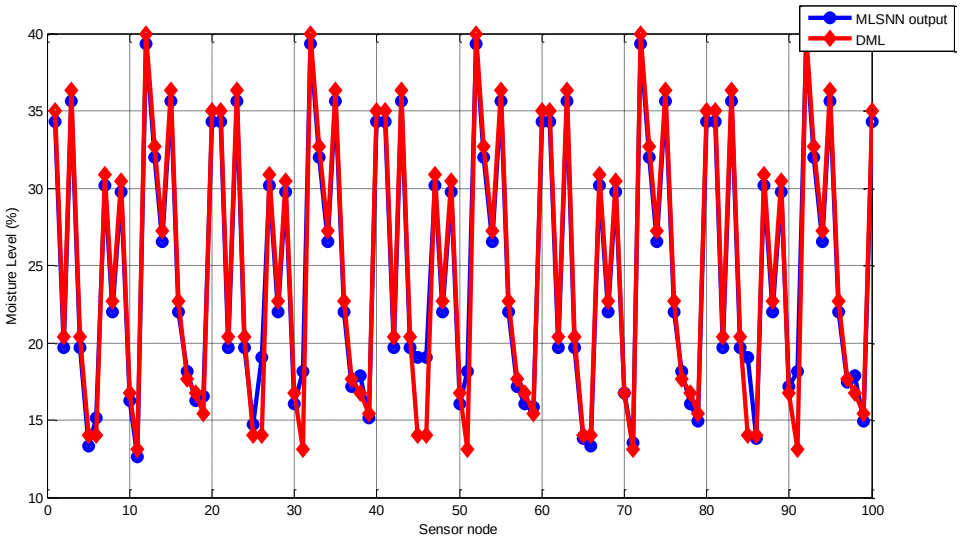

Figure 18. Moisture level for 100-node after decoding.

A comparative Isothermal and Kinetic Study of the Adsorption of Lead (II) from Solution by Activated Carbon and Bentonite

Instructor. Ziad Tark Abd Ali
Department of Environmental Engineering
College of Engineering
Baghdad University
E-mail: z.teach2000@yahoo.com

ABSTRACT

This work is aiming to study and compare the removal of lead (II) from simulated wastewater by activated carbon and bentonite as adsorbents with particle size of 0.32-0.5 mm. A mathematical model was applied to describe the mass transfer kinetic.

The batch experiments were carried out to determine the adsorption isotherm constants for each adsorbent, and five isotherm models were tested to choose the best fit model for the experimental data. The pore, surface diffusion coefficients and mass transfer coefficient were found by fitting the experimental data to a theoretical model. Partial differential equations were used to describe the adsorption in the bulk and solid phases. These equations were simplified and then solved using a technique with finite elements and orthogonal collection method for the bulk fluid and intraparticle phases, respectively. The results obtained from this work show that the equilibrium adsorption isotherms are favorable, and fitted well using the Freundlich model for activated carbon and bentonite. The activated carbon has a high value of pore diffusion coefficient, D_p, while bentonite has a high value of surface diffusion coefficient, D_s. This indicates that the pore diffusion controls the adsorption process for activated carbon, and the surface diffusion controls the adsorption process for bentonite. The activated carbon was more efficient than bentonite in removing of lead (II) from simulated industrial wastewater.

Key words: adsorption, lead (ll), activated carbon, bentonite, isotherm, kinetic

دراسة مقارنة ازالة الرصاص من محلول بواسطة الكاربون المنشط والبنتونايت

م.د. زياد طارق عبدعلي
قسم الهندسه البيئيه
كلية الهندسه/جامعة بغداد

الخلاصة

يهدف هذا البحث الى دراسة ومقارنة ازالة الرصاص من مياه الصرف بواسطة الكاربون المنشط والبنتونايت كمواد ممتزه بحجم حبيبي 0.5-0.32 ملم . تم تطبيق موديل رياضي لوصف عملية انتقال الماده بالاضافه الى اجراء تجارب الدفعات لتحديد ثوابت موديلات الامتزاز لكل ماده ممتزه وقد استخدم خمسه موديلات وتم فحصها لبيان الافضل تطابقا مع النتائج العمليه .
وتم ايضا ايجاد معامل الانتشار السطحي والمسامي, ومعامل انتقال الماده عن طريق مطابقة النتائج العمليه مع الموديل النظري وتم ايضا استخدام معادلات تفاضلية جزئيه لوصف عمليه الامتزاز وجرى تبسيط هذه المعادلات وحلها باستخدام تقنيه finite element و orthogonal collection عن طريق برنامج MATLAB . النتائج العمليه اثبتت ان معامل الانتشار المسامي D_P كان اعلى قيمة للكاربون المنشط منه للبنتونايت وان معامل الانتشار السطحي D_S كان اعلى قيمة للبنتونايت منه للكاربون المنشط وهذا يؤشر بان الانتشار المسامي هوالمتحكم في عمليه الامتزاز على الكاربون وان الانتشار السطحي هو المتحكم في عملية الامتزاز على البنتونايت وقد اثبتت النتائج ايضا بان الكاربون المنشط اكثر كفاءة من البنتونايت في ازالة الرصاص من مياه الصرف .

الكلمات الرئيسية: امتزاز, رصاص, كاربون منشط, بنتونايت, ايزوثيرم, حركي.

1. INTRODUCTION

Heavy metals as pollutants, are not biodegradable, and tend to accumulate in living organisms, **Kobya, et al., 2005.** Lead is one such heavy metal, and can be introduced into liquid wastes from different industries. In water, lead tends to accumulate in aquatic organisms through the food chain and by direct uptake. Lead can damage practically all tissues, particularly the kidneys and the immune system. Intense exposure to high levels of lead (from 10 to 20 g/day) causes encephalopathy with the following symptoms: vertigo, insomnia, migraine, irritability and even convulsions, seizures and coma. There is a critical need to treat wastewater so as to bring the concentration of toxic elements below the recommended release limit, **Smith, 1992.**

Conventional techniques for removing dissolved heavy metals from wastewater includes chemical precipitation, adsorption, electrolytic recovery, ion-exchange, chelation and solvent extraction or liquid membrane separation **,Gõksungur, et al., 2005.** Adsorption is one of the methods commonly used to remove heavy metal ions from various aqueous solutions. The efficiency of adsorption relies on the capability of the adsorbent to adsorb metal ions from solutions onto its surfaces. Different naturally occurring adsorbents, like activated carbon, tea waste, egg shells, mineral mixtures, are used as adsorbents for industrial waste management. Furthermore, bentonite has been used as an adsorbent for the removal of Pb (II), Fe (II), Zn (II) and Cr (III), **Tahir, and Rauf, 2004.**

2. ADSORPTION ISOTHERM MODELS

The study of adsorption isotherms is fundamental for supplying essential information required for designing the sorption process. The adsorption of a substance from one phase to another leads to a thermodynamically defined distribution of that substance between the phases as the system reaches a state of equilibrium, **Naiya, et al., 2009.** This distribution can be expressed in terms of adsorption isotherms. In this investigation, Langmuir, Freundlich, Radk-Prausnitz, Reddlich-Peterson, and a Combination of Langmuir-Freundlich isotherm models were used to analyze the equilibrium data.

2.1 Langmuir Model

In 1916, Irving Langmuir published a new model isotherm for gas or liquid adsorbed onto solid, which resulted in the model being named after him. The Langmuir adsorption model is valid for single-layer adsorption. It is based on the assumption that maximum adsorption corresponds to a saturated monolayer of solute molecules on the adsorbent surface. The energy of adsorption is constant, and there is no transmigration of adsorbate in the plane of the surface. The Langmuir isotherm equation is

$$q_e = \frac{q_m b C_e}{1 + b C_e} \tag{1}$$

where q_e (mg/g) is the amount of solute adsorbed per unit weight of adsorbent at equilibrium, C_e (mg/l) is the equilibrium concentration of the solute in the bulk solution, q_m is the maximum adsorption capacity, and b is the constant related to the free energy of adsorption.
The Langmuir isotherm is used most frequently to describe the adsorption isotherm which is limited by the assumptions of uniform energies of adsorption on the surface of the adsorbent. It is based on four assumptions **,Lucas and Cocero, 2004,** namely:

- The surface of the adsorbents is uniform, that is, all the adsorption sites are equivalent.
- There is no interaction between molecules adsorbed on neighboring sites.
- All adsorption occurs through the same mechanism.

- Molecules are adsorbed at the defined sites on the adsorbent's surface.

2.2 Freundlich Model

The first mathematical fit to an isotherm was published by Freundlich and Kuster in 1894. Freundlich showed that adsorption from a solution could be expressed by the empirical formula, **Lucas and Cocero, 2004.**

$$q_e = kC_e^{1/n} \tag{2}$$

Where k (mg/g)(l/mg)$^{1/n}$ is the Freundlich sorption coefficient and n is an empirical coefficient indicative of the intensity of the adsorption.

2.3 Radk-Prausnitz Isotherm Model

The Radk-Prausnitz isotherm model **, Radke and prausnitz, 1972** was expressed empirically by the following equation:

$$q_e = \frac{K_{RP}C_e}{1+\left(\frac{K_{RP}}{F_{RP}}\right)C_e^{1-N_{RP}}} \tag{3}$$

Where K_{RP}, F_{RP} and N_{RP} are the model parameters which are obtained by a nonlinear statistical fit of the equation to the experimental data. The Radk-Prausnitz equation has several important properties making it suitable for use in many adsorption systems.

2.4 Reddlich-Peterson Model

The Reddlich-Peterson isotherm model, **Lucas and Cocero, 2004** was expressed by the following equation:

$$q = \frac{A_R C_e}{1+B_R C_e^{m_R}} \tag{4}$$

where; A_R, B_R and m_R are the model parameters.

2.5 Combination of Langmuir-Freundlich Model

The Sips model for single component adsorption, **Sips, 1984,** is

$$q_e = \frac{bq_m C_e^{1/n}}{1+bC_e^{1/n}} \tag{5}$$

3. KINETIC STUDY

3.1 Intraparticle Transport

Intraparticle transport is also known as internal mass transfer. After the adsorbate passes through the hydrodynamic boundary layer, they are transported through the adsorbent to the available adsorption sites. Intraparticle transport may occur by molecular diffusion through the solution in the pores (pore diffusion), or by the diffusion along the adsorbent surface (surface diffusion) or both combined, pore and surface diffusion.

3.1.1 Pore diffusion

This is the diffusion of molecules in the liquid that fills the pores. The adsorbate first diffuses through the liquid filling the pores and is then adsorbed. The driving force for pore diffusion is the concentration gradient of the liquid in the pore, **Ivars, 1976.**

If the adsorbate is desorbed and repeatedly dissolved in the liquid, pore diffusion is prevalent. The diffusion of adsorbate within the pores is described by the pore diffusion coefficient. The unsteady state equation of the diffusion of species through a spherical particle may be written as

$$\rho_p \frac{\partial q_i}{\partial t} + \varepsilon_p \frac{\partial C_{pi}}{\partial t} = D_{pi}\varepsilon_p \left(\frac{\partial^2 C_{pi}}{\partial r^2} + \frac{2}{r}\frac{\partial C_{pi}}{\partial r} \right) \tag{6}$$

where the pore diffusion coefficient, D_{pi}, is assumed to be independent of concentration in this case, **Quek and Al-Duri, 2007.**

3.1.2 Surface diffusion

This is the diffusion of molecules in the adsorbed state. Molecules' migration takes place along the surface when an adjacent adsorption site is available and the molecules have enough energy to leave the site being presently occupied by them. This is described by the surface diffusion coefficient D_s. The driving force is the local adsorbent-phase gradient **,Hand, et al., 1983.**

The mass transport is described by the following unsteady state homogenous diffusion equation **,Fritz, et al., 1981.**

$$\frac{dq_i}{dt} = D_{si}\left(\frac{\partial^2 q_i}{\partial r^2} + \frac{2}{r}\frac{\partial q_i}{\partial r} \right) \tag{7}$$

3.1.3 Pore and surface diffusion

Pore and surface diffusion occur in parallel within the adsorbent particle. The solute diffusion inside the particle is described as

$$\rho_p \frac{\partial q_i}{\partial t} + \varepsilon_p \frac{\partial C_{pi}}{\partial t} = D_{pi}\varepsilon_p \left(\frac{\partial^2 C_{pi}}{\partial r^2} + \frac{2}{r}\frac{\partial C_{pi}}{\partial r} \right) + \rho_p D_{si}\left(\frac{\partial^2 q_i}{\partial r^2} + \frac{2}{r}\frac{\partial q_i}{\partial r} \right) \tag{8}$$

The adsorbent kinetics is governed by external mass transfer and internal diffusion, that is, by the coefficients K_f, D_p and D_s. In order to simplify the simulation, models that take into account only two coefficients were developed.

The effective intraparticle diffusion coefficients D_p and D_s are derived from a typical concentration decay curve for each solute in a certain adsorbent, with the help of an iterative search technique to minimize the sum of the square of residuals. Each iteration involves the numeric solution of a coupled set of partial differential equations with appropriate initial and boundary conditions that describe the film and intraparticle transport mechanisms in batch-wise experiments, **Liu, et al., 2006.**

4. MATHEMATICAL MODEL FOR ADSORPTION

In the present study, a mathematical model for batch adsorption will be employed following the assumption that homogeneity exists throughout the batch system. Accordingly, the model will be referred to as a pore and surface diffusion model. The model equations can be written as follows:

4.1 Mass Balance inside Particle Phase

This equation can be used for intra-particle mass transfer, **Hand, et al., 1983.**

$$\frac{1}{r^2}\frac{\partial}{\partial r}\left[r^2 D_s \rho_p \quad \frac{\partial q}{\partial r}(r,t) + r^2 D_p \varepsilon_p \frac{\partial C_p}{\partial r}(r,t)\right] = \frac{\partial}{\partial t}\left[\rho_p q(r,t) + \varepsilon_p\, C_p(r,t)\right] \tag{9}$$

4.2 Mass Balance in Fluid-Bulk Phase

The solute concentration $C(t)$ in the vessel is given by following equation **,Ping and Guohua, 2001.**

$$\frac{dC(t)}{dt} = -\frac{3k_f W_o}{RV_L \rho_p}\left[C(t) - C_p\left(r = R_p, t\right)\right] \tag{10}$$

4.3 Initial and Boundary Conditions

The initial condition for Eq. (9) is:

$$C_p(r,0) = 0 \tag{11}$$

The initial condition for Eq. (10) is:

$$C(t) = C_o \tag{12}$$

The boundary conditions for Eq. (9) are:

$$\frac{\partial}{\partial r}\left[q(r,t) + \frac{\varepsilon_p}{\rho_p} C_p(r,t)\right] = 0 \qquad \text{at } r = 0, t > 0$$

$$D_s \rho_p \frac{\partial q(r,t)}{\partial r} + D_p \varepsilon_p \frac{\partial C_p(r,t)}{\partial r} = k_f\left[C(t) - C_p(r,t)\right] \quad \text{at } r = R_p, t > 0 \tag{13}$$

Coupling equation between Eqs. (9) and (10) and solving the system of partial differential equations numerically will result in the unsteady state in concentration of the solute in the vessel.

The bulk-fluid phase and particle equations for the batch adsorber model are first discretized using finite element (FE) and orthogonal collocation (OC) methods, respectively, **Fig.1**.The resulting ordinary differential equations (ODE) system is solved using an existing ODE solver provided by MATLAB (V-7.9), **Eggers, 2000.**

5. EXPERIMENTAL MODEL AND PROCEDURES

5.1 Materials and Methods

Granular activated carbon (GAC) was used as the first adsorbent in the present work. It was supplied by Unicarbo (Italy), to the Iraqi local markets. The granulated activated carbon was crushed, sieved into 0.32–0.5 mm, (De = 0.0004 m). The required sieve fraction was removed and washed with distilled water to remove fines. The GAC was washed, then the wet GAC was

dried in an oven that was maintained at 100°C for 24 hours, after which the GAC was kept in a desiccator for experimental use.

Local bentonite (calcium base) was used as the second adsorbent; it was supplied by the State Company of Geological Survey and Mining as pieces of rocks. These rocks were crushed to granules of different sizes, and then sieved using sieves to produce granules of sizes 0.32–0.5 mm, (D_e = 0.0004 m). The granules of bentonite were dried at 100°C for 1 hour before being used.

The salt of $Pb(NO_3)_2$ (BDH, England) was used in the preparation of the stock solutions by dissolving it at a known concentration in distilled water. The solutions used for the study were obtained by dilution of the stock solution to the required concentration. The initial pH of each of the solutions was adjusted to a pH of 4 by the addition of HNO_3 or NaOH solution. The initial concentration of the metal ion, and the corresponding concentrations after fixed the time periods, were measured by an Atomic Absorption Spectrophotometer (type: ACCUSYS 211).

5.2 Equilibrium Isotherm Experiments

Two sets of adsorption experiments were carried out, activated carbon and bentonite, each one separately. An aqueous solution of 800 mg/l Pb (II) was prepared with a pH of 4. The Pb (II) adsorption isotherm equilibrium data were obtained using the batch process technique in several glass bottles of 250 ml volume at room temperature. Each flask was filled with 100 ml of prepared solutions, initially containing 2 g/100 ml of an adsorbent, activated carbon or bentonite.

The glass bottles were then placed on a shaker and agitated continuously at 300 rpm for 3 hours at room temperature (20°C) to achieve equilibrium concentrations. The adsorption equilibrium concentration could be established and then the product solution was filtered with filter paper (type: Whatman 542, England) to remove any remaining adsorbent particles in the solution. The adsorbate concentrations of the liquid samples were then analyzed by means of an Atomic Absorption Spectrophotometer (type: ACCUSYS 211). The amount of adsorbate adsorbed was calculated according to the following equation:

$$q_e = \frac{V_L\left(C_o - C_e\right)}{W} \tag{14}$$

Where C_o and C_e are the initial and equilibrium concentrations of Pb (II) in the solution (mg/l), V_L is the volume of solution in the flask (L) and W is the mass of the adsorbent in the flask (g). The adsorption isotherms were obtained by plotting the weight of solute adsorbed per unit weight of adsorbent q_e against the equilibrium concentration of Pb (II) in the solution C_e.

5.3 Kinetic Experiments

The aim of the kinetic adsorption experiments of Pb (II) onto activated carbon and bentonite was to find the external mass transfer coefficient, k_f, the pore and the surface diffusion coefficients. A solution was prepared containing the Pb (II) concentration of 800 mg/l; 100 ml of solution was placed in several glass bottles each of 250 ml volume. The adsorbents, each one separately, were accurately weighed for the desired amount of 0.2, 0.4, 0.6, 1, 1.5, 2, 3, 4 g, and placed in several individual bottles. The bottles were then placed on a shaker for agitating, and then analyzed at various time intervals. The above experiment was repeated for each adsorbent at variable speeds of 100, 150, 200, 250 and 300 rpm, and then a sample of the solution was filtered with filter paper (type: Whatman 542, England), the residual concentrations of Pb (II) in solution was determined using atomic absorption spectrophotometer (type: ACCUSYS 211). During these experiments, the solute concentration decreased with time, the rate of adsorption of solute was measured by monitoring the solute concentration as a function of time. The desired weight of the adsorbent to reach an equilibrium concentration of C/C_o = 0.05 was calculated

from the isotherm equation and mass balance equation for solute. The desired speed was obtained by repeating the experiments for each component with variable speeds (100, 150, 200, 250 and 300 rpm). The maximum speed at which the concentration ratio C/C_o remains constant at 0.05 was taken as the desired speed. The approach of C/C_o = 0.05 (equivalent to 95% removal efficiency) refers to the optimum operational durability and sustainability of the adsorption process.

6. RESULTS AND DISCUSSION

6.1 Isotherms Study

6.1.1 Determination of contact time

The plots of Pb (II) concentrations versus time for activated carbon and bentonite are presented in **Fig. 2**. On the basis of this plot, an equilibrium time of 40 min was chosen for the two adsorbents.

6.1.2 Determination of adsorbent dosage

The plots of Pb (II) concentrations versus various adsorbent quantities for activated carbon and bentonite are presented in **Fig. 3**. On the basis of this plot, the best weight that gave the higher removal was 2 g and 4 g for activated carbon and bentonite, respectively.

6.1.3 Estimation of adsorption isotherms constants

The constants of five isotherm models for activated carbon and bentonite were determined. The parameters for each model were obtained using a nonlinear statistical fit of the equations to the experimental data. All parameters with correlation coefficients are summarized in **Table. 1**, it is clear that the Freundlich isotherm model provided the best correlation compared with other isotherm models for Pb (II) sorption on the activated carbon and bentonite **Fig.4**.

From **Table 1** and **Fig. 4**, it can be concluded, that

- The equilibrium isotherm for activated carbon and bentonite are of a favorable type (i.e., somewhat convex upward).
- The sorption capacity varied from 80 mg/g to 20 mg/g, and from 52 mg/g to 17 mg/g for activated carbon and bentonite, respectively, **Table 2**. The average lead sorption capacity was the highest for activated carbon, and the lowest for bentonite.

6.2 Kinetic Study

6.2.1 Determination of diffusivity coefficients

The D_s and D_p for Pb (II) can be determined by matching experimental concentration curves with predicted concentrations at the optimum agitation speed. This can be generated by a numerical solution of the batch adsorber model. The matching requires values of the following parameters:

6.2.2 The optimum weight of adsorbent

The amount of adsorbent used for adsorption of Pb (II) was determined from the equilibrium-related concentration of C_e/C_o = 0.05 using the Freundlich equation as follows:

$$q_e = \frac{V_L(C_o - C_e)}{W_o} = KCe^{1/n} \qquad \text{where} \quad W_o = \frac{V_L(C_o - C_e)}{KCe^{1/n}} \tag{15}$$

The optimum weights W_o of activated carbon and bentonite were found to be 2 g and 4 g, respectively, under experimental conditions.

6.2.3 The best agitation speed

The efficiency of removal of Pb (II) is shown in **Figs.5** and **6** for activated carbon and bentonite, respectively, at different agitation speeds of 100, 150, 200, 250 and 300 rpm. The best agitation speed that achieved C_e/C_o = 0.05 is 300 rpm; at speed above 300 rpm, the removal efficiency is more than 95%, with possible pulverization of activated carbon and bentonite, and in this case, both adsorbents were in powder form rather than granular. On the basis of the above information, the maximum agitation speed for activated carbon and bentonite was regarded as 300 rpm.

6.2.4 External mass transfer coefficient

The external mass transfer coefficient (k_f) in the batch adsorber was determined from the concentration decay curves at optimum speed at the initial rate data, using the following equation [31]:

$$k_f = -\frac{R_p \rho_p V_L}{3W_o t} \ln\left(\frac{C(t)}{C_o}\right) \qquad 0 < C(t)/C_o < 1.0 \qquad (16)$$

Where R_p is the radius of particles (m), ρ_P is the particle density (Kg/m^3), V_L is the volume of solution (L), t is the time (min), C_o and C(t) are the solute concentration at time zero and time (t), respectively. For accurate estimation of k_f, samples were taken at 2, 4, 5 and 7 minutes and analyzed immediately, **Table 3**.

The average calculated values of k_f for adsorbents were found to be 6.05×10^{-5} and 2.65×10^{-5} m/s for activated carbon and bentonite, respectively. This indicates that the rate of mass transfer of activated carbon is higher than bentonite. In other words, lead is adsorbed by activated carbon at a higher rate than bentonite.

6.2.5 Determination of pore and surface diffusion coefficients

The pore and surface diffusion coefficients for the two adsorbents were obtained from the numerical solution of Eqs. (9) and (10), with the initial and boundary conditions that describe the film and intraparticle transport mechanism in batch-wise experiments, using the external mass transfer coefficient described in the previous section.

D_s and D_p were obtained from the typical concentration decay for each adsorbent by an iterative search technique for the minimization of the difference between experimental and predicted data from a batch model. It is clear from **Figs.7** and **8**, that for activated carbon and bentonite, respectively, there is good matching between experimental and predicted data, as can be seen from the correlation coefficients presented in **Table. 4**.

Examining **Table 4**, it can be seen that activated carbon has the largest value of D_p compared with bentonite, this indicates that the pore diffusion controls the adsorption process for activated carbon. While bentonite has the largest value of D_s, this indicates that the surface diffusion controls the adsorption process for bentonite.

7. CONCLUSION

The activated carbon was more efficient than natural bentonite for removing lead ions from industrial wastewater. The experimental data fitted well to the Freundlich equation, with good correlation coefficients 0.9850 and 0.9598 for activated carbon and bentonite, respectively. There is good matching between the experimental and predicted data in batch experiments using a pore-surface diffusion model for the two adsorbents. Hence, the transfer of solute within the

adsorbents is controlled by pore diffusion for activated carbon and by surface diffusion for bentonite. The average calculated value of k_f for activated carbon is higher than bentonite which indicates that the rate of mass transfer with activated carbon is higher than bentonite. In other words, lead is adsorbed by activated carbon at a higher rate than bentonite. The mathematical model which includes mass transfer coefficient, isotherm model constants, pore and surface diffusion coefficients provides a good description of the adsorption process for this study.

8. REFRENCES

- Eggers, R., 2000, *Simulation of Frontal Adsorption*, HIWI report by Hamburg-Hamburg University.

- Fritz, W., Merk, W., and Schlunder, E.U., 1981, *Competitive Adsorption of Two Dissolved Organic onto Activated Carbon, I-Adsorption Equilibria*, J.Chem.Eng.Sci.No.36, pp721-730.

- Gõksungur, Y., Üren, S., and Güvenc, U., 2005, *Biosorption of Cadmium and Lead Ions by Ethanol Ttreated Waste Baker's Yeast Bioresour*. Technol. 96(1): 103-109.

- Hand, D.W., Crittenden, J. C., and Thacker, A. M.,1983, *User-Oriented Batch Solution to the Homogenous Surface Diffusion Model*, J. Environmental Engineering, V.109,No.1,pp82-101.

- Ivars, N.,1976, *Analysis of Some Adsorption Experiments with Activated Carbon*, Chemical Engineering Science,No.31, pp1029-1035.

- Kobya, M., Demirbas, E., Senturk, E., and Ince, M., 2005, *Adsorption of Heavy Metal Ions from Aqueous Solutions by Activated Carbon Prepared from Apricot Stone*. Bioresour.Technol. 96(13): 1518-1521.

- Liu, B.,Yang, Y., and Ren, Q., 2006, *Parallel and Surface Diffusion of Levulinic Acid in Basic Polymeric Adsorbents*, J. Chromatography A., Vol.1132, pp 190-200.

- Lucas, S., and Cocero, M. J., 2004, *Adsorption Isotherms for Etheylacetate and Furfural on Activated Carbon from Supercritical Carbon Dioxide* , Fluid Phase Equilibrium, Vol.219, pp 171-179.

- Naiya T. K., Bhattacharya A. K., and Das S. K., 2009, *Adsorption Removal of Cd(II) Ions from Aqueous Solutions by Rice Husk Ash*, Environmental Progress & Sustainable Engineering, 28: 535-546.

- Ping, L., and Guohua, X., 2001, *Competitive Adsorption of Phenolic Compounds onto Activated Carbon Fibers in Fixed Bed* , J. Environmental Engineering, August,pp 730-734.

- Quek, S.Y. and Al-Duri, B., 2007, *Application of Film-Pore Diffusion Model for the Adsorption of Metal Ions on Coir in a Fixed-Bed Column*, Chemical Engineering and Processing, V,46,pp477-485.

- Radke, C. J. and prausnitz, J. M., 1972, *Adsorption of Organic Compounds from Dilute Aqueous Solution on Activated Carbon*, Ind. Eng. Chem. Fund., Vol.11,pp 445-451.

- Sips, R., 1984, J. Chem. Phys., Vol.16, pp 490-495.

- Smith, E. A., 1992, *Heavy Metals*. Health Science Bookstall, pp. 142–50.

- Tahir, S.S., and Rauf , N., 2004, *Removal of Fe(II) from the Wastewater of a Galvanized Pipe Manufacturing Industry by Adsorption onto Bentonite Clay*, Joumal of Environmental Management, Vol. 73, pp. 285-292.

9.NOMENCLATURE

FE Finite elements
OC Orthogonal collection
D_s Surface diffusion
D_p Pore diffusion
C_e Concentration of Pb(II) remaining in solution at equilibrium (mg/l)
K_f External mass transfer coefficient
q_e Pb(II) concentration sorbed on the adsorbent (mg/g)

Table 1. Parameters of isotherm models for adsorption of Pb(II) using activated carbon and bentonite.

Model	Parameters	Activated Carbon	Bentonite
Langmuir Eq. (1)	q_m,(mg/g)	81.7	60.8
	b, L/mg	0.0214	0.0046
	Correlation coefficient	0.9689	0.9089
Freundlich Eq. (2)	K,(mg/mg)(L/mg)$^{1/n}$	0.0147	0.0053
	n,	3.8714	3.0450
	Correlation coefficient	0.9850	0.9598
Radk-Prausnitz Eq. (3)	K_{RP}, L/mg	0.9765	0.5772
	F_{RP},	0.0006	39.0473
	N_{RP},	1.6369	0.1388
	Correlation coefficient	0.9547	0.9001
Reddlich-Peterson Eq. (4)	A_R, L/mg	0.5823	0.5739
	B_R,	12405.15	0.0033
	m_R,	-1.0419	1.0811
	Correlation coefficient	0.9460	0.9140
Combination of Langmuir-Freundlich Eq. (5)	q_m, (mg/g)	108.0789	110.4549
	b, (m^3/kg)$^{1/n}$	0.0016	0.0107
	n,	1.2719	1.1736
	Correlation coefficient	0.9476	0.9200

Table 2. Experimental lead sorption capacity values (x/m) for activated carbon and bentonite.

Adsorbent	mg lead sorbed per g adsorbent (X/M)	
	Rang	Mean
Activated carbon	80 – 20	50
Bentonite	52 – 17	34.5

Table 3. Values of K_f at different times.

Adsorbent	t, min	C/Co	K_f, m/s
Activated carbon	2	0.73	6.73×10^{-5}
	4	0.55	6.39×10^{-5}
	5	0.5	5.93×10^{-5}
	7	0.43	5.15×10^{-5}
Bentonite	2	0.8	2.34×10^{-5}
	4	0.59	2.77×10^{-5}
	5	0.52	2.74×10^{-5}
	7	0.4	2.75×10^{-5}

Table 4. Values of (D_p) and (D_s) and their correlation coefficients.

Adsorbent	D_p,m^2/s	D_s, m^2/s	Correlation Coeff.,R^2
Activated carbon	$4.45\text{x}10^{-8}$	$1.95\text{x}10^{-11}$	0.9793
Bentonite	$2.21\text{x}10^{-13}$	$3.33\text{x}10^{-9}$	0.9896

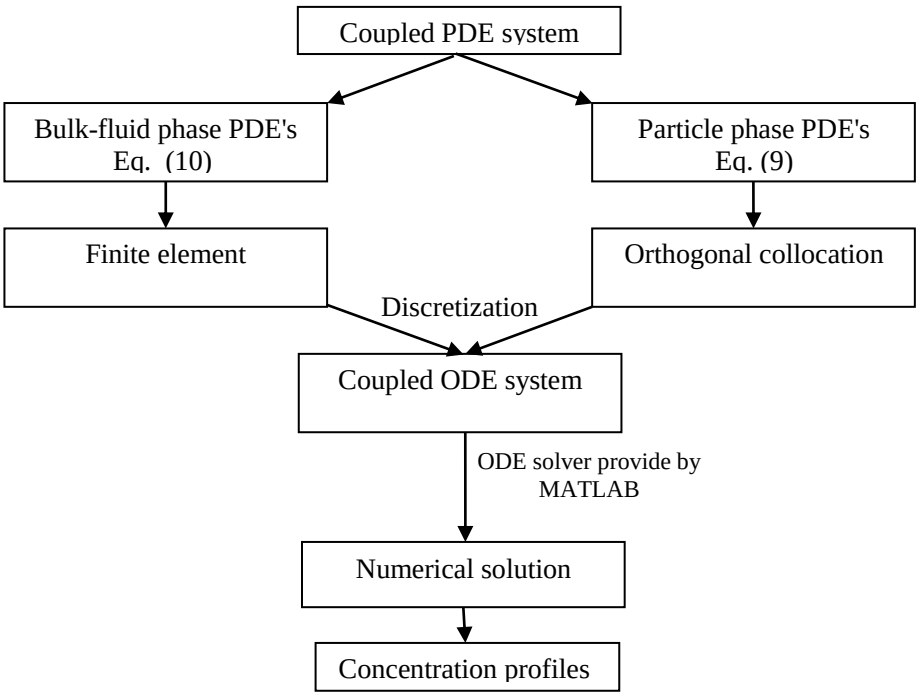

Figure 1. Flow diagram of the numerical method used to solve the PDE system in the model.

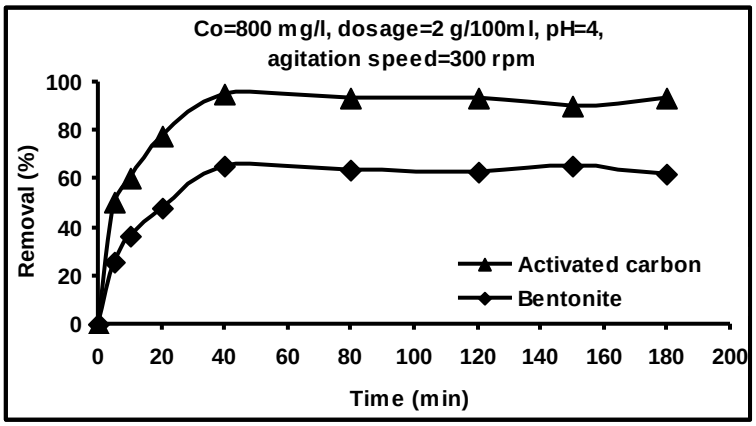

Figure 2. Equilibrium times for the sorption of Pb(II) by activated carbon and bentonite.

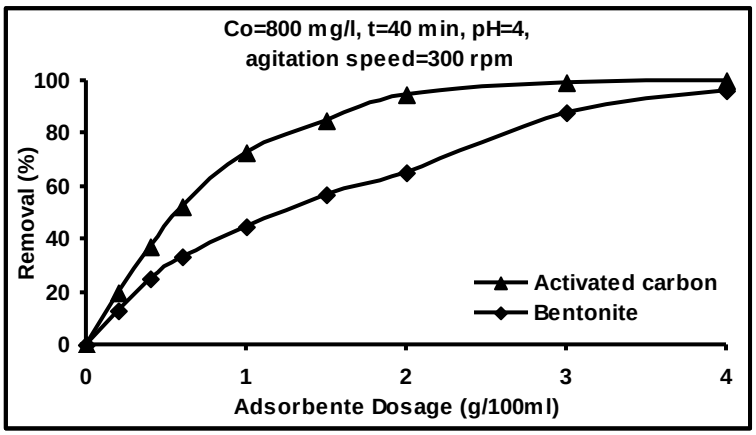

Figure 3. Adsorption of Pb(II) onto activated carbon and bentonite at different dosage.

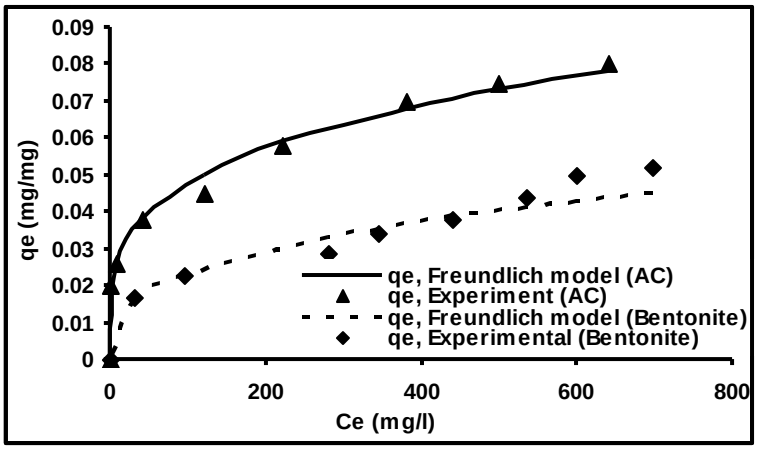

Figure 4. Adsorption isotherms of Pb(II) onto activated carbon and bentonite.

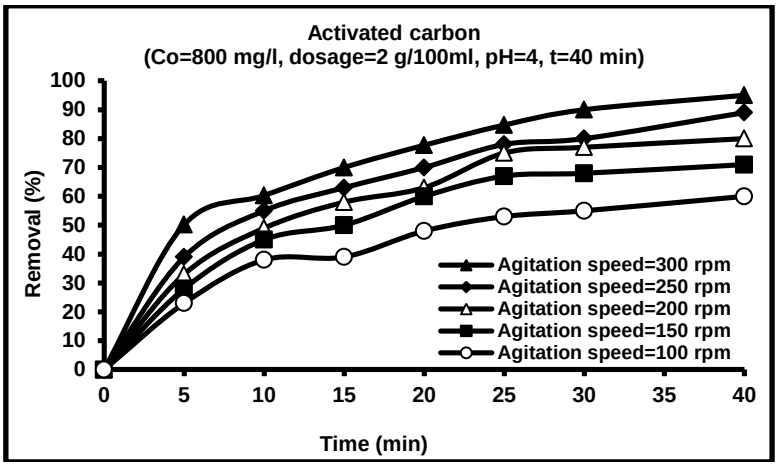

Figure 5. Removal efficiency of lead onto activated carbon at different agitation speeds.

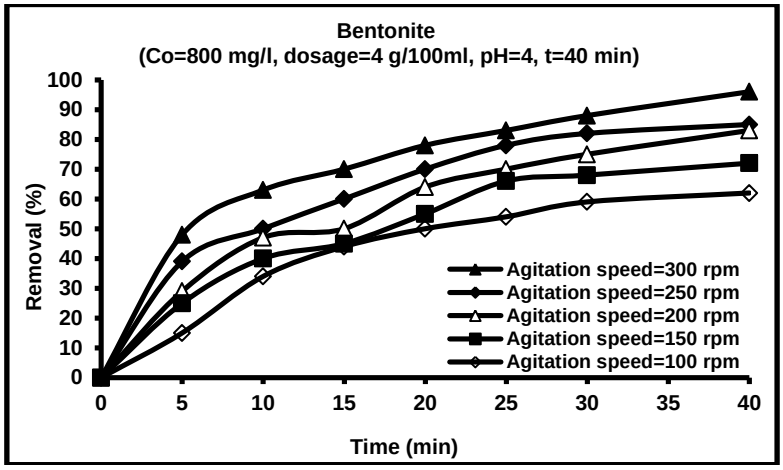

Figure 6. Removal efficiency of lead onto bentonite at different agitation speeds.

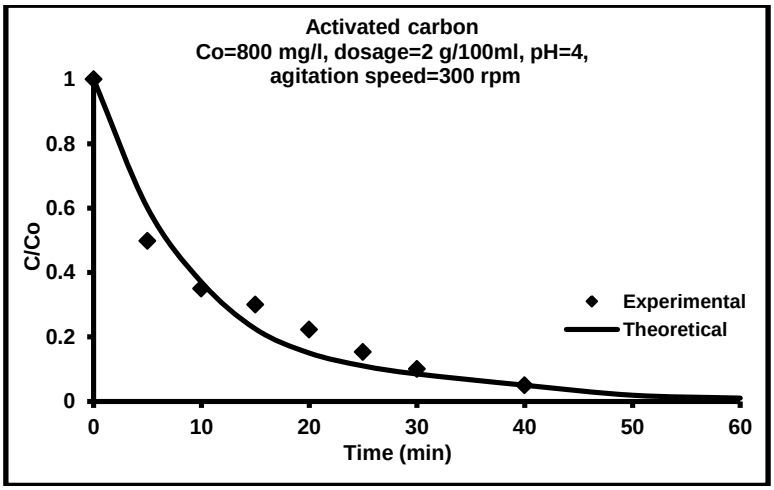

Figure 7. Comparison of measured concentration- time decay with that predicted by batch model for activated carbon system.

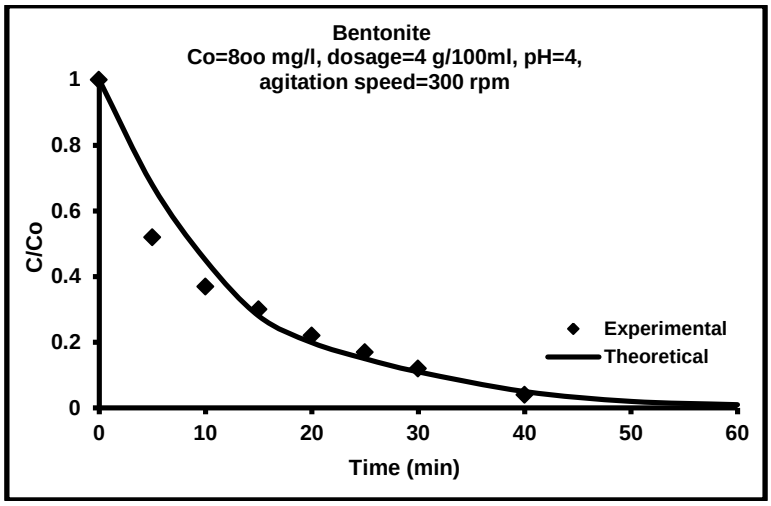

Figure 8. Comparison of measured concentration- time decay with that predictedby batch model for bentonite system.

Pharmaceutical Wastewater Treatment Associated with Renewable Energy Generation in Microbial Fuel Cell Based on Mobilized Electroactive Biofilm on Zeolite Bearer

Dr. Zainab Ziad Ismail
Assistant Professor
Department of Environmental Engineering
College of Engineering- University of Baghdad
E.mail:zismail9@gmail.com

Ali Awaid Habeeb
Researcher
Department of Environmental Engineering
College of Engineering- University of Baghdad
E.mail:envalihabeeb@gmail.com

ABSTRACT

In this study, a novel application of lab-scale dual chambered air-cathode microbial fuel cell (MFC) has been developed for simultaneous bio-treatment of real pharmaceutical wastewater and renewable electricity generation. The microbial fuel cell (MFC) was provided with zeolite-packed anodic compartment and a cation exchange membrane (CEM) to separate the anode and cathode. The performance of the proposed MFC was evaluated in terms of COD removal and power generation based on the activity of the bacterial consortium in the biofilm mobilized on zeolite bearer. The MFC was fueled with real pharmaceutical wastewater having an initial COD concentration equal to 800 mg/L and inoculated with anaerobic aged sludge. Results demonstrated that the COD removal efficiency, power density and current density were 66%, 2.4 mW/m^2 and 10 mA/m^2, respectively.

Key words: microbial fuel cell, pharmaceutical wastewater, zeolite bearer, energy production.

معالجة المطروحات السائلة للصناعة الدوائية مقترنة بتوليد الطاقة الكهربائية المستدامة بأستخدام خلية الوقود الاحيائية المجهزة بحبيبات الزيولايت كحامل بايولوجي في حجرة الانود

د. زينب زياد اسماعيل
استاذ مساعد
قسم الهندسة البيئية- كلية الهندسة-جامعة بغداد
E.mail:zismail9@gmail.com

علي عويد حبيب
باحث
قسمالهندسةالبيئية- كليةالهندسة-جامعةبغداد
E.mail:envalihabeeb@gmail.com

الخلاصة

في هذه الدراسة, تم تطوير منظومة مختبرية مبتكرة لخلية الوقود الاحيائية ثنائية الحجرات لمعالجة المطروحات السائلة للصناعة الدوائية بطريقة بايولوجية وانتاج الطاقة الكهربائية المتجددة في أن واحد. جهزت حجرة الانود لخلية الوقود الاحيائية بحبيبات الزيولايت وغشاء ايوني يسمح بمرور البروتونات من حجرة الانود الى حجرة الكاثود. تم تقييم اداء خلية الوقود الاحيائية على اساس كفاءة ازالة المحتوى الكيمياوي للاوكسجين وانتاج الطاقة الكهربائية نتيجة نشاط الكتلة البايولوجية(حمأة لا هوائية) التي تم تنميتها باستخدام حبيبات الزيولايت كحامل بايولوجي. تم ضخ مياه المخلفات السائلة الحقيقية للصناعة الدوائية

ذات محتوى كيمياوي للاوكسجين بمقدار 800 مليغرام/لتر. أظهرت النتائج المختبرية بأن مستوى ازالة محتوى الاوكسجين الكيمياوي و كثافة القدرة وكثافة التيار كانت 66%,2.4 ملي واط/م^2 و10 ملي امبير/م^2 على التوالي.

الكلمات الرئيسية:خلية الوقود الاحيائية، مطروحات السائلة للصناعة الدوائية، حبيبات الزيولايت، توليد الكهرباء

1.INTRODUCTION

The insufficient availability of oil and natural gas could be augmented by other fuels such as coal and oil shale. However, if obtainable energy from these sources using conventional technologies, it will release additional carbon dioxide, exacerbate environmental damage and accelerate global climate change. A whole new technology platform must be developed that produces clean energy, while at the same time reduces carbon dioxide emissions with a goal to meet 2050 energy needs on carbon neutral basis, **Lewis and Nocera, 2006.** Industrial processes generate a wide variety of wastewater pollutants. The characteristics and levels of pollutants vary significantly from industry to another. Pharmaceutical wastewater are characterized by high chemical oxygen demand (COD), containing a variety of organic and inorganic constituents, the most important are the priority pollutant and low biodegradable compounds or being inhibitory to conventional biological treatment systems, **Benitez et al, 1995. ,Davis and Cornwell, 2008.** Microbial fuel cell (MFC) technologies represent the newest approach for electricity generation from biomass using bacteria, which became of more interest and work on MFCs began to increase, **Allen and Bennetto, 1993.** Microbial fuel cell(MFC) is a type of fuel cell which converts the chemical energy contained in organic matter to electricity using microorganisms as a biocatalyst. In MFC, bacteria do not transfer their electron directly to their terminal electron acceptor, but, rather to a solid electrode and offers the possibility of directly harvesting electricity from organic waste and renewable biomass, **Rabaey and Verstraete, 2005. ,Lovley, 2006.** The basic components of MFCs are the anode, cathode compartments and cation exchange membrane (CEM). The electrochemically active bacteria in the anode compartment oxide the substrate and separate the electrons from protons. These electrons and protons transfer to the cathode, the electrons move through the external circuit and the protons diffuse through the anolyte and the cation exchange membrane (CEM), subsequently they combine at the cathode with oxygen to form water molecules, **Kim et al., 2008.**

Angelov et al.,2013 constructed a dual chambered laboratory scale microbial fuel cell (MFC) based on natural sulfate reducing bacterial consortium in electroactive biofilm on zeolite. The COD removal efficiency and power generation were 23% and 0.68 mW/m^2, respectively. The proposed design can be used for simultaneous sulfate purification of mining drainage wastewater and generation of renewable energy. **Karra et al., 2013** investigated the use of activated carbon Nano-fiber (ACNF) as anode material to enhance biofilm growth and improve MFC performance. Results showed that MFCs with ACNF and granular activated carbon (GAC) as an anode achieved power densities of 3.5±0.46 W/m^3 and 3.09±0.33 W/m^3, respectively. In addition, MFCs with ACNF achieved higher contaminant removal efficiency 85±4% than those with GAC of 75±5%, respectively. **Zhang et al., 2014** examined the effectiveness of refinery wastewater treatment using air cathode microbial fuel cell (MFC). It was configured with separator electrode assembly (SEA) or spaced electrodes (SPA). The MFC with SEA configuration produced a higher maximum power density 280±6 mW/m^2 than the SPA arrangement 255±2 mW/m^2 due to lower internal resistance. Both configurations produced lower power than domestic wastewater indicating poor bio-degradability of refinery wastewater.

The present study aimed to investigate the performance of a continuously operated two chambered air cathode microbial fuel cell (MFC) fueled with actual pharmaceutical wastewater and inoculated with anaerobic aged sludge mobilized on zeolite biofilm bearer for simultaneous wastewater treatment and power generation.

2. MATERIALS AND METHODS

2.1 MFC System

The experimental setup for the microbial fuel cell (MFC) system is presented in **Fig.1.** Microbial fuel cell (MFC) was fabricated of Perspex material with two different sized chambers. Dimensions of anode and cathode chambers were 20 cm*20 cm*26 cm and 10 cm*10 cm* 15 cm, respectively. The cathode chamber was fully submerged in the anode chamber with two opposite sides containing two pieces of cation exchange membrane (CEM) which was sandwiched between two perforated Perspex sheets with a net membrane area of 44 cm^2. The anode compartment contains three ports, one at the top for treated effluent outlet, two ports at the bottom, one for pharmaceutical wastewater inlet and the other for nitrogen flushing. The cathode compartment contains two ports, one for catholyte inlet and the other for air sparging. Two uncoated graphite rods were used as electrodes for each chamber. The graphite rods diameter was 1.8 cm and an effective length of 15 cm resulted in a surface area of 87.5 cm^2 for each electrode. Before the installation of electrodes in the MFC, graphite rods were abraded by sand paper to enhance bacterial attachment, they were soaked in deionized water for a period of 24 h. The electrodes in each chamber were pierced with copper wire extended outside the MFC to simply connected to an external circuit through which electrons were transported. Approximately, 60% of the volume of anode compartment was occupied with zeolite particles as a biofilm bearer and the remaining 40% was considered as a head space. Cylindrical shaped zeolite particles of 1.6 mm diameter and different lengths averaged 2-4 mm were used. The chemical composition of zeolite was as follows:39.5% SiO_2, 22.8% Al_2O_3, 1.65% Na_2O and 1.4% K_2O with a porosity of 57.5%.

2.2 Substrate, Inoculum and Chemicals

Actual pharmaceutical wastewater samples were collected from the inlet pipe of the aeration tank in the biological treatment unit of the State Company for Drug Industry, Samarra(SDI, Samarra). The characteristics of the actual pharmaceutical wastewater are given in **Table. 1** The MFC was inoculated with anaerobic aged sludge which was used as a biocatalyst in the anodic compartment of MFC.

To enrich microbial growth in MFC, mineral salts medium(MSM) was prepared according to the procedure outlined by **Ghangrekar et al., 2005.** The MSM solution was prepared by dissolving 0.56 g/L $(NH_4)_2SO_4$, 0.20 g/L $MgSO_4.7H_2O$, 15 mg/L $CaCl_2$, 1mg/L $FeCl_3.6H_2O$, 20 mg/L $MnSO_4.H_2O$ and 0.42 g/L $NaHCO_3$ in deionized water, then the solution was autoclaved at 121 ^oC for a period of 20 min and cooled under oxygen-free space using nitrogen gas flushing.

The catholyte solution was used as an oxidant at the cathode compartment of MFC. The catholyte was a phosphate buffer solution (PBS) composed of 32.93g/L $K_3Fe(CN)_6$, 20.75 g/L Na_2HPO_4 and 3.1167 g/L NaH_2PO_4.

2.3 Set Up of MFC

Before the construction and set up of MFC, the system components were cleaned well with an appropriate detergent, then repeatedly rinsed with tap water and deionized water. Cation

exchange membrane (CEM) was subjected to a course of preconditioning by immersing in 5% sodium chloride solution for 24 h to allow for membrane hydration and expansion, and then washed with deionized water.

2.4 Operation of MFC

To start up and operate the MFC, anaerobic aged sludge was placed in the anode chamber and was sparged with nitrogen gas for a period of 10 min to maintain anaerobic environment. After 10 days, the MFC was fed with a primarily treated actual pharmaceutical wastewater at a constant rate of 3 ml/min corresponding to a hydraulic retention time (HRT) of 32 h. An air compressor with a maximum flowrate of 10 ml/min was connected to the cathode chamber to supply oxygen in a continuous manner. Oxygen concentration was monitored continuously in the anodic chamber, the absence of oxygen was observed. This means that the anodic compartment can be considered as anoxic environment. Also, pH of the solution in the MFCwas monitored continuously and adjusted to 7-7.2 using buffer solution. MFC system was operated at a temperature range of 28-30 ^{o}C.

2.5 Analytical Techniques and Calculations

2.5.1 Wastewater and treated effluent analysis

Chemical oxygen demand (COD), dissolved oxygen (DO), pH and TDS tests were conducted by the researcher on a daily basis. Other tests such as nitrate, sulphate, chloride and phosphate were carried out weekly according to the procedure outlined in the standard methods, **,APHA, 2005.** Instruments and measuring devices used in this study were; COD reactor (model: RD 125, Lovibond, Germany), COD photometer (model: multi direct, Lovibond, Germany), dissolved oxygen meter (model: senso direct oxi 200, Lovibond, Germany), pH meter (model: portable HI-83141, HANNA, Romania), electrical conductivity meter (model: portable HI-99300, HANNA, Romania), voltage data logger (model: Lascar EL-USB-3, USA), multimeter (model: 175 TRUE RMS, FLUKE, USA), variable peristaltic pump (model: 77200-62 Cole-Parmer, USA), air pump (model Rs-610 China), and resistance box (100-10000 Ohm).

2.5.2 Power density

Power density is the product of voltage and current per unit of anode surface area, **Liu et al, 2005.**

$$P = \frac{V_{Cell*I}}{A_{An}} = \frac{(V_{Cell})^2}{R_{ext}*A_{An}} \quad (1)$$

$$I = \frac{V_{Cell}}{R_{ext}} \quad (2)$$

Where:P= power density (W/m^2), V_{Cell}=cell voltage(Volt), I=current (Amp), R_{ext}=external resistance and A_{An}=Anode surface area(m^2).

2.5.3 Polarization curve

The polarization was used to characterize the current as a function of voltage by changing external resistance (load), a new voltage and current values can be obtained.

3. RESULTS AND DISCUSSION

3.1 COD Removal Efficiency

The profile of COD removal for actual pharmaceutical wastewater is given in **Fig. 2.** The COD removal efficiency was observed for 45 days. A relatively steady state condition was achieved after 20 days. Maximum COD removal efficiency was observed to be 66% with an average of 44%. The organic loading rate was 0.563 kg/m^3/d. Fluctuation in COD removal efficiencies were attributed to the variation of inlet COD in the real wastewater from the source most likely due to unstable operational conditions at the pharmaceutical manufacturing plant. Results of COD removal efficiency for MFC were 3 times higher than COD removal efficiency of 23% which was previously reported by **Angelov et al., 2013,** for a microbial fuel cell inoculated with sulfate reducing bacteria mobilized on Zeolite bed**.**

3.2 Current Generation

MFC exhibited zero current generation during the first 13 days because the biomass requires an acclimation period, especially to this type of wastewater which can be characterized with recalcitrant nature associated with toxic chemicals and low biodegradability. Rapid increased for the following 4 days up to 172 mA/m^2 maintained for a period of 10 days. However, a notable decline in the generated current was observed upto 32 days of continuous operation, generated current stabilized at 30 mA/m^2 until the end of operation as given in **Fig. 3.** The open circuit voltage drop was 0.46 Volt across an external resistance of 100 Ω as shown in **Fig. 4.**

3.3 Polarization Curve

It summarized the behavior of microbial fuel cell at various external resistances ranged from 50-3000 Ω as depicted in **Fig. 5**. Maximum power and current densities were 2.4 mW/m^2 and 10mA/m^2, respectively obtained at external resistance of 1400 Ω. However, these results were potentially favorable compared to current densities observed at a range of 0.008-0.3 mA/m^2 as previously reported by **Niessen et al.,** and **,Liu et al., 2009,** for MFCs operated with starch, and glucose as substrates, respectively.

4.CONCLUSIONS

This study evaluated the performance of an upflow dual chambered microbial fuel cell for simultaneous pharmaceutical wastewater treatment and power generation. Significant relationship between COD removal and power generation was obtained. Higher COD removal efficiency up to 66% and current density 172 mA/m^{2}were obtained. A drop in voltage can be attributed to the increase of TDS concentration as a result of zeolite existence and expected release of ions such as sodium ions which inhibit and hinder biofilm growth because strong electrolyte alters the osmotic pressure of bacterial cell membrane. It is recommended to regenerate the zeolite bed to decrease TDS concentration of anolyte resulting in a better microbial biofilm growth.

REFERENCES

- Allen, R. M. and Bennetto, H.P., 1993, *Microbial Fuel Cells: Electricity Production From Carbohydrates*. Applied Biochemical Biotechnology. 39, 27-40.
- Angelov, A. Bratkova, S. and Loukanov, A.,2013, *Microbial Fuel Cell Based on Electroactive Sulfate-Reducing Biofilm.* Energy Conversion and Management. 67, 283-286.
- APHA ,2005, *Standard Methods for Examination of Water and Wastewater*. American Public Health Association. 20th ed. Washington, DC
- Benitez, J., Rodriguez, A. and Malaver, R. ,1995, *Stabilization and New Dewatering of Wastewater Using Hollow Fiber Membrane. Water* Science Technology. *29*: 2281-2286
- Davis, M.L. and Cornwell, D.A. ,2008, *Introduction To Environmental Engineering*, 4thed, McGraw Hill Inc.
- Ghangrekar, M. M., Joshi, SG. and Asolekar, S. R., 2005, *Characteristics of Sludge Developed Under Different Loading Condition During UASB Reactor Start-Up*. Water Research. 39, 1123-1133.
- Karra, U., Manikam, S. S., Jeffrey, R. M., Patel, N. and Li, B., 2013, *Power Generation and Organics Removal from Wastewater Using Activated Carbon Nanofilter (ACNF) microbial fuel cell.International* Journal of Hydrogen Energy. 38, 1588-1597.
- Kim, I.C., Jung, Y.C., Choi, M.J. and Verstraete, W., 2008, *Microbial Fuel Cell: Recent Advances, Bacterial Communities and Application Beyond Electricity Generation.* Environmental Engineering Research. 13, 51-65.
- Lewis, N. S. and Nocera, D.G.,2006, *Powering the Planet: Chemical Challenges in Solar Energy Utilization.* PNAS 10343,15729-15735.
- Liu, Z., Liu, J., Zhang, S. and Su, Z., 2009, *Study of Operational Performance and Electrical Response on Mediator-Less Microbial Fuel Cells Fed with Carbon and Protein-Rich Substrate.* Biochemical Engineering Journal. 45, 185-191.

- Lovley, D. R., 2006, *Harvesting Electricity with Microorganisms*, National Research of Microbiology, 4,497-508.
- Niessen, J., Schroder, U. and Scholz, F., 2004, *Exploiting Complex Carbohydrates for Microbial Electricity Generation, Bacterial Fuel Cell Operating on Starch*, Electrochemical Community. 6, 955-958.
- Rabaey, K. and Verstraete, W., 2005, Microbial Fuel Cells: *Novel Biotechnology for Energy Generation.* Trends of Biotechnology. 23, 291-298.
- Zhang, F., Ahn, Y. and Logan, B. E.,2014, *Treating Refinery Wastewaters in Microbial Fuel Cells Using Separator Electrode Assembly or Spaced Electrode Configurations*. Bioresources Technology. 152, 46-52.

Table.1 Characteristics of actual pharmaceutical wastewater.

Constituent	Average value	Units
Biological oxygen demand (BOD_5)	40	mg/L
Chemical oxygen demand (COD)	810	mg/L
Total suspended solids (TSS)	118	mg/L
Total dissolved solids (TDS)	355	mg/L
pH	7.27	------
Chlorides (Cl^-)	10	mg/L
Sulphate(SO_4^{-2})	138	mg/L
Nitrate (NO_3^-)	7.23	mg/L
Phosphate (PO_4^{-3})	2.13	mg/L
Zinc	Nil	mg/L
Chromium	0.05	mg/L
Copper	0.37	mg/L

Figure. 1. Microbial fuel cell system.

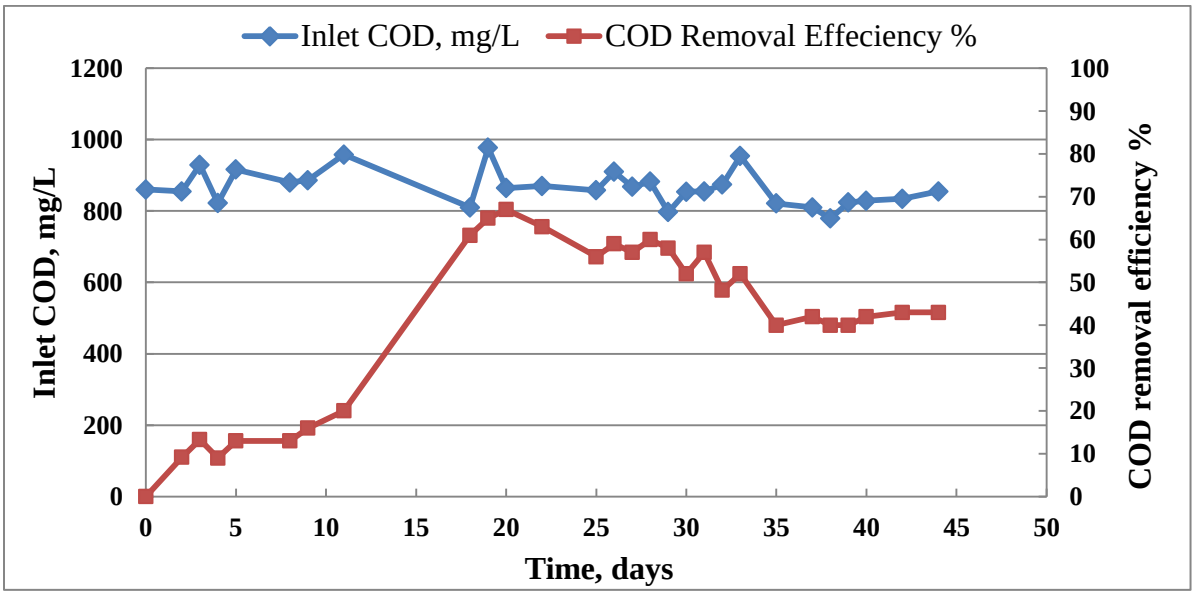

Figure 2. Profile of COD removal.

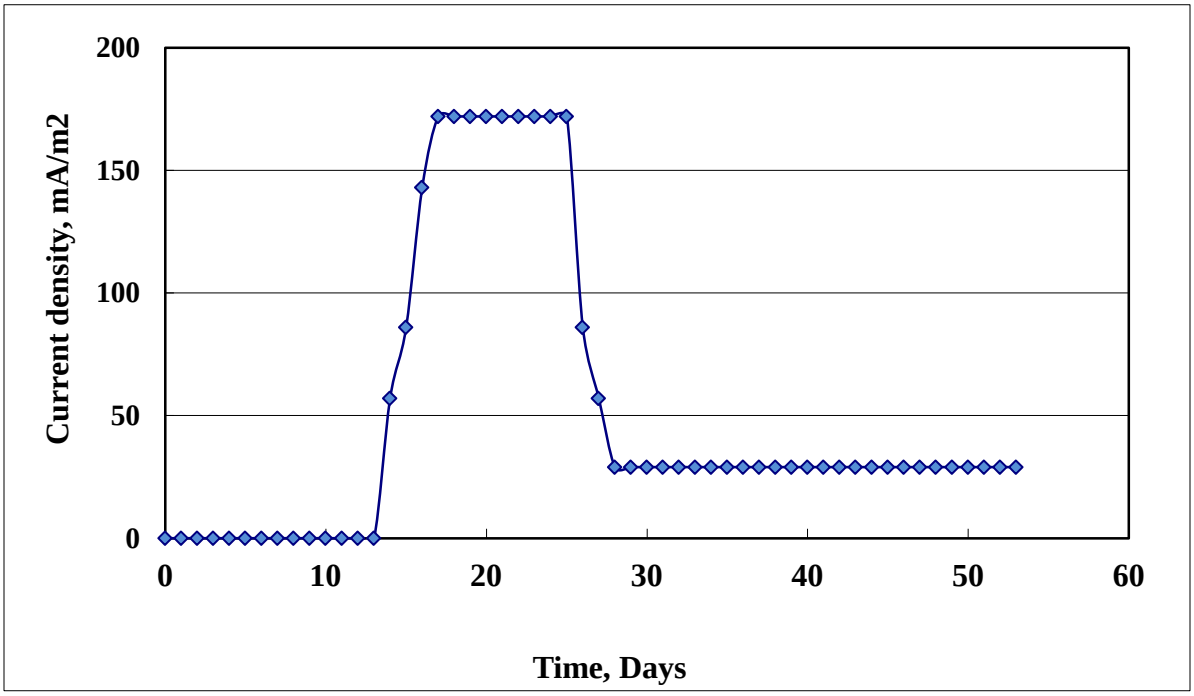

Figure 3. Profile **o**f **c**urrent generation.

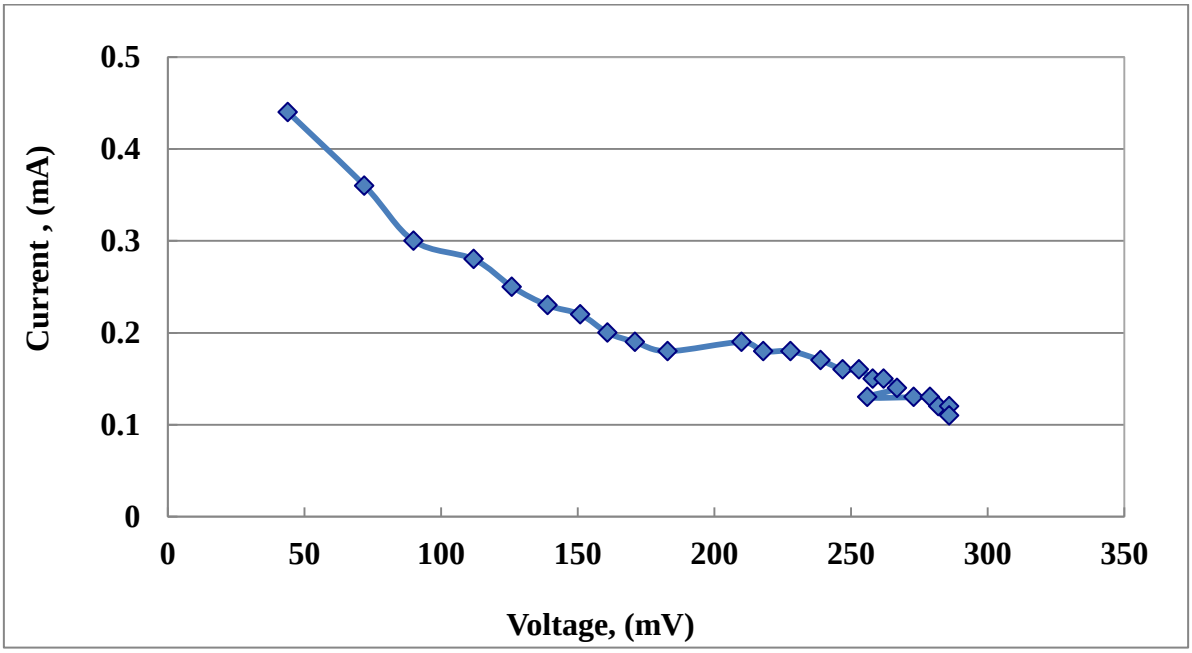

Figure 4. Current-voltage relationship at different resistances.

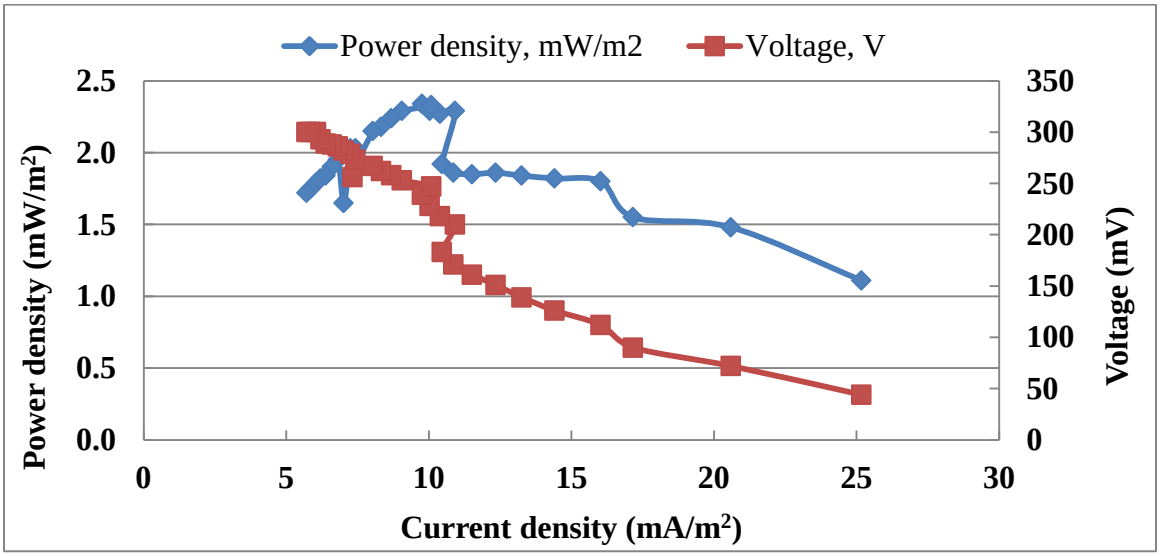

Figure 5. Profile **o**f polarization curve.

Enhancing the Performance of Piezoelectric Energy Harvesters Using Permanent Magnets

Instructor Dr. Waleed Al-Ashtari
Department of Mechanical Engineering
College of Engineering
University of Baghdad
Email: waleedalashtari@yahoo.com

ABSTRACT

A cantilevered piezoelectric beam with a tip mass at its free end is a common energy harvester configuration. This paper introduces a new principle of designing such a harvester which increases the generated voltage without changing the natural frequency of the harvester: The attraction force between two permanent magnets is used to add stiffness to the system. This magnetic stiffening counters the effect of the tip mass on the natural frequency. Three setups incorporating piezoelectric bimorph cantilevers of the same type in different mechanical configurations are compared theoretically and experimentally to investigate the feasibility of this principle. Theoretical and experimental results show that magnetically stiffened harvesters have important advantages over conventional setups. They generate more voltage and they can be tuned across a wide range of excitation frequencies.

Key words: piezoelectric bimorph, frequency tuning, generated voltage, magnetic stiffinig.

تحسين اداء حاصدات الطاقة الكهروضغطية باستخدام مغانط ثابتة

المدرس د. وليد خالد خيري الاشتري
قسم الهندسة الميكانيكية
كلية الهندسة / جامعة بغداد

الخلاصة

ان الهيكل الاكثر شيوعا لعمل حاصدة طاقة كهروضغطية هوعتبة من ماده كهروظغطية مثبتة من جانب واحد و تحمل كتلة على الجانب الحر. في هذا البحث تم تقديم مفاهيم جديدة لانتاج هكذا حاصدات حيث يتم زيادة الفولطية المتولدة بدون تغيير التردد الطبيعي الذي عنده تعمل الحاصدة بكفاءة. ويتم ذلك من خلال استخدم قوة الجذب بين مغناطيسيين لاضافة متانة الى الحاصدة وبذلك يلغى تاثير الكتلة الموضوعه على الجانب الحر على التردد الطبيعي للحاصدة. تم تصنيع و فحص ثلاثة نماذج مختلفة من الحاصدات الكهروضغطية. تم مقارنة اداء هذه الحاصدات نظرياً و عملياً و تبين ان الحاصدات التي تعمل بالمفاهيم الجديدة تستطيع ان تولد فولطية اعلى و كذلك تلك الحاصدات ممكن توليفها لتعمل بكفاءة لمدى من الترددات المسلطة.

الكلمات الرئيسية: عتبة كهروضغطية, توليف التردد, الفولتية المتولدة, التاثير المغناطيسي

1. INTRODUCTION

Energy harvesting or scavenging are two terms commonly describing process for obtaining useful electrical power from the available energy in the environment. There are three main techniques for energy harvesting: vibration harvesting, thermal harvesting and solar harvesting.

Piezoelectric material is one of three general vibration-to-electric energy conversion mechanisms, the other two are electrostatic and electromagnetic transduction **,Williams and Yates, 1996.** Literature of the last few years showed that piezoelectric transduction had received most attention in powering electronic circuits; numerous scientific journals and conferences are due to this subject. The main reason why piezoelectric transducers are preferred for mechanical

to electrical energy conversion is that their energy density is three times higher the density obtained from electrostatic or electromagnetic transduction **,Priya, 2007.**

Energy harvesting using piezoelectric materials is a promising technique, but there are a number of obstacles that currently limit the amount of the generated voltage. One major limitation is due to the necessary frequency matching: The maximum voltage is generated when the natural frequency of the harvester matches the excitation frequency. Manufacturing tolerances, excitation frequency changes and changes of electric load make frequency matching difficult. **Al-Ashtari, 2012a** had developed an analytical model for piezoelectric bimorphs and concluded that manufacturing tolerances lead to a variation of the natural frequency of up to 5%, which cause a considerable drop in power, this drop can be 95% of the generated voltage. Therefore, tuneable harvesters are essential for this technique to be commercially viable.

One technique for harvester frequency tuning is to exploit the magnetic forces between permanent magnets. Literature shows that the attractive magnetic force can be used for enhancing the operation of piezoelectric harvesters. Depending on the magnets separation distance, the alignment, and the orientation, these magnets can effect the harvester stiffness. Literature shows that the magents effect can be modelled as an additional nonconventional spring, which allows to analyse the operation of the system using linear equations, for example, **Challa, et al., 2008. and 2011** fixed two small cylindrical magnets at the free end of a cantilever, one on the top and one on the bottom, and vertically aligned two magnets above and under the first two magnets. They used magnetic repulsion for the lower side and magnetic attraction for the upper side and tuned the harvester by changing the separation distances between these magnets. **Zhu, et al., 2010** used the attraction force between two axially aligned permanent magnets to change the resonance frequency of a cantilever beam in an electromagnetic generator. The opposing faces of the relatively large magnets are curved to maintain a constant separation distance between the two magnets during operation. **Al-Ashtari, 2012b,** introduced a tuning technique using attractive magnetic force acting in longitudinal direction of the cantilever. They presented a comprehensive derivation for modelling the effect of magnetic force as that of a nonconventional spring whose stiffness depends on the nonlinear magnetic force.

Many research projects work on increasing the output power of energy harvesters but most of them focused on developing new or optimised power flow concepts based on modifying the electrical harvesting circuit such as **Ottman, et al., 2002 ,Badel, et al., 2006 ,Dicken, et al., 2009** and **,Ramadass and Chandrakasan 2010.** In contrast, a view number of researches had been conducted to investigate the increasing the generated power from manipulating the mechanical characterstics of the harvester such as the mass or stiffness.

Many physical models had been introduced for predicating the voltage generated across a resistive load connected to piezoelectric harvesters. There are two classes of models; distinguished by the way that physical parameters are handled: Models with distributed parameters and models with lumped parameters.

Models with distributed parameters are based on Euler-Bernoulli beam theory. These models evaluate the physical equations along the whole length of the beam. They generally give more accurate results than lumped parameters models, but involve complicated mathematics and long mathematical expressions. Such models have for example been used by **,Lu, et al., 2004 ,Chen, et al., 2006 ,Lin, et al., 2007** and **Erturk and Inman, 2008.** Discretization of a model with distributed parameters leads to a lumped parameters model. Such models can be considered a less accurate approximation of the distributed parameters, but they are accurate enough for many applications. They also provided an explicit understanding of the operation of piezoelectric harvesters and can be handled with circuit theory by applying electro-mechanical analogies. This

motivated **Erturk, and Inman, 2008,** to use their model with distributed parameters for deriving a correction factor for the lumped parameters model by **du Toit, et al., 2005** in order to improve its accuracy. Many researchers had used lumped parameters for modelling piezoelectric harvesters, for example **Roundy, et al., 2003 ,Sodano, et al., 2004 ,du Toit, et al., 2005 ,Shu, and Lien, 2006 ,Richter, et al., 2006 ,Twiefel, et al., 2007** and **Richter, 2010.**

In this contribution, it will be shown that the configuration introduced by **Al-Ashtari, 2013.** cannot only be used for tuning the frequency of energy harvesters over a wide range but that it can also significantly increase the harvested electrical power. The concept for power increasing introduced in this paper is based on manipulating mass and stiffness, i.e. mechanical quantities of the harvester. A new harvester configuration in which a tip mass is combined with magnetic stiffening has been developed. This allows increasing the power of energy harvesters without changing their efficient operation frequency. Compared to a simple cantilever beam this structure has two important advantages: It shows a considerable increase of the generated voltage and its natural frequency can be tuned over a wide range of frequencies.

Also in this paper, a model of lumped parameters for piezoelectric energy harvesters with and without magnetic stiffening is introduced. This model is described by simple mathematical expressions and gives fairly accurate results. This allows further development and optimization of piezoelectric harvesters.

Three setups incorporating piezoelectric bimorph cantilevers of the same type are compared due to theoretical and experimental results: One bimorph is unmodified,called reference setup; and the other two bimorphs have tip masses of different size, reducing their natural frequencies. These bimorphs are additionally stiffened to compensate the drop of the natural frequency caused by the tip masses. All bimorphs were excited at constant base velocity amplitude and tested for different resistive loads and excitation frequency.

Theoretical and experimental results show that magnetically stiffened harvesters have important advantages over conventional setups: They generate more voltage due to increasing the strain in the piezoelectric transducer and they can be tuned across a wide range of excitation frequencies. The high power output, tunability and good efficiency make magnetically stiffened harvesters a very promising option for future energy harvesting applications.

2. PIEZOELECTRIC HARVESTER MODELLING

A typical piezoelectric energy harvester is a cantilever beam consisting of a shim layer and one or two layers of piezoelectric ceramic. Often a tip mass M_t is attached to the free end of the cantilever to reduce the natural frequency and increase the deflection of the beam. The cantilever is attached to a vibrating host structure, generating an alternating voltage output $u(t)$ for powering an electric load R_l as shown in **Fig. 1**. For the following investigation, the electric load R_l is assumed to be purely resistive. $v_b(t)$ Is the velocity of the base excitation and $v_t(t)$ is the velocity of the cantilever tip. The relative velocity $v(t)$ describes the beam deflection and is expressed as

$$v(t) = v_t(t) - v_b(t) \tag{1}$$

The piezoelectric harvester is an electromechanical device with both mechanical and electrical characteristics. For system analysis and optimization it is convenient to introduce a single domain representation of the electromechanical system applying electromechanical analogies. **Fig. 2** shows the lumped parameters electrical equivalent system similar to the one used by **Richter, 2010.** Comparing to the model by **Roundy, 2003** this model allowed non-zero base velocities.

The mechanical parameters of the model are the equivalent mass M, the equivalent mechanical damping B, and the equivalent mechanical stiffness K. The parameters describing the electrical properties are the capacitance C_p, the electric load R_l and the generated voltage $u(t)$. $i(t)$ Is the current flowing through the load and α is the transfer factor between the mechanical and the electrical domain. For the investigations documented in this paper, the analytical model introduced by **Al-Ashtari, 2012a** had been used for calculating the aforementioned quantities from geometry and material parameters.

A physical model of the energy harvester is used to calculate the characteristics of the energy harvester such as input and output power, and vibration amplitude. This model can also be used to design and optimise energy harvesters. The derivation of the model starts with the governing equation of the piezoelectric harvester **,Al-Ashtari, 2013.**

$$M\dot{v}_t(t) + Bv(t) + K\int v(t)dt = -\alpha u(t) \tag{2}$$

After subtraction of $M\dot{v}_b(t)$ on both sides of Eq. (2), it leads to

$$M\dot{v}(t) + Bv(t) + K\int v(t)dt = -M\dot{v}_b(t) - \alpha u(t). \tag{3}$$

For the electrical system shown in **Fig. 2** the following equations are found:

$$C_p\dot{u}(t) - \alpha v(t) = -i(t) \tag{4}$$

$$u(t) = R_l i(t) \tag{5}$$

Laplace transformation of Eqs. (3), (4) and (5) at zero initial conditions results in:

$$\left(Ms + B + \frac{K}{s}\right)V(s) = -MsV_b(s) - \alpha U(s) \tag{6}$$

$$C_p sU(s) - \alpha V(s) = -I(s) \tag{7}$$

$$U(s) = R_l I(s) \tag{8}$$

where $V_b(s)$, $V(s)$, $U(s)$ and $I(s)$ are the Laplace transforms of base and relative velocity, generated voltage and output current, respectively. Based on Eqs. (6), (7), and (8) the following equation can be determined

$$\frac{U(s)}{V_b(s)} = -\frac{\alpha R_l M s^2}{MC_pR_ls^3 + \left(M + BC_pR_l\right)s^2 + \left(B + KC_pR_l + \alpha^2R_l\right)s + K}\ . \tag{9}$$

The sinusoidal transfer function is

$$\frac{U(j\omega)}{V_b(j\omega)} = \frac{\alpha R_l M\omega^2}{\left[K - \left(M + BC_pR_l\right)\omega^2\right] + j\left[\left(B + KC_pR_l + \alpha^2 R_l\right)\omega - MC_pR_l\omega^3\right]}. \tag{10}$$

In terms of natural frequency ω_n and damping ratio ζ it can be written as

$$\frac{U(j\omega)}{V_b(j\omega)} = \frac{\alpha R_l}{\left[\frac{\omega_n^2}{\omega^2} - 2\zeta C_pR_l\omega_n - 1\right] + j\left[2\zeta\frac{\omega_n}{\omega} + \frac{C_pR_l}{\omega}\left(\omega_n^2 - \omega^2 + \frac{\alpha^2}{MC_p}\right)\right]} \tag{11}$$

where

$$\omega_n = \sqrt{\frac{K}{M}} \tag{12}$$

And

$$\frac{B}{M} = 2\zeta\omega_n\,. \tag{13}$$

According to the equivalent electrical circuit in **Fig. 2** , the ratio $U(s)/V_b(s)$ represents an impedance, called the electromechanical impedance of the piezoelectric harvester in the following. If the base excitation velocity is given by

$$v_b(t) = V_b \sin\omega t \tag{14}$$

where V_b is the base velocity amplitude, the generated voltage will be

$$u(t) = U\sin\left(\omega t + \varphi_{u-v_b}\right) \tag{15}$$

with the voltage amplitude

$$U = \frac{\alpha R_l V_b}{\sqrt{\left[\frac{\omega_n^2}{\omega^2} - 2\zeta C_pR_l\omega_n - 1\right]^2 + \left[2\zeta\frac{\omega_n}{\omega} + \frac{C_pR_l}{\omega}\left(\omega_n^2 - \omega^2 + \frac{\alpha^2}{MC_p}\right)\right]^2}} \tag{16}$$

and the phase difference between voltage and base velocity

$$\varphi_{u-v_b} = -\tan^{-1}\left(\frac{2\zeta\frac{\omega_n}{\omega} + \frac{C_pR_l}{\omega}\left(\omega_n^2 - \omega^2 + \frac{\alpha^2}{MC_p}\right)}{\frac{\omega_n^2}{\omega^2} - 2\zeta C_pR_l\omega_n - 1}\right). \tag{17}$$

the amplitude of the relative velocity $\hat{v}$ can be calculated from Eqs. (6), (7), and (8), thus

$$\frac{V(s)}{V_b(s)} = -\frac{Ms^2\left(C_pR_ls+1\right)}{MC_pR_ls^3+\left(M+BC_pR_l\right)s^2+\left(B+KC_pR_l+\alpha^2R_l\right)s+K} \quad , \tag{18}$$

which, following Eqs. (12) and (13), can be written in terms of natural frequency and damping ratio as

$$\frac{V(j\omega)}{V_b(j\omega)} = \frac{1+jC_pR_l\omega}{\left[\frac{\omega_n^2}{\omega^2}-2\zeta C_pR_l\omega_n-1\right]+j\left[2\zeta\frac{\omega_n}{\omega}+\frac{C_pR_l}{\omega}\left(\omega_n^2-\omega^2+\frac{\alpha^2}{MC_p}\right)\right]}. \tag{19}$$

Thus, if the relative velocity is expressed as:

$$v(t) = V\sin\left(\omega t+\varphi_{v-v_b}\right), \tag{20}$$

its amplitude can be written as

$$V = \frac{V_b\sqrt{1+\left(C_pR_l\omega\right)^2}}{\sqrt{\left[\frac{\omega_n^2}{\omega^2}-2\zeta C_pR_l\omega_n-1\right]^2+\left[2\zeta\frac{\omega_n}{\omega}+\frac{C_pR_l}{\omega}\left(\omega_n^2-\omega^2+\frac{\alpha^2}{MC_p}\right)\right]^2}} \tag{21}$$

and the phase difference between the two velocities is described by

$$\varphi_{v-v_b} = \tan^{-1}\left(C_pR_l\omega\right)-\tan^{-1}\left[\frac{2\zeta\frac{\omega_n}{\omega}+\frac{C_pR_l}{\omega}\left(\omega_n^2-\omega^2+\frac{\alpha^2}{MC_p}\right)}{\frac{\omega_n^2}{\omega^2}-2\zeta C_pR_l\omega_n-1}\right]. \tag{22}$$

The amplitude of the beam deflection, which is a measure for the strain inside the bimorph, is expressed as

$$X = \frac{V}{\omega} \tag{23}$$

3. MAGNETIC STIFFENING TECHNIQUE

It can be deduced from simulating Eq.(16) that the output voltage can be increased by increasing the equivalent mass M or the natural frequency ω_n. A conventional method is to add a mass to the tip of the cantilever. This also reduces the resonance frequency of the harvester and can therefore not increase the harvested power effectively. This paragraph introduces a new configuration of a piezoelectric harvester, which increases the power of energy harvesters without changing their natural frequency. This is achieved by adding a tip mass and compensating the drop in natural frequency by an additional stiffness. The technique increases the harvested power for a given volume of piezoelectric material, keeping frequency and strain constant. If desired, the strain of the piezoelectric transducer can additionally be increased, leading to an even larger power increase.

The power increasing technique is based on the magnetic tuning method introduced by **Al-Ashtari, 2012b.** If the tip mass of a setup as shown in **Fig. 1** is replaced by a magnet and a

second magnet is attached to the vibrating structure as shown in **Fig. 3**, the resonance frequency of the harvester can be adjusted by changing the distance d between the magnets. If this technique is used to increase the resonance frequency of the harvester to match the resonance frequency of the original harvester without tip mass or magnets, the resulting magnetically stiffened harvester uses the same piezoelectric element and has the same resonance frequency, but delivers much more power compared to the original harvester without tip mass.
The equivalent electrical model of the proposed harvester setup is the same as shown in **Fig. 2**, with the value of the motional capacitance decreased to $1/(K+K_M)$ due to the additional "magnetic" stiffness K_M which can be calculated as

$$K_M = \left(\frac{15}{14l} + \frac{1}{d}\right) F_M \,, \tag{24}$$

where l is the length of the vibrating beam, d is the distance between the magnets, and F_M is the magnetic force which is a nonlinear function of magnet properties and separation distance. These parameters are constant during harvester operation. Details on the harvester model, the derivation of above formula, and the nonlinear calculation of the magnetic force can be found in **Al-Ashtari, 2012b.**

4. EXPERIMENTAL SETUP

Three different harvester setups are investigated experimentally, all using the same type of piezoelectric bimorph, Piezo Bending Actuators 427.0085.11Z" from Johnson Matthey. The specifications of the birmophs are given in **Table 1**. Their vibrating length is about 40 mm in the experiments.
As tip masses and for the magnetic stiffening, two types of neodymium magnets from HKCM Engineering were used, Q08.5x02x01.5Ni-48H with a mass of 0.19 g, and Q10x04.5x04.5Ni-N52 with a mass of 1.51 g.
The characteristics of the harvester setups are summarized in **Table 2**. While "reference setup" refers to the original cantilever beam without any mass or magnetic stiffening, "stiffened setup 1" refers to the cantilever beam with smaller magnet as a tip mass and magnetic stiffening. finally, stiffened setup 2" refers to the cantilever beam with larger magnet as a tip mass and magnetic stiffening.
The mechanical quality factor Q_m of the piezoelectric harvester for each setup can be identified by measuring the frequency sweep of the electrical admittance. A typical frequency sweep of a piezoelectric harvester is shown in **Fig. 4**.
From **Fig. 4**, the mechanical quality factor Q_m can be calculated as **,Zickgraf, 1996.**

$$Q_m = \frac{f_r}{f_2 - f_1} \,. \tag{25}$$

The frequency sweep of the electrical admittance of each setup was obtained using impedance analyzer type HP 4192A.
Fig. 5 schematically shows the experimental setup used in this paper. The harvesters are excited by an electro-dynamic shaker. The base velocity is monitored using a laser vibrometer and the amplitude of the shaker voltage is manually adjusted to achieve the desired amplitude of the base velocity. The harvester base frame is rigid compared to the bimorph structure, so that the measured velocity at any location on the base frame is the same.

The experimental setups with tip masses are similar to the ones depicted in **Figs. 1** and **3**, respectively. For technical reasons, the larger magnet has not been glued to the face of the bimorph but on top of it, aligned with the face. This reduces the free vibrating length of the bimorph assumed in the calculations by the width of the magnet. **Fig. 6** shows this setup.
In the experiments, the harvesters are excited by an electro-dynamic shaker. The base velocity is monitored using a laser vibrometer and the amplitude of the shaker voltage is manually adjusted to achieve steady base velocity amplitude. The harvester base frame is designed to be rigid compared to the bimorph structure, so that the measured velocity at any location on the base frame is the same. For measuring the beam deflection, a differential laser vibrometer is used with one beam pointed to the tip mass and the other pointed to the base frame.
It is well known that the power generated by a piezoelectric energy harvester is highly load-dependent. The output terminals of the bimorphs are therefore connected to a resistor decade to investigate the influence of the load. The load is varied between 100 Ω and 10 MΩ. The base velocity is kept constant for all loads and the steady-state amplitudes V of the beam velocity and U of the generated voltage across the load are measured.

5. RESULTS AND DISCUSSION

Figure 7 compares the theoretically and experimentally determined generated voltage of the different setups with a common resonance frequency of 250 Hz: Reference setup, stiffened setup 1 and stiffened setup 2. It is obvious that the magnetically stiffened harvesters generate much more voltage than the reference setup especially at high load resistance. Stiffened setup 2 with a larger tip mass and accordingly larger additional stiffness generates more voltage than stiffened setup 1.
The deflection of the bimorph tip is proportional to the strain inside the bimorph and as such is relevant for determining the lifetime and maximum allowable excitation amplitude. **Fig. 8** shows the corresponding deflection of the three setups. As expected, a larger tip mass leads to a larger deflection of the bimorph. The maximum deflection of stiffened setup 2 is more than 2.1 times the maximum deflection of the reference setup, and thus the generated voltage increased by the same factor.
Fig. 9 compares also the theoretically und experimentally determined generated voltage of the different setups with a common resonance frequency of 250 Hz: Reference setup, stiffened setup 1 and stiffened setup 2. These harvesters were tested at open circuit condition. Also, the magnetically stiffened harvesters generate much more voltage than the reference setup. The deflection of each setup is shown in **Fig. 10**.
All figures given above shows that the introduced model gives fairly accurate results. The difference between the simulated and the experimental results ranges from 1% to 3%. One possible reason for getting such deviations is using the lumped-parameter model which lacks the effect of the mode shape i.e. the description of the strain distribution along the beam. Also, assuming that the equivalent damping and the equivalent stiffness are linear can cause inaccurate results, especially if the excitation amplitude is large.

6. CONCLUSION

In this paper, a new principle for increasing the power generated by piezoelectric energy harvesters without changing their resonance frequency has been introduced and investigated. The attraction force between two permanent magnets is used to add stiffness to the system to counter the effect of a tip mass on the resonance frequency. Similar configurations that use the attraction force between two permanent magnets to manipulate the effective stiffness of the harvester have been introduced before tuning the resonance frequency of energy harvesters **,Al-Ashtari, 2012b.**

A physical model for the piezoelectric harvester has been introduced. Different comparisons between theoretical and experimental results show the fair accuracy of the proposed model especially when a tip mass is attached to the harvester.
The magnetically stiffened harvester has important advantages over all other investigated setups with and without tip mass: It generates more voltage and it can be tuned across a wide range of excitation frequencies. These make magnetically stiffened harvesters a very promising option for future energy harvesting applications.

ACKNOWLEDGMENT
The author gratefully acknowledge the support of Prof. Dr. Walter Sextro and the staff at the Chair of Mechatronics and Dynamics / University of Paderborn.

REFERENCES

- Al-Ashtari, W., Hunstig, M., Hemsel, T., and Sextro, W., 2012a, *Analytical Determination of Characteristic Frequencies and Equivalent Circuit Parameters of A Piezoelectric Bimorph*, Journal of Intelligent Material Systems and Structures, Vol. 23, PP. 15-23.

- Al-Ashtari, W., Hunstig, M., Hemsel, T., and Sextro, W., 2012b, *Frequency Tuning of Piezoelectric Energy Harvesters by Magnetic Force*, Smart Mater. Struct., Vol. 21, PP. 035019.

- Al-Ashtari, W., Hunstig, M., Hemsel, T., and Sextro, W., 2013, *Enhanced Energy Harvesting Using Multiple Piezoelectric Elements: Theory and Experiments*, Sensors and Actuators A, Vol. 200, PP. 138-146.

- Badel A., Guyomar D., Lefeuvre E. and Richard C. 2006, *Piezoelectric Energy Harvesting Using Synchronized Switch Technique*" Journal of Intelligent Material Systems and Structures, Vol.17, P.P.831-839.

- Challa V R, Prasad M G, Shi Y, and Fisher F T, 2008, *A Vibration Energy Harvesting Device with Bidirectional Resonance Frequency Tunability*, Smart Materials and Structures, Vol. 17, P.P 015035.

- Challa V R, Prasad M G and Fisher F T, 2011, *Towards an Autonomous Self-Tuning Vibration Energy Harvesting Device for Wireless Sensor Network Applications*, Smart Mater. Struct., Vol. 20, P.P 025004.

- Chen S-N, Wang G-J, and Chien M-C, 2006, *Analytical Modeling of Piezoelectric Vibration Induced Micro Power Generator*, Mechatronics Vol. 16, P.P 387-397.

- Dicken J., Mitcheson P.D., Stoianov I. and Yeatman E.M., 2009, *Increasing Power Output from Piezoelectric Energy Harvester by Pre-Biasing*, PowerMEMS, Washington DC, USA, December 1-4.

- du Toit N. E., Wardle B. L., and Kim S. G., 2005, *Design Considerations for MEMS-Scale Piezoelectric Mechanical Vibration Energy Harvesters*, Integrated Ferroelectrics,

Vol. 71, P.P 121-160.

- Erturk A. and Inman D. J., 2008, *On Mechanical Modeling of Cantilevered Piezoelectric Vibration Energy Harvesters*, Journal of Intelligent Material Systems and Structures, Vol. 19, P.P 1311-1325.

- Lin J. H., Wu X. M., Ren T. L., and Liu L. T., 2007, *Modeling and Simulation of Piezoelectric MEMS Energy Harvesting Device*, Integrated Ferroelectrics, Vol. 95, P.P 128–141.

- Lu F., Lee H., and Lim S., 2004, *Modeling and Analysis of Micro Piezoelectric Power Generators for Micro-Electromechanical-Systems Applications*, Smart Materials and Structures Vol. 13, P.P 57–63.

- Ottman G., Hofmann H., Bhatt A. and Lesieutre G., 2002, *Adaptive Piezoelectric Energy Harvesting Circuit for Wireless Remote Power Supply*, IEEE Transactions on Power Electronics Vol. 17: P.P 669-676.

- Priya S. 2007 "Advances in Energy Harvesting Using Low Profile Piezoelectric Transducers" Journal of Electroceramics 19:165-182

- Ramadass Y. K. and Chandrakasan A. P., 2010, *An Efficient Piezoelectric Energy Harvesting Interface Circuit Using a Bias-Flip Rectifier and Shared Inductor*, IEEE Journal of Solid- State Circuits Vol. 45, No. 1.

- Richter B., Twiefel J., Hemsel T. and Wallaschek J., 2006, *Model Based Design of Piezoelectric Generators Utilising Geometrical and Material Properties*, ASME International Mechanical Engineering Congress and Exposition, November 05-10, 2006, Chicago, Illinois, USA.

- Richter B., 2010, *Modellbasierter Entwurf Resonant Betriebener, Piezoelektrischer Biege Schwinger in Energy Harvesting Generatoren*, Ph.D. Thesis, University of Paderborn. Shaker, Aachen.

- Roundy S., Wright P. K., and Rabaey J., 2003, *A Study of Low Level Vibrations as a Power Source for Wireless Sensor Nodes*, Computer Communications, Vol. 26, P.P 1131–1144.

- Shu Y. and Lien I., 2006, *Analysis of Power Output for Piezoelectric Energy Harvesting Systems*, Journal of Smart Materials and Structures, Vol. 15, P.P 1499–1512.

- Sodano H. A., Park. G., and Inman D. J., 2004, *Estimation of Electric Charge Output for Piezoelectric Energy Harvesting*, Strain, Vol. 40, P.P 49–58.

- Twiefel J., Richter B., Sattel T. and Wallaschek J., 2007, *Power Output Estimation and Experimental Validation for Piezoelectric Energy Harvesting Systems*, Electroceramics, Vol. 20 3-4, P.P 203-208.

- Williams C. B. and Yates R. B., 1996, *Analysis of a Micro-electric Generator for Microsystems*, Sensors and Actuators A, Vol. 52, P.P 8-11.

- Zhu D., Roberts S., Tudor M. J., and Beeby S. P., 2010, *Design and Experimental Characterization of a Tuneable Vibration-Based Electromagnetic Micro-Generator*, Sensors and Actuators A, Vol. 158, P.P 284-293.

- Zickgraf B., 1996, E*rmüdungsverhalten von Multilayer-Aktoren aus Piezokeramik*, Fortschritt-Berichte VDI, Reihe 18, Nr. 191. Düsseldorf: VDI Verlag GmbH.

NOMENCLATURE

B = equivalent mechanical damping of a piezoelectric device, Ns/m
C_p = equivalent capacitance of the piezoelectric material, F
F_M = attraction force between magnets, N
K = equivalent mechanical stiffness of a piezoelectric device, N/m
K_M = equivalent stiffness due magnetic attraction, N/m
M = total equivalent mass of a piezoelectric device, kg
M_t = tip mass attached to the free end of the vibrating beam, kg
Q_M = mechanical quality factor of the piezoelectric device
R_l = connected Resistive load, Ω
U = amplitude of the generated voltage, V
V = amplitude of the piezoelectric cantilever velocity, m/s
X = amplitude of the piezoelectric cantilever displacement, m
d = separation distance between magnets, m
f_r = resonance frequency of the piezoelectric device, Hz
$f_1$and f_2 = frequencies at which the maximum magnitude of the electrical admittance decreases by 3db, Hz
$i(t)$ = current through conncted load , A
l = length of the piezoelectric cantilever, m
t = time, s
$u(t)$ = generated AC voltage of the piezoelectric harvester, V
$v(t)$ = relative velocity equals to $v_t(t) - v_b(t)$, m/s
$v_b(t)$ = excitation velocity of the base of the piezoelectric device, m/s
$v_t(t)$ = tip velocity of the piezoelectric cantilever, m/s
α = conversion factor between the mechanical and electrical domains of a piezoelectric device, N/V
ζ = equivalent damping ratio of the piezoelectric device
φ_{u-v_b} = phase difference between the excitation velocity $v_b(t)$ and the generated voltage $u(t)$, rad
φ_{v-v_b} = phase difference between the excitation velocity $v_b(t)$ and the relative velocity $v(t)$, rad
ω = angular frequency of the excitation, rad/s
ω_n = natural frequency of piezoelectric cantilever, rad/s

Table 1. Bimorph specifications.

Parameter	Value
Total length of piezoelectric layers	45.00 ± 0.1 mm
Beam width	7.20 ± 0.1 mm
Total beam thickness	0.78 ± 0.03 mm
Shim layer thickness	0.28 ± 0.05 mm
Piezoelectric layer density	$8000\ \mathrm{kg/m^3}$
Shim layer density	$1800\ \mathrm{kg/m^3}$
Piezoelectric coupling factor	0.38
Piezoelectric compliance	$15.8 \times 10^{-12}\ \mathrm{m^2/N}$
Piezoelectric dielectric constant	$61.95\ \mathrm{nF/m}$
Beam mechanical quality factor	45
Shim layer modulus of elasticity	$120 \times 10^9\ \mathrm{N/m^2}$

Table 2. Characteristics of harvester setups.

Harvester Type	Tip Mass [g]	Mechanical Quality Factor [-]	Anti-Resonance Frequency [Hz]
Reference Setup	-	45	250
Stiffened Setup 1	0.19	63	250
Stiffened Setup 2	1.51	95	250

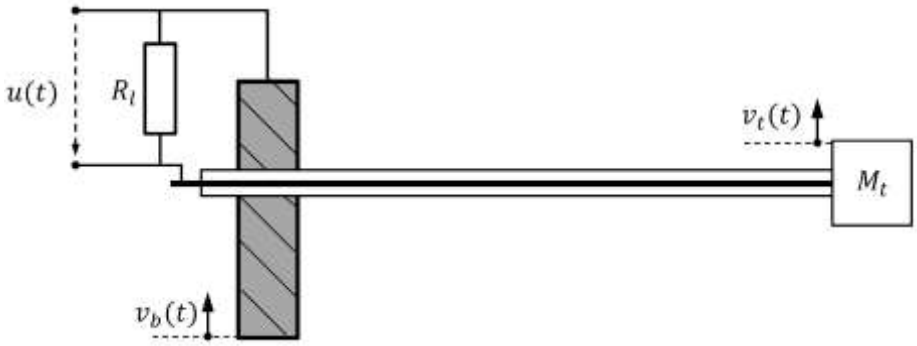

Figure 1. Typical energy harvesting system.

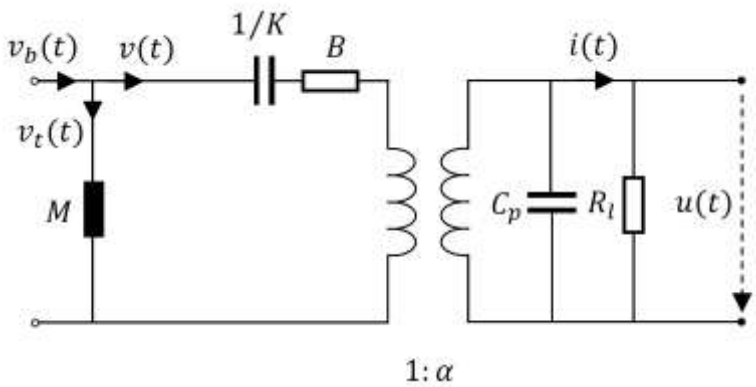

Figure 2. Equivalent electrical model of a base-excited piezoelectric energy harvester.

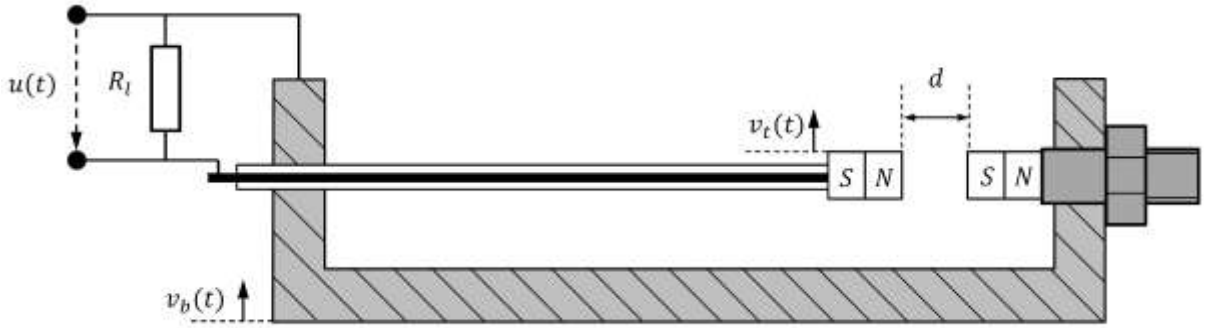

Figure 3. Principle setup of a magnetically stiffened harvester.

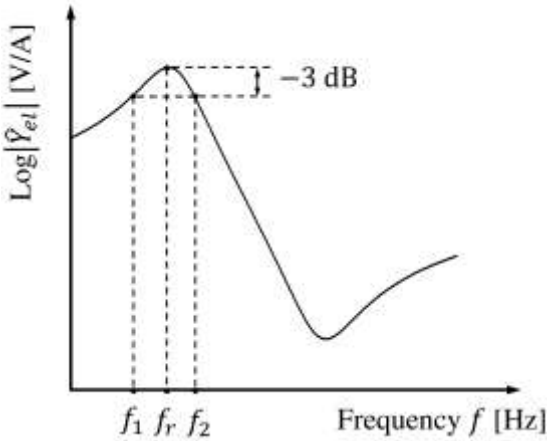

Figure 4. Typical frequency sweep of the electrical admittance of a piezoelectric harvester.

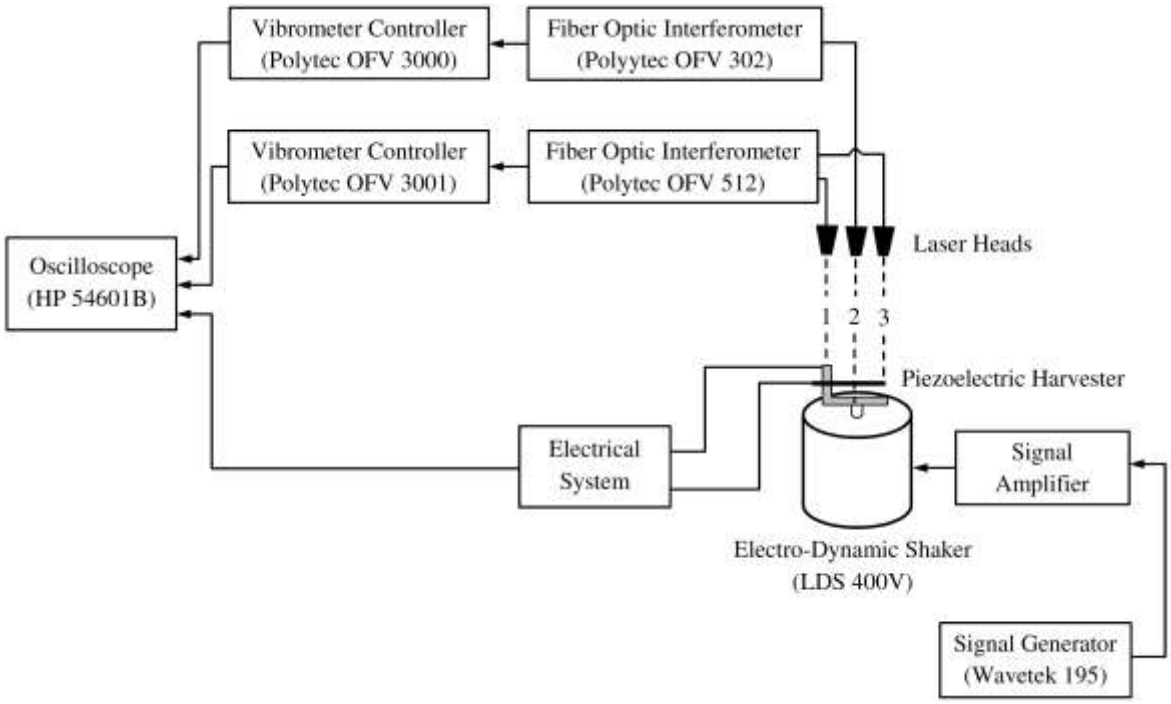

Figure 5. Schematic of the experimental setup.

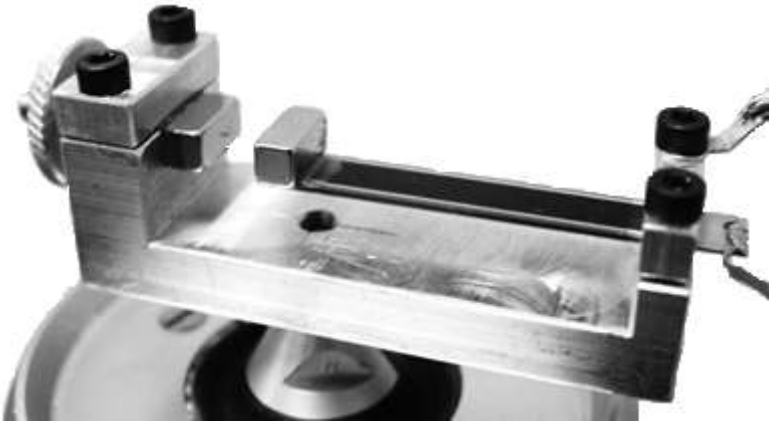

Figure 6. Magnetically stiffened harvester (Stiffened setup 2).

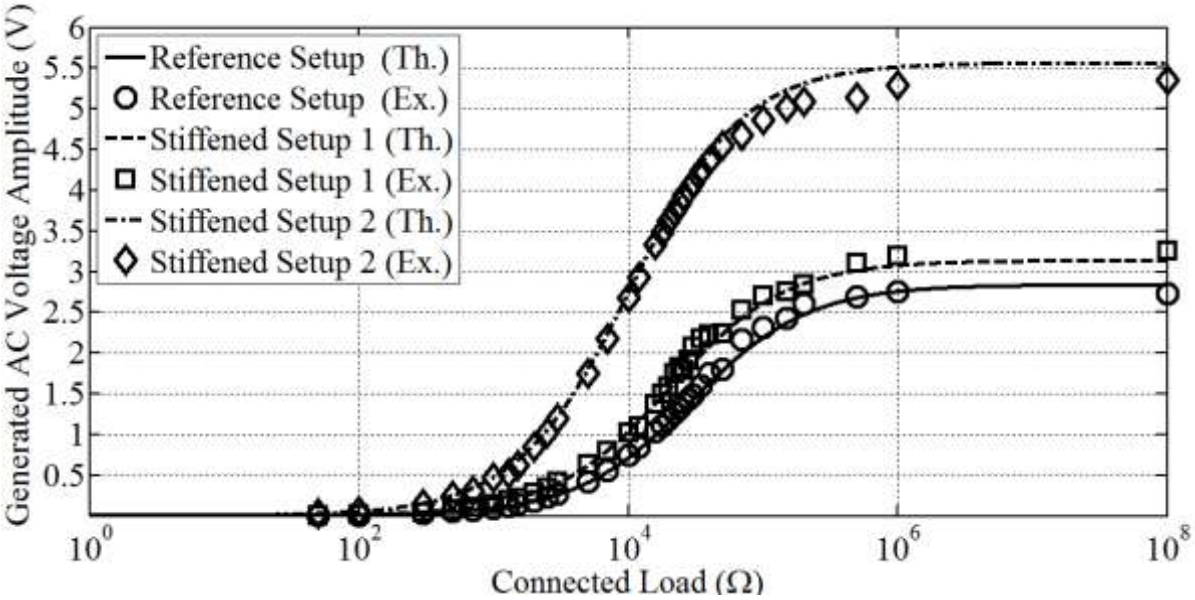

Figure 7. Variation of the generated voltage amplitude versus connected load.

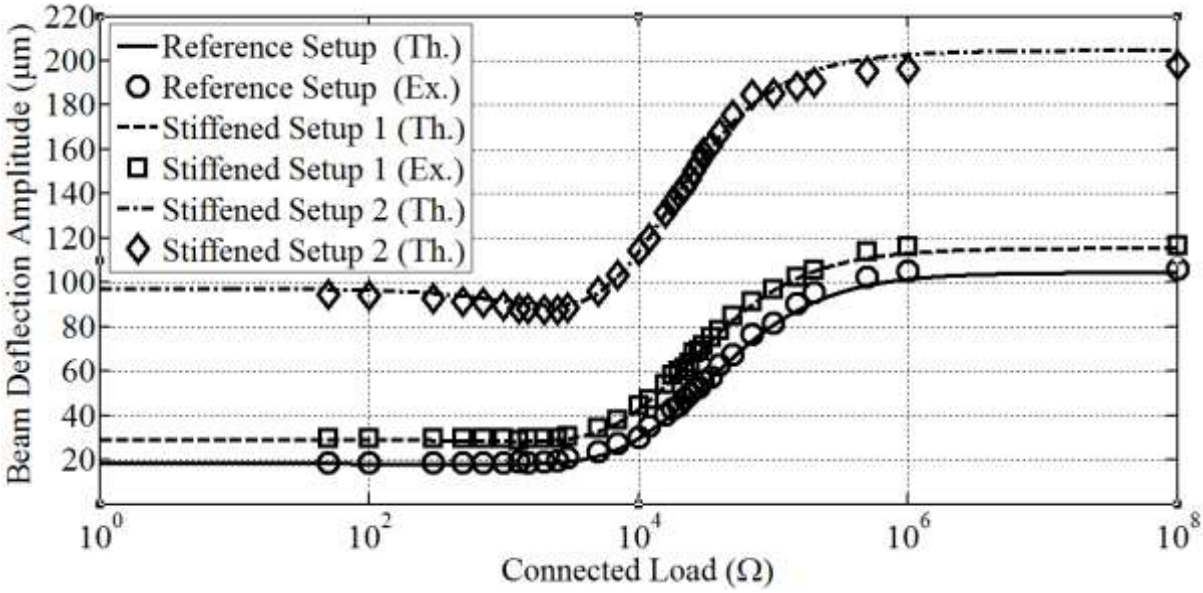

Figure 8. Variation of the beam deflection amplitude versus connected load.

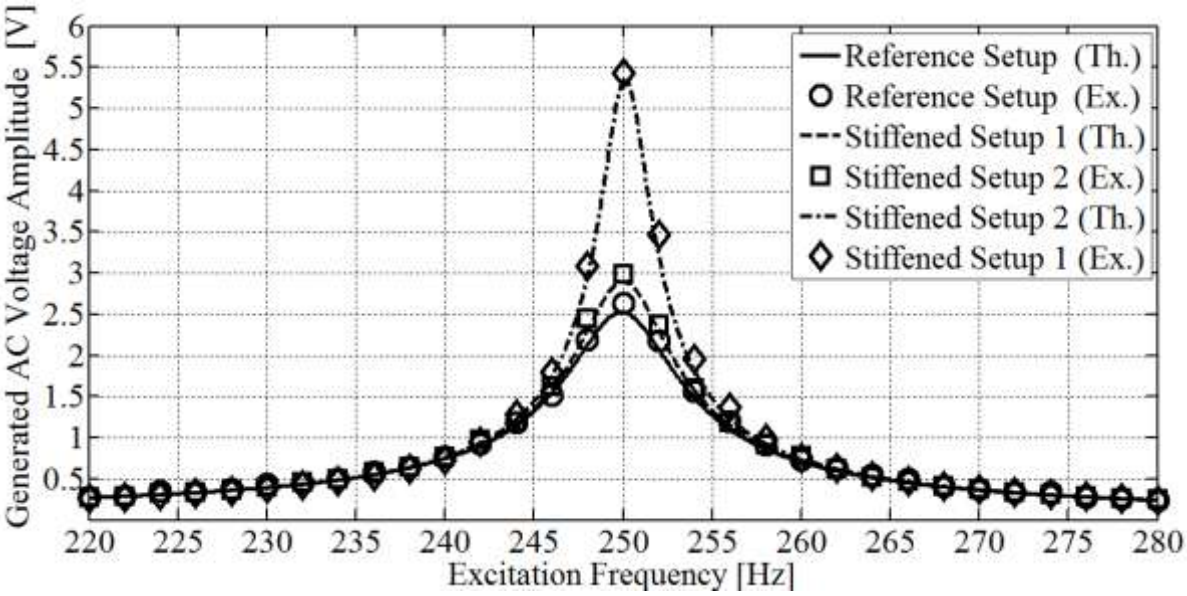

Figure 9. Variation of the generated voltage amplitude versus the excitation frequency (Excited by velocity of amplitude 3.5 mm/sat open-circuited condition.

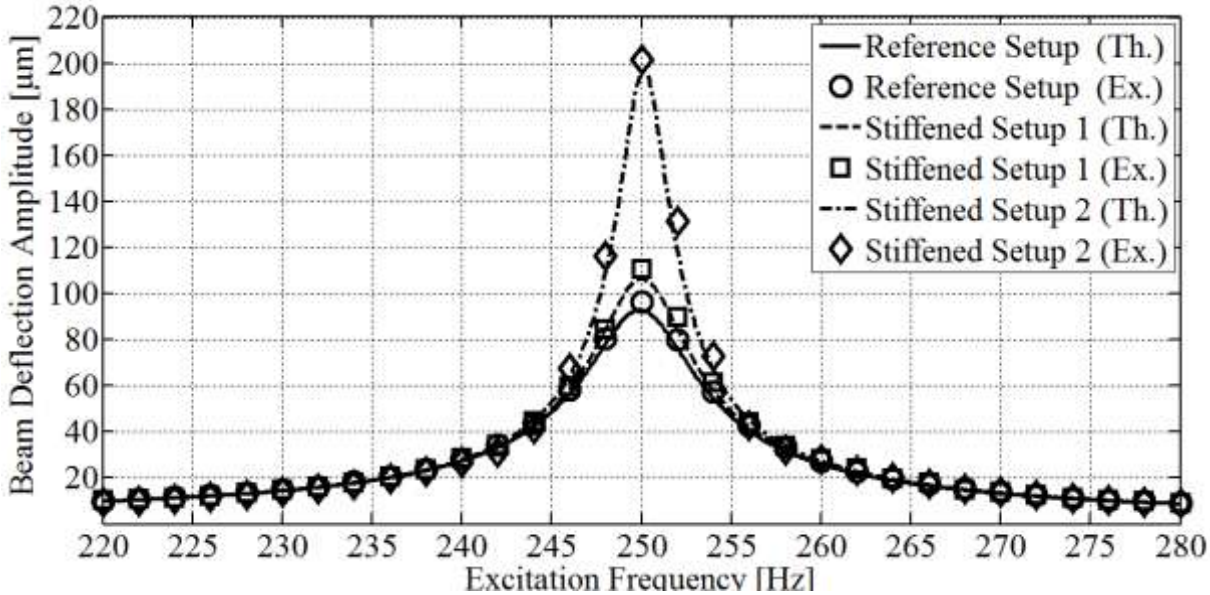

Figure 10. Variation of the generated voltage amplitude versus the excitation frequency (Excited by velocity of amplitude 3.5 mm/s at open-circuited condition.

Effect of Plasma Shot Peening on Mechanical Properties and Fatigue life of AL-Alloys 2024-T3

Prof. Hussain J.M AL-Alkawi
Department of Electromechanic Eng.
University of Technology
Email:alalkawi2012@yahoo.com

Asst. Prof. Dhafir Sadik Al-Fattal
Retired

Lect. Ahmed Adnan AL-Qaisy
Department of Mechanical Eng.
University of Technology
Email:abomrem2004@gmail.com

ABSTRACT

An Investigation of estimated Mechanical Properties of AL-Alloys 2024-T3, which is the most commonly used in industrial applications, been established experimentally. A new novel Plasma Peening techniques had applied for the whole surfaces of the material by CNC-Plasma machine for 48 specimen, and then a new investigation were toke over to figure the amount of change in mechanical properties and estimated fatigue life. It found that improvement was showing a nonlinear behavior according to peening duration time, speed, peening distance, peening number, and amount of effected power on the depth of the material thickness. The major improvement was at medium speed long duration time normal peening distance. Which shows up to 5 times improvements than the others cases. It was found that reducing in elongation of about 32% from references for 1x plasma peening for the most techniques used while a reduction in elongation of 56% for the 2x plasma peening. These results illustrated in both tables and figures. Farther study may established for other AL-Alloys to study the effects of plasma peening on it and to found the most effected one of them for the completely nine AL family.

Key words: plasma peening, mechanical properties, aluminum alloy.
القذف بالبلازما , الخصائص الميكانيكية , سبائك الألمنيوم

تأثير القذف بالبلازما على الخصائص الميكانيكية وعمر الكلال لسبيكة الألومنيوم 2024-T3

أ.د. حسين جاسم العلكاوي
قسم الهندسة الكهروميكانيكية
الجامعة التكنولوجية

أ.م.د ظافر صادق الفتال
متقاعد

م. أحمد عدنان عبدالجبار
قسم الهندسة الميكانيكية
الجامعة التكنولوجية

الخلاصة

يدرس البحث تأثير تقنية جديدة لقذف السطوح عن طريق القذف بالبلازما على الخصائص الميكانيكية وكذلك عمر الكلل لسبيكة الألومنيوم 2024-T3 والتي تعد من أكثر سبائك الألومنيوم استخداماً والأكثر شيوعاً في عمليات انتاج هياكل الطائرات والمركبات والسفن لما تمتلكه من خصائص ممتازة. تم حساب الخصائص الميكانيكية للسبيكة المستخدمة في قسم التقييس والسيطرة النوعية – العراق وتم حساب عمر الكلل الأولي في مختبر مقاومة المواد – قسم الهندسة الكهروميكانيكية – الجامعة التكنولوجية لثمانية وأربعين عينة عملياً. تم تطبيق تقنية جديدة لقذف السطوح عن طريق القذف بالبلازما باستخدام ماكينة قطع بلازما مؤتمتة بعد تحويرها من عملية قطع الى عملية قذف فقط عن طريق تقليل القدرة وتغيير رأس القطع وكذلك مسافة رأس القطع عن العينة وكما سيتم شرح تفاصيل التقنية داخل البحث لاحقاً. تم تطبيق أكثر من تكنيك كون العملية جديدة وغير مسبوقة ولا توجد مصادر معتمدة لكي يتم الاعتماد عليها في عملية القذف بالبلازما كما تم إعادة حساب الخصائص الميكانيكية وعمر الكلل بعد عملية القذف بالبلازما لمعرفة مقدار التغيير فيها. وجد ان هنالك تحسن غير نمطي في بعض الخصائص على حساب خصائص أخرى قد يصل احياناً الى خمسة اضعاف قيمته الأصلية وذلك بحسب التكنيك المستخدم وتم اجراء مقارنة بين تلك الخصائص وعمر الكلل قبل وبعد عملية القذف بالبلازما عن طريق جداول ومخططات مفصلة. وجد ان هنالك انخفاض في معدل الإستطالة يصل الى 32% في حالة القذف لمرة واحدة في حين انه يصل الى 56% في حالة القذف لمرتين. يمكن تجريب هذه التقنية على سبائك أخرى من الألومنيوم لمعرفة مقدار التغيير في خصائصها الميكانيكية وعمر الكلال لها.

1. INTRODUCTION

A traditional surface treatment technique, shot peening (SP), has been effectively and widely applied in industry for over six decades. In traditional SP process, metal or ceramic balls acting as minuscule ball - peen hammers make a small indentation or dimple on the metal surface on impact **Fig.1**. A compacted volume of highly shocked and compressed material can produced below the dimple. Using different types or size of particles will made a different effect on the surface of the material **Fig.2**.

Laser Shock peening is a cold work process, in which the metal part is struck by a high energy pulsed laser beam producing high amplitude stress waves. The surface material resists to stretching induced by the stress waves resulting in a formation of a compression stressed skin. Prior to laser peening the material surface plated with an opaque layer of black paint, metal foil or tape. The black layer then covered with a transparent overlay (commonly flowing water) **Fig.3**.

Plasma is a high-temperature, electrically conductive gas, comprised of positively and negatively charged particles as well as excited and neutral atoms and molecules. A dynamic balance exists between the dissociation, ionization and recombination processes that occur in the plasma state. Thus, the plasma behaves electrically neutral. In physics, plasma referred to as the fourth state of matter. Plasma naturally occurs in the interior of the sun and other stars due to the high temperatures. Lightning is also a natural form of plasma, caused by high electrical field strengths. To produce a technical plasma, a gas is either greatly heated using a heat source or subjected to a strong electrical field in order to transform it into an ionized state.

Plasma technique developed at the end of the 1950s for cutting high-alloy steels and aluminum. It designed to use on all metals that, due to their chemical composition, could not subjected to oxy-fuel cutting. Owing to its extremely high cutting speeds (especially with thin materials) and narrow heat-affected zone, the technique also used today for cutting non-alloy and low-alloy steels. Metal cutting today characterized by high quality demands and increasing cost pressures. The edges of cut parts should not require any further processing and expected to exhibit maximum dimensional accuracy. As a result, the ability of traditional cutting techniques to meet these demands increasingly questioned. Plasma fusion cutting is in direct competition with other techniques such as oxy-fuel cutting, laser cutting and water jet cutting. However, it can also be an alternative to the mechanical processing techniques such as nibbling, punching, drilling, **Linde, 2013.**

Recently plasma arc surface hardening is an alternative selective surface hardening method that is effective, economical and a promising technology in heat treatment industries, many studies for anther application of the plasma technique established to investigate the ability to improve materials both properties and fatigue life by using plasma-peening see **, Petrov, 2007** and **Mohd , 2012.**

2. APPLICATIONS:

This is the most common of the high-strength alloys. Aircraft quality. AL 2024-T3 aluminum sheet is the best choice for the aircraft alloy because of its strength. It has excellent fatigue resistance. Welding generally not recommended. Typical uses for 2024-T3 aluminum sheet are aircraft fittings, gears and shafts, bolts, clock parts, computer parts, couplings, fuse parts, hydraulic valve bodies, missile parts, munitions, nuts, pistons, rectifier parts, worm gears, fastening devices, veterinary and orthopedic equipment, structures aircraft skins, cowls, aircraft structures, and for restoration like airstreams because of its shiny finish. The chemical properties of the AL-Alloys 2024-T3 is as shown in **Table 1 , ASTM standards, 2012.**

3. EXPERIMENTAL WORK:

In this, study a standard tensile test specimen used of standard dimension is as shown in **Fig.6**. Where the gauge length (60 mm), shoulder length (75 mm), (R = 40 mm) for plane sheet spacemen and overall length (165 mm). The tests were taken at the COSQC-Baghdad (Central Organization for Standardization and Quality Control) according to the ISQ (Iraqis Specification Quality) 1473/1989, the tests was included general properties such as hardness, strength, toughness …etc. the results is as shown as in **Table 2.**

Usually most of CNC-Plasma Machine used for cutting materials but the novelty in this study is to use this machine (AJAN CNC-Standard Plasma Cutting Machine) **Fig.7**, to shoot the whole surfaces of the AL-Alloys used with plasma by:

1. Changing the type of nozzle head **Fig.8**. (The machine came with three types of heads one for steel with plasma arc diameter of 5 micron the second for other nonferrous materials of diameter 1 millimeter and the third one is for nonmaterial of diameter 2.5 millimeter so we used the third one).
2. Reducing the power of the plasma arc to quarter of the initial power. (To reduce the heat generation of the plasma arc).
3. Using only three bottles instead of five (Oxygen, Argonne and Nitrogen to reduce the temperature of the plasma arc).
4. Increasing the speed of head movement twice of the usual speed. (To decrease the effective time of plasma on the surface).
5. Increasing the distance between the materials sheet and the head of the plasma machine twice to three times the usual distance. (To reduce the effects of plasma arc on the surface).

According to above we toke the 48 spacemen and divided them into three groups of 16 specimen each, 8 spacemen were shouted by plasma for one time, while the other 8 shouted twice, then we take the next 16 spacemen and divided them into two groups, 8 shouted by 2x plasma head distance while the other 8 spacemen was shouted by 3x plasma head distance, finally we take the last group and divided them into two groups 8 were shouted by 2.5 kW of plasma power and the other 8 were shouted by 5 kW of plasma power as you can see in the block diagram below **Fig.9**. This a completely grand new technique there is not any guide or reference to as, so the results is according to this sequences and any one could take different sequences and cheek if the results were similar to as or not. For the CNC-Plasma machine specification, the AJAN CNC-Plasma machine usually used for cutting application and the technique used changed in its specification as in **Table 3.**

4. RESULTS AND DISCUSSION:

The results, which calculated after plasma peening for the mechanical properties is as shown as in, **Table 4.** For Hardness it has been noticed that the major value was for the two time plasma shoot peening of 16 degree higher than (COSQC) reference while the miner value is for 3x head distance of 4 degree higher than reference which is clearly due to the amount of plasma effected at the specimen surface, for both the ultimate and yield tensile strength the enhancement wasn't much higher than references but a major increment were noticed for the two time plasma shoot peening this is also indicated that the alloys brittleness is increased due to the excessive heat from the plasma for two times which might made some changes in phases of the alloys surfaces leads the gran size to decrease. The extension of the alloys is decreased generally from references for all types due to the same reasons above but

the major increment is as expected for two times plasma shoot peening about 50% less than reference, while not noticed change in the modulus of elasticity for all sets the major decrement in fatigue strength was also for two times plasma shoot peening of about 9 MPa. **Fig.10** shows the effect of plasma peening for one time and two times plasma peening, **Fig.11** shows the effect of plasma peening power changing, while **Fig.12** illustrates the effect of head distance changing all with the standard P-S diagram the. **Fig.13** shows the changes in grain size due to SP treatments, where DT (dislocation tangles), DW (dislocation wall) and DDW (dense dislocation wall).

Finally, **Fig.14** shows the improvement in S-N curve from standard ASTM and that calculated from plasma shot peening of AL 2024-T3 for set one time peening, 1x head distance with 2.5KW power. The S-N carve for this set of this technique shows a god improvement with the ASTM Standard for low stresses and high cycles as we can see that for the same load say 100 MPa we get 2.22E+05 cycles for ASTM S-N standard and 3.37E+05 cycles for modified plasma shot peening S-N diagram which is a major improvement, this might be according due to decrement in dislocation as in slip and diffusion as in grain boundary sliding or both for the same reason above knowing that we used (High Cyclic Fatigue) test and Basquin equation ($\sigma_a = \sigma_f (N_f)^b$) for calculating fatigue life to get ($\sigma_a = 154(5.25E+05)^{-0.0335}$) with ($\sigma_a = 99.06\ MPa$).

7. CONCLUSION

Its well-known that the yielding dependent upon nature of the material or alloy, also known that if the yielding increased this leads the materials to became more brittle which decreases the extension percentage at the tensile test and verse versa. Inscrutably this technique decreases the yielding with decrement in extension percentage too. The explanation of this criterion is that the heat produces from plasma hardened the surface of the alloy only, while the center of the alloy still the same. Then, when the surface cooled, its grin cells became smaller in size with respect to the internal grin cells which remains at its original size because it cooled slower, so when we test the alloy for tensile test and check the result it was found that an increment of about 25%-50% according to the technique used in both yielding and extensions percentage both ,this is only can be done by this technique while other treatments does not give such condition.

From this work it can be re-discovered the great benefits of plasma techniques in industrial application ,by using a unique novel technique by the use a CNC-Plasma Cutting Machine to perform plasma peening on AL 2024-T3 and it was found that this technique changes it's mechanical properties in deferent levels ,this change depends upon the parameters applied from changing the nozzle head distance of the plasma arc to change the power of the plasma applied and number of plasma peened the amount of mechanical properties that changed even if it was not huge but clearly noticed especially if we know that this technique is kind of cheap with respect to other shoot peening applications gives this technique privilege as the other applications not doesn't optimize the material beater, so for those how need quick not expensive easily handled this technique is the best choice for them.

8. REFERENCES

- Adnan Akkurt, 2009, *Surface Properties of the Cut Face Obtained by Different Cutting Methods from AISI 304 Stainless Steel Materials* , Indian Journal of Engineering & Materials Sciences Vol. 16, pp. 373-384.

- Ali A.Ali, Esam A.Ebrahim, Mohammed H.Sir, Barazan A.and Hamah Said, 2013, *Effect of Shot Peening Time on Mechanical Properties of Aluminum Alloys AA2017-T4 And AA6063-T5*, Diyala Journal for Eng. & Sci. Vol. 06, No. 02, pp. 1- 8.

- AJAN manual catalog, 2014, *İAOSB 10014 Sk. No: 1 Çiğli – İZMİR* – TURKİYE.

- ASME, 2003, *Influence of Shot Peening on Surface Durability of Plasma Case-Hardened Sintered Powder Metal Gears*, ASME 2003 Design Engineering Technical Conferences, Computers, and Information in Engineering Conference, Chicago, Illinois, USA, and September 2-6.

- ASTM, 2012 ,*(ASTM) Standard Specification for Aluminum and Aluminum-Alloy Sheet and Plate*.

- E.R. de los Rios. M.Troolr and A.Levers, 2011 , *Improving the Fatigue Crack Resistance of 2024-T35l Aluminum Alloy by Shot Peening*, British Aerospace Airbus Chester Road,Ch4.

- James Campbell, April 2 - 5, 2001, *Effects of Shot Peening Processing on the Fatigue Behavior of Three Aluminum Alloys and Ti-Al-4v*, Proceedings of the 55th Meeting of the Society for Machinery Failure Prevention Technology. Virginia Beach, Virginia.

- Locke, J.E, Kumar,B and Salah,L. 2007, *Effect of Shot Peening on the Fatigue Endurance and Fatigue Crack Growth Rate Of 7050 and 7075 Aluminum Alloys*, National Institute of Aviation Research, Wichita State University, USA.

- Linde Group, 2014, BOC Limited ,*Facts About Plasma Technology and Plasma Cutting*.

- Mohd Idris Shah Ismail, and Zahari Taha, 2014, *Surface Hardening of Tool Steel by Plasma Arc with Multiple Passes*, International Journal of Technology (2014) 1: 79-87.

- Béjar,M.A and Henríquez,R., 2009, *Surface Hardening of Steel by Plasma-Electrolysis Bronzing*, University of Chile, Casillas 2777, Santiago 6511265, Chile, Available online 12 July 2009.

- Petrov,S.V and Saakov,A.G., 2007 , *Technology and Equipment for Plasma Surface Hardening of Heavy-Duty Parts*, Materials and Manufacturing Processes, Vol.17, Issue 3.

➢ Trdan,U., Skarba,M. and Gruma,J., 2014, *Laser Shock Peening Effect on the Dislocation Transitions and Grain Refinement of Al–Mg–Si Alloy*, Elsevier Materials Characterization Journals, 97 (2014)57 68.

Table 1. Chemical properties of al-alloys 2024-T3.

Component	% Si	% Fe	% Cu	% Mn	% Mg
Standard	≤ 0.5	≤ 0.5	3.8-4.9	0.3-0.9	1.2-1.8
Actual	0.25	0.09	4.53	0.81	1.51
Component	% Cr	% Zn	% Ti	% other	% Al
Standard	≤ 0.1	≤ 0.25	≤ 0.15	≤ 0.2	Reminder
Actual	0.014	0.13	0.014	0.065	Reminder

Table 2. Mechanical properties of al-alloys 2024-T3 as taken from the COSQC.

Mechanical Properties	Value
Hardness , Rockwell B	72 Converted from Brinell Hardness Value
Ultimate Tensile Strength	482 MPa
Tensile Yield Strength	340 MPa
Elongation at Break	16.5%
Modulus of Elasticity	71.5 GPa
Poisson's Ratio	0.32
Fatigue Strength	135 MPa
Shear Modulus of Elasticity	27.35 GPa
Shear Strength	281 MPa
Specific Heat Capacity	0.875 J/g-°C
Thermal Conductivity	121 W/m-K

Table 3. Both standard and the new technique machine specification.

Specification	Original Specification	New Specification
X, Y, Z axis feed rate	600 mm/min	1200 mm/min
Plasma head distance	25 mm	50 mm,75 mm
power	11 KW	2.5 KW, 5 KW
Gases used	5	3
Positioning increment	10 micron	10 micron
Max air volume	1200 m^3 / hour	1600 m^3 / hour
Plasma gas consumption	52 liter/min	29 liter/min

Table 4. Experimental results of mechanical properties of al-alloys 2024-T3, The yellow refers to highest while the red to lowest changes green for standard.

Properties	One time Shoot	Two time shooting	2x head Distance	3x head distance	2.5KW Power	5KW power	Standard
Hardness, Rockwell B	80	88	78	76	80	83	72
Ultimate tensile Strength (σ_{ut}) MPa	440	412	447	435	445	461	482
Tensile yield strength (σ_{yt}) MPa	348	305	345	325	356	333	340
Elongation at break %	12.7%	8.8%	5.9%	11.4%	11.7%	12%	16.5%
Modulus of elasticity (E) GPa	70.3	69.8	70.8	70.05	70.5	71.1	71.5
Poisson's ratio υ	0.32	0.32	0.32	0.32	0.32	0.32	0.32
Fatigue strength (σ_f) MPa	131	127	135	140	137	125	135

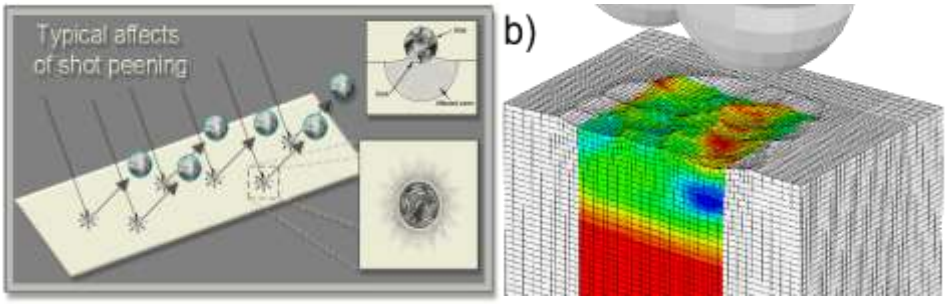

Figure 1. a) Typical effects of SP, **b**) finite model of SP at spacemen surface.

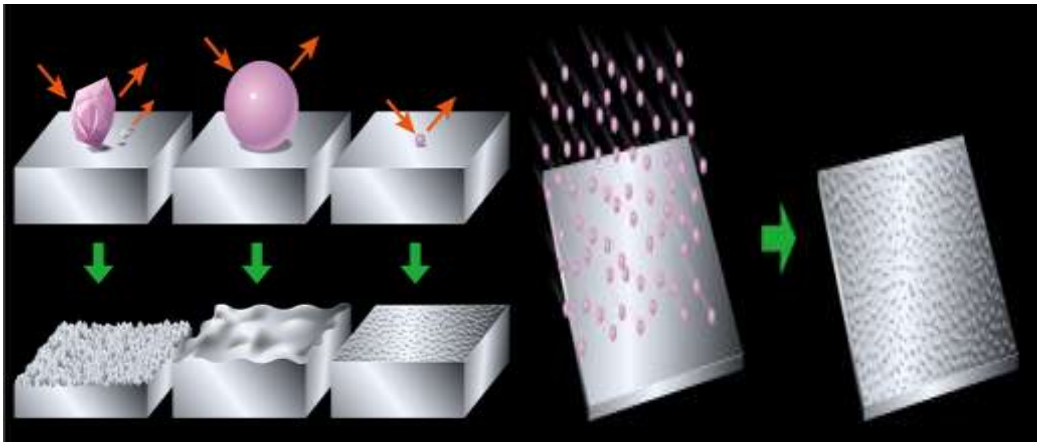

Figure 2. Effects of different types or size of particles on SP.

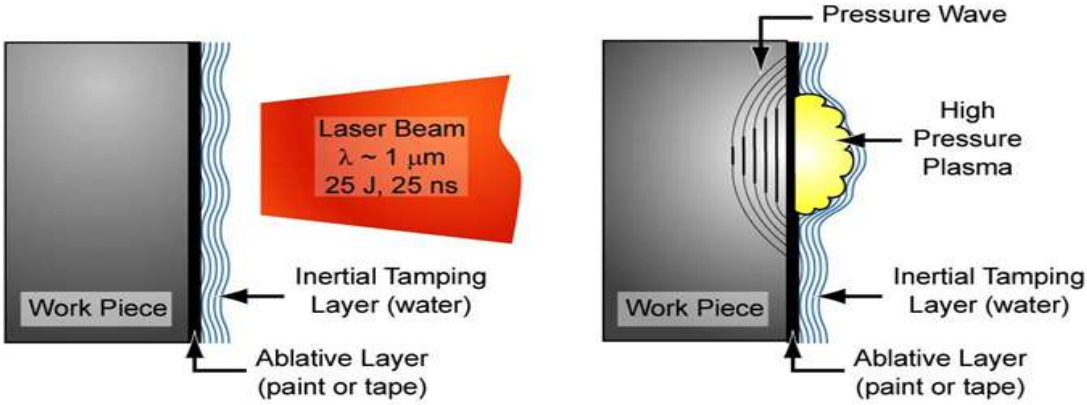

Figure 3. Schematic configuration of laser shock peening LSP.

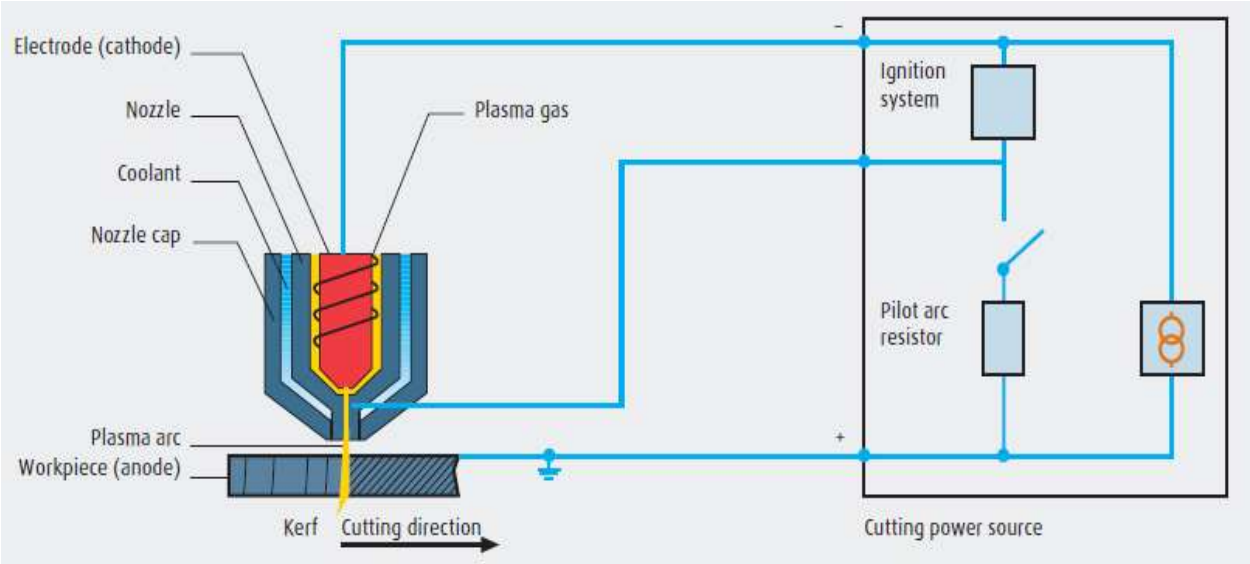

Figure 4. Principle of plasma technique, **Linde Group, 2013.**

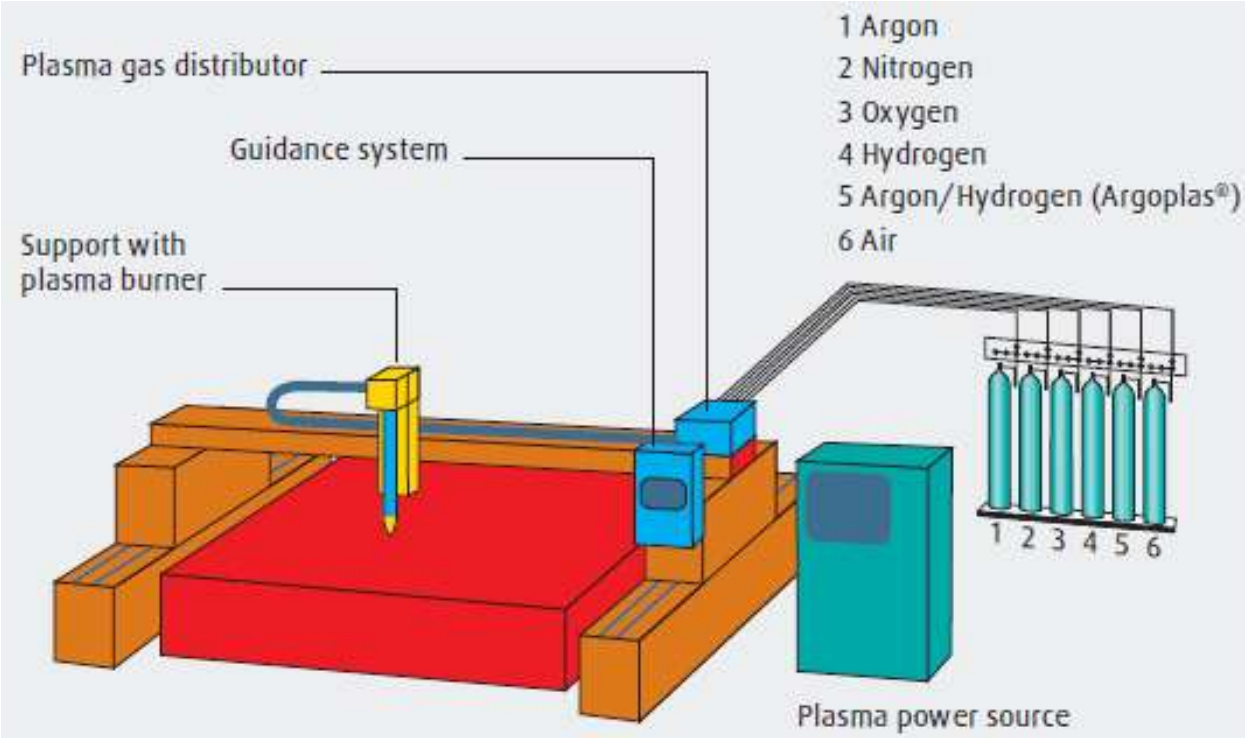

Figure 5. Example setup for standard plasma machine **,Linde Group, 2013.**

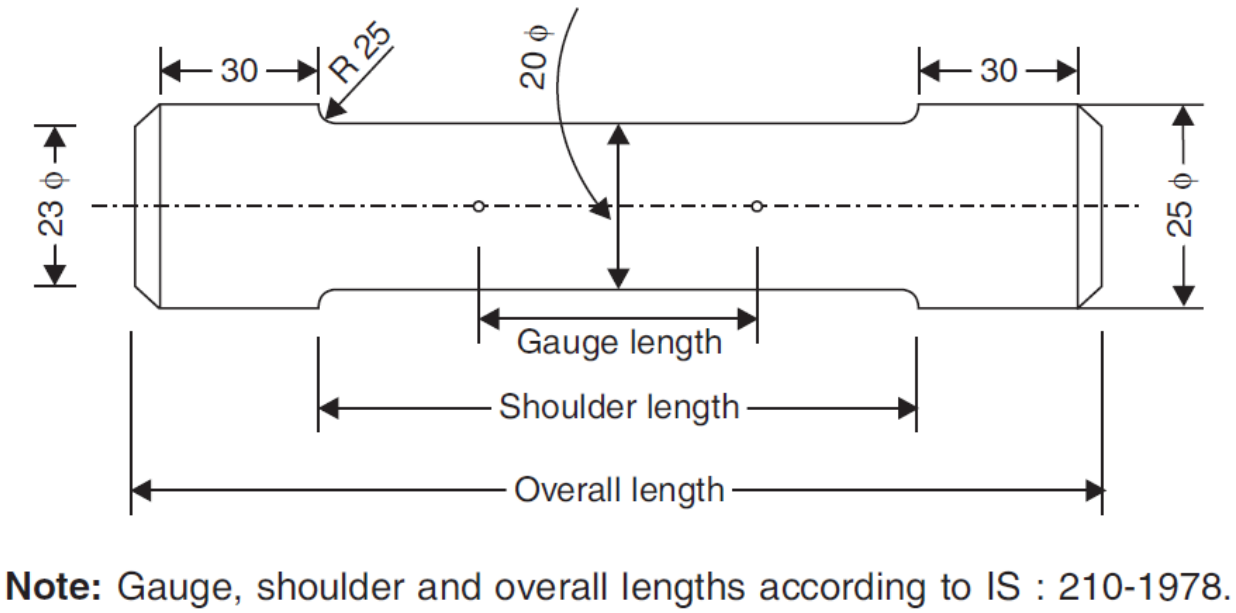

Figure 6. ASTM standard tensile test specimen for both shafts and plane spacemen with R = 40 for plane model, all dimension in (mm), **ASTM Standards, 2012.**

Figure 7. AJAN CNC-plasma machine.

Figure 8. Machine heads.

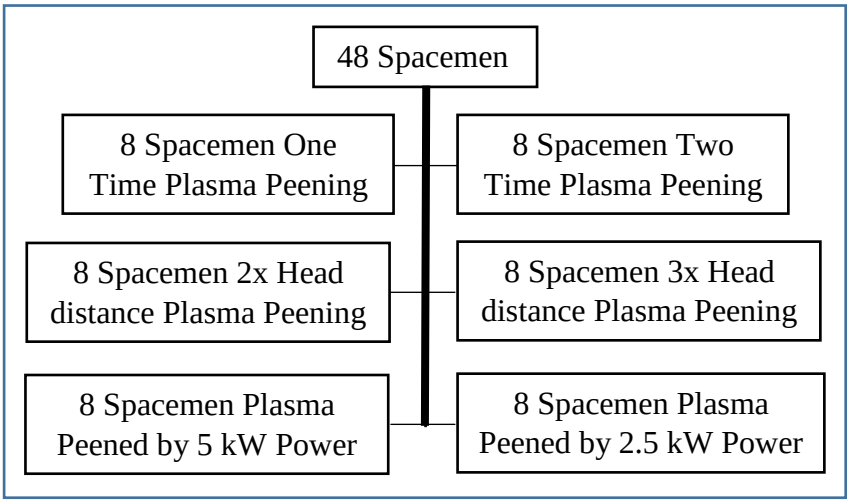

Figure 9. Block diagram of the technique procedure.

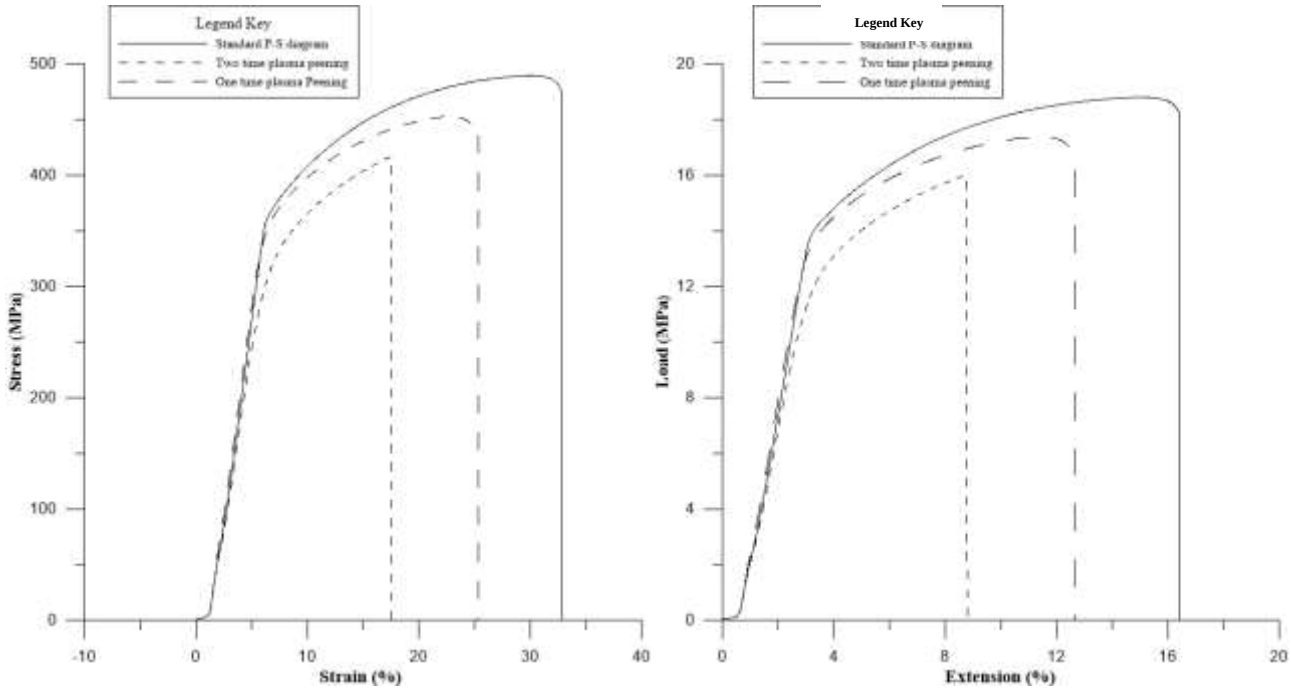

Figure 10. The effect of one time and two times plasma peening on P-S diagram of AL 2024-T3.

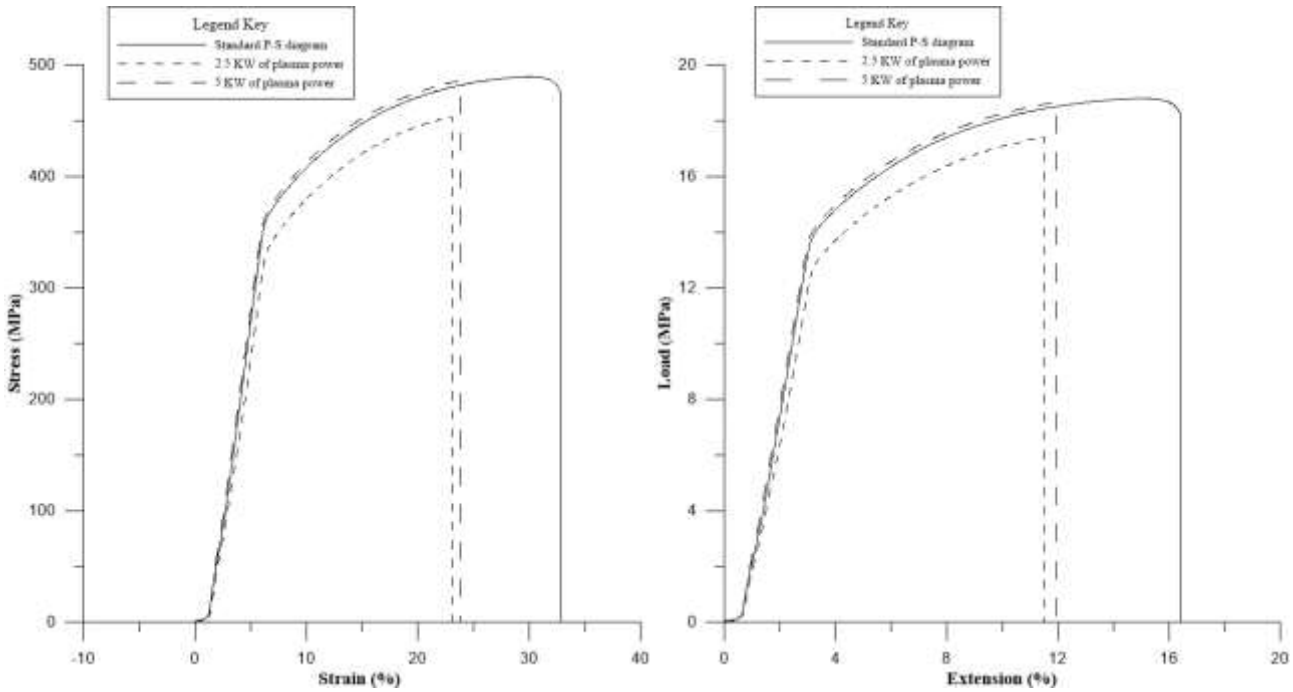

Figure 11. The effect of power changing of plasma peening arc on P-S diagram of AL 2024-T3.

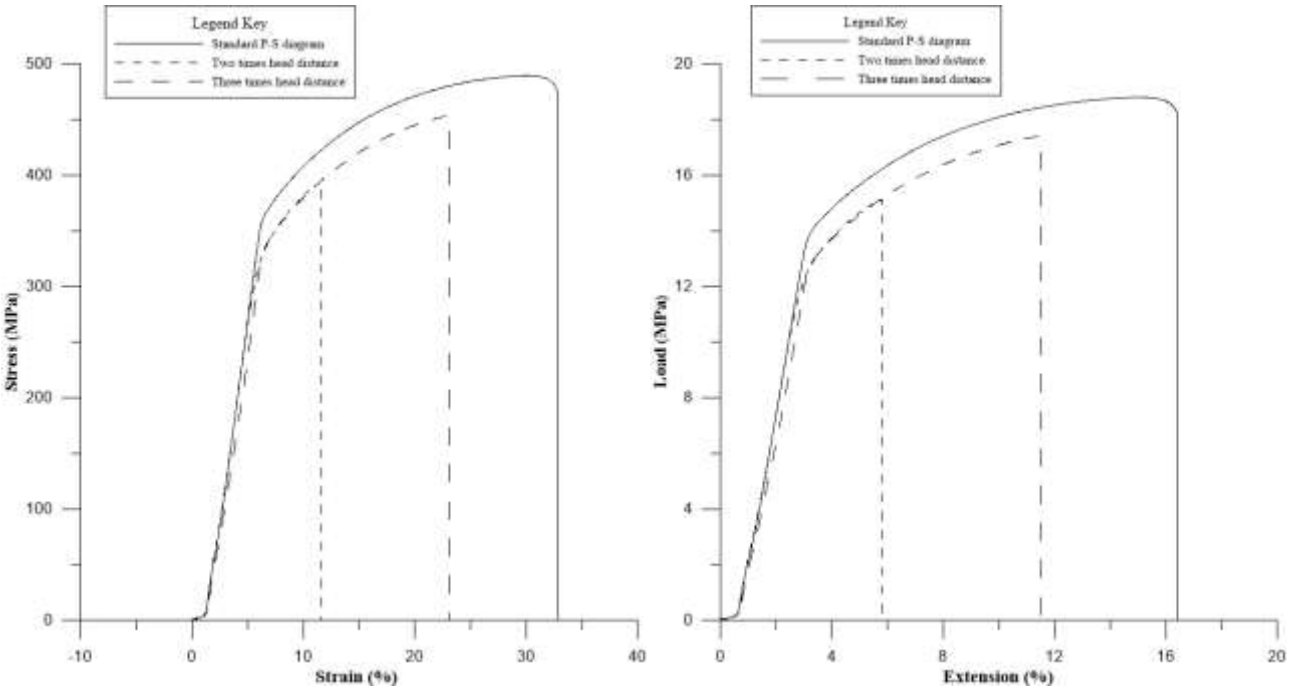

Figure 12. The effect of changing of plasma peening arc head distance on P-S diagram of AL 2024-T3.

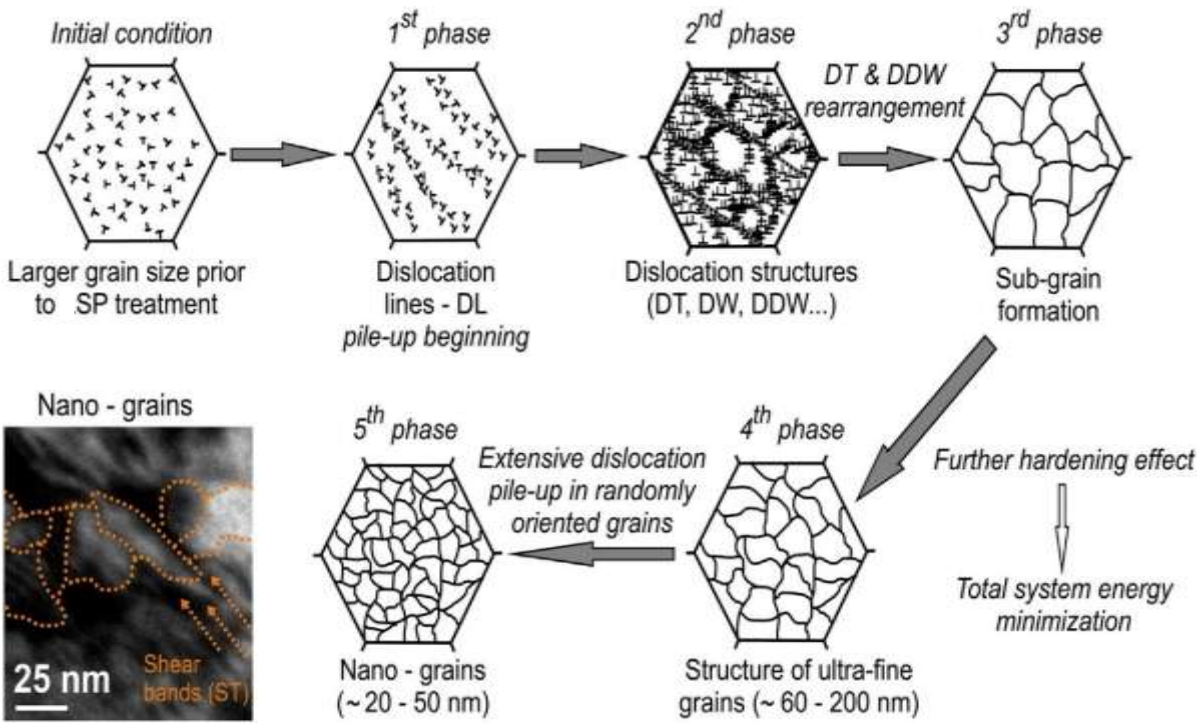

Figure 13. Schematic diagram shows the changes in grain size due to SP treatments.

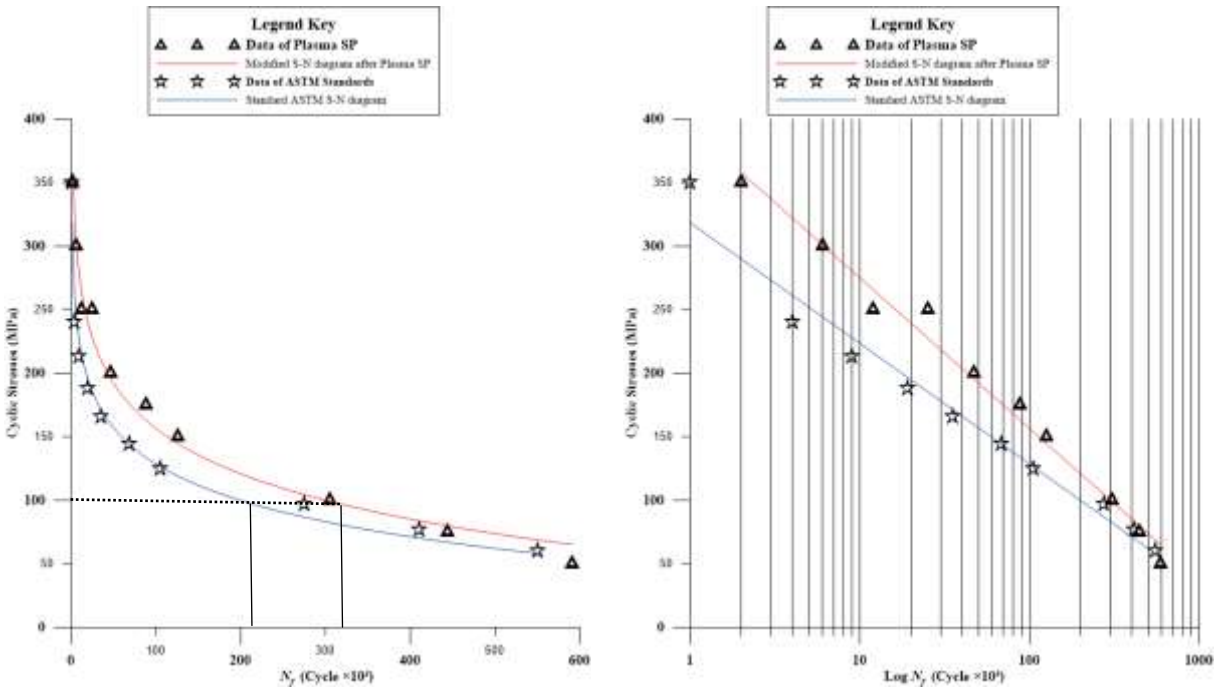

Figure 14. The improvement in both Liner and logarithmic S-N diagram of the AL 2024-T3 shot penning by plasma of the set (One time peening, 1x head distance with 2.5KW power) with the ASTM standard.